The Pennsylvania State University

The Graduate School

Department of Mechanical and Nuclear Engineering

CHARACTERIZATION OF DISTRIBUTED PERFORMANCE OF POLYMER ELECTROLYTE FUEL CELLS UNDER LOW HUMIDITY CONDITIONS

A Thesis in

Mechanical Engineering

by

Qunlong Dong

Submitted in Partial Fulfillment
of the Requirements
for the Degree of

Doctor of Philosophy

December 2006

The thesis of Qunlong Dong was reviewed and approved* by the following:

Matthew M. Mench
Assistant Professor of Mechanical Engineering
Thesis Advisor
Chair of Committee

Chao-Yang Wang
Professor of Mechanical Engineering

Kendra V. Sharp
Assistant Professor of Mechanical Engineering

Bruce E. Logan
Kappe Professor of Environmental Engineering

H. Joseph Sommer III
Professor of Mechanical Engineering
Head of the Department of Mechanical and Nuclear Engineering

*Signatures are on file in the Graduate School

ABSTRACT

Low humidity operation is helpful to restrain flooding within polymer electrolyte fuel cells (PEFCs), as well as to reduce system overhead. However, low humidity operation also brings challenge on membrane hydration. In order to better understand the water transport in PEFCs under low humidity condition, as well as provide detailed experimental validation for development of advanced modeling of PEFCs, an experimental study combining simultaneous current, resistance and species distribution measurements was conducted, and a quasi-two-dimensional mass transport model was developed to analyze the effect of transport properties of fuel cell materials on water management for low humidity operation.

Two segmented fuel cells with very different flow field configurations and thermal boundary conditions were designed and developed for this study. The actively control on the backing plate temperature of the improved design enables an isothermal boundary condition. Two new techniques for *in-situ* species measurement, a Micro Gas Chromatograph (Micro GC) and a Real Time Gas Analyzer (RTGA), have been applied with the ability to measure up to saturated levels in the flow stream.

Typical PEFC steady-state and transient behaviors under low humidity operating conditions were investigated respect to various operation parameters, including inlet humidity, reactant stoichiometry, temperature, and pressure. The results show that, under reduced humidity conditions the anode water content has dominating effect on current density profile. The current distribution curves look qualitatively similar to water mole fraction in the anode curves, and the inverse of the high frequency resistance (HFR) profiles. Based on these experimental results, a characteristic profile of current density, species, and HFR distributions is proposed for low humidity operation. The change of thermal boundary does affect the distributed performance, although the essential distribution profiles are maintained, reaffirming the importance of thermal management on water management.

The dynamic response of fuel cell performance to step change in voltage is heavily affected by humidification condition. For a dry cathode condition, the anode

water content adjusts relatively slowly from high to low current, while for a dry cathode condition, the adjustment is relatively fast. For both cases, the current density adjustment time corresponds to the time of mass adjustment in the anode side, not the cathode side, indicating a non-linear water content profile in the electrolyte membrane.

With low inlet humidities, the fuel cell performance is more limited by insufficient electrolyte hydration instead of depletion of oxygen. In general, the higher overall input relative humidity results in the higher bulk cell performance, despite very different local distributions. The humidifying effect from water production on the cathode catalyst layer is another critical factor for the performance PEFCs under low humidity condition. Higher cathode stoichiometry, elevated cell temperature, and lower exit pressure can all increase the amount of water required for humidification and reduce the humidifying effect of water production, resulting in lower cell performance. However, a high overall inlet relative humidity can negatively impact the cell performance under the combination of high temperature and low pressure due to the extremely low oxygen concentration.

A mass transport model was developed to examine the transport properties of Gore SELECT® MEAs, as well as be a tool to look at ideal low humidity operation design. The mass transport model found that the water diffusion coefficient in Gore SELECT® reinforced membrane roughly equals the coefficient in Nafion® membrane. It was also detected that the mass transport resistance of porous gas diffusion media can create considerable water activity difference between the gas flow channel and the catalyst layer, which boosts the humidifying effect of generated water. The relatively high binary diffusion coefficient of H_2O/H_2 in the anode compared to the air cathode contributes to the dominating effect of local anode water profiles on local cell performance. These findings also provide direction to the development of MEA for low humidity operation.

TABLE OF CONTENTS

LIST OF FIGURES

LIST OF TABLES

NOMANCLATURE

English symbols

a	activity
C	molar concentration, mol/m^3
D	diffusion coefficient of species, cm^2/s
E	voltage, V
E^0	theoretical equilibrium potential, V
EW	equivalent weight of dry membrane, kg/mol
F	Faraday's constant, 96,485 C/mol
G	Gibbs free energy, kJ/kg
i	current density, A/cm^2
i_0	exchange current density, A/cm^2
i_L	limiting current density, A/cm^2
j	$\sqrt{-1}$
k_{hyd}	hydraulic permeability coefficient
L	overall flow field path length, m
N	mole flow rate of species in the flow channel, mol/s
n	equivalent electrons transferred
n	molar flux, mole/s·m^2
n_d	electro-osmotic drag coefficient
P	pressure, Pa
R	the universal gas constant, 8.314 J/mol·K
R_{el}	resistance of the electrolyte membrane and fuel cell components, Ω
R_{ct}	the charge transfer resistance, Ω
R_{total}	total resistance of fuel cell
T	temperature, K
V	voltage, V
w	width of the membrane, cm

x	mole fraction
y	position in through-the-plane direction
Z	impedance, Ω

Greek symbols

α	charge transfer coefficient
α	effective drag coefficient, ratio of net water flux to proton flux in membrane
β	ratio of water diffusion coefficient in reinforced membrane to water diffusion coefficient in Nafion® membrane
Δ	change in
δ	thickness, cm
ε	porosity, or volume fraction of ionomer in catalyst layer
η	overpotential, V
ξ	stoichiometry
λ	membrane water content
ρ	density, kg/m^3

Subscripts and superscripts

A	anode
act	activation
C	cathode
cell	fuel cell
CL	catalyst layer
conc	concentration
diff	diffusion
eff	effective value
ele-osm	Electro-osmotic drag
g	gas phase
GDL	gas diffusion layer

H	hydrogen, H_2
i	species i
in	inlet of the flow channel
j	species j
m	ionomer phase
MPL	micro porous layer
N	nitrogen, N_2
O	oxygen, O_2
ohm	ohmic
out	outlet of the flow channel
re	reinforced membrane
sat	water saturation
total	total
W	water, H_2O

ACKNOWLEDGEMENTS

First and foremost, I would like to thank my advisor Dr. Matthew M. Mench for his guidance, academic and financial support throughout my entire graduate studies at Penn State University. I highly appreciate his advice, and it has been a great pleasure being his student. I would also like to recognize the other members of my advisory committee: Dr. Chao-Yang Wang, Dr. Kendra V. Sharp, and Dr. Bruce E. Logan for their support and for all their recommendations to my thesis.

I extend my appreciation to Gore Fuel Cell Technologies of W. L. Gore & Associates, Inc. for their financial, and test material support. Special thanks to Dr. Uwe Beuscher and Dr. Simon Cleghorn of Gore Fuel Cell Technologies who provided very helpful information on material properties and excellent discussions on experimental results. I would also like to appreciate Air Products and Chemicals, Inc. for their financial support during the third semester of my Ph.D. study, and Agilent Technologies for their help and training on MicroGC and RTGA.

I would like to acknowledge Mr. Achim Heibel and Dr. Roychelle Ingram-Ogunwumi of Environmental Technologies of Corning Inc., for their help and support since I started working for Corning. I highly appreciate their allowance on my work schedule when I was writing my thesis.

I would like to sincerely thank Mr. Berk R. Gerdes for his hard work on fuel cell design and the long weeks of trouble-shooting and testing, thank Mr. Suhao He for his insight discussion on the model, thank Mr. Oliver H. Finckh and Mr. Daniel Burford for their guidance on fuel cell testing, and thank Mr. Daniel Shields and Mr. Jon Koll for their assistance on experiment and data analysis. I would also like to thank all my lab mates and the entire MNE department staff and faculty for all their help.

Finally, I would like to thank all my family and friends who were always strong supporters.

Chapter 1

INTRODUCTION

1.1 Background

Fuel cells are electrochemical devices that convert the chemical energy of a reaction directly into electrical energy. They have been considered as one of the most promising candidates for future power generation due to their high energy-conversion efficiency, near zero emission, quiet, and scalable operation. The basic physical structure of a fuel cell consists of an electrolyte layer in contact with a porous anode and a porous cathode on either side.

The invention of fuel cell can be traced to the year of 1839, when lawyer and scientist Willam Robert Grove discovered the reverse electrolysis process of water for the first time. Because of the limits of low catalyst specific active area and high electrolyte resistance, the current that can be supplied by the prototype fuel cell was too small to be applied for any realistic usage. It was soon found that there were many scientific hurdles to overcome if this technology were to be commercialized, and the early interest on Grove's invention diminished. By the end of 19th century, the inventions of variant thermal engines and electrical generators, the widespread exploitation of fossil fuels, and the advances in batteries relegated the fuel cell to a scientific curiosity.

The research and development of fuel cell did not get much attention until late 1950s, the time of the space competition between the Unite States and the former Soviet Union. Space applications have special requirements in compactness and high efficiency for power generation device in order to decrease the weight that must be carried. Batteries were too heavy; solar energy was too expensive at that time; and nuclear power was too risky. So NASA had to seek alternatives and fuel cell got noticed again. Fuel cells meet these requirements of space application. Furthermore, an additional benefit of fuel cell powers is that they produce drinkable water as a by-product.

A variety of fuel cells are in different stages of development. They can be classified by use of diverse categories. The most common classification of fuel cells is by the type of electrolyte used in the fuel cells: 1) polymer electrolyte fuel cell (PEFC), 2) alkaline fuel cell (AFC), 3) phosphoric acid fuel cell (PAFC), 4) molten carbonate fuel cell (MCFC), and 5) solid oxide fuel cell (SOFC).

So-called polymer electrolyte fuel cell has an ion conducting polymer membrane as the electrolyte. Compared to other kinds of fuel cells, there is no corrosive liquid presenting in this kind of fuel cells, thus corrosion problems are minimal in PEFCs. Because the cell separator is a polymer membrane and there is no highly corrosive material, issues such as sealing, assembly, and handling are much less complex than other fuel cell systems. This makes PEFC system be able to generate high power densities. PEFC systems also typically operate at low temperatures (around 80 °C), and then permit faster startup. Therefore, PEFCs is attractive for transportation application and for stationary power applications less than 100kW.

Willard Thomas Grubb, a chemist of General Electric (GE), invented PEFC in 1955, while he was considering new application areas for ion-exchange membranes. He modified the fuel cell design by using a sulphonated polystyrene ion-exchange membrane as the electrolyte. Three years later, Leonard Niedrach, another GE chemist, found a way to deposit platinum on to the membrane, this greatly improved the power density of PEFC and led to the application of GE manufactured PEFC in U.S. Gemini space program beginning 1962.

In these early PEFCs, the electrolyte membranes were based on hydrocarbon polymers, and the easy oxidative degradation effect of C-H bonds in these polymers limited the lifetime of these fuel cells. In addition of the lifetime problem, as high as 28 mg/cm2 platinum loading was also required to provide suitable power densities. As a result, Alkaline Fuel Cells (AFCs) replaced the role of PEFCs in the Apollo and early space shuttle missions. The development of PEFC met bottleneck and went into abeyance in the 1970s and early 1980s.

In mid 1980s, the research of PEFCs became active again because of the breakthroughs in electrolyte material and catalyst technology. The developments of

proton exchange membranes based on stable sulphonated fluoropolymers (commonly fluoroethylene) greatly lengthened the lifetime of PEFCs. The most famous one and almost the industry standard is Nafion®, an ionomer developed by Dr. Walther Grot at DuPont in 1970s. On the other hand, due to the outstanding contribution done by the fuel cell group of Los Alamos National Laboratory, the amount of necessary platinum used in electrode catalyst was decreased by over 100 times. This made the PEFC technique affordable for common usages.

At present, it could be said that the scope of the possible applications of PEFCs exceeds those of all other electrical energy generation technologies. PEFCs are a possible power source at a few watts for cell phones and other portable electronic equipment such as laptop computers, through a few kilowatts for domestic systems, to tens of kilowatts for cars, to hundreds or thousands of kilowatts for industrial combined heat and power systems. Compared to batteries and heat engines, PEFCs have following advantages:

1) The energy converting efficiency of PEFCs is 40~60%, much higher than the 25~35% efficiency of internal combustion engines.

2) Fuel cell technology is an environmentally friendly technology. The only emission of hydrogen fuel cells except that produced to obtain hydrogen is water; while heat engines such as gas turbines and internal combustion engines using fossil fuels produce carbon monoxide (CO), nitro oxides (NOx), hydrocarbons (CHs), and carbon dioxide (CO2) that are harmful to the environment.

3) PEFCs are typically quiet compared to heat engines because there is no moving part in operating fuel cells and the auxiliary equipment are also quiet.

4) PEFCs can be scaled due to the simple structure and similarity among different PEFCs, simplifying the design and production process.

5) PEFCs do not have a time-consuming recharge process. A fuel cell can run as long as fuel and oxidant are supplied, and the refilling of fuel and oxidant can be rapid.

1.2 Operating Principles of Polymer Electrolyte Fuel Cells

1.2.1 Basic structure of PEFCs

As shown in Figure **1-1**, a polymer electrolyte fuel cell (PEFC) consists of a solid polymer membrane as the electrolyte, porous electrodes containing platinum catalyst, solid porous gas diffusion layers (GDLs), and current collector plates, which also form the flow field. The catalyst layers also function as electrodes. To operate a hydrogen PEFC, humidified hydrogen or hydrogen rich fuel is required for the anode, and humidified oxygen or air is required for the cathode.

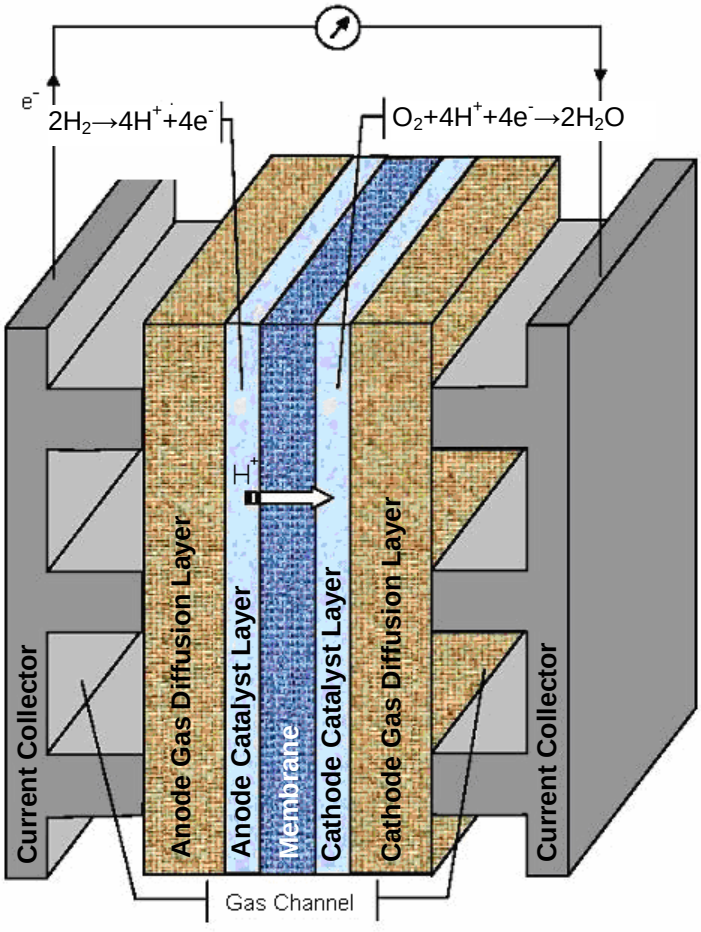

Figure **1-1**: Schematic Structure of Single PEFC [**1**]

In the anode side, hydrogen diffuses from the flow channel to the catalyst layer through the GDL. And then on active catalyst sites, hydrogen molecules ionize, releasing electrons and creating H^+ ions (or protons), as shown by Equation **1.1**.

$$2H_2 \rightarrow 4H^+ + 4e^- \qquad [\mathbf{1.1}]$$

In the cathode side, oxygen also diffuses from the flow channel to the catalyst layer, and then reacts with electrons flowing through the out circuit and H^+ ions flowing through the electrolyte membrane on active catalyst sites. Water is generated by the cathode electrochemical reaction, as shown by Equation **1.2**

$$O_2 + 4H^+ + 4e^- \rightarrow 2H_2O \qquad [\mathbf{1.2}]$$

Clearly, for both reactions to proceed continuously, electrons produced at the anode must flow through an electrical circuit to reach the cathode. On the other hand, the generated protons must pass through the electrolyte membrane. In the prototype fuel cell by Willan Grove, diluted sulphuric acid provided free H^+ ions, and served as pass path of H^+ ions produced in anode. In PEFCs, membranes made in proton conductive polymers serve the similar function of fluid acids. Because these membranes are called proton exchange membranes (PEM), PEFCs are also called proton exchange membrane fuel cells (PEMFC).

The common theme of polymer electrolyte membranes is the use of sulphonated fluoropolymers. The main features of this kind of ionomers are high chemical resistance due to C-F bonds, high mechanical strength, and good proton conductivity. The most famous and nearly “industry standard” polymer for PEFCs is Nafion®, a trade mark of DuPont, which is based on perfluorosulfonic acid (PFSA) technique and has much better chemical stability than the hydrocarbon-based membranes used in earlier PEFCs. Figure **1-2** shows the chemical structure of Nafion®.

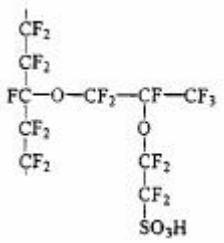

Figure **1-2**: Chemical composition of Nafion®

As shown in Figure **1-3[2]**, Nafion® are composed of polytetrafluoroethylene (PTFE or Teflon®) backbone and perfluorinated-vinyl-polyether side chains containing a sulfonic acid group at the end. With available water in the membrane, highly hydrophilic sulfonic acid groups on side chains will absorb water and ionize to enable mobility of H^+ ions. The mobility or conductivity of proton is highly dependent on the water content of the membrane. For a Nafion® membrane, the conductivity can be achieved as high as 0.1S/cm with full hydration at 80°C.

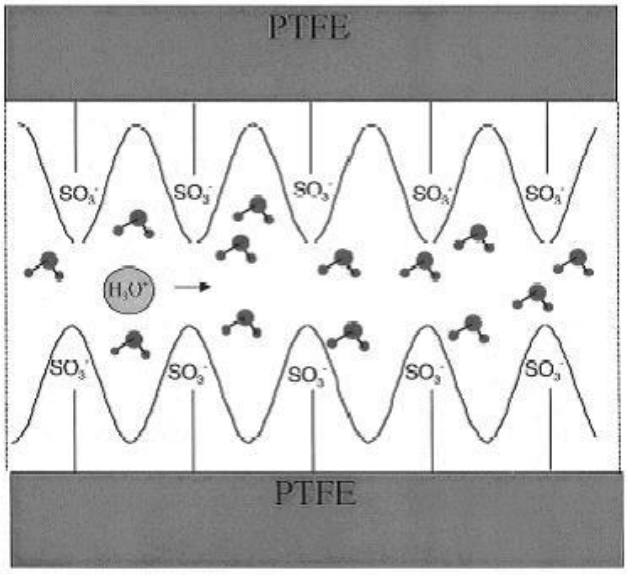

Figure **1-3**: Schematic Structure of Nafion® [**2**]

The electrode is applied either directly on the surface of the membrane or on the GDL and then hot-press to the membrane. The catalyst, integral with its binder, forms the

electrode. The binder performs multiple functions. It forms the overall architecture of the electrode. At the same time, the binder also fixes the catalyst particles. There are two schools of thought on the composition of binder. The first school of electrode science applied polytetrafluoroethylene (PTFE) as the binder to get an overall hydrophobic property, which facilitates the removal of excessive liquid water from the electrode. The second school of thought developed a hydrophilic electrode in which the binder is perfluorosulfonic acid. The motivation for this development was to enhance the membrane/catalyst contact to minimize the platinum loading requirements. For PEFCs operating with pure hydrogen, the cathode and anode commonly have identical carbon supported platinum catalyst. For other fuels, such as reformate (containing H_2, CO_2, CO, and N_2), an alloy of platinum containing ruthenium is the desired catalyst. At present, platinum loading of the-art-of-state PEFCs have been reduced to 0.2 mg/cm^2, making the cost of platinum a small fraction in total cost.

The gas diffusion layer (GDL) is a thin layer of porous material, which is typically carbon-based, in cloth form or a no-woven pressed paper-like fiber configuration, and typically has a thickness of 100-300 μm. The GDL plays an important role in PEFC. It allows diffusion of reactants to, and products from the catalyst layers, conducts the electrons between catalyst layers and the current collecting landings, controls heat transfer from the catalyst surface, and also provides extra mechanical support to the thin electrolyte membrane. GDL commonly incorporates a hydrophobic material, such as polytetrafluoroethylene (PTFE or Teflon®) to gain hydrophobicity. The function of this property is to prevent water from “pooling” within the pore volume of the GDL, to maintain a path for the gas transportation between flow channels and the catalyst layer. Furthermore, it facilitates product water removal on the cathode as it creates a non-wetting surface within the passages of the GDL.

1.2.2 PEFC performance

The maximum achievable open circuit potential for an electrochemical cell can be described with the thermodynamic concept of available energy, or Gibbs free energy, ΔG, and is shown in Equation **1.3**. The maximum achievable voltage for a hydrogen PEFC at standard operating conditions is 1.18 V.

$$E^o = \frac{-\Delta G}{nF} \qquad [\mathbf{1.3}]$$

As other electrochemical power systems, the actual voltage of PEFC is lower than its theoretical equilibrium potential, due to multiple irreversible losses, which are also called polarization or overpotential. As shown in Figure **1-4 [3]**, the performance of a PEFC is characterized by three kinds of losses: Activation polarization, Ohmic polarization, and Concentration (mass transfer) polarization. These polarizations dominate different parts of the operating range of PEFC and result in a cell voltage that is less than its ideal potential.

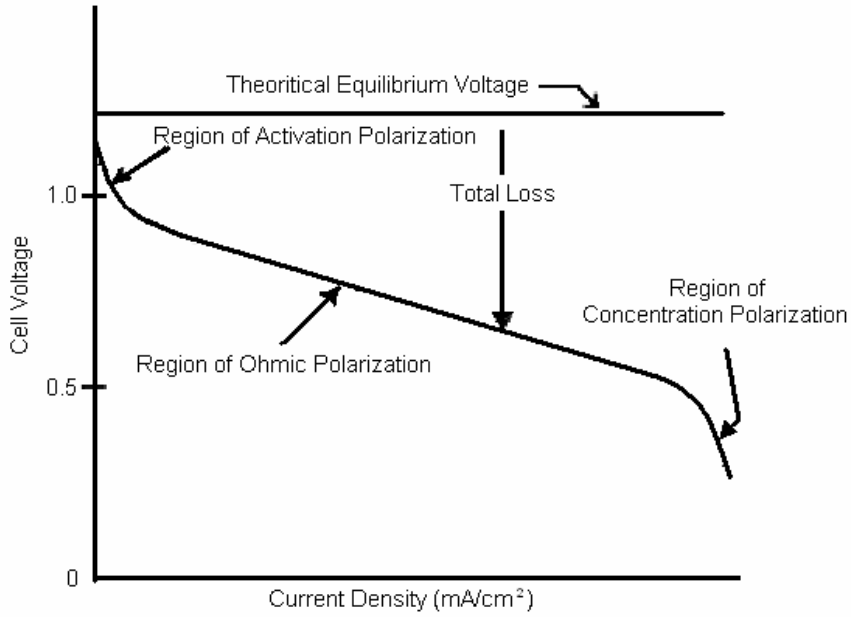

Figure **1-4**: Typical Fuel Cell Voltage/Current Curve[**3**]

The activation polarization dominates the low current density region. Activation polarization presents when the rate of an electrochemical reaction is controlled by sluggish electrode kinetics. Similar to chemical reaction, electrochemical reactions also involve activation energy that must be overcome by the reacting species. In other words, electrical barriers must be overcome prior to current and ion flow. The activation loss of an electrode increases as current increases, and can be described by Butler-Volmer equation:

$$i = i_0\left[\exp\left(\frac{\alpha_A nF}{RT}\eta_{act}\right) - \exp\left(-\frac{\alpha_C nF}{RT}\eta_{act}\right)\right] \qquad [\mathbf{1.4}]$$

In the above equation, i_0 is the exchange current density, η_{act} is the activation overpotential, n is the number of electrons transferred in an electrode reaction, α_A is the anodic transfer coefficient, and α_C is the cathodic tranfer coefficient.

Ohmic polarization is caused by limited ionic conductivity of the membrane, resistance of the porous GDL and the current collector, and the contact resistance between the current collector and GDL. Ohmic polarization (loss) varies directly with current, increasing over the entire range of current. Since contact and cell resistances are essentially constant, the ohmic variations with conditions can be attributed to changes in electrolyte conductivity, which is directly related to water content. Ohmic losses dominate the moderate current density region. Compared to other components, the majority of ohmic loss is contributed by the membrane; so good hydration of the membrane is necessary to reduce ohmic loss of the membrane. The Ohmic losses can be expressed by Ohm's law:

$$\eta_{ohm} = iR_{total} \qquad [\mathbf{1.5}]$$

where R_{total} is the total internal ohmic resistance of the fuel cell.

The potential difference produced by a concentration change at the electrode is called the concentration polarization. The high current density region of the polarization curve is dominated by this kind of polarization. Concentration polarization actually occurs over the entire range of current density, but the polarization becomes prominent in

the high current density regime because of the rapid increases of reactant activity losses in mass transport processes. With high current densities, high reactant fluxes to the electrode catalyst layer are required to maintain the electrode reaction. However, the reactant fluxes are limited by variant mass transport barriers from the gas flow channel to active catalyst sites and thus result in higher concentration gradients. That means the activities of reactants and products at the surface of active catalyst sites are different from the bulk concentrations in the gas flow channel, and subsequently a lower electrode potential. The concentration polarization can be described by the following equation

$$\eta_{conc} = \frac{RT}{nF} \ln\left(1 - \frac{i}{i_L}\right) \qquad [\mathbf{1.6}]$$

Here, i_L is the limiting current density, indicating the maximum rate at which a reactant can be transported to the electrode catalyst layer from the gas flow channel.

The dimensions and transport properties of gas diffusion media and catalyst layer have significant effects on the limiting current density. Water management of the fuel cell also can affect the limiting current density significantly. Excessive water is generated with high current densities, and will condense in the catalyst layer and gas diffusion media if the local water vapor partial pressure exceeds the saturation limit. If liquid water is excessive, it will block the pores of the porous GDL and catalyst layer, and then further prevent the transport of reactant to active reaction sites. This phenomenon is defined as the electrode flooding in PEFC, and is an important limiting mechanism for cell performance, particularly for higher current densities.

From this section, one can see the importance of proper fuel cell hydration level and water flooding elimination on the operation of PEFCs. To achieve optimal performance, a careful consideration of water management is required. In next section, water transportation in PEFCs is discussed in more detail.

1.3 Water Transportation in PEFCs

Perfluorosulfonic acid based membranes, such as Nafion® and Gore SELECT®, are the primary polymeric materials used as electrolytes in PEFCs. The performance of PEFCs is strongly influenced by the ionic conductivity of these membranes due to its major weight in total ohmic polarization. Figure **1-5** [**4**] shows the ionic conductivity of Nafion® 117 as a function of membrane water content λ, which is defined as the ratio of water molecules and sulfonic acid groups in the membrane. From the plot we can see that the hydration level of the membrane greatly affects the ionic conductivity of this kind of membranes. When the membrane equilibrates with liquid water (the respective water content λ is about 22), the ionic conductivity of Nafion® can reach 0.1 S/cm, whereas at dry status (the respective water content λ is roughly 2), the ionic conductivity is only 0.002 S/cm, about 2 percent of the conductivity of fully hydrated condition. So maintaining the membrane fully hydrated is important to reduce ohmic polarization and achieve optimal fuel cell performance, although sometime this objective is contrary to the requirements of eliminating flooding.

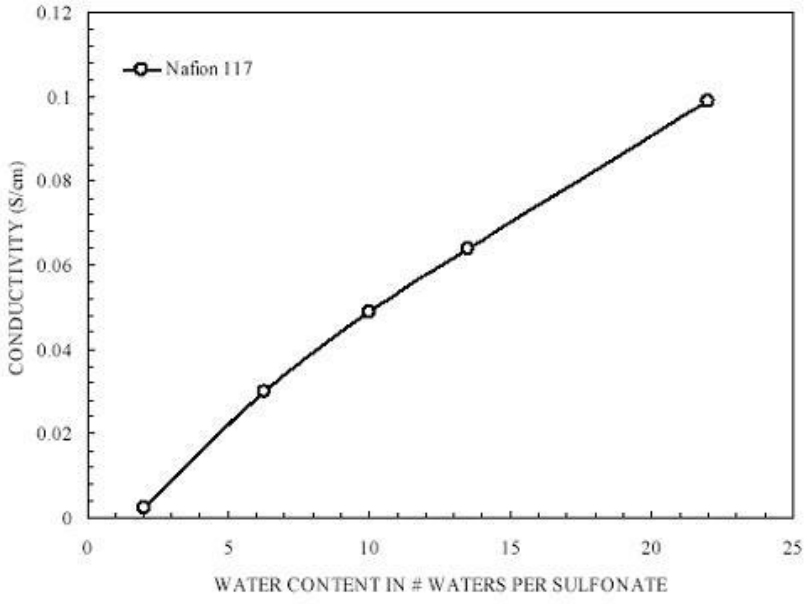

Figure **1-5**: Ionic Conductivity of Nafion 117 as a Function of Water Content [**4**]

Figure **1-6** schematically summarizes the water transport phenomena in an operating PEFC. Water is carried into the fuel cell by pre-humidified reactant gas streams. Some water passes through the gas diffusion layers and electrodes to the interface of electrode/membrane in the form of vapor, liquid or the mixture of both, and then assists the hydration of the membrane. In addition to the input streams, water is generated in the cathode catalyst layer by the electrode reaction. Water also can be removed from the electrode and GDL by reactant flow, where a higher water activity or excessive liquid water present. Furthermore, water can be transported across the membrane via several modes in the operating PEFC. Water can diffuse through the membrane when there is a water activity gradient; water also can be transported from the anode to cathode by electro-osmotic drag of proton migration when the cell is under current; water can also be transported by hydraulic permeation when there is a differential pressure across the membrane.

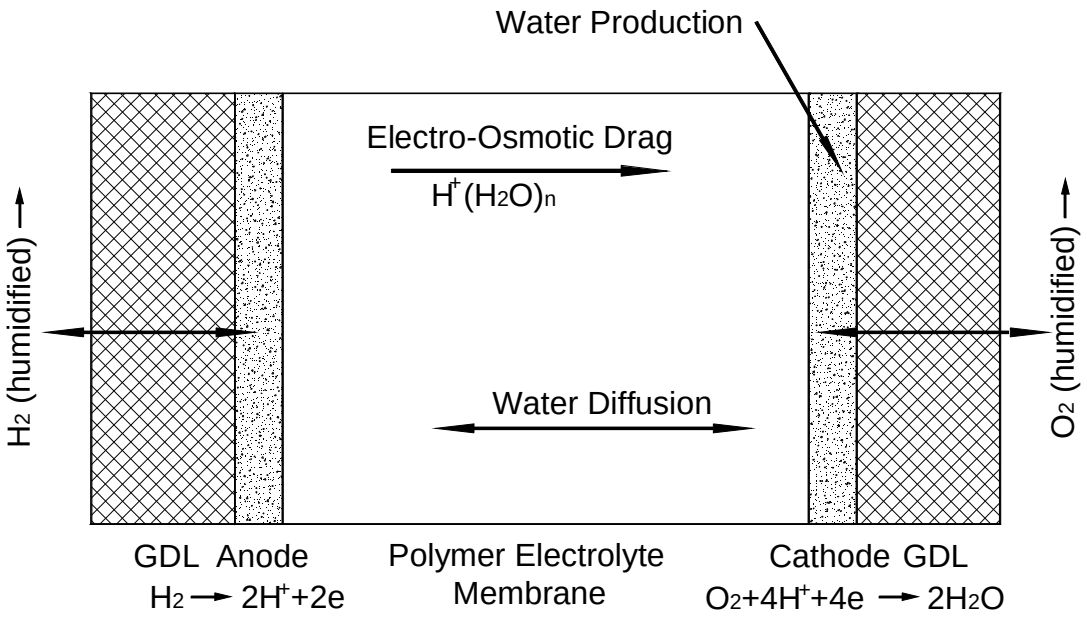

Figure **1-6**: Schematic Summary of Water Transport Modes in PEFC

The water flux by electro-osmotic drag is proportional to the proton flux under a given condition (hydration level, temperature, *etc*), and is described in Equation **1.7**:

$$N_{w,ele-osm} = \frac{i \cdot n_d(\lambda)}{F} \qquad [\mathbf{1.7}]$$

Here, i is the local current density, F is Faraday's constant, λ is the water content of membrane, which indicates the number of water molecules adsorbed by each sulfonic acid group, and n_d is a proportional constant termed as "electro-osmotic drag coefficient", which physically indicates the number of water molecules dragged by each proton. The coefficient strongly depends on the water content of the membrane due to the structure change of the membrane in various states of hydration.

Bi-directional water diffusion driven by activity gradient plays an important role in maintaining the water balance of PEFCs. In an operating PEFC with current passage, the anode tends to dry-out because water is transported to the cathode by electro-osmotic drag, and the cathode tends to be flooded because both electro-osmotic drag and water production by the oxygen reduction reaction create an excess of water in the cathode. Back-diffusion of water from cathode to anode compensates the water loss of the anode, and tends to flatten the water content profile across the membrane, preventing the dry-out and cathode flooding phenomena. Water diffusion through the electrolyte can be modeled by Fick's law of diffusion, and is described in Equation **1.8**:

$$N_{w,diff} = -D_w^m(\lambda) \cdot \frac{dC_w}{dx} \qquad [\mathbf{1.8}]$$

Here, D_w^m is the diffusion coefficient, which is a function of local water content of the membrane, and $\frac{dC_w}{dx}$ is the water concentration gradient in the membrane.

Water transported by hydraulic permeation is directly related to the pressure gradient across the membrane, and can be described by Equation **1.9**:

$$N_{w,hyd} = -k_{hyd}(\lambda) \cdot \frac{dP}{dx} \qquad [\mathbf{1.9}]$$

Where k_{hyd} is the hydraulic permeability coefficient of the electrolyte membrane, which is also a function of water content, and $\frac{dP}{dx}$ is the pressure gradient in the membrane.

Figure **1-7** shows the variation of water diffusion coefficient and electro-osmotic drag coefficient in Nafion® membrane as functions of membrane water content. The two coefficients are all strong non-linear functions of the membrane water content. This makes the water management in PEFCs more complicated.

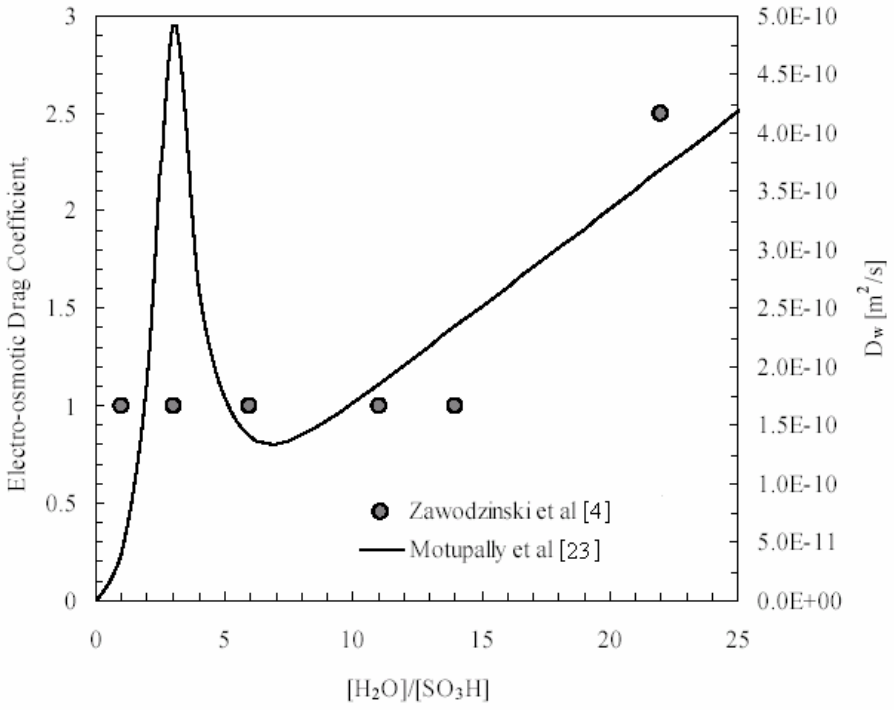

Figure **1-7**: Dependence of Electro-osmotic Drag Coefficient and Water Diffusivity on Water Content of the Membrane

1.4 Literature Review on Water Management of PEFCs

As mentioned in previous sections, water management of PEFCs is regarded as one of the central and most challenging tasks for PEFC operations. Maintaining the

polymer electrolyte membrane fully hydrated while controlling cathode flooding are the key issues to obtain optimal cell performance. Therefore, much experimental and modelling effort has been made to find various modes of water transport, such as diffusion, convection, electro-osmotic drag, pressure and capillary-driven liquid water transport.

1.4.1 Water Uptake of Polymer Electrolyte Membranes

Several studies [**4-9**] have been carried out to determine the relation between membrane water content and water activity of the surrounding environment. The water content of membrane is defined as the number of moles of water associated with a mole of sulfonic groups in the membrane. Zawodzinski *et al*.[**5**][**6**] measured water content of PFSA-based membranes immersed in liquid water and equilibrated with the water vapor at variable water activity by comparing the weight of hydrated membrane with the original dry membrane. It is seen that there is a difference in the water content between the membrane equilibrated with liquid water and the membrane equilibrated with saturated water vapor, although both of which correspond to unit water activity. This difference is called "Schröeder's paradox." As shown in Figure **1-8 ,** other researchers [**4**][**7**][**10**] also have gotten similar results. Futerko and Hsing [**9**] have presented a thermodynamics model to describe the water vapor uptake of PFSA-based membranes. Water uptakes of other types of membranes, for example aromatic-based membranes, also have been investigated by some researchers [**11**].

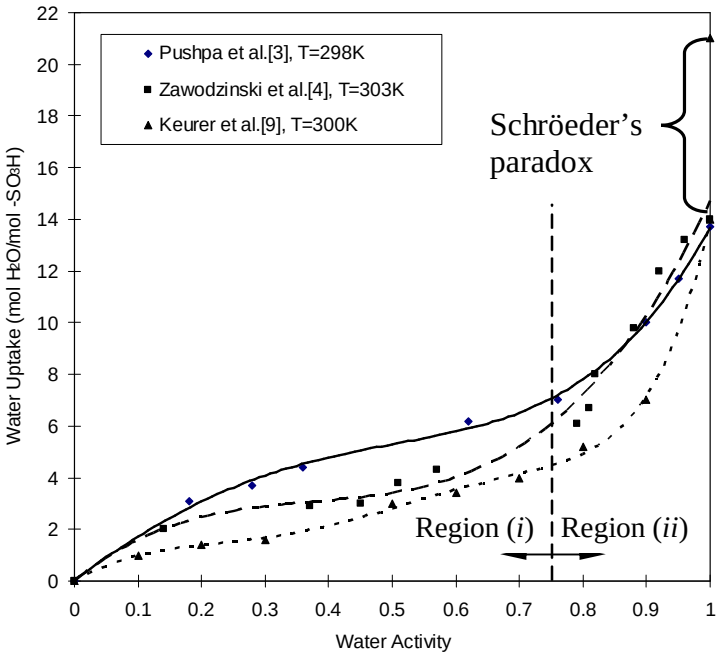

Figure **1-8**: Water Uptake of Nafion®-117 Membrane

Over the entire range of water activity, two regions can be discriminated: (*i*) a region of relatively small increase of water content with increasing water vapor activity (0 to 0.75) and (*ii*) a region of significantly greater increase of water content with increasing activity (0.75 to 1). Region *i* corresponds to water uptake for salvation of the proton and sulfonate ions. In region *i*, water in the polymer membrane has strong interactions with the ionic components of the polymer, however these interaction have to overcome the strong tendency of the polymer hydrophobic backbone to exclude water and resistance to swelling. Region *ii* corresponds to water for polymer swelling. In region *ii*, the resistance to water uptake are surmounted once the water surrounding has sufficient chemical potential.[**6**]

1.4.2 Microscopic View of Water Transport in Polymer Electrolyte Membranes

The structure of Nafion® membrane in various states of hydration has been studied or reviewed by many reserechers [**10-14**]. Yeo *et al* [**12**] have indicated that Nafion® combines the extremely hydrophobic perfluorinated polymer backbone with the extremely hydrophilic the terminal solfonic acid group ($-SO_3H$). One important feature of such structure is that the hydrophobic part can provide good mechanical strength with the presence of water, while the hydrated hydrophilic domain provides high proton conductivity. They have also indicated that this kind of composition leads to a spontaneous hydrophilic/hydrophobic nano separation even in the dry state; with presence of water, because only the hydrophilic part of the micro structure is hydrated, the phase separation will be aggravated further; then a stationary micro structure is formed which absorbs and desorbs water almost reversibly.

Kreuer [**10**] determined that the activation enthalpy for water diffusion in Nafion membrane is almost equal to that in pure water when water contents are higher than the value required for primary hydration of the sulfonic acid groups ($\lambda=[H_2O]/[SO_3H]>3.0$) while the water diffusion coefficient is increasing with increasing water content. He has further indicated that the phenomenon implies the water dynamic within the molecular scale (nm) heterogeneous microstructure of Nafion® similar to the dynamic of liquid water within geometric restrictions, and the polymer material acts as a nano porous inert "sponge" for the water of hydration, which shows very little interaction with the water except for the first three water molecules per sulfonic acid group required for its primary hydration.

Gebel [**13**] has investigated the structure evolution of Nafion® membrane in various states of hydration from dry membrane to Nafion® solution by small-angle scattering technique i.e. small-angle X-ray scattering and small-angle neutron scattering. In their research, large swelling degrees are obtained by using high temperatures in a pressure vessel. As shown in Figure **1-9** [**13**]**,** a schematic description of hydration process is proposed based on their experimental results. Dry Nafion® membranes are

characterized by the presence of isolated spherical ionic clusters, i.e. a microphase separation between the hydrophobic backbone matrix and hydrophilic solfonic group domains. Partial hydration induces a modification of the cluster structure and spherical water pools form in the polymer matrix with the ionic groups at the polymer/water interface, but these water pools are still isolated as revealed by the extremely low ionic conductivity at low water content. With more water uptake, these water pools grow and form interconnections with each other based on a percolation-type phenomenon. Between $\phi_w = 0.3$ and $\phi_w = 0.5$, where ϕ_w means the volume fraction of water, the structure of spherical ionic domains connected with cylinders of water dispersed in the polymer matrix is formed. With increased water uptake, the structure of connected network of polymer rods formed; eventually, a Nafion® solution is formed with colloidal dispersion of rod-like Nafion® particles.

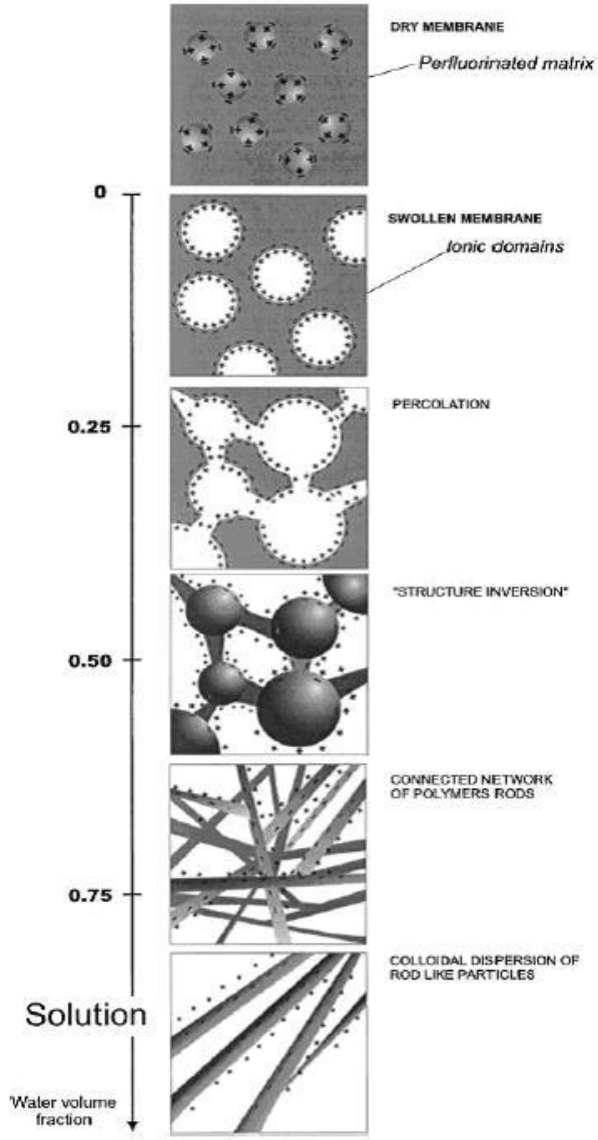

Figure **1-9**: Schematic representation of the structural evolution depending on the water content [**13**]

Rollet and Gebel et al. [**14**] have further investigated effects of external conditions on the nano structure of Nafion membrane by small-angle neutron scattering (SANS). The effects of counterions, equilibrium electrolyte concentration, temperature, and membrane pretreatment have been studied. Their results showed: changing counterions and concentration can lead to a reversible local reorganization of the hydrophilic cavities,

whereas changing temperature and pretreatment leads to a irreversible reorganization on a larger scale.

Paddison *et al.* [**2**] have presented a statistical mechanical model of proton and water transport in polymer electrolyte membrane. Their model described the transport of a water molecule (vehicle-type mechanism) via the displacement of an hydronium ion in a water-filled pore of a polymer electrolyte membrane.

Weber and Newman [**16**][**17**][**18**] have presented a semi-phenomenological physical model. Their model describes the structure evolution of Nafion® under increasing water content, and accounts the evolution in terms of capillary phenomena. Then Schroeder's paradox is elucidated in this fashion. Two transport mechanisms were proposed in their physical model. Between unconnected clusters, driven by electrical force or activity gradient through the hydrated sulfonic acid sites in the polymer matrix, hydronium ions (H_3O^+) or water molecules move in a diffusion-like mode. Whereas between clusters connected by water pathway, hydrated protons are conducted by the Grotthuss mechanism and diffusion, and water is transported by hydraulic pressure gradient and vehicle mechanism due to the proton hydration effect. For common states, the transport mode in a membrane is combined by the two mechanisms. Then a relation regarding the weight of the two mechanisms and the water content of membrane was assumed. Based their physical model, a mathematic model describing the microscopic transportation has been developed and validated in a simple fuel-cell model.

Although these microscopic models are insightful, it is often too complex to apply them directly into an overall fuel cell model, due to the small scale of the pores and clusters in membrane. So polymer electrolyte membrane are commonly treated as homogeneous media and bulk diffusion coefficient, permeability, and electro-osmotic drag coefficient are introduced to describe the transport phenomena in polymer electrolyte membrane. The major research to determine these bulk parameters is reviewed in following sections.

1.4.3 Bulk Water Diffusion Coefficient

The bulk diffusion coefficient of water in Nafion and related membranes is an important parameter for the analysis of the performance of fuel cells based on these membranes. When the fuel cell is under current, the hydration level of the membrane varies significantly with position due to water production by cathode reaction and electro-osmotic drag by proton migration. Therefore, it is necessary to know the relation between the diffusion coefficient and water content of the membrane. Different values of water diffusion coefficient through Nafion® have been reported in the literature. [**19-26**]

Zawodzinski *et al.* [**19**] have measured the ^{1}H self-diffusion coefficients in hydrated Nafion membrane at 30 °C by pulse field gradient Nuclear Magnetic Resonance (NMR) techniques. The advantage of NMR techniques is that self-diffusion coefficients can be obtained in the absence of a concentration gradient in the membrane. The dependence of the ^{1}H self-diffusion coefficient was investigated for the membrane water content range of 2-14 water molecules per sulfonic acid group. The membrane water content was determined by equilibration with water vapor above aqueous LiCl solutions of well-defined water activities. Zawodzinski *et al.* [**20**] also have indicated the identification of the measured ^{1}H self-diffusion coefficients with the water self-diffusion coefficient in Nafion®. In another paper about fuel cell modeling, considering the effect of the swelling, they have derived a corrected Fickian diffusion coefficient based on their former self-diffusion coefficients. The corrected diffusion coefficient increases with increasing water content at low water content region, whereas decreases with inceasing water content at high water content region, and attains a peak value around λ=3. Later, their research group [**5**][**6**] have further investigated the self-diffusion coefficients of water in other perfluorosulfonate ionomeric membranes and got similar trend for different kinds of membranes. Ye and LeVan [**21**] have also reported a similar relation of Fickian diffusion coefficient with the water content of membrane with a peak value around λ=3.3.

Gang, Inglefield, and co-workers [**22**] have investigated the water content and temperature dependencies of the self-diffusion coefficient of water in Nafion®

membranes of 1250 equivalent molecular weight (EW) by pulse field gradient NMR (Zawodzinski *et al.* investigated 1100 EW Nafion [**19**]). The water content dependence reported by them is similar to the results reported by Zawodzinski *et al*. Their results also show that temperature can strongly affect the values of the self-diffusion coefficient of water. At high water contents, the value at 85 °C is about 3 times higher than that at 25 °C. This implies higher operation temperature helpful in reducing or eliminating anode dry-out.

Zelsmann *et al.* [**23**] have also measured the water content dependence of water self-diffusion coefficient of water in Nafion. The self-diffusion coefficient was determined by measuring ^{1}H transport through a membrane, which separated two compartments containing H_2O and D_2O at different partial pressure. Their values of the water diffusion coefficients are significantly lower than Zawodzinski's. Because they conducted the measurement in the environment of vapor, the two vapor/membrane interfaces included in the transport path might significantly affect the water flux across the membrane, and then leads to much lower values of self-diffusion coefficient.

Fuller [**24**] measured the Fickian diffusion coefficient of water by measuring the water flux across Nafion® membranes which contacted with liquid water on one side and flowing nitrogen on the other side. His results showed that the Fickian diffusion coefficient is linearly proportional to water content.

Motupally *et al.* [**25**] have studied the diffusion of water in Nafion® 115 membranes in a fuel cell like setup. Their experimental principle was similar to Fuller's: Nafion® 115 membranes contacted with liquid water on one side and flowing nitrogen on the other side. The water flux across the membranes was measured by cooling the exiting nitrogen stream. Then they carried out the water flux calculations by using diffusion coefficients reported by Zawodzinski *et al.* [**19**] and Fuller [**24**]. They found that the flux of water could be predicted accurately by using Zawodzinski's expression.

Based on the sponge-like microstructure of Nafion, some researchers have argued that the back-diffusion of water in PEFCs is driven by a gradient of the capillary pressure inside the membrane, which is caused by the gradient of the membrane water content [**26**][**27**]. And hydraulic permeability instead of diffusion coefficient should be applied to

describe the water transport in membranes. However, for low humidity operation of PEFCs, the water activity inside fuel cell is less than 1.0 and liquid water doesn't present in large scale, so the application of hydraulic model is limited for this situation.

In recent years, some researchers found that a perfluorosulfonic acid based membranes takes on the order of 100-1000 s to reach its equilibrium sorption state when the membrane is in water vapor [**28**][**29**], and only about 20 s for Nafion® 117 membrane to get to 80% of its equilibrium water content when it is immersed into liquid water [**5**]. That means the water transport resistance at the interface may not be negligible. So some researchers introduced a mass transfer coefficient to describe the flux of water into and out of the membrane [**30**][**31**][**66**]. Ge *et al.* have introduced two mass transfer coefficients to model the absorption and desorption of water respectively [**32**].

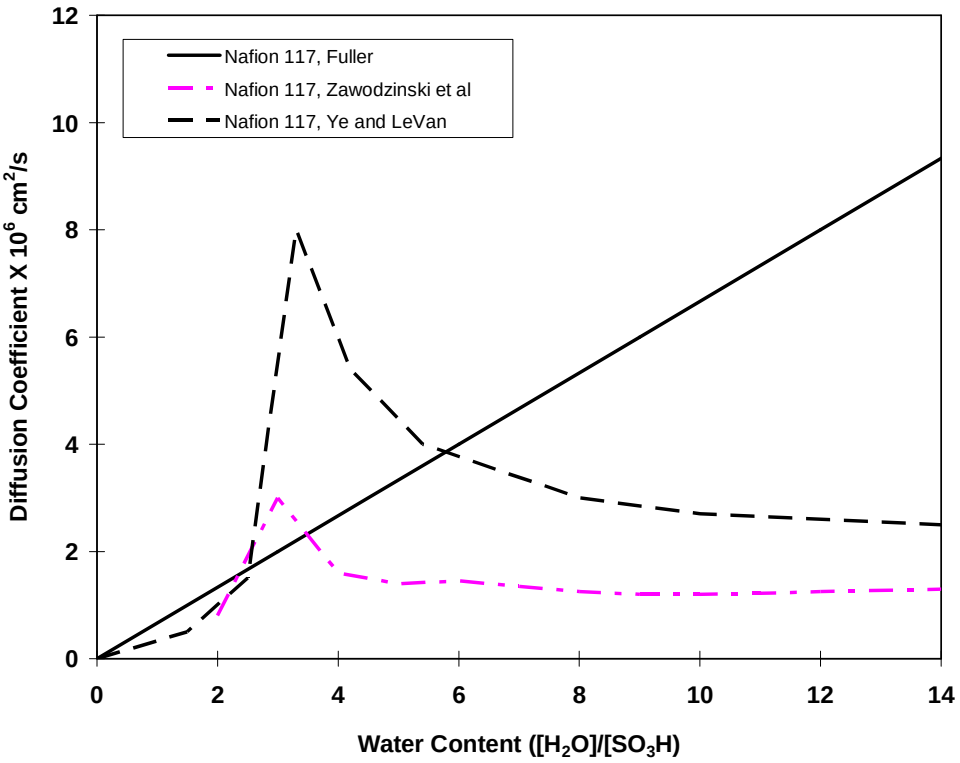

Figure **1-10**: Comparison of Diffusion Coefficient of Water in Nafion 117 at 300 K

1.4.4 Electro-osmotic Drag Coefficient

The electro-osmotic drag coefficient n_d of Nafion has been obtained by several techniques in the literature **[33-42]**. Some of the electro-osmotic drag coefficients reported in literature are shown in Figure **1-11**.

Verbrugge and Hill [**33-35**] studied the proton and water transport characteristics

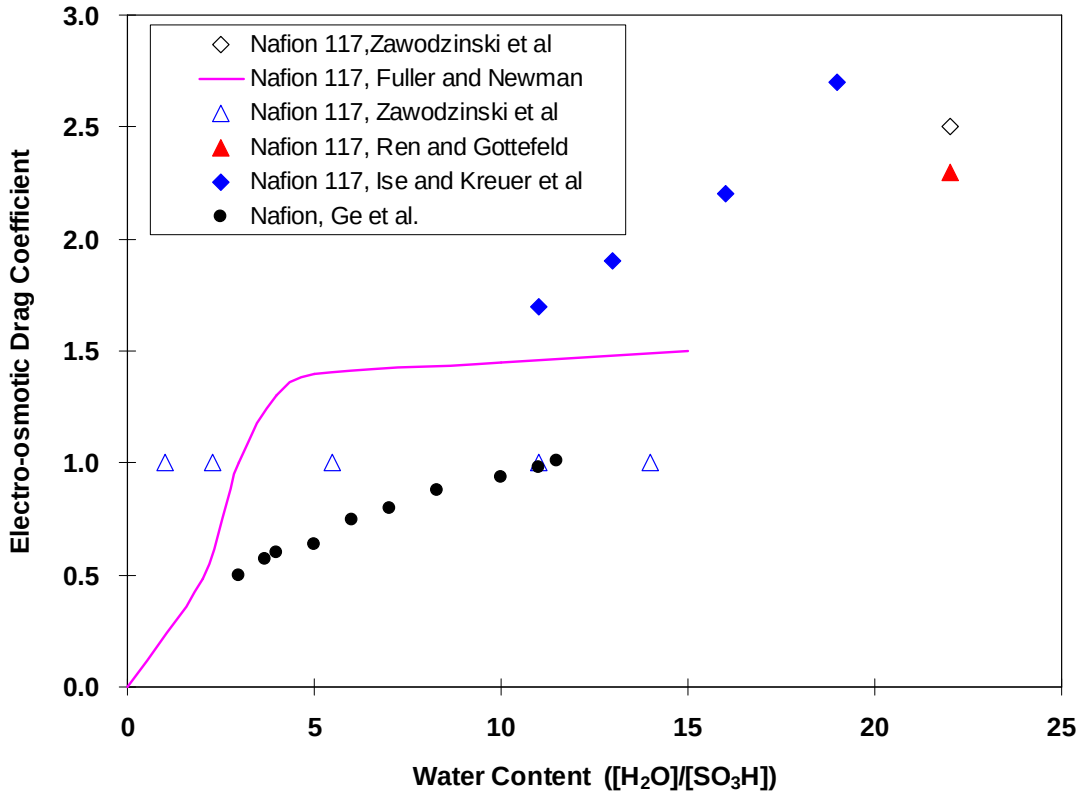

Figure **1-11**: Electro-osmotic drag coefficient as a function of membrane water content at 300 K

in perfluorosulfonic acid membranes during the passage of current. Radiotracer technology was employed in their study by adding tritiated water to a sulfuric acid, perfluorosulfonic-acid membrane system. Their analysis allows for the determination of the number of water molecules associated with each proton transported across the membrane. Their values of the electro-osmotic drag ranged from 3.2 to 8.0 for different

sulfuric acid concentration. Although these data and methods were insightful, the experimental conditions of full hydration and additional electrolyte mean that these results and techniques could not be applied to PEFC directly.

Zawodzinski *et al.* **[5]**, **[6]** investigated the electro-osmotic drag coefficient of Nafion®117 and other ionomeric polymer electrolyte membranes at 30 °C under conditions relevant to PEFCs. They applied a constant current through a cell with the structure of Pt/H|Nafion membrane|Pt/H and filled with deionized water on the both sides of the membrane, and measured the transported water volume by using capillary columns. For a fully hydrated Nafion 117 membrane (λ=22), they obtained n_d=2.5. For a membrane with a water content of λ=11, a much smaller value, n_d=0.9 was obtained. Because in their experiment, the Nafion membranes contacted with liquid water, the possible water contents of membranes were limited. The low water content of λ=11 was obtained by pretreating the sample at 105 °C. As indicated by Rollet and Gebel [**14**], high temperature pretreatment can change the microstructure of Nafion irreversibly and it is not clear if the sample has a comparable structure with normal membranes.

Fuller and Newman **[36]** researched the water content dependence of electro-osmotic drag for Nafion 117 by measuring the potential differences in a H_2O concentration cell. Their cell consisted of two compartments that were separated by the membrane and connected respectively to two reservoirs containing aqueous LiCl solutions of different given water activity; and then hydrogen streams with the same water activities were supplied to two sides of the cell respectively. They obtained n_d=1.4 for λ=5-14 and n_d=0 for dry membranes at 25°C. From the same kind of measurement, however, Zawodzinski *et al.* **[37]** obtained n_d =1.0 for λ<14 at 30°C. On the other hand, their experiment setups were not convenient for measuring the electro-osmotic drag coefficient at elevated temperatures.

Ren *et al.* [**38**, **39**] presented a method to determine the electro-osmotic coefficients in ionomeric membranes. A direct methanol fuel cell with the structure of 1M MeOH/Pt/Ru/ ionomeric membrane/Pt/O_2 (dry) was used in their research. Water flux across the membrane was measured by absorbing the existing stream of the cathode. The advantage of this method is the convenient for the measurements of electro-osmotic

drag coefficient at higher temperature. Their results showed that the drag coefficient in Nafion increases with temperature, from 2.0 H_2O/H^+ at 15°C to 5.1 H_2O/H^+ at 130°C. The electro-osmotic drag coefficients in other membranes have similar trend. However, contacting with liquid water obviously limited this method to fully hydrated conditions.

Ise and Kreuer et al. [**40**] measured the electro-osmotic drag coefficients in Nafion 117 membranes by electrophoretic NMR at 300K. They obtained ξ=2.6 for λ=20, which is very close to the value reported by Zawodzinski *et al.* [**5**]

Ge *et al.* [**42**] applied a fuel cell like setup to experimentally determine the electro-osmotic drag coefficient by running the setup as a hydrogen pump and collecting effluent water with cold trap. The electro-osmotic drag reported by them increases with membrane water content and temperature. However, their model used for deducing the coefficient doesn't include the water transport in catalyst layer and micro-porous and macro-porous layers, which can cause considerable water activity change as reported by both experimental and modeling research [**43**][**44**][**45**].

Except experimental study, the electro-osmotic drag of water in the Nafion membrane has been modeled by several groups [**46-49**]. The transport of proton and water was described by molecular dynamics simulations. However, in all of the simulation works, the complex structure of a polymer electrolyte membrane is neglected. In this case, the simulation results may be far away from the experimental data. Kreuer has reviewed the microstructure and transport in Nafion recently [**50**].

From above review, it could be found that the dependence of drag coefficients on membrane water content for elevated temperatures is still rare in literature and need further validation. On the other hand, the drag coefficient values reported in literature for a membrane equilibrated with water vapor are also quite different, despite the coefficients reported for a Nafion® membrane equilibrated with liquid water are close.

1.4.5 Water Transport Modeling

Researchers have also attempted to employ computer simulations to predict the operation and performance of fuel cell systems. Many modeling studies of PEFCs have been reported in the literature, containing various complexities [**2**, **20**, **25-27**, **51-73**].

Some researchers [**2**, **51**] have proposed microscopic models for the transport phenomena in Nafion® based on statistical mechanics and molecular dynamics. This kind of model provides the fundamental understanding of transport processes like diffusion and electro-osmotic drag in the membrane on microscopic scale, and allows the evaluation of small-scale effects such as pore size and tortuosity of the micro channels. However, they are usually too complex to be used in an overall fuel cell model.

Considering only the bulk transport and relevant parameters of the membrane, most of the models reported in literature are macroscopic models [**20**, **25-27**, **52-73**]. Based on the underlying physical assumptions of the membrane structure, the macroscopic modeling studies can be classified into two categories: diffusion-type model [**20**, **25**,**53-73**] and hydraulic-type model [**26**, **27**, **52**]. Both kinds of models have their advantages and limitations.

The diffusion-type model assumes that the membrane is a single-phase homogenous media, and the water is transported by diffusion-like mechanism in the membrane. Springer and Zawodinzski *et al* [**20**] have provided a foundation for this kind of model. They used detailed experimental data of diffusion coefficients, water uptake and electro-osmotic drag coefficients obtained by them to predict the steady-state water profile and resulting ionic conductivity. In their model, the membrane water content at the membrane/electrode interface is related to the humidity of the reactant gases by the water uptake relation. Diffusion-like models have been further developed by some researchers to fit wider operating conditions. However, due to the existence of Schröder paradox for Nafion membranes, diffusion model is less suitable for fully hydrated conditions where liquid water commonly exists. For example, Büchi *et al.* [**67**] have argued that diffusion-type model fails to predict the observed sharp decreasing water content on the anode side of the membrane, when a substantial current density is drawn.

Hydraulic-type models [**26**, **27**, **52**] treat the membrane as a two-phase porous medium system, where there are liquid channels for water transport and the hydraulic pressure differences are responsible for the back transport of water. One of the earliest and most recognized hydraulic-type models is that proposed by Bernardi and Vebrugge. [**52**] Hydraulic-type models fit the experimental data well under saturated conditions. However, hydraulic-type model is not suitable for the conditions of low humidity without liquid water. Some researchers [**60**] also have indicated that the observed water back transport flux in a running fuel cell with a hydraulic pressure difference across the membrane is much smaller than that predicted by hydraulic model.

Except the transport processes in the membrane, in order to predict flooding, two-phase transport phenomena in gas diffusion layer also have been extensively studied. [**68-73**] Most of the PEFC models assume a isothermal boundary condition, however, due to the exponential dependence of water saturation pressure on temperature, a small temperature change can greatly change the membrane hydration level. Recently, a non-isothermal PEFC model has been developed by Ju and Wang to simulate the coupled heat and water management in a PEFC under low humidity conditions.[**74-76**] Hwang presented a PEFC model to consider the temperature effect on electrochemical reactions.[**77**] Except steady-state PEFC models, transient response of PEFCs is also modeled by some researchers. [**79**]

1.5 Motivation for Study-Combined Current, HFR, and Species Distributions

In addition to the measurements of transport parameters in polymer electrolyte membranes, numerous experimental studies also have been conducted to examine the effects of various operating conditions on PEFC performance [**67**, **80-93**]. These experimental investigations have advanced the understanding of the physicochemical phenomena in PEFCs as well as provided necessary inputs and verification to computer-aided models of PEFCs, especially the data of current and species distributions.

The current distribution in an operating fuel cell is a critical indicator of many local conditions, for example uneven contact resistance, uneven manufactured MEA, various species concentration, temperature gradients, poisoning, and flooding of the electrodes. So it is an important tool to understand key phenomena including water management, CO poisoning, and concentration limitation. Several techniques of current distribution measurement have been discussed in a few papers [**80**-**84**]. Cleghorn *et al.* [**80**] have employed a printed circuit board technology to segmented the current collector and flow field. With segmented anode catalyst layer and GDL, the effects of stoichiometry on cell performance were investigated. Stumper *et al.* [**81**] have demonstrated three methods for the determination of current distribution in PEFC: the partial MEA technique, the subcell technique, and the current mapping technique, which involves the use of a passive resistor network distributed over the whole MEA area. Wieser *et al.* [**82**] have described a technique using a magnetic loop array embedded in a segmented current collector plate to map the two-dimensional distribution in a fuel cell. Mench and Wang [**83**] have demonstrated a new method using an electrically segmented current collector and none altered MEA. However, because dry-out, flooding, concentration limitation can all lead to a similar degradation of the local current density, pure current distribution measurement cannot distinguish the effects of these factors, and other combined measurements are needed to identify the weight of different factors.

Because the protonic conductivity of the membrane strongly depends on the water content of the membrane, the measurement of local resistance of the membrane can help the identification between dry-out and flooding. Some researchers have studied the resistance change of PEFCs by the imbedded potential sensor technique, the impedance spectroscopy technique and the current interrupt technique [**67**, **85**-**88**]. Their research shows that a resistance increase takes place when the current density of the fuel cell increases or when the humidities of the inlet streams decrease due to the dry-out of the membrane. However, just the bulk resistances of the fuel cell were studied by them, and more details about the distributed effects were not available. On the other hand, the measurements of the resistance can only qualitatively reflect the water content of the membrane, and also lack the ability to capture the flooding phenomenon.

While the concentration distributions of the reactants and productions in PEFCs are critical for advanced understanding of the operation of PEFCs and the development of computer-aided models, scant experimental data are available at present. Some authors [**25**, **86**, **89**] have conducted detailed modeling research of water management of PEFCs, and have completed overall water balance studies by condensing the water vapor in the fuel cell effluents or measure the dew point of the effluents. While insightful, these studies did not provide details on the water distribution throughout the cell, which could vary widely according to operating conditions, current distribution, and temperature distribution even the total water flux was kept the same.

While each of the three techniques for the diagnostics of PEFCs has advantages and provides valuable results for the understanding of the operation of PEFCs, it is desirable to combine them together. The simultaneous measurements of current, high frequency resistance, and species distribution reported in this thesis combine the advantages of all the three diagnostic techniques, and can provide an advanced understanding of the water management in PEFCs as well as contribute to the development of PEFC modeling.

In this study, the three diagnostic techniques were combined to study the operation of PEFC under a wide variety of low humidity. Effects of variant PEFC operating parameters, including inlet humidity, reactant stoichiometry, temperature, and pressure, are investigated extensively.

The thesis is composed of eight chapters, which includes this introduction chapter. Chapter 1 presents the background information on PEFCs fundamentals and water management, and a literature review section of the work of previous researchers in water transport parameters, distributed diagnostic techniques, and modeling of PEFCs. Chapter 2 presents the method of approach for distributed performance studies. Fuel cell test stand, designs of highly instrumented fuel cells, Micro GC, and RTGA instrumentation specifications are also presented in this chapter. Chapter 3 presents the application of a Micro GC in measuring steady-state species distribution in an operating PEFC. The work was conducted by the author under the direction of Dr. Mench and Dr. Wang. The work has been published on Journal of Power Sources. [**96**] Chapter 4 presents the application

of a RTGA in determining real-time species distribution in an operating PEFC. The study was mainly completed by the author under the direction of Dr. Mench, Mr. J. Kull helped reducing the experimental data. The content of this chapter has been published on Journal of Power Sources.[**97**] Chapter 5 discusses the distributed performance of a PEFC under low humidity conditions with an emphasis on the effects of cathode stoichiometry and inlet humidity. The experimental study was done by the author under the direction of Dr. Mench and financial support from Gore Fuel Cell Technologies. The content of this chapter has been published on Journal of the Electrochemical Society.[**112**] Chapter 6 presents the distributed performance of a PEFC under low humidity conditions with an emphasis on the effects of thermal boundary condition, temperature, and pressure. Chapter 7 presents a quasi-2D mass transport model, which demonstrates the capability on evaluating the effect of PEFC materials on the low humidity operation of a PEFC. The experimental results in chapter 6 are used to fit water transport parameters. Chapter 8 presents the conclusions of this research and provides recommendations for future research.

Chapter 2

METHOD OF APPROACH FOR IN-SITU MEASUREMENTS

2.1 Introduction

The importance of careful water management to PEFC performance has been emphasized in many papers. The conflicting requirement of the avoidance of the membrane dry-out and the elimination of electrode flooding must be satisfied at the same time to reach an optimal cell performance. This challenge is even more serious for fuel cells running under low temperature, elevated pressure, and high fuel utilization. Because much less water vapor can be carried by the reactant stream, or the mole fraction of generated water is much higher under these conditions, the drying-out of the membrane and the flooding of the cathode electrode may occur more easily.

In this sense, a detailed experimental study combining measurements of current, HFR, and species distribution is very useful for understanding the water transport processes that occur during PEFC operation and for further refining of transport parameters.

In order to serve the above purposes, two highly instrumented fuel cells with segmented current collectors for current distribution measurement and multiple ports for species extraction was used; two techniques of in situ species measurements, micro gas chromatograph (Micro GC) technique and real time gas analysis (RTGA) technique were developed; and a specialized multichannel fuel cell testing system (Arbin Instruments Inc.) was employed.

In following sections, more details about the test stand and approach methods will be described and discussed.

2.2 Overall Layout of the Experimental Setup

As shown in Figure **2-1**, the whole experimental setup for the combined studies of current, species, and resistance distributions consists of a highly instrumented fuel cell, a gas supply unit, a multi-channel integrated fuel cell test stand, a species diagnostic equipment, and respective control computers.

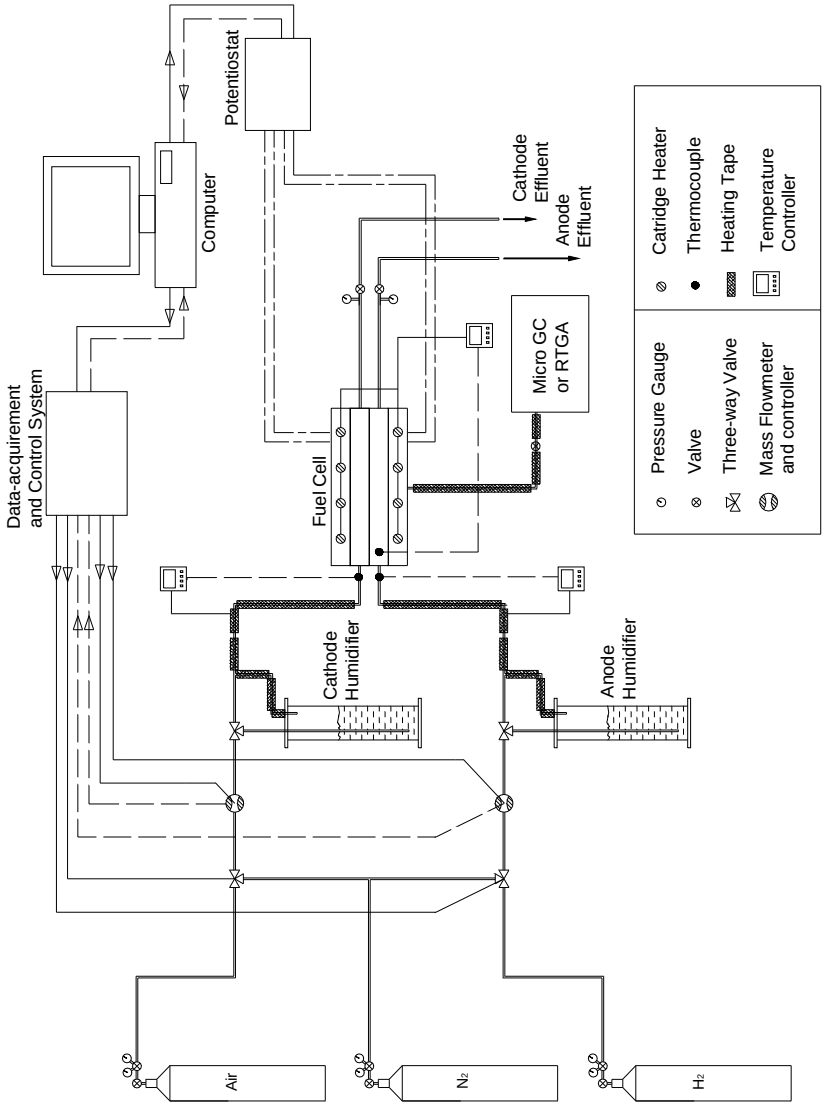

Figure **2-1**: Schematic Showing of the Test Stand Setup

As shown in Figure **2-1**, standard gas regulators installed on the exits of the gas-cylinders regulated the pressures of ultra-high purity hydrogen and breathing grade air ($79\%N_2/21\%O_2$) to 125 psig. Then hydrogen and air were supplied to two dew point humidifiers under the regulations of mass flow controllers for humidification, and were delivered to the fuel cell. Between humidifier and fuel cell, electric heating tapes were wrapped around the flow lines to prevent condensation of water vapor. Directly upstream of the inlets to the fuel cell, a gas sampling port was installed to measure the input humidity to the fuel cell by an Agilent 3000 MicroGC or an Agilent RTGA. The sampling ports were in addition to those along the fuel cell anode and cathode flow paths to provide accurate measurement and control of the humidification entering the cell. Backpressures of both anode and cathode sides were hand-adjusted through two needle valves according to the pressure gages installed downstream of the fuel cell. A force-cooling condenser and a liquid separator installed downstream of the fuel cell condensed and separated the water in the effluents. Two electric controlled three-way valves installed in the pipeline permit purge process to the whole system with nitrogen.

The fuel cell was then connected to 12 or 14 channels of the multi-channel potentiostat module of the Arbin test system. To get the current distribution at a given operation cell voltage, all the used channels were maintained the same voltage, and the current sensors measured the respective amperage emerging from each current collector group.

For the first generation instrumented fuel cell, 16 electrical cartridge heaters governed by an Omega PID temperature controller were used to heat up the fuel cell and maintain it at target operating temperatures. But there was no active cooling measure to cool down the fuel cell, and the heat generated by the fuel cell was dissipated by the natural convection of ambient air.

For the second generation instrumented fuel cell, a VRW Scientific 1157P Heated/Refrigerated Recirculator was applied to actively heat or cool the fuel cell by pumping fluid maintained at set temperature through the fluid channels in the backing plate of the fuel cell. The recirculator has a 13 L bath of 70/30 glycol/water solution. HC-50 is also a recommended fluid that does not experience boil-off at the higher

temperatures and has a lower viscosity but has yet to be tested. The recirculator has its own built-in temperature control and pump, which gives the user quantitative temperature control and qualitative flow rate control. For this study, the highest flow rate was used in order to maintain an isothermal boundary. Figure **2-2** shows a picture of the test setup with the second generation fuel cell installed.

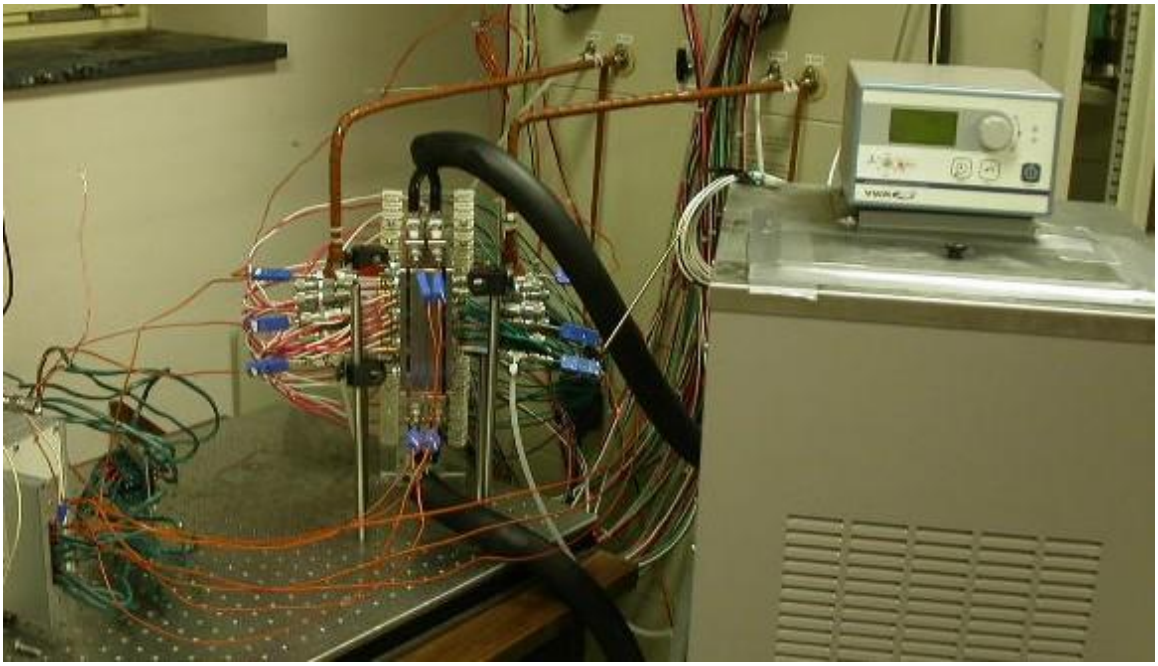

Figure **2-2**: VRW Heated/Refrigerated Recirculator and fuel cell test stand

2.3 Multi-channel Fuel Cell Test Stand

The specialized integrated fuel cell test stand is manufactured by Arbin Instrument Inc., which has integrated galvanostat/potentiostat, fuel cell operation condition control and respective data acquisition subsystems together. The galvanostat/potentiostat functions as an electrical load and can control and monitor the current/voltage of the fuel cell. In addition to that, the system also provides accurate control and monitoring on gas mass flow rates, fuel cell back pressures, gas inlet temperatures and relative humidities. Each of the 25 potentiostat modules (12 or 14

modules were used.) in the system has the ability to draw at least 5A current in the voltage range of 0~5V. The test system is capable of controlling volume flow rates up to 5 slpm (standard liter per minute) on both the oxidizer-side and the oxidant-side. The two dew point humidifiers in the system can fully humidify the reactant streams to the saturation of the set temperature in a wide flow rate and temperature range. Three Omega PID temperature controllers are also installed in the system to provide additional temperature controls for inlet pipes and fuel cell assembly.

2.4 First Generation Instrumented Fuel Cell with Natural Convection Cooled Boundary

To investigate the water transport in PEFCs by combining the measurements of current, resistance and species distributions, a highly intrumented fuel cell that can meet following requirements has been developed to: (1) permit current distribution and HFR measurements over the entire electrode; (2) be capable for reactant extraction along the channel for species concentration measurements; (3) and provide comparable operating conditions to common single fuel cell. The fuel cell adopts essentially the same design developed by Oliver Finckh [**95**].

The CAD-assembly and three digital photos of the highly instrumented fuel cell are shown in Figure **2-3** and Figure **2-4**. The active catalyst area of the fuel cell is 50 cm^2. 48 0.03-inch wide stainless steel ribs were embedded into an electrical insulating plate made in polycarbonate plexiglass. The ribs are gold-plated in order to maintain good electrical contact with the gas diffusion layer and improve the resistance to corrosion. The ribs were arranged to form a single path serpentine flow field. Each rib has a conductive wire, which extends through the insulating plate and the slots in stainless steel endplates to enable current measurement. Eight sample ports are evenly distributed in the flow path (4.3%, 17.4%, 30.4%, 43.5%, 56.5%, 69.6%, 82.6% and 95.7% fractional distances respect to the inlet) of both anode and cathode sides. Two thick Teflon™ gaskets with a thickness proximately equaling to the height of the protruding ribs were applied to form the outer edge of the flow field. Two or more additional thin Teflon™

gaskets surrounding the gas diffusion layers were used to provide better sealing and compensate the thickness of the MEA.

The forty-eight gold-plated ribs of each side were divided into twelve groups along the flow channel with four ribs in each group. Extending wires of the four ribs in same group were combined together and then connected to one channel of the multi-channel potentiostat

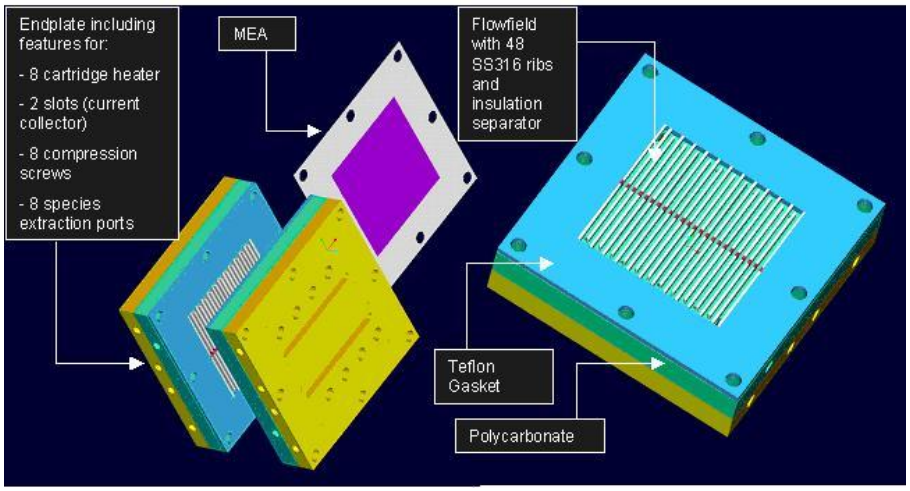

Figure **2-3**: 3-D CAD Drawing of the Highly Instrumented Fuel Cell [**95**]

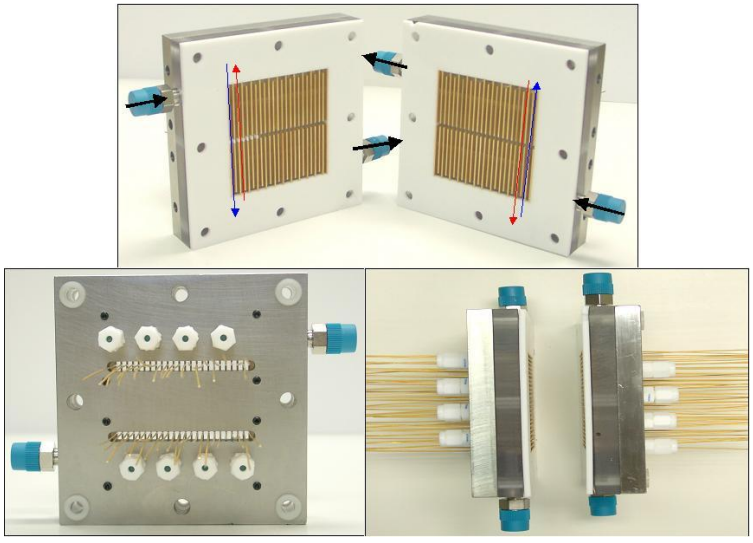

Figure **2-4**: Photos of the highly instrumented fuel cell showing the flow field, current collector, species extraction ports, and ports of inlet and outlet [**95**]

As shown in Figure **2-5**, the dimension of the flow channel is 2.16 mm in width and 3.18 mm in depth, and the average pass length is approximately 71 mm. With total 22 serpentine passes formed by 48 gold-plated ribs, the total length of the flow channel is about 1577 mm. Both the anode and the cathode side share an identical design of flow field, so the flow characters of the fuel cell is overall co-flow, and individual counter-flow, a little bit different from common fuel cells.

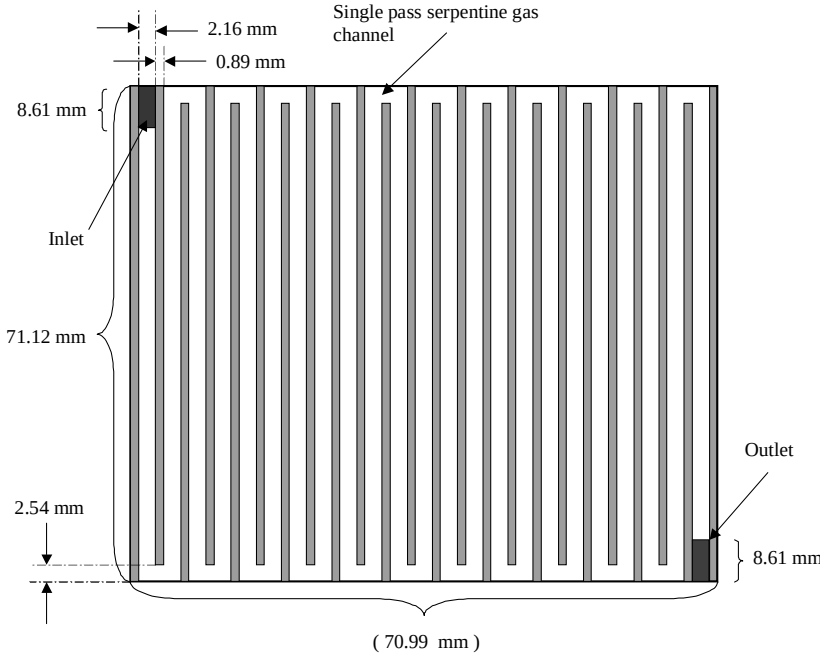

Figure **2-5**: Flow field of the 1st generation highly instrument fuel cell with natural convection cooling boundary [**96**]

A few updates have been added to the original design by Finckh: (1) a segmented gas diffusion layer instead of a nonsegmanted one is applied for the cathode side to minimize the degree of spreading out of the current due to the in-plane conductivity of the gas diffusion layer; (2) the stainless steel wires connected to the gold-plated ribs have been replaced by silver wires to significantly reduce the ohmic loss caused by the wire resistance; (3) Swagelok stainless steel quick connectors were applied to the sample ports to simplify the switch process between ports; (4) the method of the sealing between the steel endplate and the polycarbonate plexiglass plate has been updated for better sealing and easier assembling.

The MEAs used were Gore PRIMEA® Series 57 MEAs, kindly provided by W. L. Gore and Associates, with a membrane thickness of 18 μm and a Pt catalyst loading of 0.4 mg/cm^2 on both the anode and the cathode. The gas diffusion medium consisted of CARBELl MP gas diffusion media as the microporous layer and Toray 060 (wetproofed) as the macroporous layer, with a total thickness of 200 μm, also provided W. L. Gore and Associates.

Due to the high conductivity of the carbon paper GDL used in this research, the in-plane leakage of current between individual channels in the GDL was significant. To reduce the error caused by the in-plate conductivity of the GDL, the cathode gas diffusion layer was segmented into 12 pieces, but left contacted after segmentation to leave the performance unaffected. A compression torque of 35 in. lb was applied to the eight bolts to minimize the contact resistance between the ribs and the gas diffusion layer and maintain sealing. The entire fuel cell assembly was leak-proof tested at 0.3 MPa under water.

After the fuel cell was assembled, a resistance analysis was conducted by measuring the resistance between the wire ends of two adjacent groups at the same side. A typical result of the resistance measurement is shown in Figure **2-6**. The resistance analysis indicated that the resistances between two GDL pieces at the cathode side varied in the range of 1200~1800 mΩ, whereas the resistances between two adjacent groups at the unsegmented anode side were in the range of 18~26 mΩ. That proved the segmented cathode GDL could significantly minimize the spreading out the current although the MEA was non-segmented. Cleghorn *et al*. [49] at Los Alamos National Laboratory has implemented a segmented anode GDL in their printed circuit board approach for current density measurements. The reason for us to segment the cathode GDL is that all the channels in the multi-channel potentiostat share a common ground. That means all the anode input ends of the potentiostat are physically connected together, if only the anode GDL was segmented, the current spreading out still can occur through the common ground.

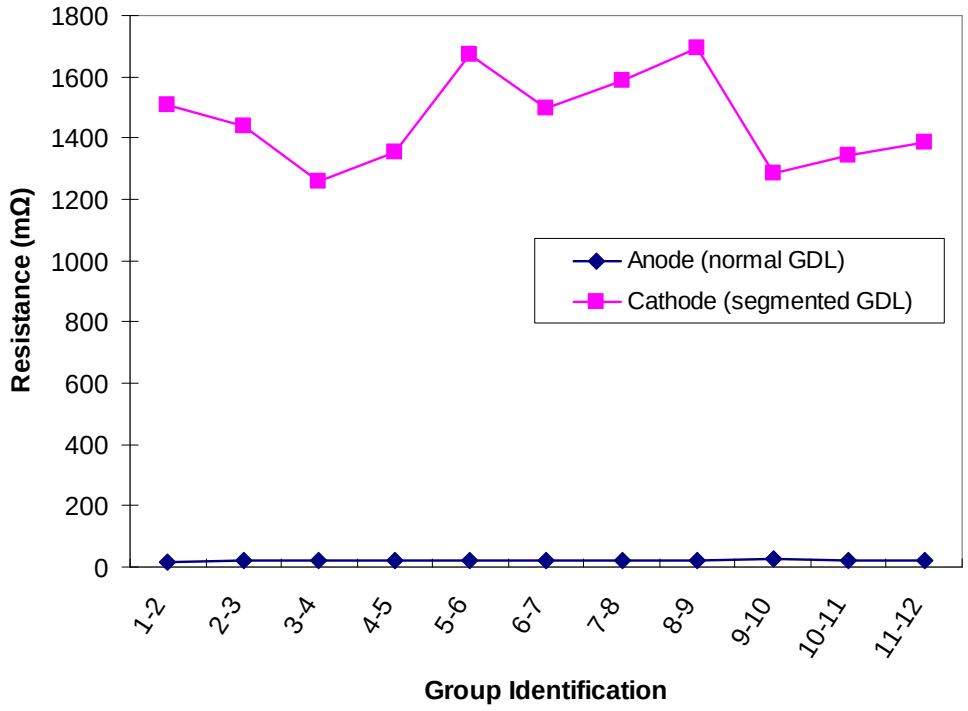

Figure **2-6**: In-plate resistance comparison for segmented cathode and unsegmented anode

2.5 Second Generation Instrumented Fuel Cell with Forced Convective Isothermal Cooling Boundary

The 1st generation instrument fuel cell has shown good capability for simultaneous measurements of distributions of current density, species, and high frequency resistance (HFR), however, the following design issues limit the cell performance and diagnostic accuracy and are highly desired to be further improved:

1) Flow field configurations – multi channel design is more widely used in real world due to its relative low pressure loss and its capability to achieve big active area, and the original single channel configuration cannot fully reflect the processes taking place in multi channel PEFCs; the 2.16 mm channel width leads to insufficient compression on the GDL under flow channels and thus increases the contact resistance,

especially for flexible carbon cloth GDL; the over wide flow channel also leads to higher in-plane ohmic loss; the 3.18 mm channel depth increases diffusion resistance as well as affects the accuracy of species measurements; the low landing fraction increases the contact resistance.

2) Lack of active control on the fuel cell boundary temperature – under high current densities, the heat generation rate of fuel cell is significant and well exceeds the dissipation capability of the natural convection cooled boundary. An elevation as high as 5 °C of the fuel cell body temperature has been observed. This kind of temperature increase may greatly change the MEA humidification and alter the measured distributed performance. On the other hand, most of the fuel cell models on literature assume an isothermal boundary condition, but there is no true isothermal validating data available on literature yet, with the exception of extremely low current value. So it is highly desired to actively control the fuel cell body temperature under high current density conditions.

3) 48 individual current collectors as in the 1st generation design required extensive adjustment to achieve uniform compression of the GDL.

4) Unchangeable flow field – it is highly desired to be able to change the flow field configurations without altering other parts of the fuel cell, and the 1st generation design cannot do this.

To meet these purposes, a newly instrumented fuel cell was designed and fabricated in the FCDDL. The fuel cell has the ability to take the three distributed measurements (current, species, and high frequency resistance) simultaneously, actively control the current collector temperature, examine multiple flow field configurations, and provide similar performance to that of a multi channel non-segmented fuel cell. Figure **2-7** shows the 3-D Solidworks drawing of the left half of the fuel cell, more design details about the fuel cell can be found in B. Gerdes's Masters' thesis [**99**]. B. Gerdes designed and initially tested this design with feedback from Dong on the limitation in the previous generation design.

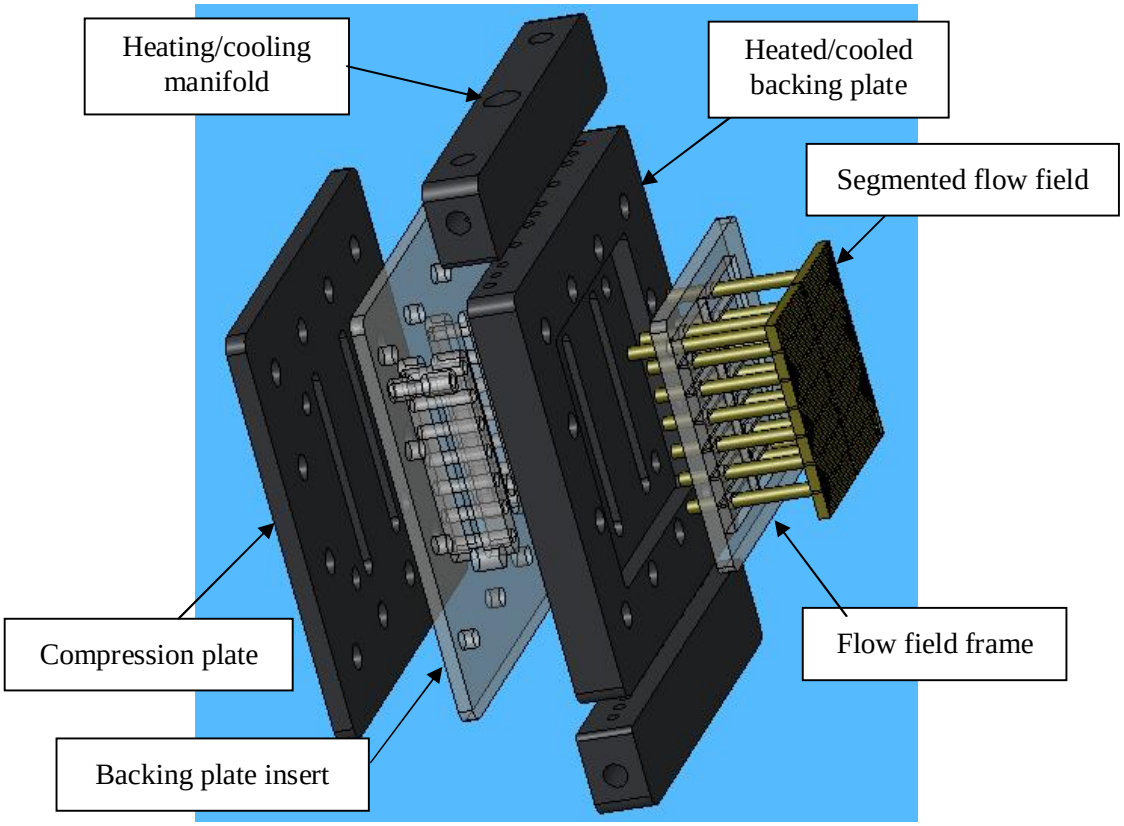

Figure **2-7**: 3-D CAD drawing of the left half of the highly instrumented fuel cell [**99**]

The new fuel cell still adopted the segmented current collector scheme for current distribution measurement. But different from the old cell, to achieve a flat upper surface, the current collector segments of the new cell were first grinded as a whole stainless steel plate, and then the plate was cut to 14 identical pieces. The flow field and current drawing column were then machined out for each segment. To improve the spatial resolution of species measurement, the species sample ports were combined with the current drawing column by drilling a tiny port at the center of the column. The thickness of the flow field segments and current drawing column were designed so that the maximum amount of current drawn through the cross-sectional area at any given point would produce a negligible voltage loss. The segments were also gold-plated in order to maintain good electrical contact with the gas diffusion layer and improve the resistance to corrosion. Figure **2-8** shows the 3-D CAD drawing of a segment.

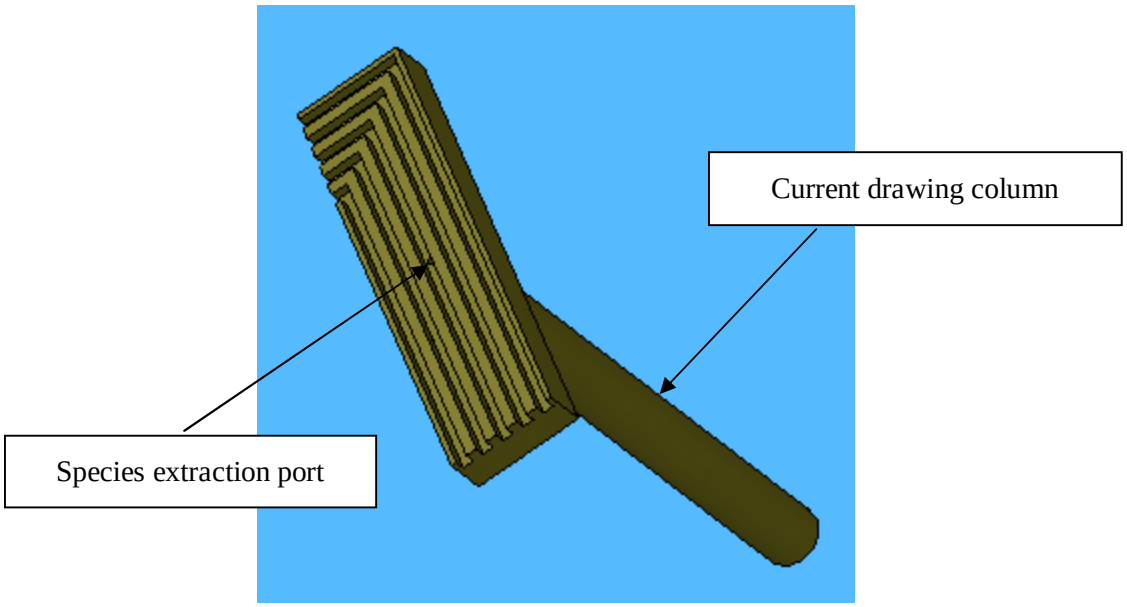

Figure **2-8**: A current collector segment with current/species collecting tube

A Lexan® flow field frame with 14 machined grooves was used to hold the segments. This also allows for the ability to test completely different flow field paths and channel configurations as long as the external dimensions of the segments not altered. To actively heat/cool the fuel cell and achieve an isothermal boundary condition, a stainless steel heated/cooled backing plate containing 8 even spaced coolant channels was introduced. Because the thermal conductivity of Lexan® is much lower than stainless steel, excessive temperature change across the flow field frame was observed under high current densities. To maintain the isothermal boundary condition, two thermocouples were inserted to both 10th gas sample ports of anode and cathode sides to directly measure and control the flow field temperature, instead of coolant temperature.

Figure **2-9** shows the relevant configurations of the flow field. The flow field of the fuel cell is a co-flow five-channel serpentine design. The total active area of the flow field is 50 cm^2, and the channel to landing ratio is roughly 1:1. The total length of the flow path is 515 mm, which is much shorter than the old cell's 1577 mm. Figure **2-10** shows the dimensions of the channel and landing. Both of them have the same width of 0.92 mm, and the depth of channel is 1 mm to reduce the mass transport loss. These values are also very similar to what widely used in common un-segmented experimental

fuel cells. Although the amount of gas sample extracted from the fuel cell for species measurement was very small and commonly less than 3% of the total gas flow, because the species sample was extracted from the middle channel only of the segments, the gas flow rate and species concentrations in the middle channel could be a bit different from the average values of all the five channels. To minimize this issue, 1-mm wide gas mixing regions without channel landings are arranged between segments to promote gas mixing between channels.

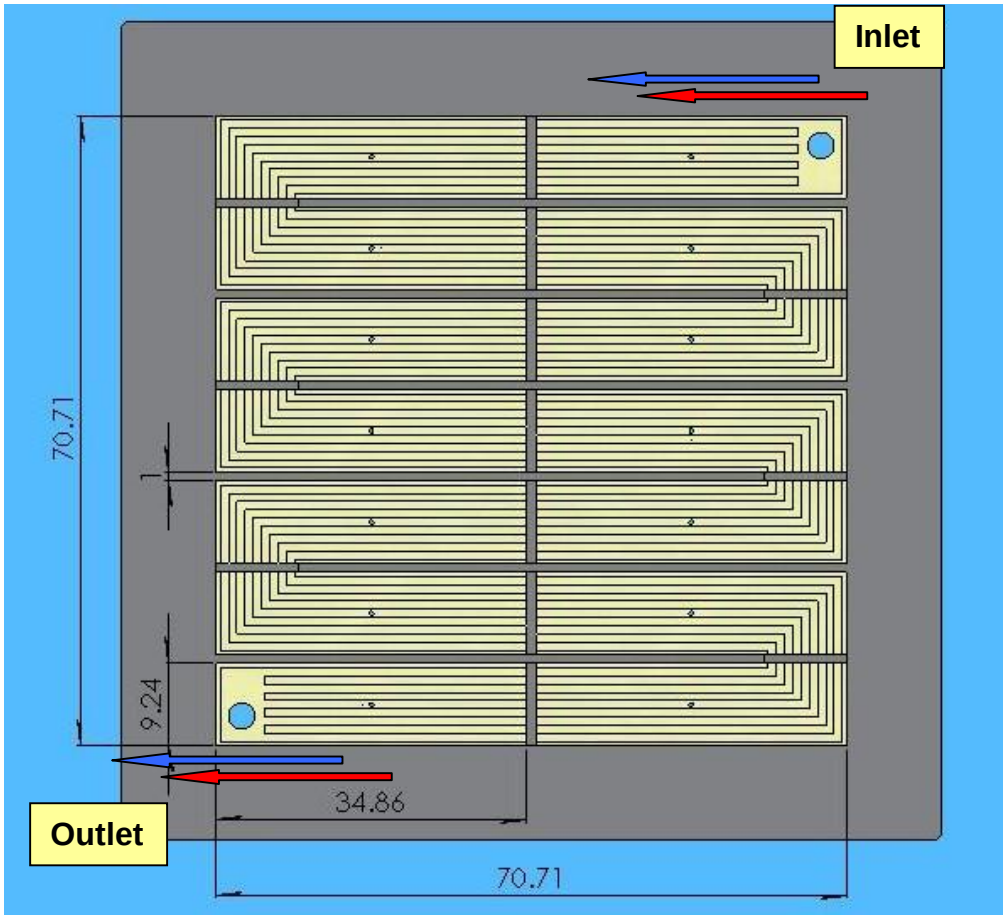

Figure **2-9**: Flow field of the 2nd generation highly instrumented fuel cell with forced convective cooling isothermal boundary

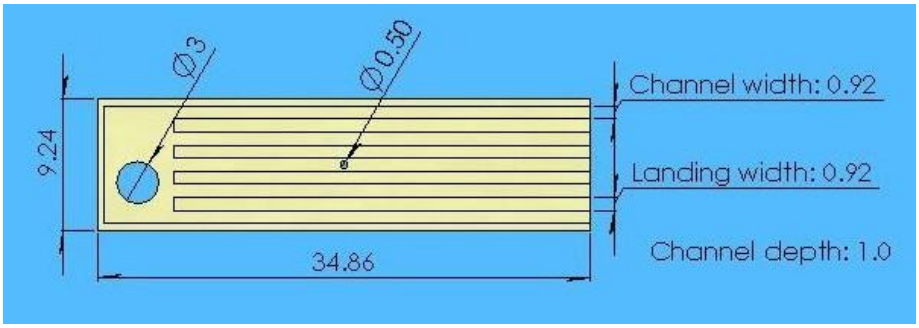

Figure **2-10**: Channel and landing dimensions

The MEAs used were also Gore SELECT® MEAs provided by W. L. Gore and Associates. The thickness of the electrolyte membrane is 18 μm and the Pt loading of the catalyst layer is 0.5 mg/cm^2. The gas diffusion layer used was carbon cloth with a thickness of 300 μm, which was also provided by W. L. Gore and Associates.

To avoid excessive in-plane current leakage between segments, the GDL was also segmented based on the size of flow field segments. A compression torque of 25 in. lb was applied to the 12 bolts to minimize the contact resistance between the current collectors and the gas diffusion layer and maintain sealing. After the fuel cell was assembled, a similar resistance analysis was conducted by measuring the resistance between two adjacent segments. And then the entire fuel cell assembly was leak-proof tested with 0.3 MPa internal pressure in water.

2.6 Equipment for Species Measurement

2.6.1 Micro GC

An Agilent 3000 MicroGC gas chromatograph (GC) was interfaced with the fuel cell to measure the mole fraction of species presenting in the anode and cathode gas flow channels, including hydrogen, oxygen, nitrogen, and water [**96**]. The GC is capable of performing a single measurement about every two minutes. For gas species separation, a Plot-U and a molecular sieve (molesieve) GC column were used. The molesieve column

was installed with a backflush module to prevent damage of excess water. This type of GC is capable of dealing with high water level samples up to saturation. The column temperature was set to 130 ^{o}C to avoid water condensation in the column. UHP Argon was used as the carrier gas for both columns in measurements. UHP Helium also can be used as carrier gas.

The GC was interfaced to the fuel cell through a 0.32 cm outer-diameter (0.125 in.) cooper, heated tube connected to the sample ports of the cell. The sample line temperature from fuel cell to the GC was monitored and kept well above 120^{o}C to prevent any condensation of water in the sample steam. The flow was directed toward a Swagelok T-fitting that located 3 cm upstream of the GC and allowed continuous flow of atmospheric pressure sample gas from the fuel cell to the GC sample inlet. Sample availability at atmospheric pressure eliminates error associated with varying sample inlet pressure, which may greatly affect results. The extraction flow rate was controlled by a needle valve installed in the sample tube and the flow rate was measured with a flow meter to ensure that the extracted sample was a small fraction of the total fuel cell reactant flow. Typical values of bypass were 2-3% of the total flow, and this value never exceeded 5% during measurement. The possible local disruption of performance by sample extraction was examined and determined to be minimal due to the small relative sample volume. Since low-pressure gas flow can hold a greater mole fraction of water than higher-pressure gas flow, there is no condensation resulting from the pressure drop from the fuel cell channel to the GC inlet.

Depending on the pressure of the fuel cell, the delivery time for species from the fuel cell to the GC varied from 1~3 seconds, based on calculations of interior tube volume and known sample flow rate. All GC measurements were given adequate time to ensure ample tube purge had occurred, and several measurements were taken to ensure repeatability.

What makes this research novel is the fact that we have directly measured sample with high mole fraction of water without dehumidification. In typical GC measurement applications, water vapor is condensed from the flow before entering the GC device. This is to prevent damage or degradation to the columns and detector elements. Indeed,

if liquid water reaches the inlet of the GC or condenses inside the detector, system failure will likely occur. However, all temperatures of the columns, inlets, and sample tubes are kept well above 100^{o}C to prevent this. Frequent GC column bakeout was also conducted to maintain the sensitivity of the columns. If all flow is maintained well above the dew point, very accurate and repeatable measurement of water content up to 90% mole fraction was achieved.

2.6.2 Real Time Gas Analyzer

Although Micro GC technique provides measurement of the water vapor content across the flow channels, the measurement time required on the order of 2 minutes per data point limits the application of the technique to steady state species distribution analysis. The Agilent G3163A Real-Time Gas Analyzer (RTGA) has the ability of performing a measurement per second. [**97**] The significant decrease in data collection time compared to the MicroGC method enables continuous monitoring of changes in species mole fractions at selected locations along the anode or cathode flow path. The application of a RTGA in species distribution measurement can provide detailed understanding and perspective of the time scales of the various intercoupled phenomena.

The RTGA was interfaced with the fuel cell in the similar way of the Micro GC. The temperature of the heated sample line was also monitored and kept well above 120 °C to avoid any water condensation in the tube. Because the RTGA samples continuously, sample bypass was eliminated to reduce the diverted sample flow rate. The sample flow rate has been checked to ensure that the extracted sample was a small fraction of the total fuel cell reactant flow not higher than 5% of the total flow of the fuel cell.

Depending on the pressure of the fuel cell, the average delivery time for species from the fuel cell to the RTGA was determined to be around 0.3 seconds, based on calculations of interior tube volume and known flow rate. This quick response time allowed many different measurements to be taken in a relatively short amount of time

compared to a GC. Several measurements were taken to ensure repeatability of the measurement.

2.7 Method for Membrane Resistance Measurement

In addition to current and species distributions, an understanding of the local hydration state of the electrolyte through high frequency resistance measurements is important to delineate mass transport effects from water transport effects. While this technique in itself is useful to delineate reactant transport/cell compression from electrolyte hydration/degradation losses, the same data on a localized distributed scale provides much more information about the locations of local membrane humidity and health.

Figure **2-11** shows the equivalent Randles cell circuit of a PEFC, which only contains three equivalent circuit elements, the fuel cell components and electrolyte membrane resistance R_{el}, the charge-transfer resistance R_{ct}, and the double-layer capacitance C_d [**100**]. More complex equivalent circuit models are also available according to the requirement of accuracy [**101**]. The equivalent impedance can be expressed as [**100**]:

$$Z = R_{el} + \frac{R_{ct}}{1 + j \cdot 2\pi f \cdot R_{ct} \cdot C_d} \qquad [\mathbf{2.1}]$$

Here, f is the applied frequency and j is $\sqrt{-1}$. Obviously, $Z \to R_{el}$ as $f \to \infty$ and $Z \to R_{el} + R_{ct}$ as $f \to 0$. That means that the resistance of the electrolyte membrane can be obtained if a high enough frequency is applied.

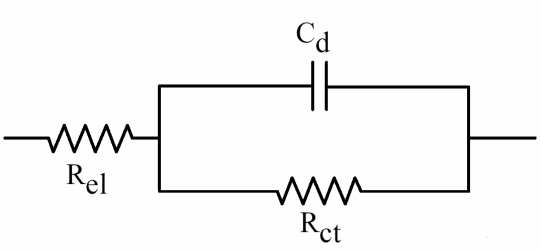

Figure **2-11**: Equivalent Randles cell circuit for a PEFC containing the electrolyte resistance (R_{el}), and the charge-transfer resistance (R_{ct}) in parallel with the double-layer capacitance (C_d) [**100**].

In present research, the impedance of the fuel cell was approximated with high frequency resistance measured at 3 kHz through the multi-channel potentiostat. To verify the accuracy of this approximation, AC impedance spectroscopy was conducted and the results were compared to the high frequency resistance. The AC impedance was measured by a Solatron 1255b Frequency Response Analyzer with the ability of ±2A in the voltage range of –2V~ +2V. The impedance spectroscopy was obtained at frequencies between 10 kHz and 0.01 Hz with 10 steps per decade, while the amplitude of the sinusoidal voltage signal was set 10 mV. The cell voltage was 0.7V, same to the voltage for high frequency resistance measurements.

Figure **2-12** shows the AC impedance spectrum obtained for the first segment. At low frequencies, the imaginary part of the impedance was negative because of the double-layer capacitance C_d, while at high frequencies, the imaginary part of the impedance was positive due to the diminishing impedance of the capacitance and the increasing impedance of the distributed inductance in the measurement circuit. The membrane resistance was determined from the intercept on the real impedance axis. And the charge transfer resistance was determined from the circular arc of the impedance spectrum. The spectrum curve intercepts the real impedance axis at 0.6 kHz, and shows a membrane resistance of 0.332 $\Omega.cm^2$. At the frequency of 3.0 kHz, while there was significant non-zero imaginary impedance, the value of the real part of the impedance was very close to the intercept value. The error was less than 5%. That means that the real part of the high frequency resistance measured at 3.0 kHz is an accurate

approximation of the membrane resistance under most circumstances involved in this research. In fact, 1 kHz is typically considered to be high enough for this purpose.

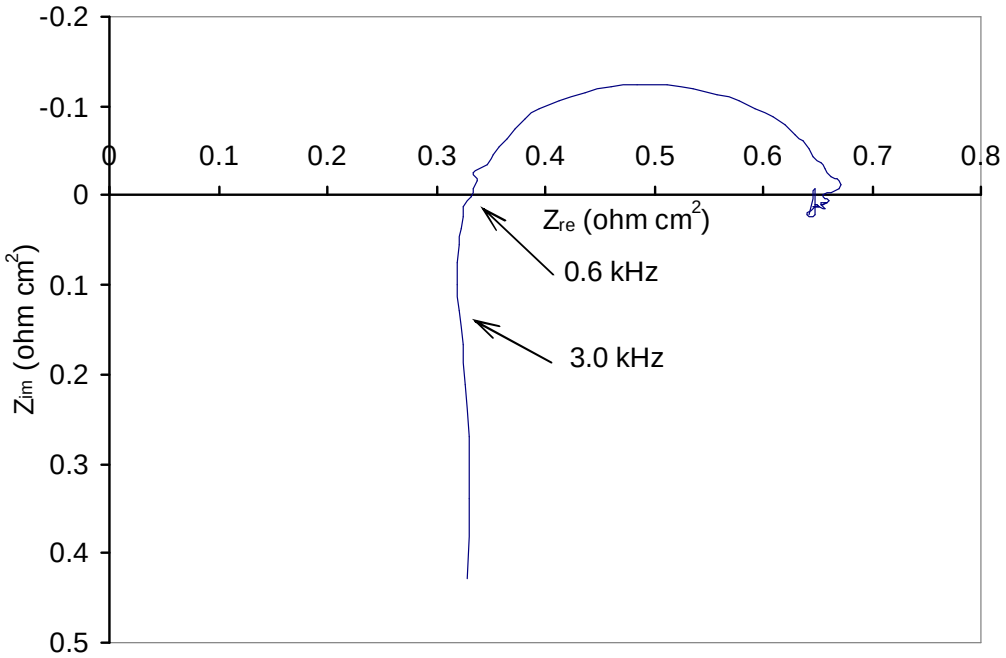

Figure **2-12**: AC impedance spectrum obtained for the first segment. Test conditions: fuel cell temperature = 80 °C, exit pressure A/C = 3.0 atm, inlet temperature A/C = 80 °C, 0% RH @ 80°C hydrogen anode, 50% RH @ 80°C air cathode, ζ_c = 1.5, ζ_a = 1.2.

It should be noted that the values obtained from high frequency resistance and ac impedance are not the true membrane resistance.[**86**] The resistance components of these values include the contact resistance, the grain-boundary resistance and the membrane resistance. However, the membrane resistance is most affected by operation conditions for example the inlet humidity, while other components are almost not affected by operation conditions, so that change in the HFR can be attributed to change in the membrane resistance.

Chapter 3

Application of Micro GC on *In-situ* Species Measurement

3.1 Introduction

The hydrogen polymer electrolyte fuel cell (PEFC) has tremendous promise as a future power system due to its low pollution, high efficiency, and stealth. Many studies, too numerous to completely list, have examined various aspects of PEFC performance as a function of operating conditions [**67**, **80**-**93**]. In addition to experimental characterization, much research has been focused on first-principles based modeling of the PEFC system [**2**, **20**, **25**-**27**, **51**-**73**]. However, advances in modeling of the PEFC have thus far outpaced the ability to experimentally verify the predicted performance. In particular, scant experimental data are presently available regarding current density and species distributions. As indicated by Wang [**102**], it is this type of detailed validation that will permit an ultimate understanding of the physicochemical phenomena in the PEFC as well as development of useful computer-aided tools for design and development.

Determination of the mass distribution is critical to understanding water management and reactant distribution effects. In particular, it is desirable to understand the water vapor distribution within the gas channels of the flowfield. Many authors have conducted detailed studies or deduced models that describe the water transport through fuel cell components including the electrolyte and porous gas diffusion layers [**68**-**79**]. In order to integrate these models and validate their accuracy, it is desired to determine the in situ mole fraction distribution of water vapor, at various locations within the gas channel flow path. A few authors have completed detailed studies of the water balance in an operating cell by collection of the fuel cell effluent, and condensation or absorption of the gas-phase water vapor [**25**, **32**, **38**, **39**, **42**, **89**]. While insightful, these studies do not provide data on the water distribution throughout the cell, which could vary widely

depending on operating conditions, current distribution, and local non-isotropic transport parameters. In order to delineate the effects of current distribution on water distribution, it is also desirable to couple water and current distribution measurements to provide detailed information on non-uniform transport and generation effects. The instrumented cell used in this study allows for simultaneous measurement of current and mass distribution.

In this chapter, the first successful application of a Micro GC to *in-situ* measure PEFC gaseous species concentrations with the presence of high water content is presented in detail. A unique aspect of this technique is the capability to directly measure gaseous samples containing high water vapor levels up to saturation without dehumidification of the flow stream. The capability enables the direct interfacing of the Micro GC to the gas flow channels of PEFCs. An isobaric bubble humidifier running at low flow-through gas flow rate was used to supply humidified sample gas for the calibration of the Micro GC. The known dependence of water saturation pressure on temperature was applied to verify the accuracy of this calibration method. Then the Micro GC technique was applied to determine the species mole fraction distributions in an operating PEFC focusing on the effects of fuel cell operating voltage. The new technique shows good accuracy and capability in directly mapping the steady state species distribution in an operating fuel cell.

3.2 Micro GC Calibration

Calibration of the GC was accomplished with a gas-bubbler humidifier running at low flow-through gas flow rate and controlled temperature. The humidifier was used to provide a calibration gas mixture with known humidity. The water mole fraction of the exiting gas mixture was calculated from the ratio of the saturation pressure of water at the temperature and the humidification pressure by treating the exit gas mixture as idea gas. The exit pressure of the humidifier was precisely monitored during the whole calibration process to correct the effect of humidification pressure on saturation water mole fraction. Then a single point calibration was made at a relative lower humidification temperature

of around 50 ˚C, by assuming the humidifier 100% efficient, and then correlating the measured response areas of species to the thermodynamically determined mole fractions based on saturation vapor pressure of water. The correlation constants were the averages of the results of six measurements to minimize the error caused by the temperature variation of the humidifier. Then, the accuracy of the calibration was checked by comparing the output species mole fractions with the respective theoretical values for higher humidification temperatures, while the calibration correlation coefficients were kept the same numbers.

As well known, the saturation vapor pressure of water is a strong nonlinear function of temperature. At a humidification pressure around 1 atm, the thermodynamic water mole fraction curve changes very steeply with temperature in the range of fuel cell operation. For example, the theoretical water mole fraction changes from 12.7% to 70% as the temperature increases from 50 ˚C to 90 ˚C. If the humidifier were significantly less than 100% efficient, the measured calibration curves would not follow the rapidly changing slope of the theoretical curves.

Calibration curves taken for fully humidified hydrogen and fully humidified air are shown in Figure **3-1** and Figure **3-2**. The humidification pressure was maintained at 1.1 atm. Theoretical curves are also included in the figures for comparison. Close agreement can be observed between the measured values of water fraction and the thermodynamically expected saturation values. The data shown represent an average of five measurements with very little scatter, and it can be seen that the expected accuracy is around ± 2%. The results were very consistent. The measured mole fraction was typically within ±2% of the theoretical value, up to very high values of water mole fraction humidified at 95^{o}C. This calibration also indicates that the precisely temperature and pressure controlled humidifier can humidify gas in near 100% efficiency at these extremely low flow rate conditions.

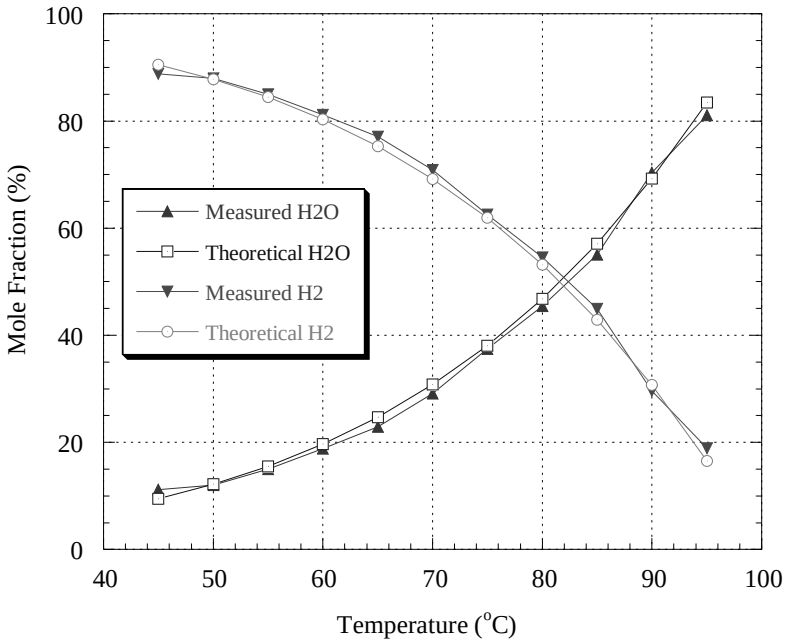

Figure **3-1**: Comparison between measured with GC and theoretical water vapor, nitrogen and oxygen concentrations with baseline value at 50 °C. The inner pressure of the humidifier bottle was at 1.1 atm.

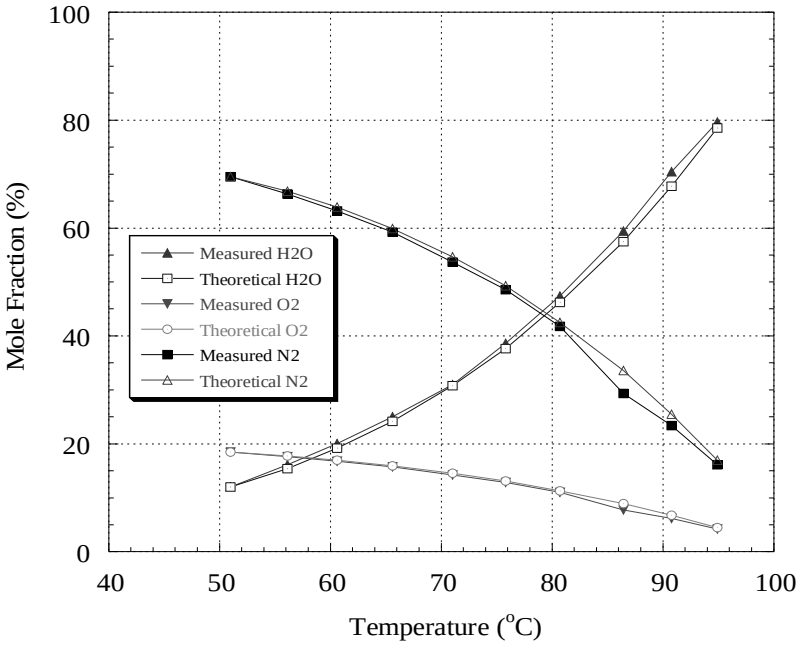

Figure **3-2**: Comparison between measured with GC and theoretical water vapor, nitrogen and oxygen concentrations with baseline value at 50 °C. The inner pressure of the humidifier was at 1.1 atm.

3.3 Effects of Fuel Cell Voltage on Species Distribution

Following the calibration process, the effects of current density on species distribution were investigated with the Micro GC and the 1st generation highly instrumented fuel cell. The species mole fractions were measured at various locations within the flow channels of the anode and cathode.

The MEAs used here were purchased from Lynntech Inc., different from the Gore MEAs used in other sections. The MEAs consisted of Nafion® 112 (51 μm thick) membrane as the polymer electrolyte, sandwiched between the catalyst and single-sided ELAT™ (E-TEK, Inc.) gas diffusion layers. All MEAs used had a carbon-supported catalyst loading of 0.5 mg Pt/cm^2 on both anode and cathode. More information about the base operating conditions are given in Table **3-1.**

Table **3-1**: Baseline operating conditions

Parameter	Value	Units
Electrolyte	Nafion® 112 (E.I. du Pont de Nemours and Company)	N/A
Gas diffusion layer	ELAT® (E-TEK of De Nora North America) anode and cathode	N/A
Catalyst loading (carbon supported)	0.5	mg/cm^2
Cell temperature	80	°C
Anode inlet temperature	90	°C
Cathode inlet temperature	80	°C
Anode gas	Ultra high purity H_2 (>99.999%)	N/A
Cathode gas	Breathing air (79% N_2, 21% O_2)	N/A

Constant anode and cathode flow rates were used to simply the adjustment of flow rates. The anode gas flow rate was 0.7 A/cm^2 equivalent, and the cathode gas flow rate was 1.75 A/cm^2 equivalent. It should be noticed that the cathode dry gas flow rate was about 5 times higher than the anode dry gas flow rate due to the 21% mole fraction of O_2 in dry air vs. the ultra high purity hydrogen for the anode. That means the amount

of water carried by the anode feeding for a given inlet relative humidity was much less than the water carried by the cathode feeding.

Four inlet relative humidity conditions were chose to investigate the effects of cell voltage on species distributions. For anode species measurements, the cathode inlet relative humidity was maintained 100% at 80°C, and the anode inlet relative humidity were set to either 0% or 100% at 65°C, and both the anode and cathode back pressures were 1.0 atm. Due to the much lower anode gas flow rate, to get acceptable cell performance, the anode inlet humidity for cathode species measurements was maintained 100% at 90°C, 10°C higher than the fuel cell temperature to input more water into the fuel cell, and the back pressures were also increased to 1.5 atm for the same reason. And the cathode inlet relative humidity was either 0% or 100% at 65°C. The bulk polarization curves for these four fuel cell operating conditions are shown in Figure **3-3**. Since the 0.5atm higher back pressure could improve the reactant concentrations within the catalyst layers as well as reduce the amount of water required for hydration because of the lower gas volume flow rates under higher pressure, the cell performance for the case of anode RH = 100%@90°C and cathode RH = 100%@65°C was higher than the performance for the case of anode RH=100%@65°C and cathode RH=100%@80°C, although the proceeding condition had less water input. For the case of anode RH=100%@90°C and cathode RH=0%@90°C, because the input water was much lower than all other three inlet humidity cases, the respective cell performance was the worse.

Three fuel cell voltages, 0.4, 0.6, and 0.8 V, were applied to get different current densities. The values of fuel cell bulk current densities with different voltages and inlet humidity can be found from Figure **3-3**. To calculate the current density of a set of current collecting landings, the active area directly under the landings and half of the area of the adjacent gas channels were taken. The reported location of the pin along the cathode flow path is the center of this total area in the flow path. Area under current collection landings is counted toward current density calculations. It is important to note that the current density data are represented as current density at a discrete distance along the flow channel, when it actually is gathered from a distributed region. In order to represent this area as a discrete location, the lengths have been weighted in order to take

into account adjacent channels and more accurately represent the mean location of current collection. This discretization gave very consistent results.

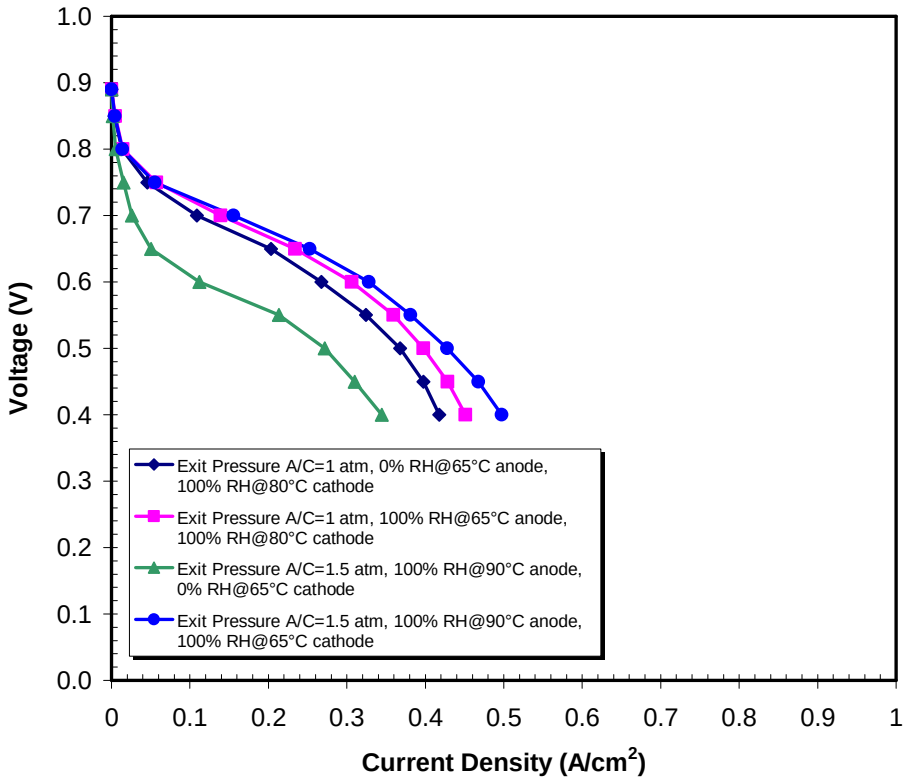

Figure **3-3**: Bulk polarization curves for fuel cell operation conditions of GC species measurements

Figure **3-4** shows the real-time continuous monitoring of the fuel cell performance while the cell voltage was changed between 0.4, 0.6, and 0.8 V, and at the same time sample extraction was occurring at many locations along the anode path. During this continuous measurement, the sample extraction line was removed and replaced at several different locations, and many samples were taken. It is clear from this figure that no significant performance change resulted from withdrawal of such a small fraction of total flow from the channel. In addition, the reproducibility of the current distribution results over long time scales and through voltage cycling can also be seen in Figure **3-4**. Thus the species distribution results got from different measurements still can be regarded as simultaneous results although they were not acquired at the same time.

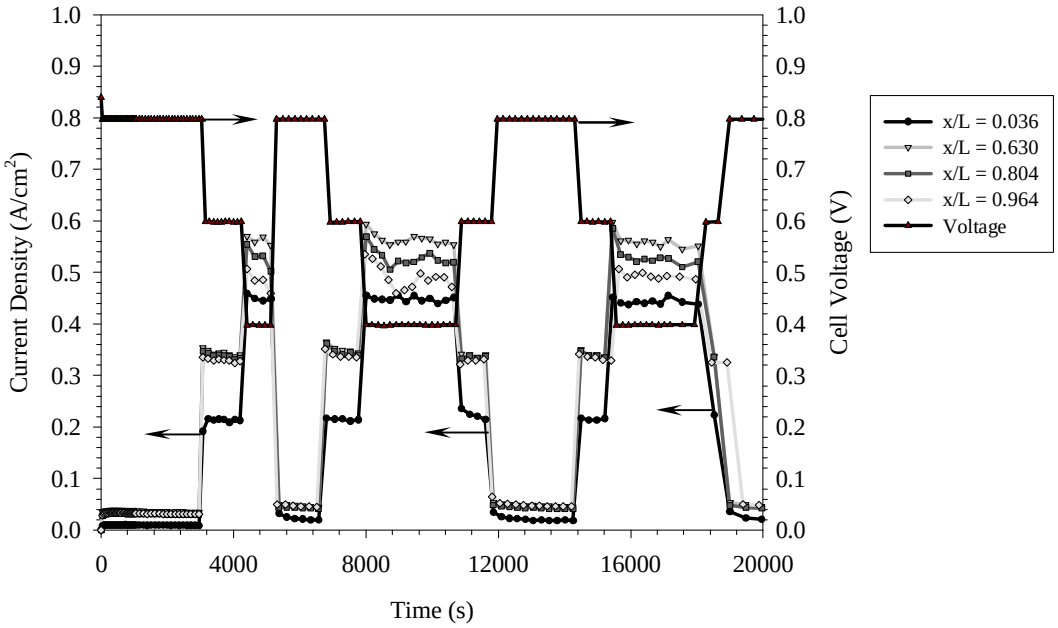

Figure **3-4**:Time varying performance at 0.4, 0.6, and 0.8 V while mass distribution measurements were taken along anode flow path, indicating little effect of measurement on cell performance and the reproducibility of the current distribution results over long time scales

It can be seen from Figure **3-5**, that for both cases of different inlet humidity with three different voltages, the anode water mole fraction curves follow an exponential approach to an asymptotic value. The anode water mole fraction increases along the flow path due to the diffusion flux of water from the cathode driven by the water activity difference across the membrane. Along with the increase of the anode water concentration, the driving force of the diffusion decreases, so an exponential style was observed for all the six curves. It also can be found that the asymptotic value is greater than the thermodynamically allowed maximum at the cell temperature of 80^{o}C. One explanation for this increased water content higher than the saturation limit of cell temperature is that the cell inner temperature is actually higher than the prescribed 80^{o}C, due to heat generation from electrochemical reaction and resistive dissipation. This kind of temperature elevation has been measured by Burford *et al* [**98**]. With a high current density of 2.0 A/cm^2, temperature increases up to 30 ˚C in the electrolyte membrane, up to 9 ˚C for the anode exit, and up to 12 ˚C for the cathode exit, have been reported.

Because a one-degree temperature difference can cause a 5% change of the saturation water mole fraction in the temperature range of PEFCs operation, these temperature elevations would significantly increase the maximum water that can be carried by the reactant gases.

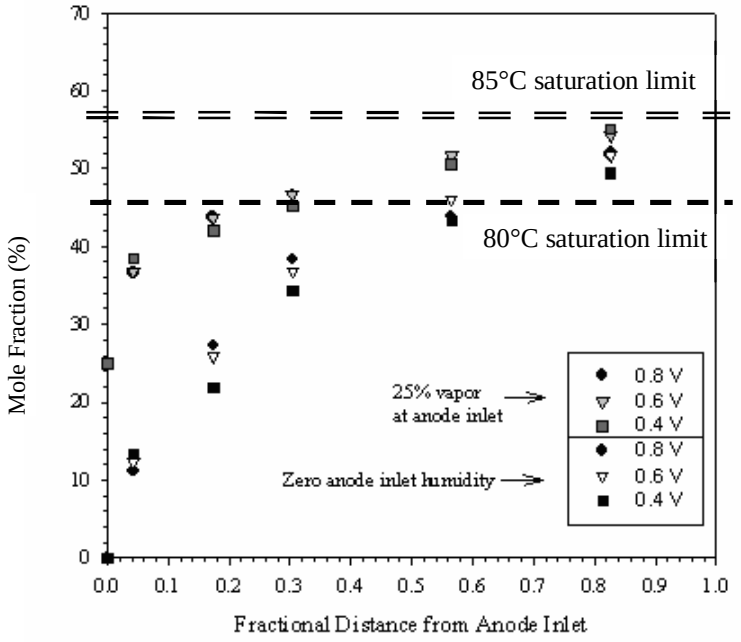

Figure **3-5**: Anode water distribution as a function of fractional distance from anode inlet for partially, and non-humidified anode inlet conditions. Test conditions: exit pressure A/C = 1 atm, 100% RH @ 80°C air cathode, 100% or 0% RH @ 65°C neat H_2 anode, ξ_c= 1.75 A/cm^2 equivalent, ξ_a = 0.7 A/cm^2 equivalent.

It also can be seen from Figure **3-5**, that for both cases of different inlet humidity, a lower fuel cell voltage (higher current density) always leaded to a lower anode water mole fraction because of the greater flux of electro-osmotic drag. However, it also should be noticed that the measured anode channel water content was not affected in a great degree by the cell voltage (and hence current density) draw. In most cases, the highest current output (lowest cell voltage) condition resulted in the lowest measured anode channel water vapor content, especially for the case of 0% anode inlet RH. Considering the lower cell voltage also resulted in higher water generation at the cathode side, and then resulted in higher cathode water mole fraction and higher water back diffusion flux,

the respective lower anode water mole fraction strongly indicates the effect of electro-osmotic drag. However, the small relative difference of anode water mole fraction also implies electro-osmotic drag of water from the anode to the cathode is nearly balanced by back diffusion under low current density (i < 0.5 A/cm^2). This is expected for very thin membranes such as the 51 μm Nafion® 112 membranes used for this study. This near balance of drag and diffusion of water with thin membranes has been observed experimentally by water condensation and collection techniques as well [**60**].

Figure **3-6** shows the respective hydrogen mole fraction variation along the anode flow path for the water distributions shown in Figure **3-5**. It can be seen from the figure, that the hydrogen mole fraction in the anode is higher for lower cell voltage conditions although the hydrogen consumption is higher for these conditions. Because hydrogen is the only other species present in the anode gas channel, the slower water uptake process of lower cell voltages lead to higher hydrogen mole fraction.

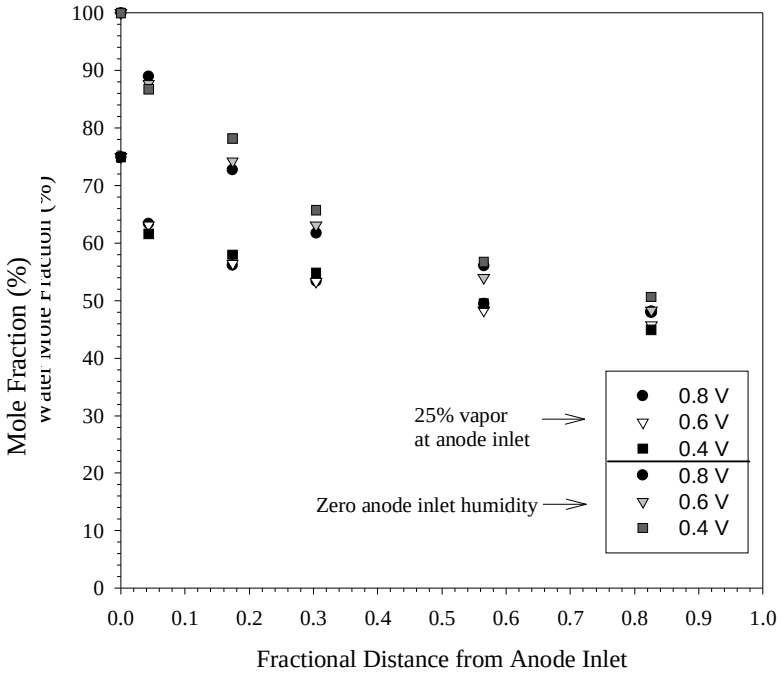

Figure **3-6**: Hydrogen distribution as a function of fractional distance from anode inlet for partially, and non-humidified cathode conditions. Test conditions: exit pressure A/C = 1 atm, 100% RH @ 80^{o}C air cathode, 100% or 0% RH @ 65^{o}C neat H_2 anode, ξ_c= 1.75 A/cm^2 equivalent, ξ_a = 0.7 A/cm^2 equivalent.

Figure **3-7** shows the measured water mole fraction at various locations within the cathode flow channel for three fuel cell voltages. The anode inlet relative humidity was set 100%@90^{o}C to increase the amount of water carried by the anode feeding stream, and the cathode inlet relative humidity was set either 0 or 100%@65 ^{o}C. Each data point shown represents an average of at least five data points with scatter less than ± 2.5% mole fraction in the data.

The cathode water uptake increases along the gas flow channel due to electro-osmotic drag and water generation for both inlet humidity conditions and three various fuel cell voltages. The water uptake curves of cathode can be divided into two regions. In the region near the cathode inlet (x/L<0.2), the fuel cell voltage (or current density) does not show a significant effect on cathode water uptake. The measured water mole fractions for three voltages almost overlap together in this region. This phenomenon can be explained by the dominating effect of water diffusion from the anode. As indicated in previous discussion for anode water uptake, under moderate current density conditions (i < 0.5 A/cm^2), the electro-osmotic drag of water from the anode to the cathode under lower cell voltage could be balanced by back diffusion with a slightly higher concentration difference across the membrane. In the inlet region of the cathode, there was a large concentration difference between the anode side and the cathode side, so the water uptake of the cathode was dominated by diffusion from the anode, and the contributions of electro-osmotic drag and water generation were minor. However, in the down streaming region (x/L>0.2), cell voltage has significant effects on cathode water uptake, especially for the zero cathode inlet humidity condition. It should be noticed that the dry gas mole flow rate of the cathode was about five times higher than the dry gas molar flow rate of the anode for the conditions of this series of tests, because of the low 21% mole fraction of oxygen in dry air and the higher cathode stoichiometry. So the amount of water carried by anode hydrogen cannot fully humidify the cathode gas flow, and the difference of water concentration between the anode and cathode would be diminished because of the diffusion and electro-osmotic drag. Since the anode uptake was not affected to a great degree by changes in current output, indicating electro-osmotic drag to the cathode was nearly compensated by diffusion of water to the anode, it

seems that the water uptake in the cathode gas channel is mostly the water produced via water generation, which is directly related to fuel cell voltage.

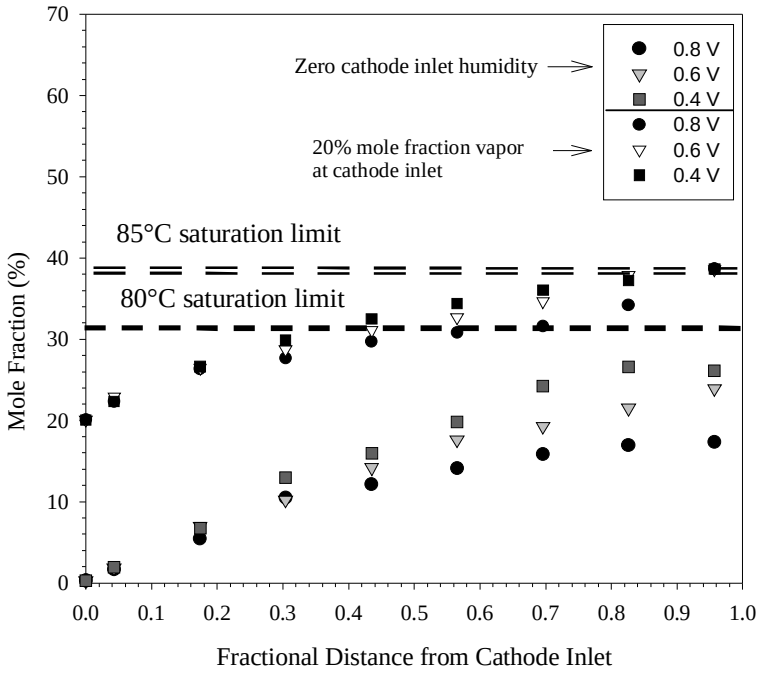

Figure **3-7**: Cathode water vapor distribution as a function of fractional distance from cathode inlet for partially, and non-humidified cathode inlet conditions. Test conditions: exit pressure A/C = 1.5 atm, 100% RH @ 90°C hydrogen anode, 100% or 0% RH @ 65°C Air cathode, ξ_c= 2.0 A/cm^2 equivalent, ξ_a= 1.5 A/cm^2 equivalent.

It also can be found from Figure **3-7,** that the water vapor uptake results for the two cathode inlet humidity cases had obvious differences. For the case of inlet relative humidity of 100%@65°C, cell performance was sufficient to provide adequate water generation at the cathode to ensure a saturated flow condition at the exit. However, for the 0% relative humidity inlet condition, there was very low cell performance. The maximum cell average current density for the conditions shown was only 0.4 A/cm^2. Therefore, water uptake was not complete to saturation.

Figure **3-8** and Figure **3-9** show the measured nitrogen and oxygen mole fractions in the cathode flow path for the two cases of different cathode inlet humidity shown in Figure **3-9**. Because of the high true stoichiometry, the changes in oxygen mole fraction are only around 7%, not very significant. It should be noted that the stoichiometry values

reported are for an equivalent total current density. That is, the flow rate is constant for each cell voltage, regardless of the resultant cell current output. This is required with the segmented cell approach, as each location will have a different output and it is thus extremely difficult to match the flow rate with the measured bulk current density. Values of both Figure **3-8** and Figure **3-9** are within 5% of the expected theoretical value based on current output and flow rate.

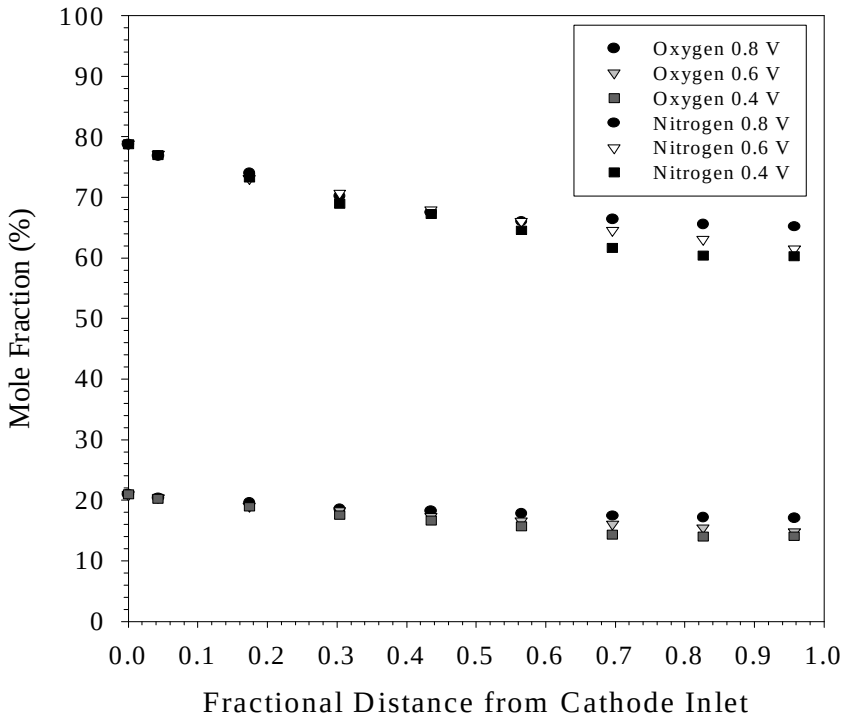

Figure **3-8**: Measured oxygen and nitrogen distribution as a function of fractional distance from cathode inlet for non-humidified cathode conditions. Test conditions: exit pressure A/C = 1.5 atm, 100% RH @ 90 ^{o}C hydrogen anode, 0% RH air cathode, ξ_c= 2.0 A/cm^2 equivalent, ξ_a= 1.5 A/cm^2 equivalent.

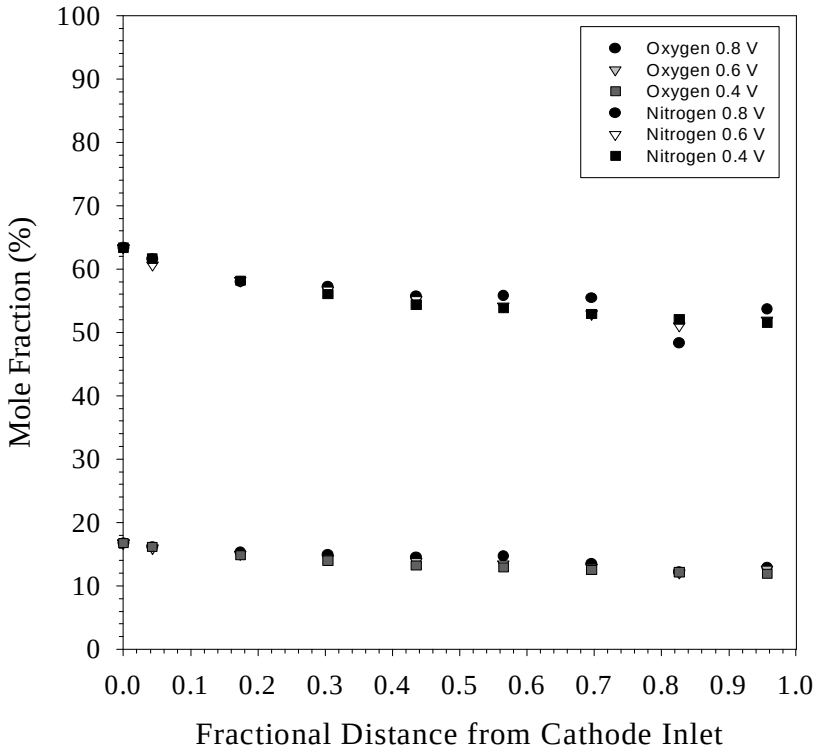

Figure **3-9**: Measured oxygen and nitrogen distribution as a function of fractional distance from cathode inlet for under humidified cathode conditions. Test conditions: exit pressure A/C = 1.5 atm, 100% RH @ 90°C hydrogen anode, 20% mole fraction inlet air cathode, ξ_c : 2.0 A/cm^2 equivalent, ξ_a : 1.5 A/cm^2 equivalent.

3.4 Summary

An Agilent 3000 Micro GC has been used for the first time to measure the *in-situ* species distributions in an operating fuel cell with water content up to full saturation at 90°C. This newly developed technique can be used to directly map steady state species distributions in the anode and cathode of an operating fuel cell with a time resolution of approximately two minutes, and a spatial resolution limited only by the proximity of sample extraction ports located in the reactant gas flow channels. Along with other diagnostic techniques such as current distribution mapping and high frequency resistance

mapping, this species mapping technique provides an important tool to understand water management and reactant distribution in PEFCs.

The effects of fuel cell voltage on species distribution were investigated for varies inlet humidity and constant inlet flow rate. With a dry anode and a fully humidified cathode, lower fuel cell voltage generally resulted in lower anode water content due to increased drag flux. However, because lower cell voltage also led to higher cathode water mole fraction and then stronger water back diffusion from the cathode, the anode water contents for lower voltage at some locations along the flow channel were higher than the respective water content for higher voltage. With a fully humidified anode and a dry cathode, the cathode water mole fraction always increases with decreasing cell voltage (increasing current density) because electro-osmotic drag, water generation, and diffusive flux tend to increase the cathode water content.

For the thin (51 μm) membranes used, the electro-osmotic drag of water from the anode to the cathode is nearly evenly balanced by back diffusion under low to medium current densities ($i < 0.5$ A/cm^2).

Chapter 4

Development and Application of RTGA on Real-time Species Measurement of PEFCs

4.1 Introduction

In recent work [**96**], Mench et al. demonstrated the ability to accurately measure the in-situ water vapor mole fraction distribution in an operating PEFC with an Agilent 3000 MicroGC Gas Chromatograph, without the need for condensation of the water vapor. While this technique provides molar percent level accuracy of the water vapor content across the flow channels, it still requires on the order of five minutes per data point, and has limited accuracy for low levels of some important species such as CO. Thus, the utility of this technique is still essentially limited to analyzing steady state species distribution. In order to enable the study of species transport dynamics in the fuel cell, it is necessary to decrease the time between consecutive data points by another order of magnitude, while increasing accuracy.

In this chapter, the ability to measure various species including water vapor, nitrogen, and oxygen in near real time (~1 seconds per data point) is demonstrated with an Agilent Real Time Gas Analyzer system. The 300-fold decrease in data collection time compared to the MicroGC method makes it possible to continuously monitor species mole fraction changes at selected locations along the anode or cathode flow path, and also provides detailed understanding and perspective of the time scales of the various intercoupled multi-phase dynamic transport phenomena.

Since water generation is directly proportional to current density, it is also desirable to couple water and current distribution measurements to provide detailed information on non-uniform transport and generation effects. This can be accomplished with a segmented cell approach, developed and described in reference. [**83**]. Along with current and species distribution, high frequency resistance (HFR) distribution can be used

to reveal the local ionic conductivity (and thus hydration state) of the electrolyte. This is accomplished in this study with a multi-channel 3 kHz AC impedance analyzer that scans the same areas where current density is measured through the segmented cell technique.

4.2 RTGA Calibration

The Real Time Gas Analyzer (RTGA) applied here is a mass spectrometer, set up to allow continuous sampling and measurement of species without separation or delay. However, a non-negligible base value of water is always observed even the gas sample is UHP hydrogen (>99.999%). It was necessary to determine if the output of water from the RTGA can be corrected by simply subtracting the zero point error from the measured water molecule numbers. In the discussion to the calibration of Micro GC, the humidification efficiency of the bubble-humidifier has been proved near 100% at extremely low gas flow rate and accurate temperature control conditions. So the same humidifier can be used to check the accuracy of RTGA.

Calibration of the RTGA was accomplished with the same gas-bubbler humidifier used in the calibration of Micro GC, which was running at low flow rate and controlled temperature. The humidifier was used to provide a calibration gas mixture with known humidities derived from the saturation pressure of water at the humidification temperature and the humidification pressure by treating the exit gas mixture as idea gas. The inner pressure of the humidifier was also precisely monitored during the whole calibration process to correct the effect of humidification pressure. Then measurements were made every 5°C in the humidification temperature range from 40°C to 90°C. The measured water mole fractions were calculated by subtracting the zero point error from the original output. All shown measured data were the averages of the results of at least 5 minutes to minimize the error caused by the temperature variation of the humidifier. Then, the measured mole fractions were compared with the respective theoretical values.

Figure Figure **4-1** shows the continuous variations of species ion signals recorded by RTGA in the calibration process. The curve of water signal clearly shows the increase of water mole fraction due to the increasing humidification temperature and the decrease

of water mole fraction due to the decreasing humidifier temperature after the calibration. While the ion signal of oxygen shows a reverse trend compared to the water signal. To show the water signal with more details, the much higher nitrogen signal is not shown in the figure. Because nitrogen and oxygen were the two main compensate species in the gas mixture, the ion signal of nitrogen has a similar trend compared to the oxygen signal. The figure also shows the curves of argon and carbon dioxide. That shows the ability of RTGA in CO poisoning research. The captured signal variation of water that caused by oscillation of humidification temperature also implied the ability of RTGA in real-time continuous monitoring of changes in species mole fractions.

Calibration results taken for fully humidified air are shown in Figure **4-2**. The humidification pressure was maintained at 3.0 atm (29.4 psig), the same as the working pressure of the fuel cell to minimize any possible error associated with pressure change. Theoretical curves are also included in the figures for comparison. Close agreement can be observed between the measured values of water fraction and the thermodynamically expected saturation values. All the data points shown here represent an average of 5 minutes measurements. The measured mole fraction was typically within ±0.5% of the theoretical value, up to very high values of water mole fraction humidified at 90^{o}C. This calibration indicated that the zero point error of water could be corrected by simple subtraction of the zero output, and the RTGA technique is very accurate.

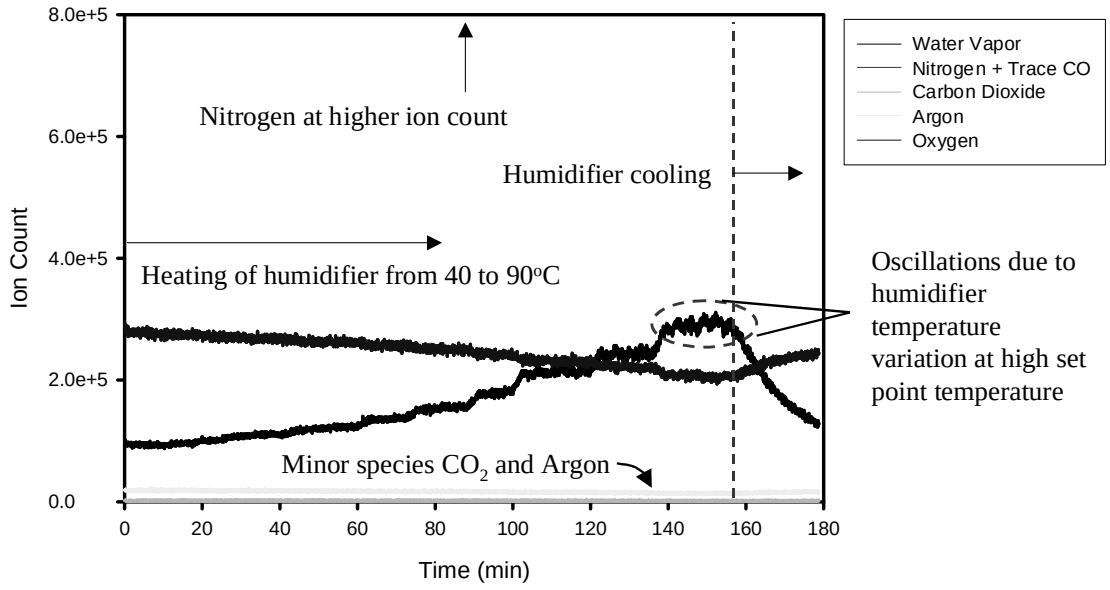

Figure **4-1**: Continuous record of the calibration process. Gas sample was generated from the humidifier at temperatures between 40 and 90 °C with set increment of 5 °C. The variation in the signal circled above corresponds to the temperature oscillation of the saturator at a high set point temperature.

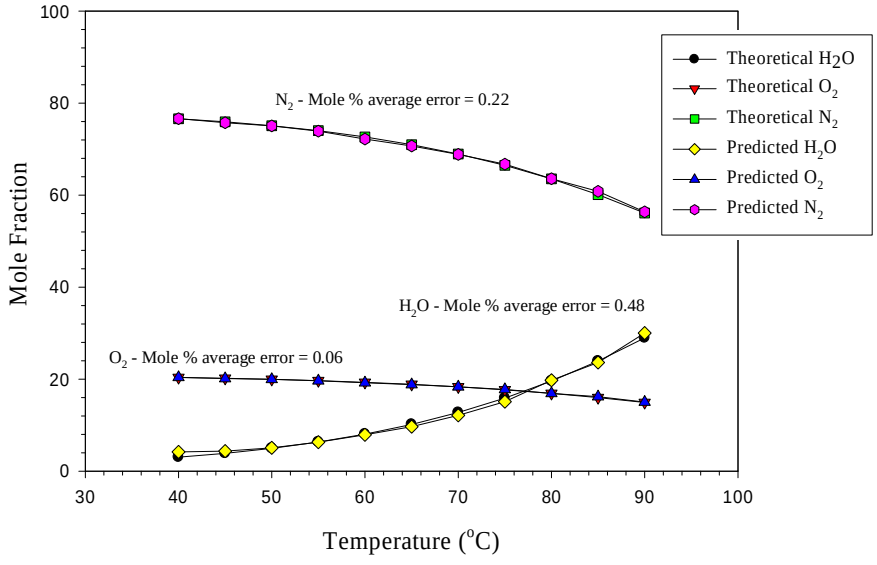

Figure **4-2**: Comparison between measured and theoretical water vapor, oxygen, and nitrogen concentrations measured with RTGA with baseline value at 50°C. The humidifier bottle was at 20.6 psig pressure.

4.3 Real-Time Monitoring of Species Variation

The transient species variations at selected locations along the cathode flow path were continuously monitored for the 1st generation instrumented fuel cell. The experiments were designed to investigate the effects of current density variation on cathode species distribution and illustrate the increase of flooding and formation of water droplets at increasing distances from the inlet of the cathode flow path. Four fuel cell voltages, open circuit voltage, 0.8, 0.65, and 0.5 V, were applied to get different current density. The operating conditions for this series of test were listed in Table **4-1**. During the measurement process, the fuel cell showed reproducible performance while the sample extraction line was removed and replaced at several different locations, and fuel cell voltage had been changed for several cycles.

Table **4-1**: Operating conditions for real-time monitoring of species

Parameter	Value	Units
Electrolyte	Nafion 112 (E.I. du Pont de Nemours and Company)	NA
Gas diffusion layer	ELAT® (E-TEK of De Nora North America) anode and cathode	NA
Catalyst loading (carbon supported)	0.5	mg/cm^2
Cell temperature	80	^oC
Anode inlet temperature	80	^oC
Cathode inlet temperature	80	^oC
Cathode flow rate	2.0	A/cm^2 equivalent
Anode flow rate	1.5	A/cm^2 equivalent
Cathode pressure	30	psig
Anode pressure	30	psig
Cathode inlet humidity	50% RH at 80 ^oC	NA
Anode inlet humidity	100% RH at 80 ^oC	NA
Cell voltages	OCP, 0.8, 0.65, 0.5	V
Anode gas	Ultra high purity H_2 (>99.999 %)	NA
Cathode gas	Commercial air (79% N_2, 21% O_2)	NA

Figure **4-3** shows the current distributions of the fuel cell at 3 operating voltages. Current was minimized near the middle of the flow channel due to anode dry-out caused by net water flux from the anode to cathode. And current density increased at the exit as a result of higher moisture content due to water generation. Species mole fractions within the cathode flow path were continuous monitored at three sampling ports. The locations (4.3%, 56.5%, and 82.6% fraction distance from cathode inlet) of these sampling ports were marked by dash lines.

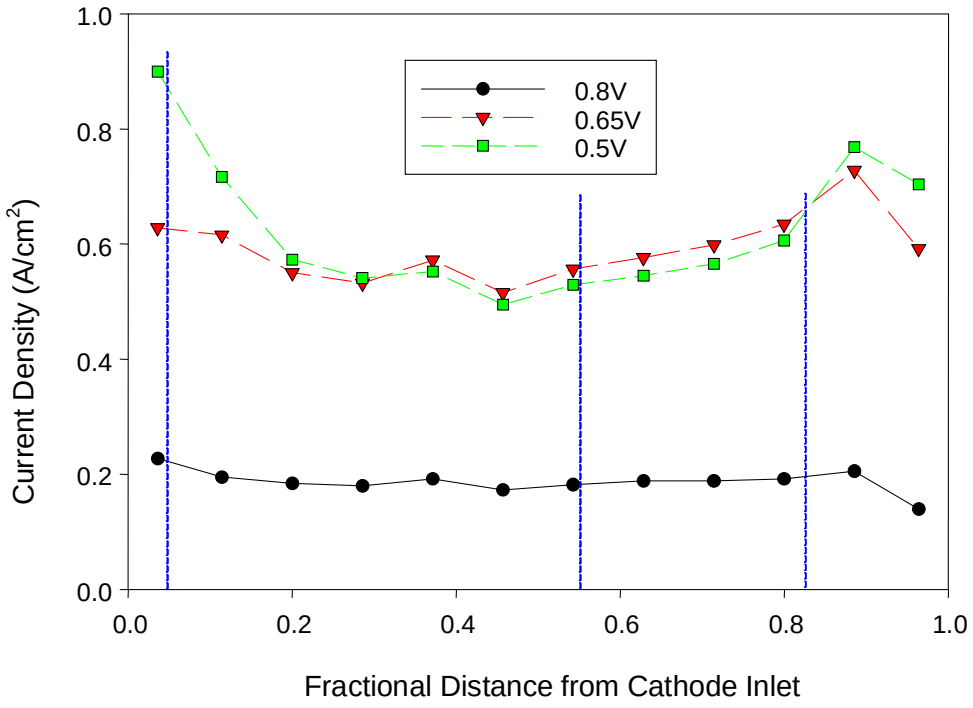

Figure **4-3**: Current distributions of the fuel cell at three different voltages. The vertical dashed lines represent the location of three sampling ports

Figure **4-4** shows the real-time variations of cathode species mole fractions at 4.3% fractional distance from the cathode inlet. There were two decreases of fuel cell voltage that are marked by vertical dash lines in the figure. One voltage drop occurred at t=33 min from 0.8V to 0.65V, and the other drop took place at t=43 min from 0.65V to 0.5V. The changes of current density responding to these voltage changes can be found in Figure **4-3**. It can be seen from Figure **4-4** that current density had no significant effect on the species mole fractions at this location since they were dominated by cathode inlet flow, and also due to the concentration boundary layer effect.

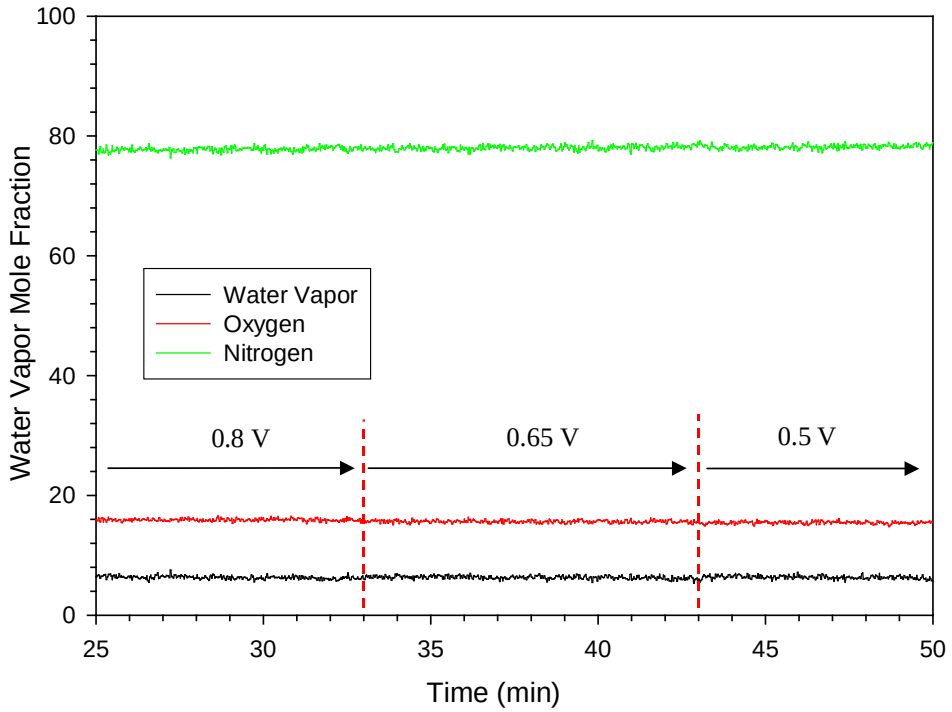

Figure **4-4**: Species Variation at x/L = 0.043 along cathode flow path. Changes in cell voltage are marked by the vertical dashed lines from 0.8 to 0.65 V and from 0.65 to 0.5 V.

Figure **4-5** shows the real-time variations of cathode species mole fractions at 56.5% fractional distance from the cathode inlet. There also were two decreases of fuel cell voltage that are marked by vertical dash lines in the figure during the sampling process. One voltage drop occurred at t=114 min from 0.8V to 0.65V, and the other drop took place at t=134 min from 0.65V to 0.5V. The changes of current density responding to these voltage changes at this location can be found in Figure **4-3**. It can be seen from Figure **4-5** that current density had much larger effect on the species mole fractions at the mid-cell location, compared to the inlet condition. When the fuel cell voltage dropped from 0.8V to 0.65V, the current density also tripled, resulting an obvious jump of measured water mole fraction and obvious drops of measured oxygen and nitrogen mole fraction. When the fuel cell voltage dropped from 0.65V to 0.5V, because just the current density at inlet region had a significant increase, and other region only showed minor change in current density, the respective mole fraction changes were much weaker than

the earlier voltage change. However, flooding was also evident as spikes were observed after the voltage drop. These spikes were formed by water droplets entering and evaporating in the RTGA from the sample line.

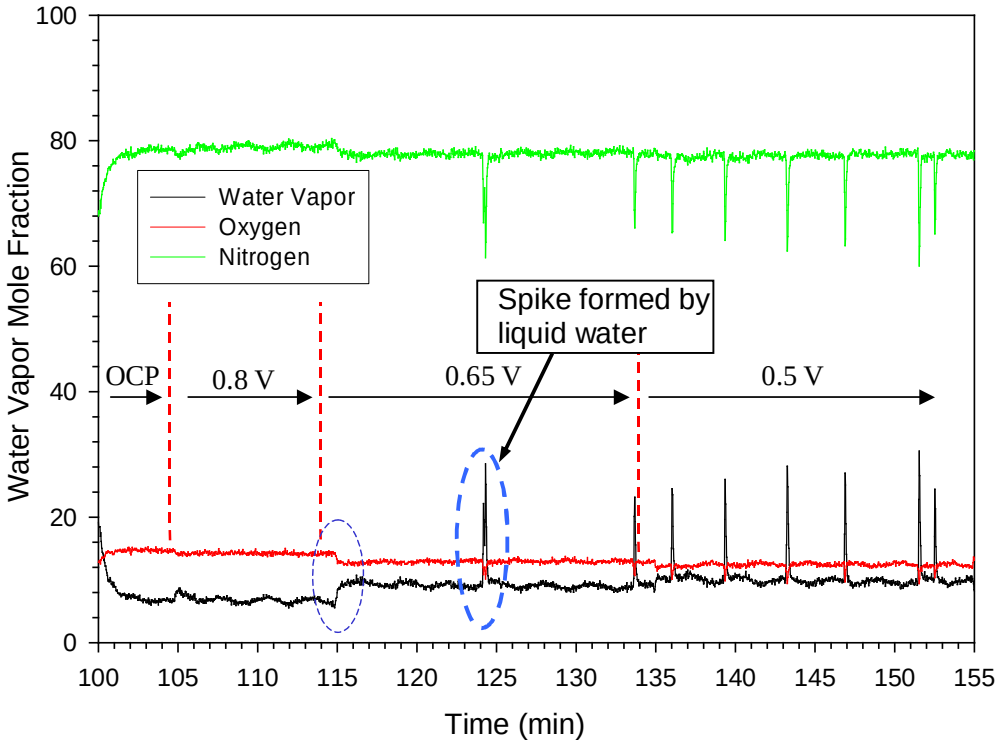

Figure **4-5**: Species Variation at x/L = 0.565 along cathode flow path. Changes in cell voltage are marked by the vertical dashed lines from 0.8 to 0.65 V and from 0.65 to 0.5 V.

Figure **4-6** shows the variations of cathode species mole fractions at 82.6% fraction distance from the cathode inlet. The two voltage dropped occurred at t=68 min and t=78 min. Respective voltage changes were from 0.8V to 0.65V and from 0.65V to 0.5V. The changes of current density responding to these voltage changes at this location can be found in Figure **4-3**. It can be seen from Figure **4-6**, that current density also had significant effect on the species mole fractions at this location. However, compared to the location of x/L = 0.565, when the fuel cell voltage dropped from 0.65V to 0.5V, although the overall current density changes for both cases were similar, a more obvious jump of water mole fraction can be observed due to the larger path length in front of the measured

location to accumulate changes in species distribution. Due to the same reason, an increased number of water spikes could be seen while cell voltage was 0.65V and 0.5V.

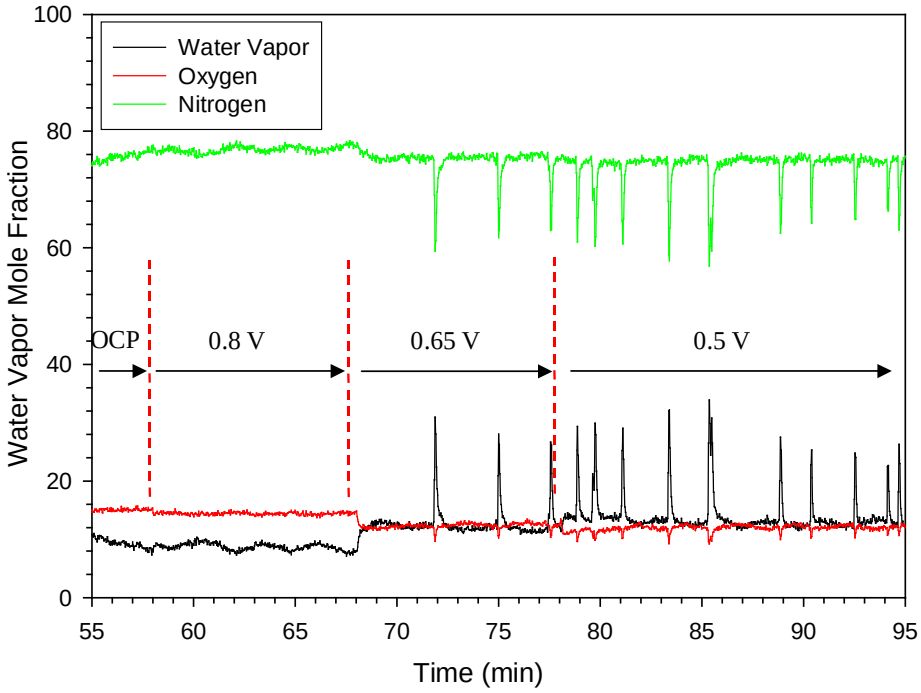

Figure **4-6**: Species variation at x/L = 0.826 along cathode flow path. Changes in cell voltage are marked by the vertical dashed lines from 0.8 to 0.65 V and from 0.65 to 0.5 V.

Figure **4-7** shows the measured water mole fraction at various locations within the cathode flow channel for three fuel cell voltages. The plateau behavior for locations greater than 56.5 % fractional distance along the cathode flow path can be attributed to increasing water content despite nearly the same net local current density. This could be caused due to higher local temperatures at lower efficiency conditions. Each data point shown represents an average of data measured in at least five minutes.

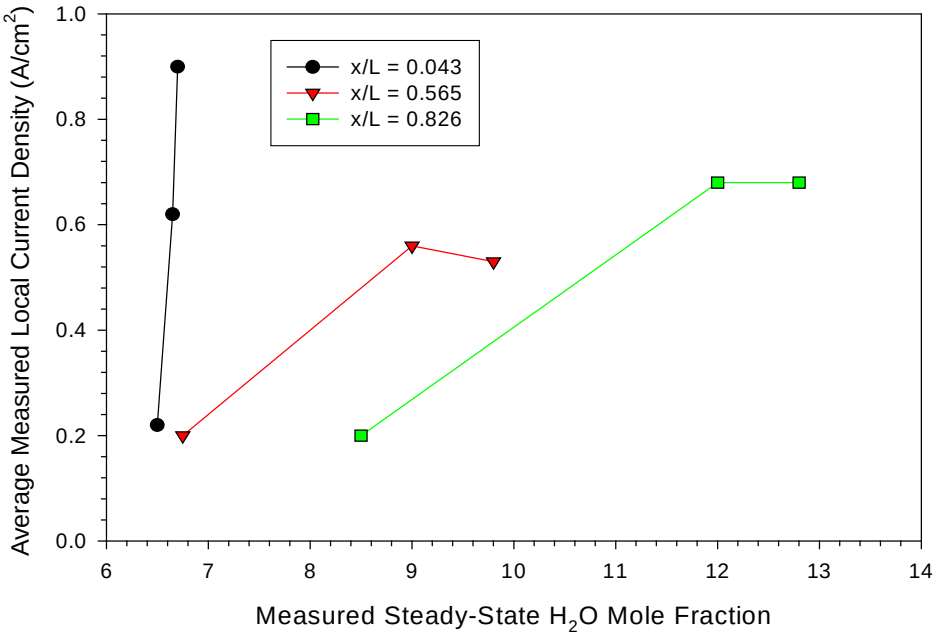

Figure **4-7**: Average local current density vs. water mole fraction at different fractional distances along cathode flow path and voltages.

Steady state water vapor uptake at varying distances from the cathode inlet and voltages are shown in Figure **4-8** and Figure **4-9**. As seen in Figure **4-8**, water generation at the cathode and diffusion from the electrolyte to the gas channel increases cathode water content with travel down the flow path. In Figure **4-9**, at higher cell voltages less current is generated and lower water vapor mole fractions are observed.

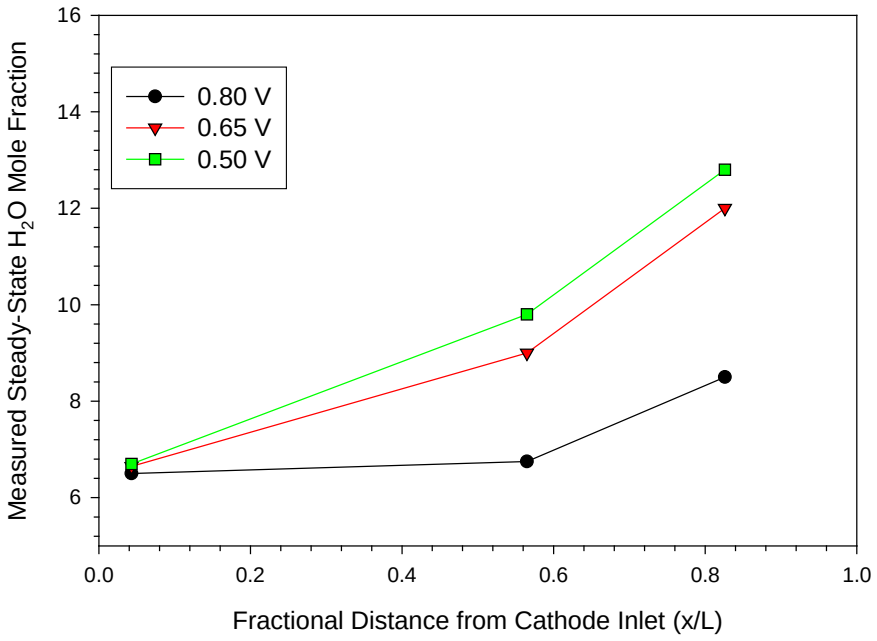

Figure **4-8**: Plot of the steady state water vapor uptake in the cathode flow channel vs. the fractional distance along cathode flow path for three different voltages.

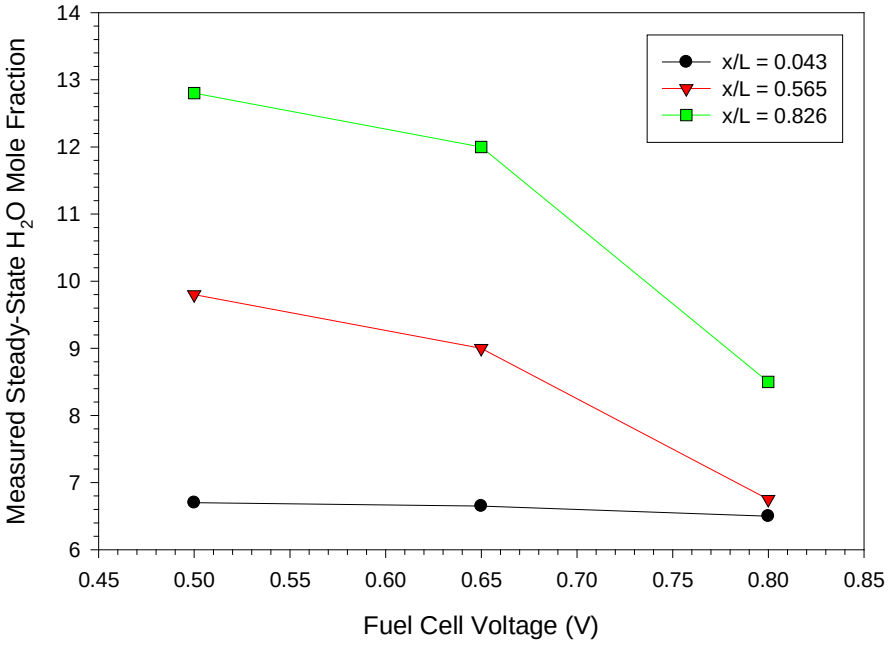

Figure **4-9**: Plot of the steady state water vapor uptake in the cathode flow channel vs. fuel cell voltage for three different fractional distances through the cathode flow path.

4.4 Dynamic Response of Current, Species of PEFCs

As mentioned in previous chapters and sections, many experimental study and deduced models have been conducted to investigate the water transport in PEFCs. However, most of the presented researches were conducted under steady-state operation, and scant research results under dynamic conditions are available in literature, which are very common in operation of PEFC systems, especially for automotive applications.

In this section, dynamic response of distributed current, species to step voltage change for a PEFC under low operating inlet humidity conditions is examined by RTGA.

All the dynamic experiments were performed using a Nafion® 112 (51 μm) equivalent MEA which was hot pressed from two Nafion® 111 half MEAs. Typical dynamic behaviors of PEFCs under low-humidity condition were investigated for two basic inlet humidity conditions. One is a dry cathode condition with 75% relative humidity anode and 0% relative humidity cathode, and the other is a dry anode condition with 0% relative humidity anode and 75% relative humidity cathode. Tests were conducted with a constant flowrate on the anode and cathode. The anode flowrate was 1.5 A/cm2 equivalent, and the cathode flowrate was 2.0 A/cm2 equivalent. The exit pressures of the fuel cell were 2 atm for both anode and cathode. The tests for steady-state electrolyte temperature were taken under a more wide range of operating conditions.

Figure **4-10** and Figure **4-11** show the distributed transient current response to voltage perturbation for the A/C RH=75/0 case and the A/C RH=0/75 case. The voltage perturbation mode is cyclic 10-minute 0.7V followed by 10-minute 0.4V. From the plots, we can see two kinds of transient behaviors: rapid response and slow adjustment. The rapid response cannot be well captured by the sampling frequency of 1 Hz, whereas the slow adjustment is much slower, and has a time order of minute. For both humidity conditions, when cell voltage decreases from 0.7V to 0.4V, local current densities first increase with an overshoot, and then slowly decrease to new steady-state values; when cell voltage increases from 0.4V to 0.7V, local current densities first decrease with an undershoot, and then slowly increase to new steady-state values. However, for the dry cathode case, the current densities have obvious high frequency instability, which has

also been observed by other researchers [**103**]. This phenomenon may be caused by the competing electro-osmotic drag and back-diffusion.

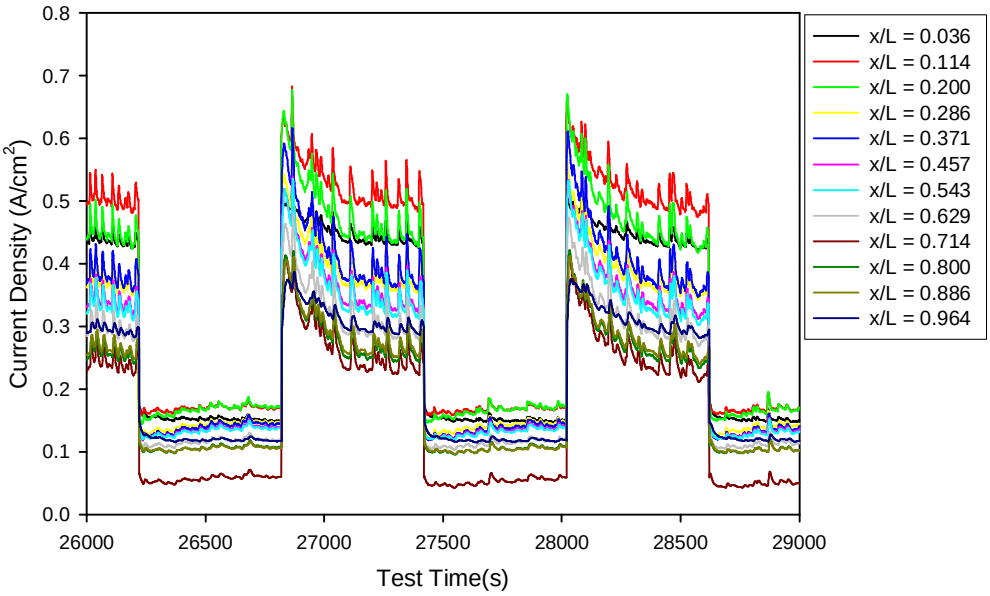

Figure **4-10**: Distributed transient current response for voltage perturbation (0.7V-0.4V) with A/C RH=75/0.

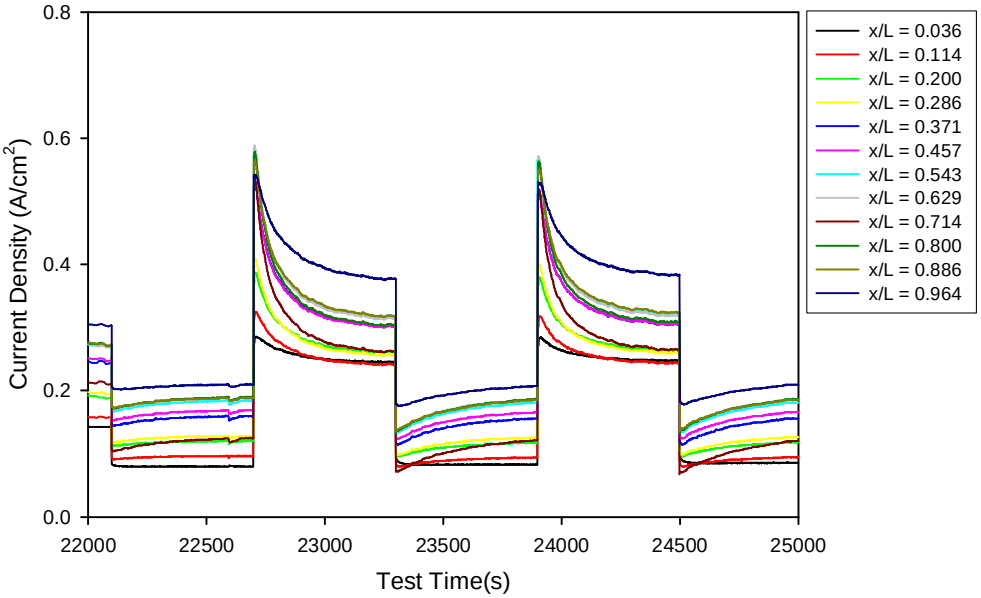

Figure **4-11**: Transient current response for voltage perturbation (0.7V-0.4V) with A/C RH=0/75

Figure **4-12** and Figure **4-13** presents the transient species response to the voltage perturbation taken at 83% along the anode and cathode flowpaths—essentially near the exits of the flowpaths for the A/C RH=75/0 case. Similar to the response of current, there are two kinds of response here: rapid response and slow adjustment. Compared to the current response of this case, the slow adjustment processes of the water species have basically the same adjustment time of current. The rapid responses of species also cannot be well captured by the 1Hz measuring ability of the RTGA. The less than 1-second rapid response of measured species to voltage perturbation indicates mass transfer process from the catalyst layer to the flow channel is very fast. So the minutes long adjustment time indicates that the uptake/loss of water in the membrane is relative slow.

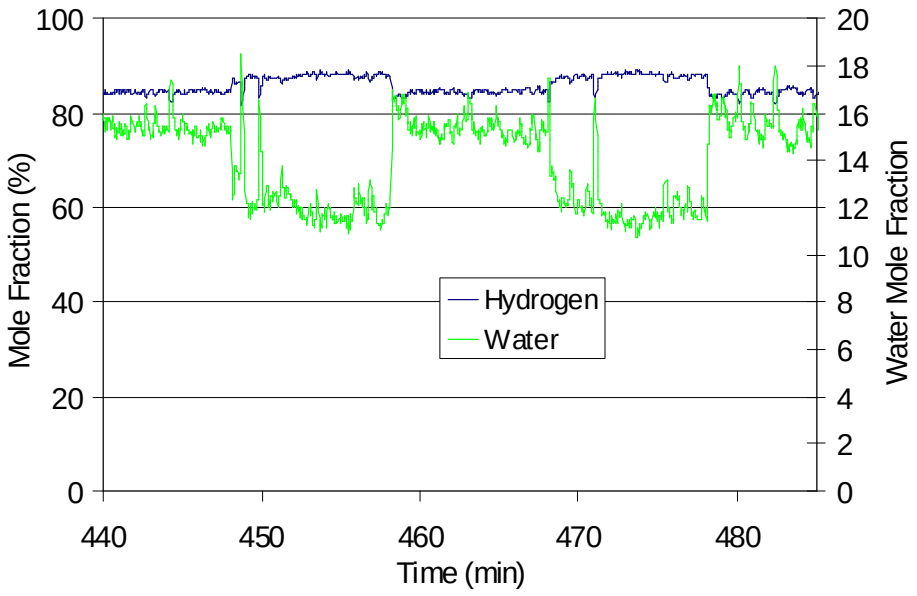

Figure **4-12**: Transient anode species response at x/L=83% for voltage perturbation (0.7V-0.4V) for the dry cathode case, A/C RH = 75/0.

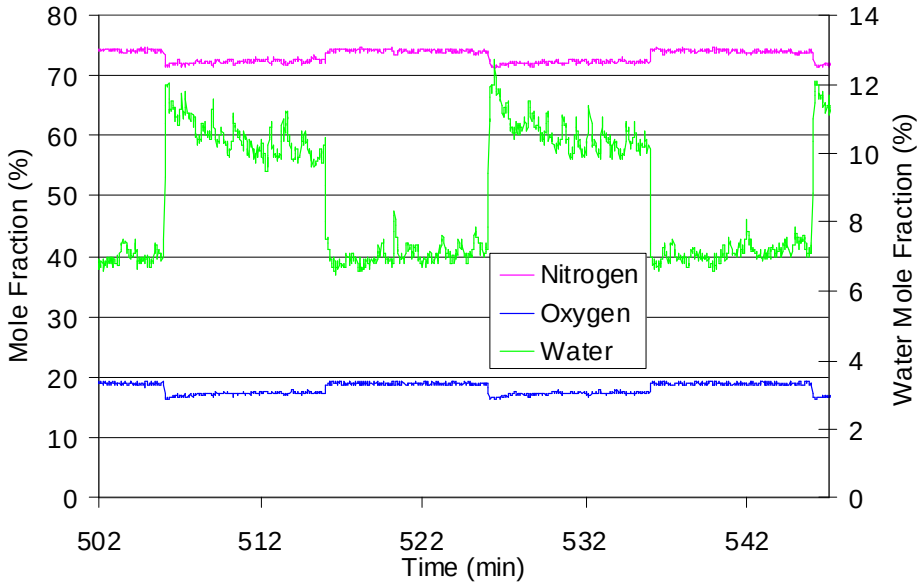

Figure **4-13**: Transient cathode species response at x/L=83% for voltage perturbation (0.7V-0.4V) for the dry cathode case, A/C RH = 75/0.

Figure **4-14** and Figure **4-15** show the transient species response for the A/C RH=0/75 case. Gas sample was still taken at 83% along the anode and cathode flowpaths. From the plots, we can find that the anode adjustment of dry anode case approaches asymptotically to steady state, very different from dry cathode case. In addition, the amplitude of the water species instability for this dry anode case is much smaller than the amplitude for dry cathode case, although they have similar input humidity variation. The instability for dry cathode implies the water profile in membrane is nonlinear, and membrane dry-out mainly takes place close to the anode interface. For both cases, the current density adjustment time corresponds to the time scale of mass adjustment in the anode side, not cathode side.

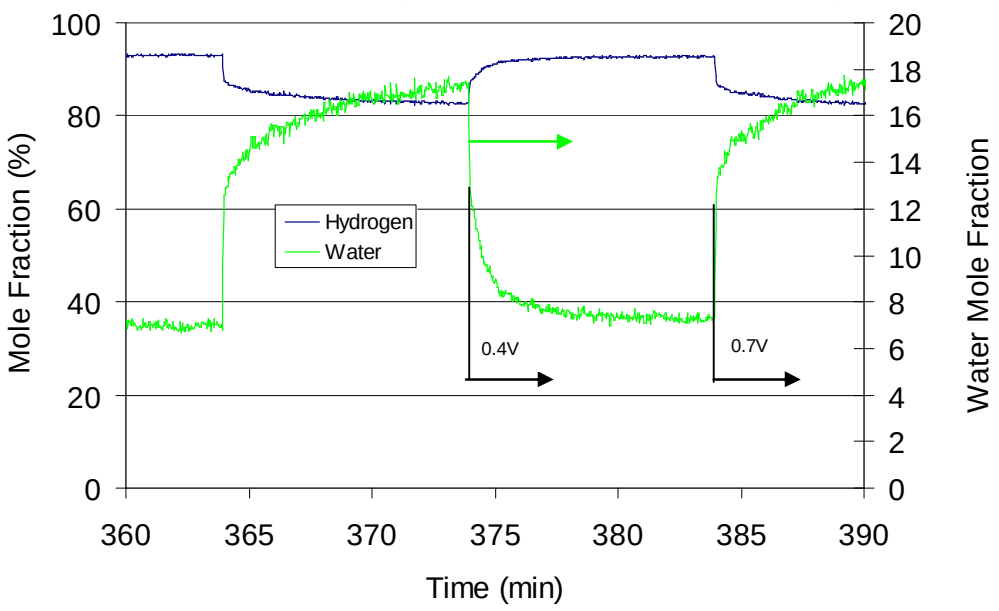

Figure **4-14**: Transient anode species response at x/L=83% for voltage perturbation (0.7V-0.4V) for the dry anode case, A/C RH = 0/75.

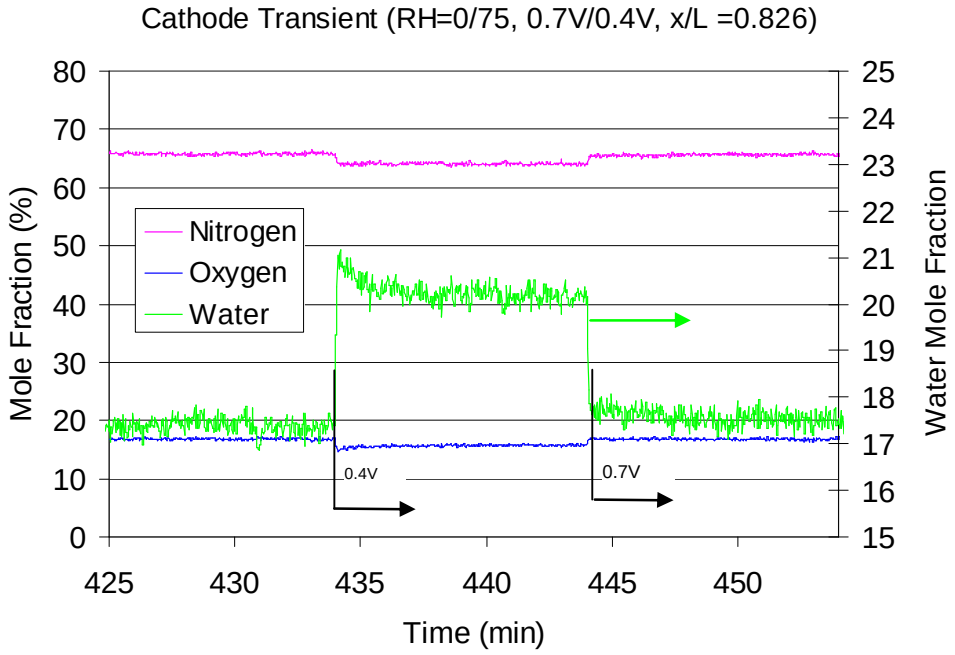

Figure **4-15**: Transient cathode species response at x/L=83% for voltage perturbation (0.7V-0.4V) for the dry anode case, A/C RH = 0/75.

4.5 Summary

The ability to rapidly measure precise species distribution in real time (1 Hz) has been demonstrated for the first time with an Agilent Real-Time Gas Analyzer (RTGA), which has been calibrated and interfaced to a PEFC.

A current density plateau along the cathode channel path was shown of increasing water vapor content despite nearly the same net local current density. This may be due to higher local temperatures at lower efficiency conditions.

Evidence of cathode water droplet formation and motion in the flow channel was shown, occurring regularly as the current density is increased and more often at locations closer to the cathode flowpath exit. While the Micro GC is a less expensive choice and has better tolerance to liquid water, the relative long operation time of 2 minutes per measure limits the technique to steady-state applications. The RTGA has a much shorter response time of about 1 second per measurement, making possible the near real-time monitoring of species mole fractions, and provides the ability to determine the time scale of many intercoupled phenomena. However, RTGA cannot distinguish N_2 and CO due to identical molecular weights.

The dynamic response of fuel cell performance to step change in voltage is quite different between dry anode and cathode conditions. For the dry cathode condition, the anode adjusts asymptotically from high to low current, while for a dry cathode condition, the adjustment is very rapid. For both cases tested, the current density adjustment time corresponds to the time scale of mass adjustment in the anode side, not the cathode side, indicating a non-linear water content profile in electrolyte.

Chapter 5

Distributed Performance of PEFCs under Low Humidity Conditions

5.1 Introduction

In Chapter 3 and Chapter 4, two new diagnostic techniques were developed to measure the species distributions in a PEFC, using a MicroGC and a RTGA accompanied with simultaneous current distribution and high frequency resistance measurements. In the gas chromatograph (GC) method, only steady-state data can be obtained, while in the real-time gas analysis (RTGA) method, real-time (1 Hz) data can be obtained to reveal the water and other species transport dynamics in the flow channel. The effects of current density on water uptake, and transient response of water mole fraction on fuel cell voltage change were investigated. The results clearly demonstrated the ability of both techniques to determine species mole fraction variations along the anode and cathode flow path.

In this chapter, the combined current, species, and HFR distributions for a PEFC with co-flow arrangement are examined under a wide range of operating inlet humidity conditions to determine the relative importance of anode and cathode humidity, provide insight into distributed performance in undersaturated inlet conditions, as well as provide supporting data for advanced model development.

5.2 Experimental

Instrumented cell design.— All experiments in this chapter were performed using the 1st generation highly instrumented fuel cell. The fuel cell utilizes segmented current collector similar to that described in Mench et al.[**83**] Additional specific details of the fuel cell design can be found in chapter 2. Forty-eight stainless steel landing segments

for each side were embedded into electrical insulating plates made in polycarbonate plexiglass to serve as landings, and also form a flow field with single-pass serpentine overall co-flow arrangement. The landings were gold-plated, and each was welded to individual silver wires to minimize contact and wire resistance. The landings of each side were divided into 12 groups, along the flow channel, with four landings in each group. Extension wires of the four landings in each group were combined together and then connected to one channel of the potentiostat. The cathode GDLs were segmented to 12 pieces along the flow channel. A resistance check, after the cell was assembled, showed that the in-plane resistances between GDL pieces were all significantly greater than 1200 mΩ. This high resistance greatly diminishes internal current spreading, and also enables distributed current and HFR measurement. For mass distribution measurements, eight species extraction ports were located at 4.3, 17.4, 30.4, 43.5, 56.5, 69.6, 82.6, and 95.7% of the fractional distance of the anode and cathode flow paths.

As shown in Figure **2-5**, the dimension of the flow channel is 2.16 mm wide and 3.18 mm deep, and the average pass length is approximately 71 mm. With 22 total serpentine passes formed by 48 gold-plated landing segments, the total length of the flow channel is about 1577 mm. This single-path, deep-channel design described herein is nonoptimal from a performance standpoint, but was instead designed with computational model validation simplicity in mind. All experiments were performed using Gore PRIMEA® Series 57 membrane electrode assemblies (MEAs) with a dry membrane thickness of 18 μm and a platinum loading of 0.4 mg/cm^2 on both anode and cathode. The gas diffusion medium consisted of CARBEL MP gas diffusion media as the microporous layer and Toray 060 (wetproofed) as the macroporous layer. Ultrahigh-purity (>99.999%) hydrogen and standard dry air were supplied from compressed gas cylinders.

Calculation of active area segments.— The current density data are represented at a discrete distance along the flow path, when they actually are gathered from a distributed region. To calculate the current density of an individual segment, the active area directly under the landings, and half of the adjacent gas channels, were taken. The reported discrete location of the measured current density along the flow path is the center of the

total measurement area (including the area under current collection landings). This discretization gave very consistent results. Local current was measured at 12 different locations with an equivalent fractional distance from the inlet of 0.036, 0.114, 0.200, 0.286, 0.371, 0.457, 0.543, 0.629, 0.714, 0.800, 0.886, and 0.964, respectively.

Testing system.— The experimental setup shown in Figure Figure **2-1** was used for this study. For current density measurement, the test station maintains a constant voltage while measuring the current from each segmented channel. The control system is equipped with dew point humidifiers, which were extensively calibrated using a desiccant and mass balance technique. To achieve different inlet relative humidities, the temperatures of the humidifiers were set by assuming 100% humidification efficiency, and the actual output water mole fraction was determined by the real-time gas analyzer (RTGA). Sources of error with this measurement can be the error in humidification used for calibration of the RTGA, imprecision in measurement of flow rate, pressure, and temperature, and some transients that can occur during apparent steady-state operation. The humidifier used for RTGA calibration was itself carefully calibrated using a dessicant absorption technique. Between the humidifier and the cell, heating tapes were used to prevent condensation and maintain the desired humidification levels. Fuel cell and humidified reactant gas inlet temperatures of 80°C were maintained by model 8500 PID controllers (Omega Engineering Inc.). The cell temperature was measured by a thermocouple within the cathode backing plate.

Species measurement.— Species were measured using an Agilent Technologies RTGA as described in chapter 4. The fuel cell was allowed to reach a steady state for each operating condition prior to species data collection. All species collection data were taken at a cell potential of 0.7 V. The sample line to the RTGA was maintained well above 100°C to prevent condensation and loss of proper mole fraction precision. In a few cases, an Agilent 3000 Micro GC was used to record test data, as described in chapter 3.

Operating conditions.— Tests were conducted at baseline operating conditions given in Table **5-1**, with varying inlet flow rates and relative humidities. Table **5-2** shows the five different conditions chosen for study of anode and cathode inlet relative humidity effects. The bulk performance of a fully humidified condition is also listed as a

benchmark reference. Tests were conducted with a constant flow rate on the anode and cathode. Constant reactant flow rate was chosen because it is more convenient for model validation and interpretation of results. Experiments were performed at two different dry air flow rates on the cathode of 1599 and 2357 sccm (standard referenced at 0°C). For comparison, these constant flow rates represent a stoichiometry of 2.4 and 3.6, respectively, at a current density of 0.8 A/cm^2. The dry hydrogen flow rate on the anode was kept constant in all experiments at 367 sccm, which represents a stoichiometry of 1.3 at 0.8 A/cm^2. Pressure drops through the fuel cell were measured for different gas flow rates under fully humidified conditions. Small pressure drops, 0.34 psi (0.023 atm or 2.3 kPa) for the 2357 sccm cathode flow rate and 0.023 psi (0.0016 atm or 0.16 kPa) for the 367 sccm anode flow rate, indicate that the pressure change along the flow path had a negligible effect on water content for the flow-field design and operation conditions tested.

At each operating condition, current density, species, and HFR profiling was measured after steady state was achieved (>30 min for most cases). After reaching steady state, current measurements were taken once per second for 5 min, and an average local current density was calculated from the 300 data points taken for each location, at each voltage. For all test conditions, a distributed highfrequency (3 kHz) resistance measurement was taken at 0.7 V. Additional HFR data were obtained for comparison at 10 kHz using a Solatron 1255b frequency response analyzer on three segments (inlet, center, and outlet of fuel cell). The 10 kHz resistance measured was nearly identical to the value obtained at 3 kHz for the conditions tested. Therefore, 3 kHz was deemed to be sufficiently high.

Table **5-1**: Baseline experimental conditions

Parameter		
MEA		
Gas diffusion layer	Carbel® MP and Toray 060	NA
Catalyst loading (carbon supported)		mg/cm^2
Cell temperature	80	^oC
Anode inlet temperature	80	^oC
Cathode inlet temperature	80	^oC
Cathode flow rate	1559 and 2357	
Anode flow rate	367	sccm
Cathode pressure	3.0	atm
Anode pressure	3.0	atm
Cell voltages	0.85, 0.75, 0.7, 0.6	
Anode gas	Ultra high purity H_2 (>99.999 %)	NA
Cathode gas	Commercial air (79% N_2, 21% O_2)	NA

Table **5-2**: Relative humidity of total inlet flow

Test Condition	Relative humidity (RH) (anode/cathode) at 80°C	Total input RH low cathode flow at 80°C	Total input RH high cathode flow at 80°C	Average current density at 0.7 V (A/cm^2)[a]
1	50/0	9.9	7.1	0.29/0.26
2	100/0	21.2	15.4	0.48/0.36
3	0/50	41.3	43.8	0.49/0.41
4	0/100	83.9	88.5	0.55/0.50
5	25/25	25.0	25.0	0.44/0.35
Baseline	100/100	100	100	0.60/0.68
[a] Lower cathode flow rate (1599 sccm)/higher cathode flow rate (2357 sccm)				

5.3 Results and Discussion

Bulk performance.— In order to analyze the results, it is useful to normalize the test conditions to the total relative humidity of the bulk flow. This way, the total water input to the fuel cell for the various conditions can be compared without ambiguity. Table **5-2** shows the overall relative humidity input, derived by combining anode and cathode inlet flows at both the high and low cathode flow rate conditions. For example, condition 1, anode/cathode relative humidity (A/C RH = 50/0) has about one-sixth to one-fourth the total relative humidity value of condition 3 (A/C RH = 0/50) in the cell, despite the same individual reactant relative humidity percentages. This is a result of the higher cathode flow rate compared to the anode. It is clear that for undiluted hydrogen and air flow, an identical anode and cathode relative humidity will have a far greater molar rate of water entering from the cathode than the anode. Therefore, condition 5 (A/C RH = 25/25) is a relatively dry cathode inlet condition, even though the values of the relative humidity on both inlets are the same.

Low anode humidity operation.— According to the test matrix in Table **5-2**, four series of tests were conducted with inlet anode humidity less than 100%. Test condition 4 is most illustrative of an undersaturated inlet anode effect because, for this test series, the cathode inlet was fully humidified, while the anode was fully dry. Figure **5-1** and Figure **5-2** show the bulk polarization and distributed current density plots as a function of location for this test condition, respectively. Due to small variations of local compression, there is some scatter in the measured local current density, an overall increasing to a maximum, and then a decreasing trend can be seen in Figure **5-2**. The bulk (Figure **5-1**) and local (Figure **5-2**) performance of the high- and low cathode flow rate conditions are very similar until high current density, when the low flow rate cathode condition has slightly increased local performance, despite less input water molar rate.

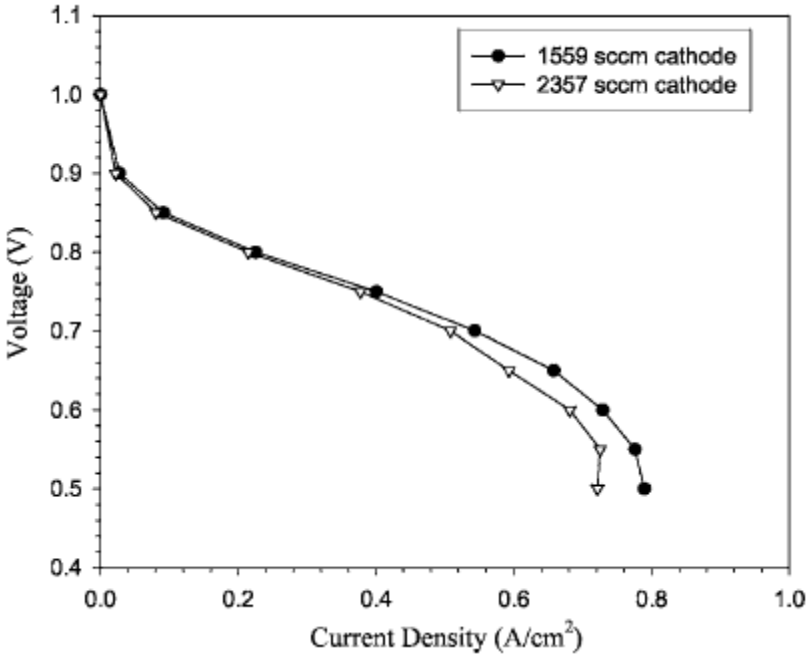

Figure **5-1**: Steady-state polarization curve for condition 3. RH = 0/100 anode/cathode.

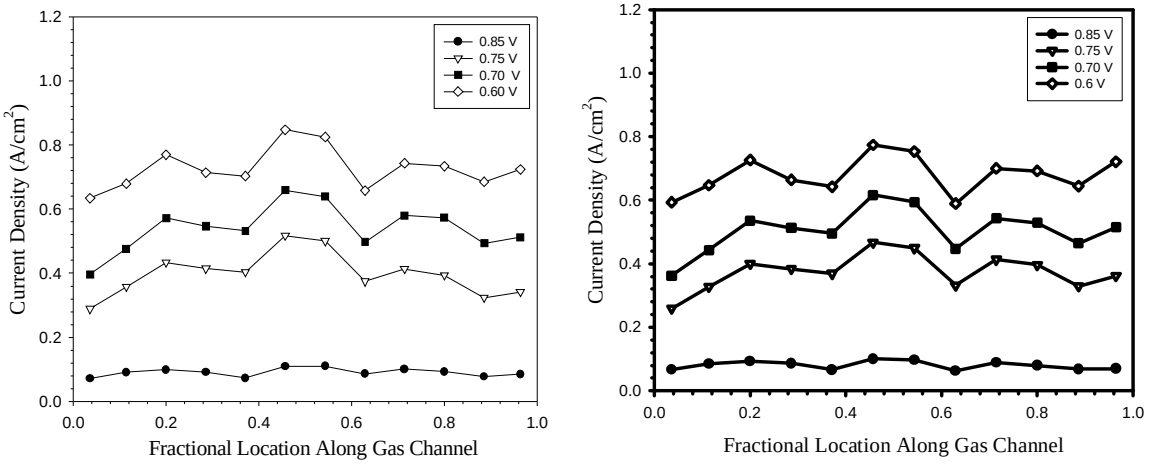

(a) 1559 sccm cathode

Figure **5-2**: Distributed steady-state current density as a function of cell location for condition 4. RH = 0/100 anode/cathode.

Figure **5-3** are the distributed steady-state species distributions at 0.7 V for condition 4 for the anode and cathode. On the anode side, the anode water content increases almost monotonically to saturation due to uptake, and the hydrogen mole fraction concomitantly decreases along the flow path, as the only other major species in the anode. In the cathode, both the nitrogen and the oxygen content decrease as the water vapor mole fraction increases. At the inlet the current density is low, depressing drag and generation, while the concentration gradient for diffusion is at a maximum at this location. Toward the exit of the serpentine channel in both flow rate cases, the cathode flow apparently saturates, reaching a plateau around 16% mole fraction, slightly higher than the saturated water mole fraction at this test conditions. As described previously, although the backing plate temperature was controlled to 80°C by the thermocouple, gas temperature in the flow path can be higher due to waste heat generation. Therefore, the exit gas can appear oversaturated compared to the setpoint temperature of 80°C.

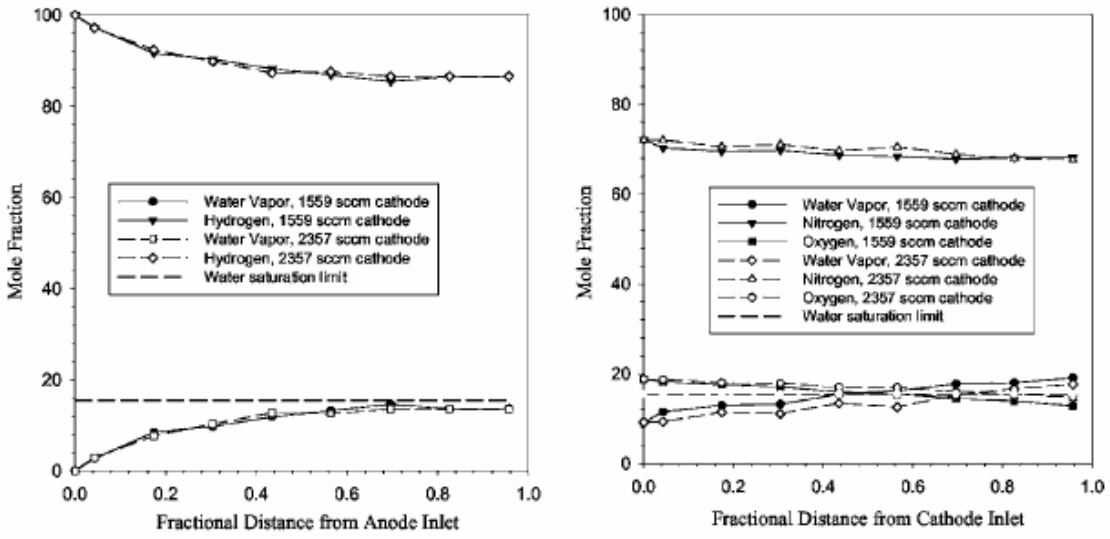

(a) The anode (b) The cathode

Figure **5-3**: Distributed steady-state species distribution on the anode and cathode for condition 4. RH = 0/100 anode/cathode. Data taken at steady state, 0.7 V.

Figure **5-4** shows the distributed steady-state HFR for test condition 4 at 0.7 V. Reversing the general trend of the anode-side water vapor content, there is an overall

decreasing trend in the cell resistance with location along the flow path, corresponding to increased electrolyte water content in the electrolyte and catalyst layers as the anode-side water mole fraction increases. There is nearly a 100% decrease in resistance of the cell from inlet to outlet. The data show that the HFR for the low-flow condition is higher at the inlet of the cell due to the lower combined RH at the inlet (84 to 88%, respectively). However, the reaction-generated water humidifies the lowflow gas streams more due to the lower cathode flow rate, which results in a higher hydration of the membrane and a lower HFR. This observation is in agreement with the total cell performance shown in Figure **5-1** and Figure **5-2**.

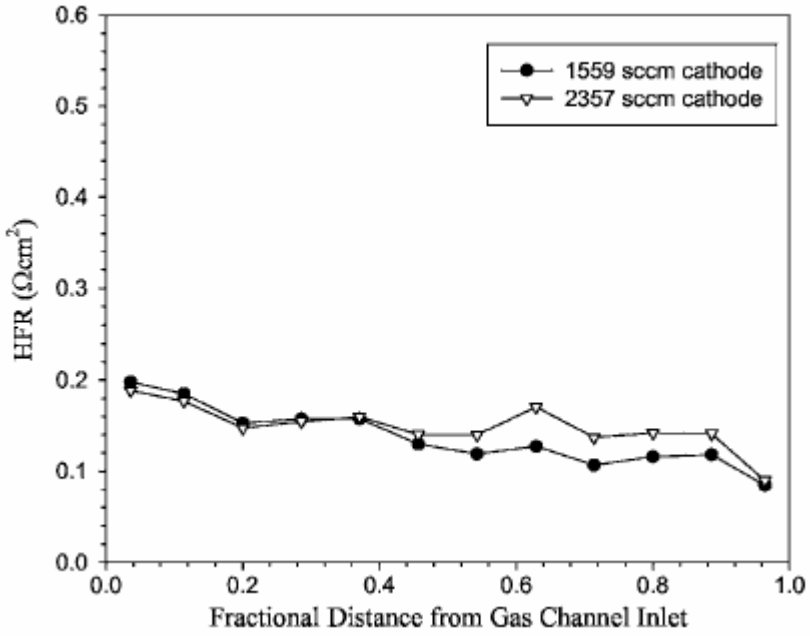

Figure **5-4**: Distributed steady-state high-frequency resistance distribution for condition 4. RH = 0/100 anode/cathode, 0.7 V. Data taken at steady state, 0.7 V.

The distributed current, water vapor, and HFR data for the other low anode humidity condition 3 follows a similar overall increasing (current, water vapor) and decreasing (HFR) trend, indicating that the distributed performance is strongly related to the anode-side water vapor content.

Low cathode humidity operation.— According to the test matrix in Table **5-2**, four series of tests were conducted with reduced cathode humidity. Test condition 2 is most

representative of an undersaturated inlet cathode effect because, for this test series, the anode inlet was fully humidified and the cathode inlet dry. Figure **5-5** and Figure **5-6** show the bulk polarization and distributed current density plots as a function of location for this test condition, respectively. In this case the higher dry cathode flow rate has much lower bulk performance, due to increased drying from the zero inlet humidity cathode flow. Compared to the fully humidified cathode condition of condition 4 (A/C RH = 0/100), condition 2 (A/C RH = 100/0) has a much lower combined inlet relative humidity; therefore, condition 2 is much dryer overall compared to condition 4. Note the local current density profile is very different for a dry anode condition than for the dry cathode condition 2. Instead of an overall local performance increase, local current density is initially high, dips to a minimum, and then gradually increases up to a maximum. This resulting decrease to a local minimum, then increasing trend, is observed for all cases with a dry or low relative humidity cathode compared to that of the anode. This is in agreement with modeling results from Van Zee et.al. [**89**] and Wang et al.[**75**] The general trend found was that more water overall input to the cell resulted in greater bulk performance. However, it is clear that local anode dryout can occur, and anode humidification is necessary, to avoid local dryout and poor performance that can also lead to accelerated degradation near the anode inlet location

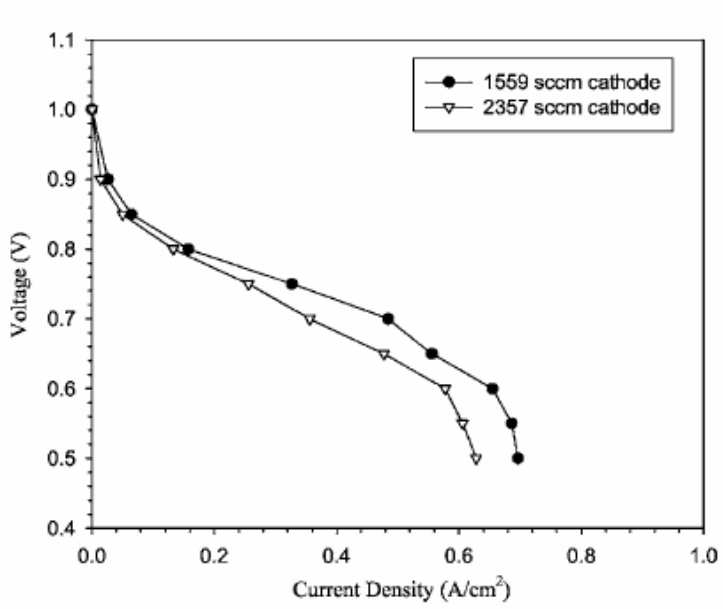

Figure **5-5**: Bulk polarization curves for condition 2. RH = 100/0 anode/cathode.

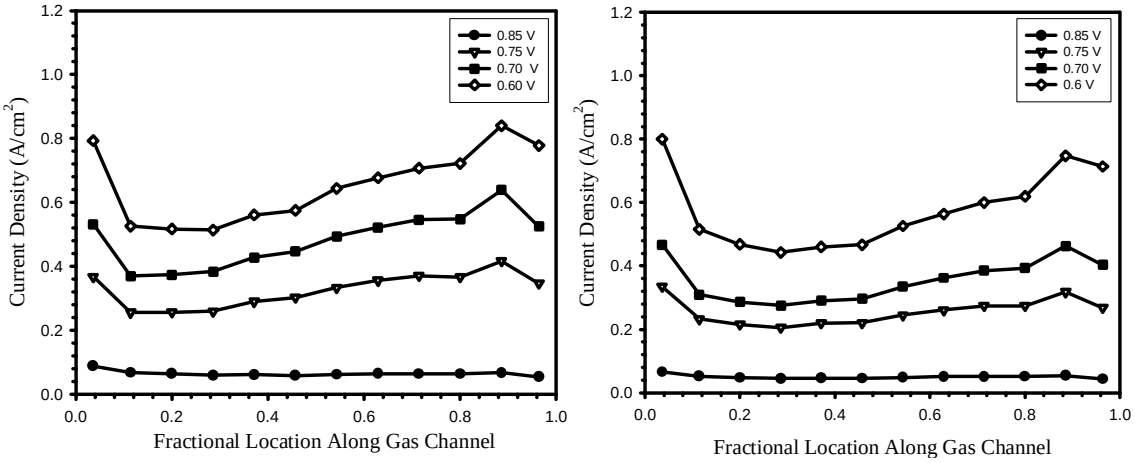

(a) 1559 sccm cathode (b) 2357 sccm cathode

Figure **5-6**: Distributed steady-state current density as a function of cell location for condition 2. RH = 100/0 anode/cathode.

Figure **5-7** shows the distributed steady state-species distributions for condition 2 for the anode and cathode. In the cathode, both the nitrogen and the oxygen content

decrease, as the water vapor mole fraction increases. The anode-side distribution is most interesting. At the inlet of the anode for a dry cathode case, there is a dip in the vapor fraction along the gas channel until a minima is reached, then the vapor fraction increases, creating a very similar decrease to a local minima, then increasing trend compared to the local current distribution trend of Figure **5-6**.

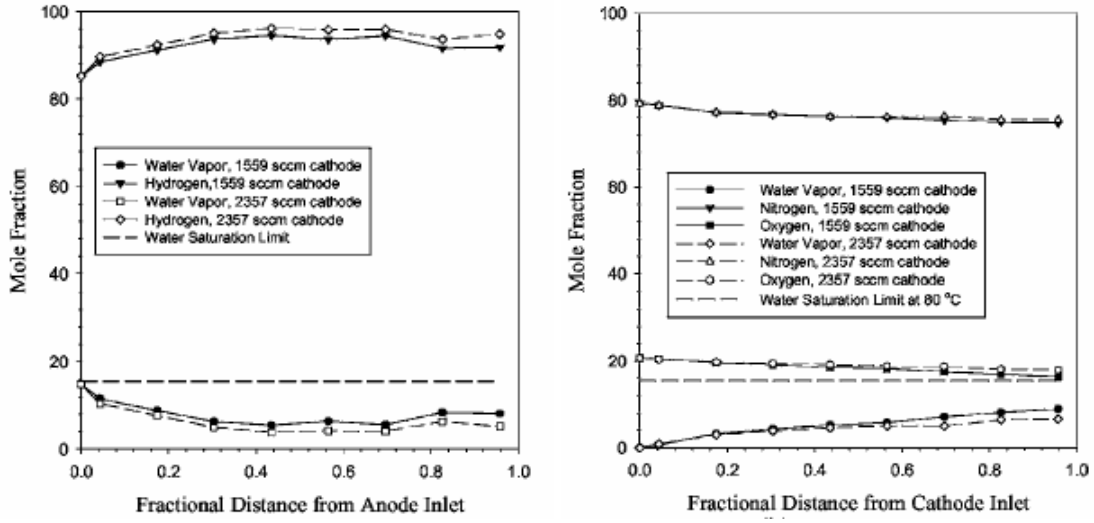

(a) The anode (b) The cathode

Figure **5-7**: Distributed steady-state species distribution on the anode and the cathode for condition 2. RH = 100/0 anode/cathode. Data taken at steady state, 0.7 V.

The decreasing-increasing profile phenomenon is mainly a result of a diffusion reversal process between the anode and cathode for underhumidified cathode conditions, as schematically shown in Figure **5-8**. Near the inlet, where the cathode is underhumidified compared to the anode, all modes of water transport are toward the cathode (electro-osmotic drag and diffusion), and generation is of course at the cathode. At locations further along the single serpentine path, the water activity at the cathode increases above that of the anode, and the direction of diffusion mass transport reverses, eventually overcoming electro-osmotic drag and initiating a net flux of water back toward the anode. This water mass flux reversal results in the rehumidification of the anode flow path observed. Additionally, the higher oxygen fractional pressure at the inlet for dry cathode conditions also increases the local current density to some extent. Note that the

diffusion flux reversal location and location of net water mass flux reversal is not the same, as the net water flux reversal point is also a function of the electro-osmotic drag (and therefore current).

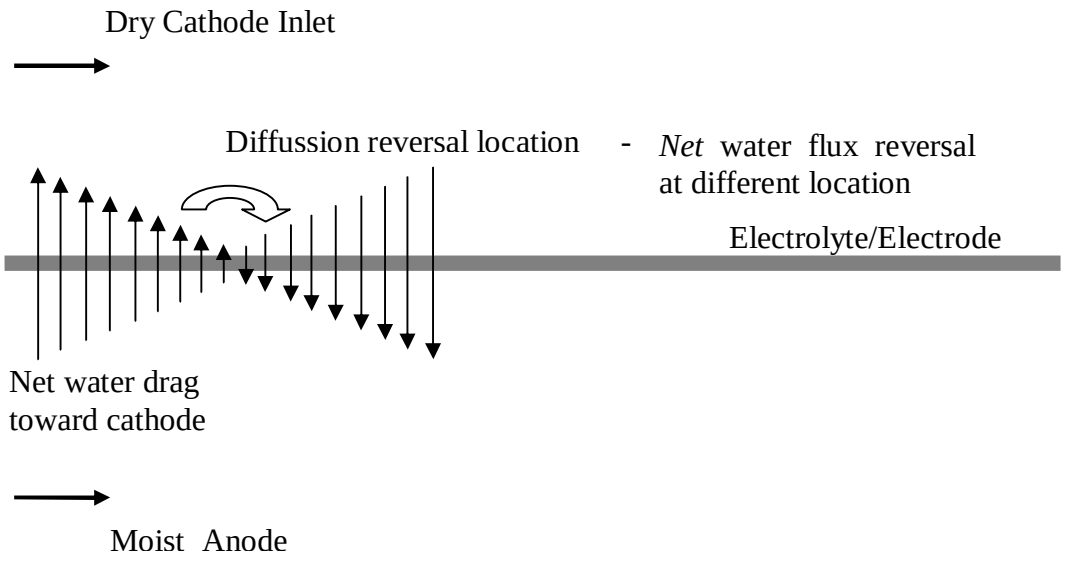

Figure **5-8**: Illustration of the diffusion reversal process in the electrolyte occurring for undersaturated inlet cathode conditions, resulting in locally varying current phenomenon.

Figure **5-9** shows the distributed steady-state HFRs for test condition 2 at 0.7 V. In this case, the anode-side water content has a strong effect on the HFR profile. The HFR trend roughly inverses the decreasing-increasing profile observed for anode water vapor content. At the beginning, following the decreasing trend of the anode-side water vapor content, there is an increasing trend in the cell resistance with location along the flow path, although the cathode-side channel-level water vapor content increases. Further downstream, the HFR decreases as the anode water content increases. However, it should be noticed that the local resistance maxima are earlier than the local anode water content minima due to the increasing cathode water content. In fact, it is evident that before diffusion reversal, there is localized anode dryout caused by diffusion and migration of water from the anode. The dryout, evident even for the ultrathin 18 μm electrolytes used, results in increased impedance that drives down local current density. The humidification condition of a dry cathode is commonly much better than a dry

anode, even with a dry inlet condition, due to water generation at the cathode catalyst layer. Anode moisture profile has a more pronounced effect on the local current profile (through the local HFR) than the cathode vapor profile.

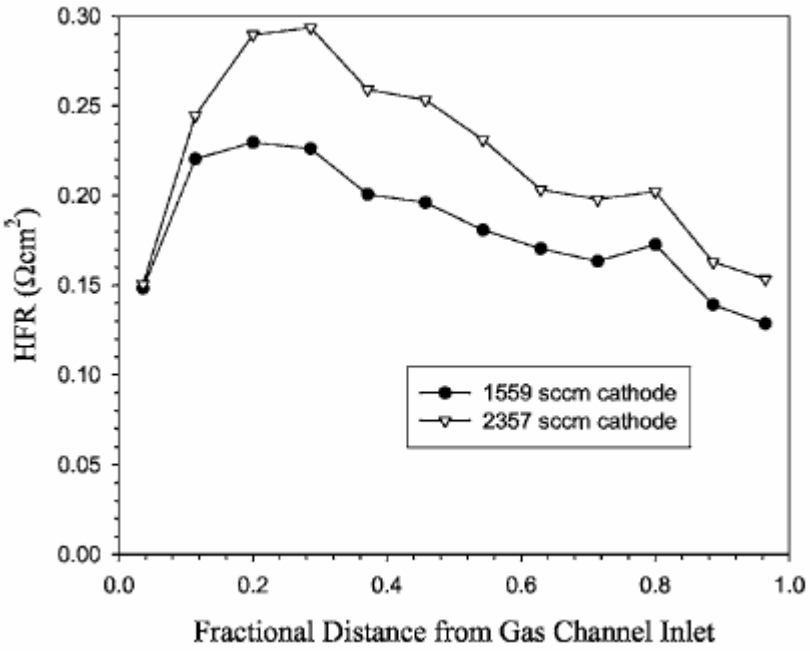

Figure **5-9**: Distributed steady-state high-frequency resistance distribution for condition 2. RH = 100/0 anode/cathode. Data taken at steady state, 0.7 V.

For the higher cathode flow rate, the increase in local HFR is greater than the low cathode flow rate case. This corresponds to the decreased anode water vapor content caused by increased diffusion to the dry cathode for higher flow rate. Note that the inlet region HFR for condition 2 (Figure **5-9**) is 25% lower than the initial HFR for condition 4 (Figure **5-4**), despite much higher inlet bulk relative humidity for condition 4. This indicates the importance of maintaining high inlet anode humidity for increased inlet performance, and avoidance of local anode inlet dryout that has been implicated in pinhole formation and concomitant performance degradation.

Other low-humidity test condition comparisons.— For all other test cases, the results follow the same characteristic trends described for low anode or cathode humidity operation. All other test cases fall between the extremes of conditions 2 and 4. Figure **5-10** shows comparisons of the current profiles for other conditions 1, 3, and 5,

respectively. Condition 1 (A/C RH 50/0) and condition 5 (A/C RH = 25/25) are relatively dry cathode inlet conditions. Condition 3 (A/C RH 0/50) is a relatively dry anode inlet condition. The decreasing-increasing profile is evident for the two dry cathode cases, and a generally increasing trend in local current is shown for the dry anode case (condition 3).

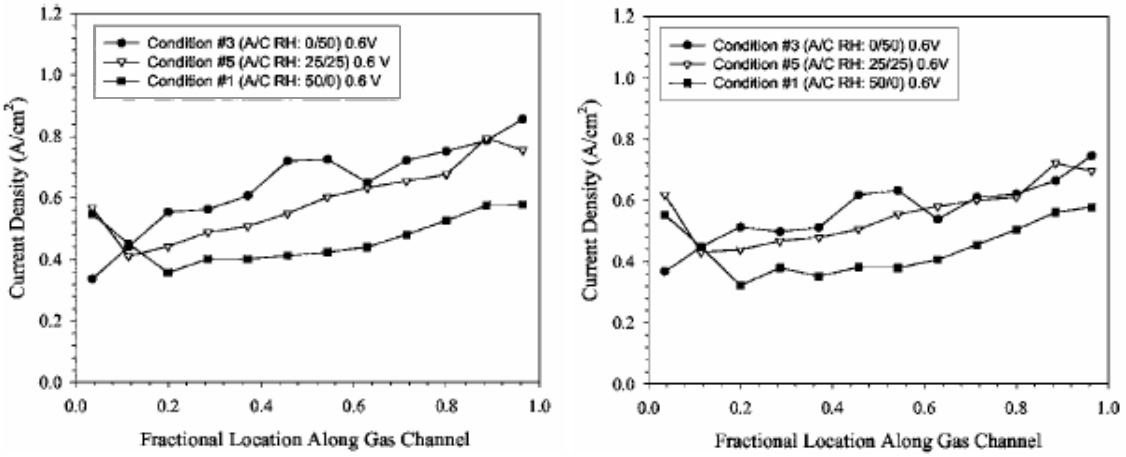

(a) 1559 sccm cathode (b) 2357 sccm cathode

Figure **5-10**: Comparison of current density distributions for several different conditions at two cathode flow rates.

Note, from Figure **5-10**, that condition 3 (A/C RH = 0/50) is the test condition with the greatest total water content at the inlet for these three cases, but it is all at the cathode. This is also the condition with the worst local performance at the inlet region, although its average bulk performance is the best among the three cases. In contrast, condition 2 (A/C RH = 500) has the least total water content at the inlet and has the best local performance in this region. However, it suffers the lowest overall bulk averaged performance. Although in these cases the greater amount of water resulted in better bulk performance, even better performance and avoidance of anode dryout can be achieved with some moisture at the anode inlet.

Even for a test case of complete inlet saturation (A/C RH = 100/100), the authors have observed a similar anode dryout at high current densities (>1.0 A/cm2), as shown in Figure **5-11**. Since it is possible that electrolyte dryout exacerbates the physical degradation of the electrolyte, the need for high anode humidification at the inlet of the

flow field (although bulk performance may improve only slightly) is clear. It is anticipated that the trends observed for this single path serpentine flow field would be maintained for parallelized concurrent flow as well, and ongoing study is verifying this. Additionally, although these trends are shown for constant flow rate, the authors have verified substantively identical qualitative trends for constant stoichiometry conditions. Figure **5-12** shows a current distribution result for condition 5 with constant stoichiometry rather than constant flow rate, and in all such cases a similar qualitative trend was observed comparing relatively dry anode and cathode cases to the constant flow rate cases.

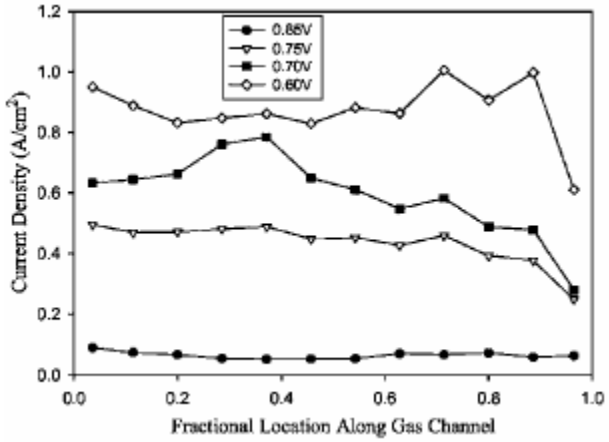

(a) 1559 sccm cathode

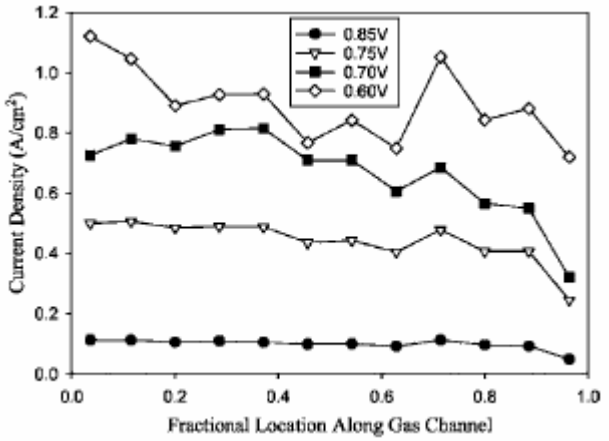

(b) 2357 sccm cathode

Figure **5-11**: Distributed steady-state current density as a function of cell location for fully humidified condition. RH = 100/100 anode/cathode.

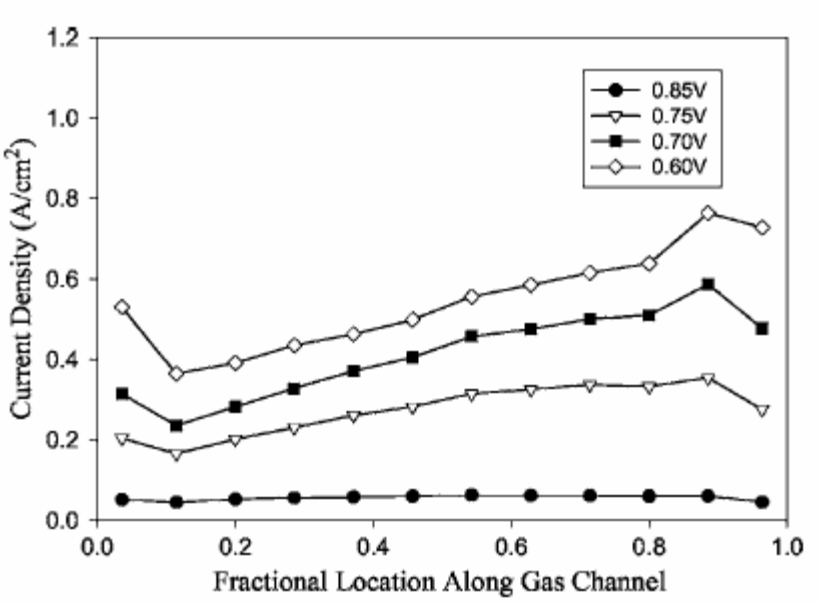

Figure **5-12**: Distributed steady-state current density as a function of cell location for a constant stoichiometry operation. Condition 5, RH = 25/25 anode/cathode, anode stoichiometry = 1.2, and cathode stoichiometry = 2.0.

The species distribution comparisons at 0.7 V for two cathode flow rates for the three cases 1,3, and 5 are shown in Figure **5-13** and Figure **5-14** and follow the trends noted before to different degrees, depending on the water imbalance. Anode channel-level water vapor profile is the rough qualitative inverse of the current profile, while the cathode profile is not, again indicating that the anode moisture profile strongly influences the local current distribution.

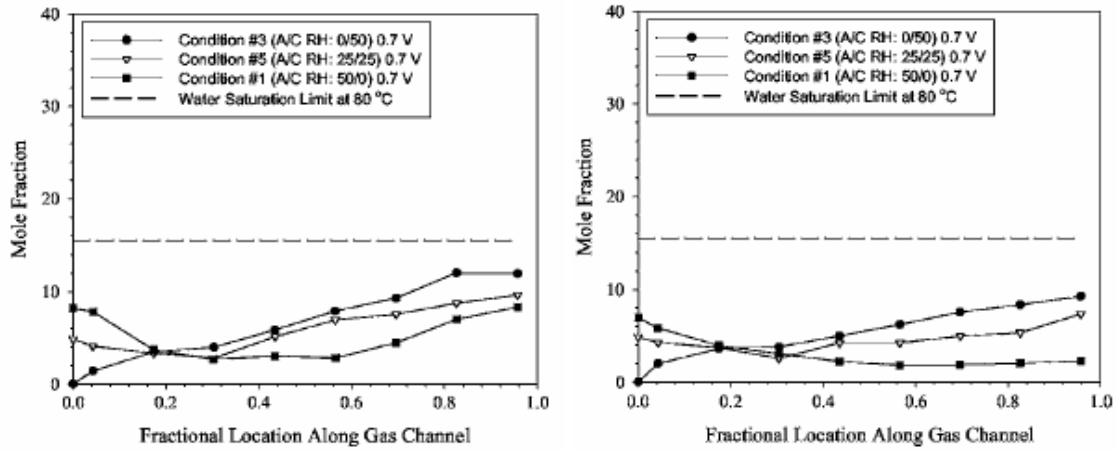

(a) 1559 sccm cathode (b) 2357 sccm cathode

Figure **5-13**: Comparison of anode water vapor profile for several different conditions at two cathode flow rates. Data taken at steady state, 0.7 V.

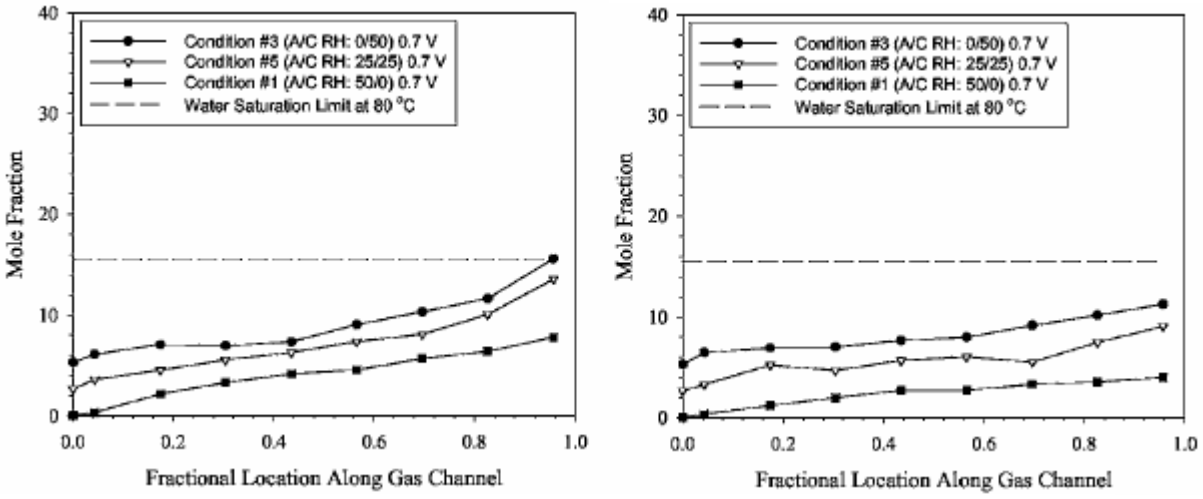

(a) 1559 sccm cathode (b) 2357 sccm cathode

Figure **5-14**: Type Caption Here

The HFR data shown in Figure **5-15** are also consistent, and confirm the performance variation is strongly linked to anode gas-channel moisture profile. Note the

differences between the two flow rates of the HFR plots. For the dry cathode case, a higher dry cathode flow rate results in an increased HFR, while for the dry anode case, higher cathode flow rate decreases the bulk HFR. Simply stated, the more water, the lower the overall HFR, although the inlet region is most influenced by the anode condition, and distributed profiles vary greatly.

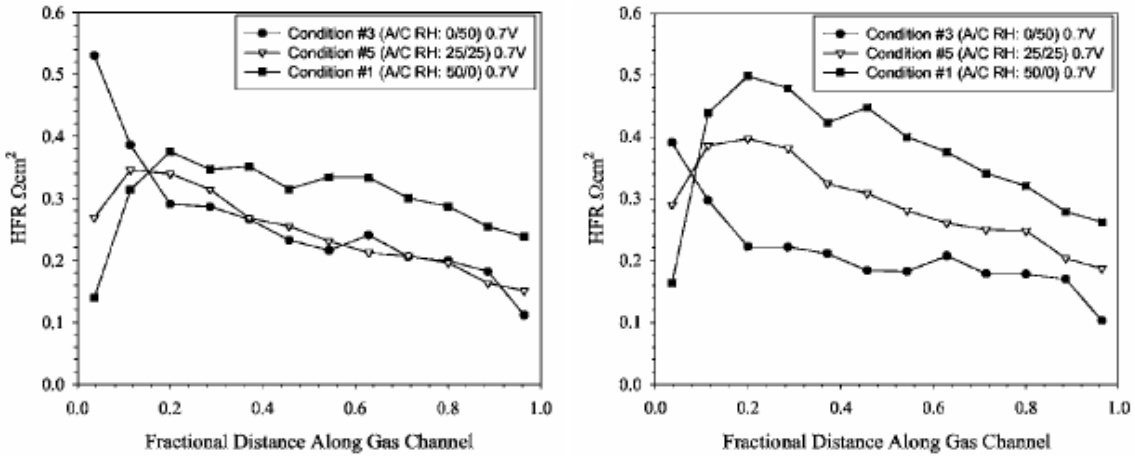

Figure **5-15**: Comparison of high-frequency resistance profile at 3 khz for several different conditions at two cathode flow rates. Data taken at steady state, 0.7 V.

Generalized distributed performance.— Based on the data generated, a generalized performance plot for undersaturated inlet current distribution with a concurrent flow field can be constructed. Performance is highly coupled to the anode-side water vapor content in the inlet region through the local electrolyte conductivity, indicating electro-osmotic drag acts to dry the anode side and is not completely compensated for by back-diffusion, even for the thin 18 μm electrolytes used. This demonstrates that the anode water profile contributes significantly to the overall performance of a fuel cell inlet with undersaturated inlet flow.

Figure **5-16** is a sketch of the generic relative current versus location along the flow channel for different combinations of inlet humidity on the anode and cathode, and is key to understanding local performance. The generalized performance curve is qualitatively sinusoidal in shape (although not necessarily symmetric or with equal amplitude or wavelength, as shown for convenience).

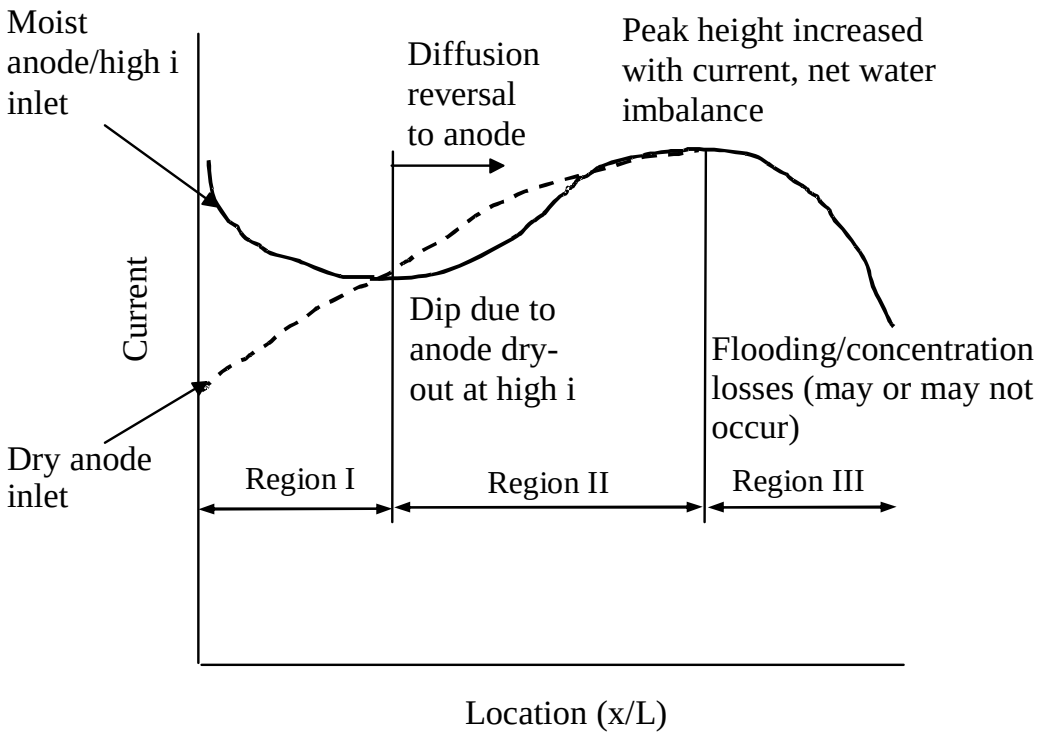

Figure **5-16**: Characteristic local current curve for undersaturated inlet conditions.

Region I begins at the inlet of the fuel cell. If the anode is dryer than the cathode and the current is relatively low, the net flux of water is always neutral or toward the anode, resulting in an increasing performance through region I. The steepness of the slope of this portion is exacerbated with increased moisture imbalance between anode and cathode, increased current density, and other thermodynamic and geometric parameters. In contrast, if the water vapor imbalance initially favors the anode (dryer cathode), diffusion and electro-osmotic drag are both initially toward the cathode, resulting in a drying condition at the anode catalyst layer and electrolyte, reducing performance until a local minima is reached, which terminates region I. The minimum in performance is exacerbated by increased current density and moisture difference between anode and cathode, as well as flow rates and other thermodynamic and geometric parameters. Note that, for closely hydrated anode and cathode at low to moderate current density, performance in region I can be homogeneous, as illustrated in Figure **5-16**. Note

that the end of region I is shown as the same location for dry anode and dry cathode conditions, when this is not necessarily the case. In fact, region II for a relatively dry anode inlet is really a continuation of region I and no discrete boundary between the two regions is defined.

In region II, the case with relative dry anode feeding continues increasing performance to a maximum (if reached), that ends region II. The decrease from the maximum current is a result of decreasing reactant availability or flooding, and depends on operating conditions, and therefore may not be severe as shown in Figure **5-16**. The dry relative cathode case begins region II at the point of water mass flux reversal from cathode to anode results. In this situation, this reversal may not occur with a thick electrolyte if back-diffusion never overcomes electro-osmotic drag to the cathode. This flux reversal reduces anode-side dryout performance loss and initiates an increase in performance. Due to time-varying upstream temperature effects, the precise location of the mass flux reversal may fluctuate, causing bulk performance instability. This effect was observed over extended periods in testing with low inlet cathode humidity, and is the subject of continued investigation and analysis. For both the dry relative anode and cathode cases, region II concludes with a maximum in performance, if reached at all. Note that the location of the maxima is dependent on the fuel cell and operating conditions, as discussed, and is therefore not the same for the different humidity cases, as shown in Figure **5-16** for simplicity.

In region III, for convenience, both dry anode and cathode cases are shown to peak at the same location, although this depends on the individual conditions and is not necessarily the case. Following the maximum local current, there is a downward trend resulting from local flooding or gas-phase mass transport losses at the electrode (s). This peak and downward trend will only occur if a reactant starvation condition (via flooding or high utilization) is reached.

The generalized performance curve of Figure **5-16** closely follows anode gas-channel water vapor content through region II, indicating anode catalyst layer and electrolyte moisture content plays a key role in controlling the distributed performance of an undersaturated inlet PEFC. Cathode conditions are generally locally moist at the

catalyst layer, and control the location of the maximum performance which initiates region III. The region I trend depends on the side with greatest hydration and local water activity. The amplitude of the peaks is increased with increasing current density and water imbalance between anode and cathode at the inlet. The width of regions I-III depends on current density, flow rate, water imbalance, and membrane and electrode thickness as well. As discussed, the same general trends in local performance for various humidity combinations is achieved for constant stoichiometry conditions, but is too much coverage for a single publication. It is quite difficult to achieve homogeneous performance at high current density (>0.5 A/cm^2) with basic humidification schemes and co-current flow. Either the inlet is dry and performance is depressed, or the outlet is flooded, or both.

5.4 Summary

Experimental data including species, current, and impedance distributions in a PEFC with single-path coflow configuration have been obtained over a wide range of operating humidity and flow rates. Results indicate that anode humidity has strong effect on the current distribution (CD) in the inlet region, through the ionic resistance, under low-humidity conditions. The CD curves are qualitatively similar to H_2O mole fraction distribution in the anode, and the HFR profile data confirm that the CD is strongly affected by the anode side dryout, even for the thin 18 μm electrolytes used. For a coflow low-humidity cathode condition, local performance and anode water vapor content follow a decrease to a local minimum, and then an increasing trend resulting from a net water flux reversal from the anode to the cathode.

For the low-humidity conditions tested, the bulk performance was generally higher with increased total inlet moisture content. However, humidification of the anode, rather than the cathode, was demonstrated to be most critical to achieve high inlet region performance, even with more than twice the water content available at the cathode inlet. This has important implications in limiting performance degradation, where local anode dry out may be linked to the formation of pinholes in the electrolyte near the anode inlet.

Due to the lack of active cooling on the fuel cell, the temperature elevation of the membrane is believed to contribute to this generalized profile in some degree.

A generalized local current distribution was constructed to show the expected qualitative shape of the coflow current profile for a wide range of inlet humidity conditions, with amplitude of local peaks and valleys dependent on current, flow rate, initial water imbalance between anode and cathode, and other thermodynamic and geometric parameters. These data demonstrate the importance of the anode water vapor distribution and back-diffusion, and can be used to guide water management systems for more efficient water injection, and also should be highly useful for detailed validation of computational modeling.

Chapter 6

Distributed Performance of PEFCs under Elevated Temperatures and Low Humidities

6.1 Introduction

Due to the tight space and strong competition from low cost internal combustion engines for automotive applications, it is highly desirable to operate the PEFCs under low humidity conditions to simplify the external humidification and condensation subsystems, improve the system compactness, minimize parasitic power consumption, and reduce the overall system cost. At the same time, for automotive applications, it is also very advantageous to operate PEFCs at elevated temperatures in order to minimize the effect of CO poisoning and simplify the cooling system.[**104**][**105**] Good tolerance to CO can greatly simplify the reforming systems and enable directly use of existing infrastructure of liquid hydrocarbon fuels, such as gasoline and diesel.

In Chapter 5, the characteristic distributed performance of PEFCs under low humidity and normal operating temperature of 80°C is presented. Benchmark data were experimentally gathered for distributed species, current, and high frequency resistance data as a function of operation conditions that emphasized the effect of inlet humidity on distributed performance. A generalized distributed performance curve for co-flow fuel cell was presented that describes the shape of the current, HFR, and species distributions. The overall objectives of the work presented in this chapter are to: (1) extend the previous research to cover higher-temperature operation designed for automotive applications, (2) upgrade the experimental configuration and provide additional suitable benchmark data for model validation and understanding, (3) investigate the impact of fuel cell pressure on cell performance under low inlet humidity and elevated temperature.

In this chapter, distributed performance of PEFCs under low humidity conditions and elevated operating temperatures of 95 and 110°C is investigated using the 2nd

generation segmented fuel cell with isothermal boundary condition. Influences of operating temperature, inlet humidity, and back pressure were studied extensively with combined simultaneous current density, species, and HFR distribution measurements.

6.2 Experimental

All experiments were conducted using the 2nd generation instrumented fuel cell with isothermal boundary condition. Configurations of the fuel cell are described in chapter 2, and more details can be found in reference [**99**].

Similar to the study described in Chapter 5, current and HFR distribution measurements were accomplished with the 25-channel potentiostat/galvanostat contained in the Arbin integrated fuel cell test system. And the Agilent Technologies RTGA was used to obtain species distribution and was also used to monitor and control the inlet relative humidities. The calibration of the RTGA was re-checked periodically with desiccant absorption technique to maintain a high accuracy. To achieve approximately isothermal boundary conditions, the fuel cell flow field temperature was active heated/cooled by the recirculator. Two thermocouples inserted in the 10th species sampling ports of anode and cathode were used to provide the temperature of the flow field by averaging the two readings. Then the coolant temperature of the recirculator was adjusted until the target flow field temperature was achieved. With a step change of cell voltage of 0.05V, the temperature adjustment process might take 10~20 minutes depending on the change of heat generation rate.

Experiments were conducted at baseline operating conditions given in Table **6-1** with two elevated flow field temperatures of 95°C and 110°C, two pressures of 25 psig and 7.5 psig, and three representative inlet relative humidities. The inlet relative humidities of A/C RH=50/0, 0/50, and 30/30 were chosen to represent three typical kinds of low inlet humidity conditions: partially humidified anode/dry cathode, dry anode/partially humidified cathode, and partially humidified anode and cathode. As shown in Chapter 5, the distributed performances at different cathode stoichiometry with the same inlet relative humidities are always qualitatively same. So for all conditions,

constant stoichiometries of 2.0 on the cathode and 1.2 on the anode were chosen because they are more similar to the operation conditions of real applications. similar to the study reported in Chapter 5, all experiments were also performed using Gore PRIMEA Series 57 MEA, which has a dry membrane thickness of 18 μm and a platinum loading of 0.4 mg/cm^2 for anode and cathode catalyst layers. The gas diffusion medium consisted of CARBEL MP gas diffusion media as the microporous layer and Toray 060 (wetproofed) as the macroporous layer. Ultrahigh-purity (>99.999%) hydrogen and standard dry air were fed to the fuel cell from compressed gas cylinders.

Table **6-1**: Baseline operating conditions

Parameter	Value
MEA	Gore PRIMEA® Series 57 MEA
Gas diffusion layer	Carbel MP microporous gas diffusion media and Toray 060 macroporous gas diffusion media
Catalyst loading (carbon supported)	0.4 mg/cm^2
Flow field temperature	95 and 110 °C
Anode inlet temperature	95 and 110 °C
Cathode inlet temperature	95 and 110 °C
Anode and cathode pressure	25 and 7.5 psig
Cathode stoichiometry (constant)	2.0
Anode stoichiometry (constant)	1.2
Anode gas	Ultra high purity H_2 (>99.999%)
Cathode gas	Commercial air (79% N_2, 21% O_2)
A/C RH	50/0, 0/50, 30/30
Cell voltages for current density and HFR distributions	0.6, 0.7, 0.75, 0.85 V
Cell voltages species distributions	0.7 V (25 psig only)

At each operating conditions, current density, species, and HFR distributions were measured after isothermal boundary condition and steady state fuel cell performance were achieved. To measure current distribution, the fuel cell was first allowed to reach steady state for at least 30 minutes in voltage control mode, and the average of the data

recorded in the last 5 minutes at steady state was taken as the final result. And the HFR profile was taken by a 2-second AC impedance 3 kHz step following the current distribution step. For species measurement, the average of the species data in the last 2 minutes was taken after steady-state was achieved. Current and HFR distributions were measured at four fuel cell voltages of 0.6, 0.7, 0.75, and 0.85 Volts for all three humidity conditions and two pressures. Species distribution was only measured at 0.7 V and 25 psig for each inlet humidity condition due to tremendous time required for the measurement.

6.3 Results and Discussion

6.3.1 Bulk performance

Compared to normal operating temperature of 80°C, operating at higher temperature requires much more water for full humidification because the water saturation pressure changes exponentially with the increase of temperature, and consequently the self-humidification effect of generated water is weakened and worse cell performance. At the same humidity level, higher temperature operation also leads to lower reactant concentration due to the dilution effect of water vapor. In order to analyze the results for different conditions, bulk inlet relative humidity and bulk outlet relative humidity are calculated to evaluate the relative amount of input water and generated water. In this way, the overall humidification of the fuel cell for the various conditions can be compared without ambiguity. The inlet and outlet cathode oxygen mole fractions are also calculated for comparison purpose by assuming equal water activity on both anode and cathode.

Table **6-2** shows the overall inlet and outlet relative humidities, and the inlet and outlet oxygen mole fractions for the six low humidity operating conditions with various inlet relative humidities and temperatures for the higher pressure of 25 psig. The relative

humidities and oxygen mole fractions of respective fully humidified conditions are also listed as benchmark references.

Table **6-2**: Total relative humidity and oxygen concentration for 25 psig

Inlet RH and flow field temperature	Overall RH_{in} *	Overall RH_{out} *	$y_{O_2,in}$	$y_{O_2,out}$ **	i_{avg} at 0.7V
RH=50/0 @95°C	11.46	70.01	21.00%	9.22%	0.38
RH=0/50 @95°C	42.21	96.15	18.66%	8.28%	0.64
RH=30/30 @95°C	30.00	86.36	19.72%	8.63%	0.57
RH=100/100 @95°C	100.00	146.57	14.57%	6.47%	0.71
RH=50/0 @110°C	12.56	47.96	21.00%	8.94%	0.26
RH=0/50 @110°C	42.04	73.62	15.78%	7.43%	0.51
RH=30/30 @110°C	30.00	63.23	17.86%	8.04%	0.42
RH=100/100 @110°C	100.00	122.12	10.56%	5.19%	0.61

* Anode and cathode are considered together
** Assume anode and cathode have the same water activity

As shown in Table **6-2**, because the hydrogen flow rate is only about one fourth of the cathode air flow rate, the overall inlet relative humidity of A/C RH = 50/0 is much lower than the relative humidity of A/C RH = 0/50, despite the same individual reactant relative humidity percentages. Since water saturation pressure increases exponentially with increasing temperature, the increase in overall relative humidities from the inlet to the outlet for the 110°C cases are smaller than the respective increases of the 95°C cases. Comparing to the 95°C cases, the inlet oxygen mole fractions of the 110°C cases are also 2~4 percentage lower. Both the lower overall hydration of the electrolyte membrane and the lower cathode oxygen concentrations contribute to the lower performances of the 110°C cases. Although higher inlet relative humidity is always accompanied by lower oxygen mole fraction on the cathode, for the same flow field temperature, the average current density at 0.7 V always increases with higher water input, revealing high membrane resistance, and not oxygen concentration, is the main limiting factor of fuel cell performance at high temperatures and low humidity conditions at 0.7V.

Figure **6-1** shows the bulk polarization curves and bulk current density as function of input relative humidity for the four inlet humidity conditions at 95°C and pressure of 25 psig. Compared to the bulk performance of the fuel cell shown in Chapter 5, the current density at 0.6 V of the fully humidified condition of the new fuel cell improved 28.6%, (1.08 A/cm^2 vs. 0.84 A/cm^2) which is comparable with the performance of un-segmented fuel cells with similar flow field configurations. Similar to the bulk performance results of the Chapter 5 fuel cell at 80°C, higher bulk input relative humidity yields higher performance, although local distributions may vary a lot. However, due to reduced oxygen mole fraction and more severe flooding for higher input RH cases, the benefit of higher input relative humidity decreases significantly above 40%, as the oxygen mole fraction effect becomes dominant. Figure **6-2** shows the bulk polarization curves and bulk current density as function of input relative humidity for the four inlet humidity conditions at 110°C and the same high pressure of 25 psig. Compared to the cases of 95°C, input relative humidity has more effect on bulk performance since 110°C is dryer average condition at the same inlet relative humidity due to weakened self-humidification effect. Similar to the cases of 95°C, due to lower oxygen mole fraction and more severe flooding under higher input relative humidity conditions, benefit of input relative humidity also decrease quickly above 40%, although not as sharply as 95°C case.

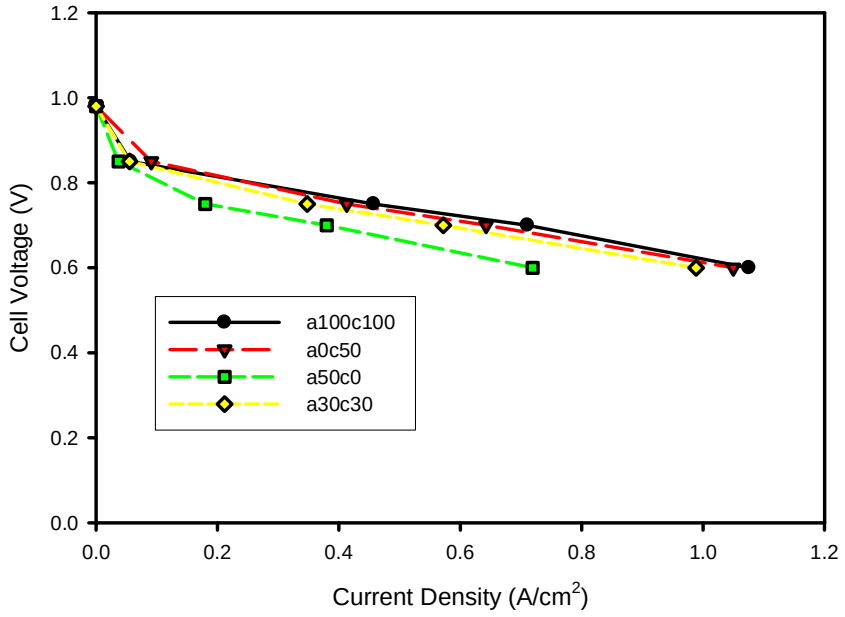

(a) Bulk polarization curves

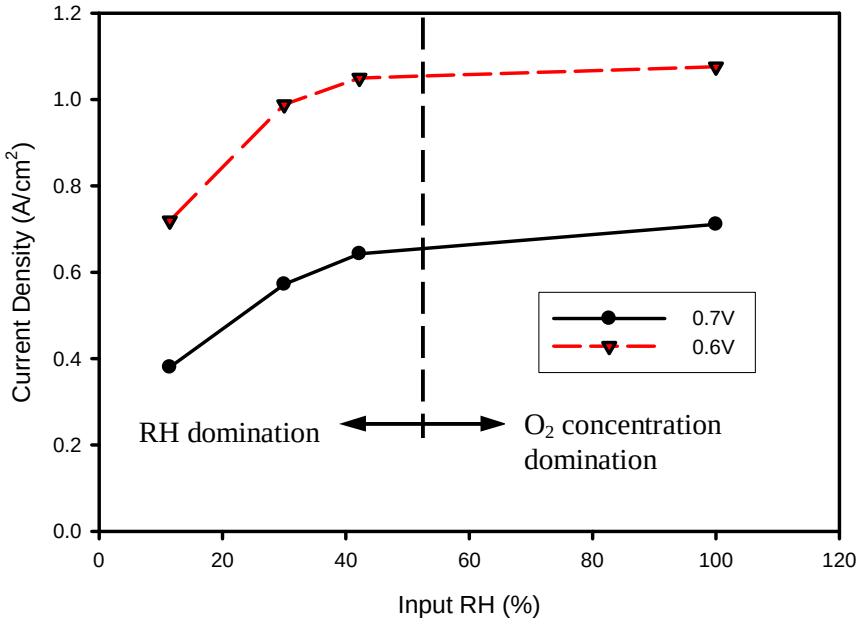

(b) Bulk current density vs. input RH

Figure **6-1**: Bulk performances comparison for different inlet humidities of 95 °C with 25 psig pressure.

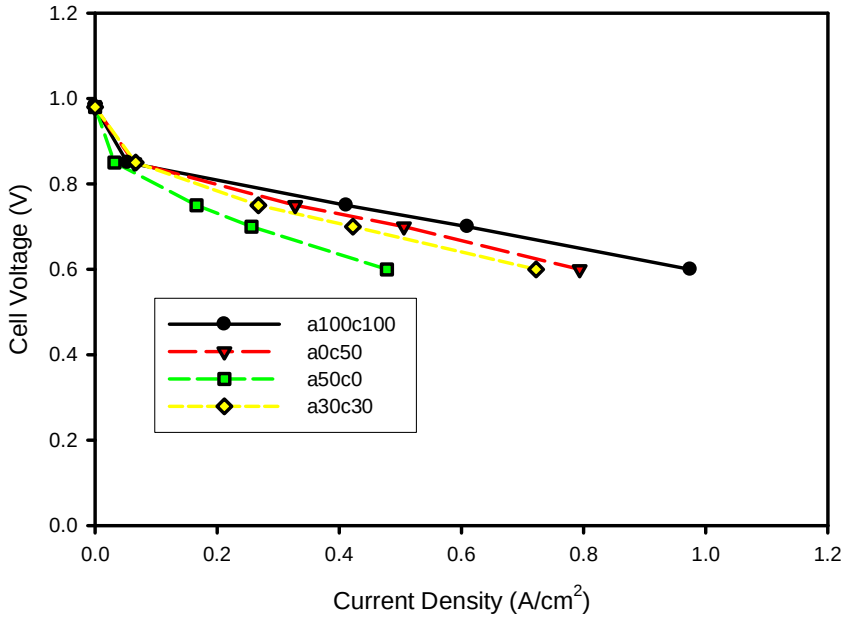

(a) Bulk polarization curves

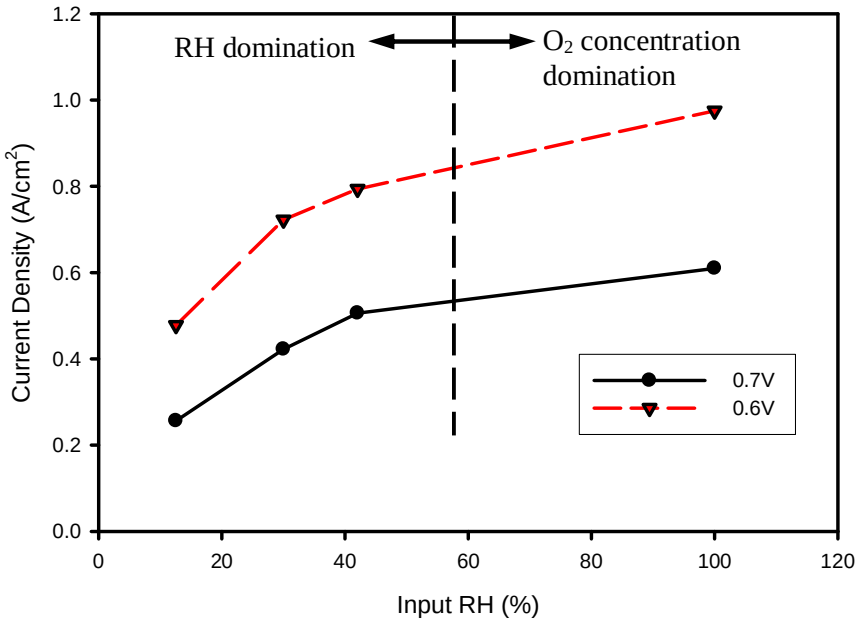

(b) Bulk current density vs. input RH

Figure **6-2**: Bulk performances comparison for different inlet humidities of 110 °C with 25 psig pressure.

Table **6-3** shows the overall inlet and outlet relative humidities, the inlet and outlet oxygen mole fractions, and the bulk current densities at 0.7V for the six low humidity operation conditions with various inlet humidities and temperatures for the 7.5 psig case. The relative humidities and oxygen mole fractions of the fully humidified conditions are also listed as benchmark references. Since the high humidifying temperature of 110°C is too close to the water boiling point (~114°C) at 7.5 psig, the humidifiers used for this study had difficulty to achieve 100% RH without boiling the internal water, and the oxygen mole fraction is also too low to maintain a stable cell performance. The fully humidified benchmark performance at 110°C was not conducted. However, performance would be almost zero, since the inlet oxygen mole fraction would be only 2.33%, from Table **6-3**.

Table **6-3**: Total relative humidity and oxygen concentration for 7.5 psig

Inlet RH and flow field temperature	Overall RH_{in} *	Overall RH_{out} *	$y_{O_2,in}$	$y_{O_2,out}$ **	i_{avg} at 0.7V
RH=50/0 @95°C	12.87	44.93	21.00%	8.85%	0.20
RH=0/50 @95°C	42.26	70.43	15.27%	7.22%	0.32
RH=30/30 @95°C	30.00	59.88	17.56%	7.90%	0.26
RH=100/100 @95°C	100.00	118.46	9.53%	4.14%	0.36
RH=50/0 @110°C	15.56	34.33	21.00%	7.04%	0.16
RH=0/50 @110°C	43.86	58.35	11.66%	4.39%	0.25
RH=30/30 @110°C	30.00	46.70	15.40%	5.49%	0.22
RH=100/100 @110°C	100.00	103.05	2.33%	1.30%	N/A

* Anode and cathode are considered together
** Assume anode and cathode have the same water activity.

Comparing to the high pressure case, the dilution effect for water vapor with lower pressure is more significant, especially at 110°C. At lower pressure of 7.5 psig, dry gaseous streams at the same mole flow rate require almost two times more water to reach the water saturation limit, so the self-humidification effect of water generation was much weakened. Co-affecting with much lower oxygen concentration resulted from both low oxygen mole fraction and low cell pressure, the worse hydration of polymer

electrolyte in membrane and catalyst layer led to obvious decreases of fuel cell performance compared to the 25 psig cases.

Figure **6-3** shows the bulk polarization curves and bulk current density as function of input relative humidity for the four inlet humidity conditions at 95°C and the lower pressure of 7.5 psig. Similar to the result of the cell at 25 psig, higher bulk input relative humidity yields higher performance. Again, the lower oxygen mole fraction and the cathode flooding in downstream region for the fully humidified inlet humidity condition significantly limits the cell performance, and the much higher input relative humidity doesn't show much benefit compared to 42.3% inlet relative humidity of A/C RH= 0/50. Figure **6-4** shows the bulk polarization curves and bulk current density as function of input relative humidity for the four inlet humidity conditions at 110°C and the same low pressure. Different from the other conditions, for this combination of high cell temperature and low pressure, although higher inlet relative humidity can still show positive effect on cell bulk performance at 0.7V, the higher inlet relative humidity of 42.3% of A/C RH=0/50 shows negative effect on the cell bulk performance at 0.6V compared with the lower inlet relative humidity of 30% of A/C RH=30/30, due to the more significant oxygen concentration polarization for high current density (inlet O_2 11.7% vs. 15.4%, outlet O_2 4.4% vs. 5.5%). Because the cell temperature of 110°C is only 4°C lower than the water boiling point at 7.5 psig and thus extremely low oxygen mole fraction, stable cell performance even cannot be easily achieved for fully humidified inlet condition without sophisticated control on humidifier temperature and cell pressure.

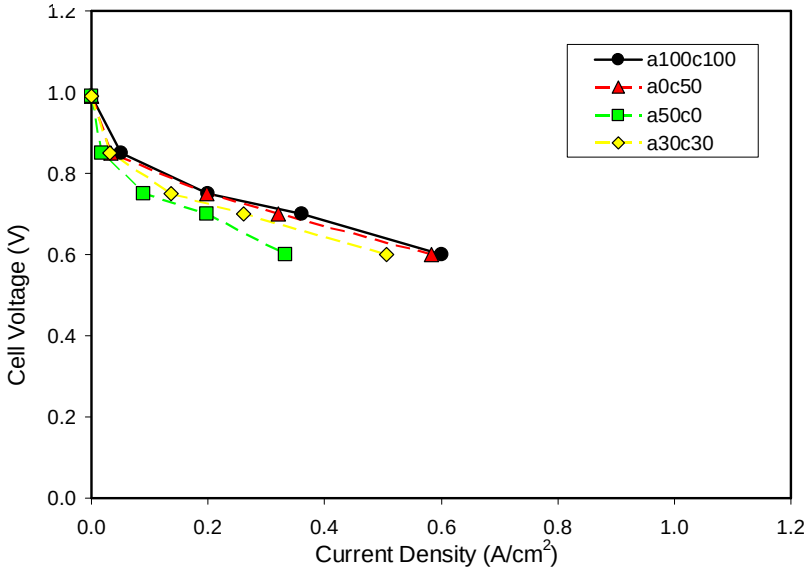

(a) Bulk polarization curves

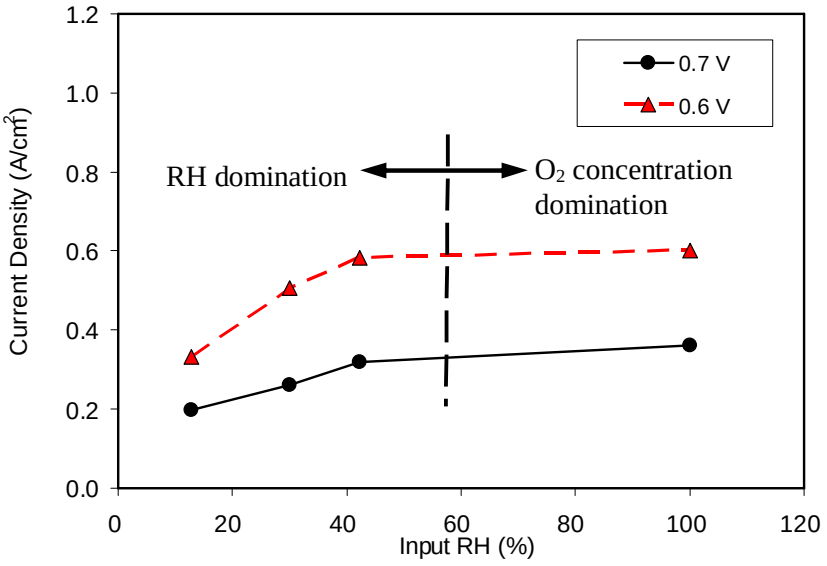

(b) Bulk current density vs. input RH

Figure **6-3**: Bulk performances comparison for different inlet humidities of 95 °C with 7.5 psig pressure.

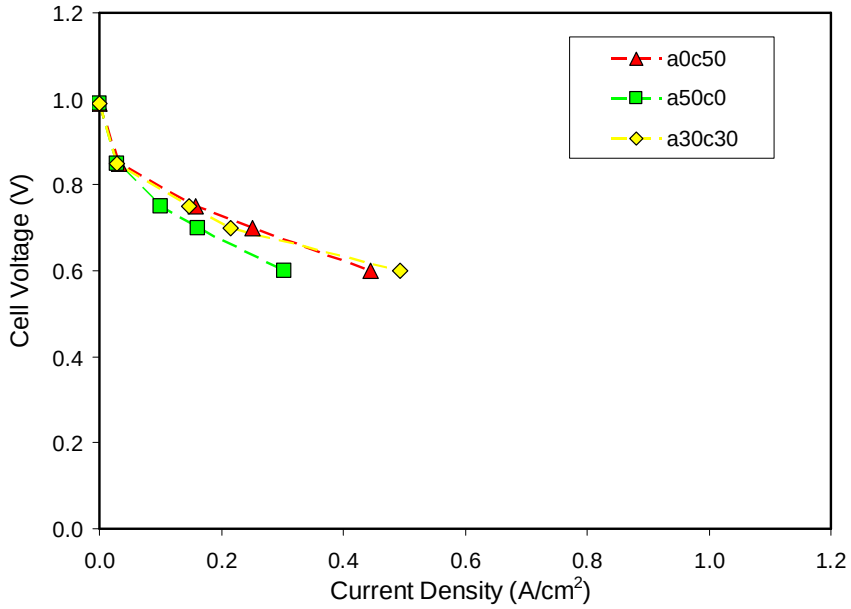

(a) Bulk polarization curves

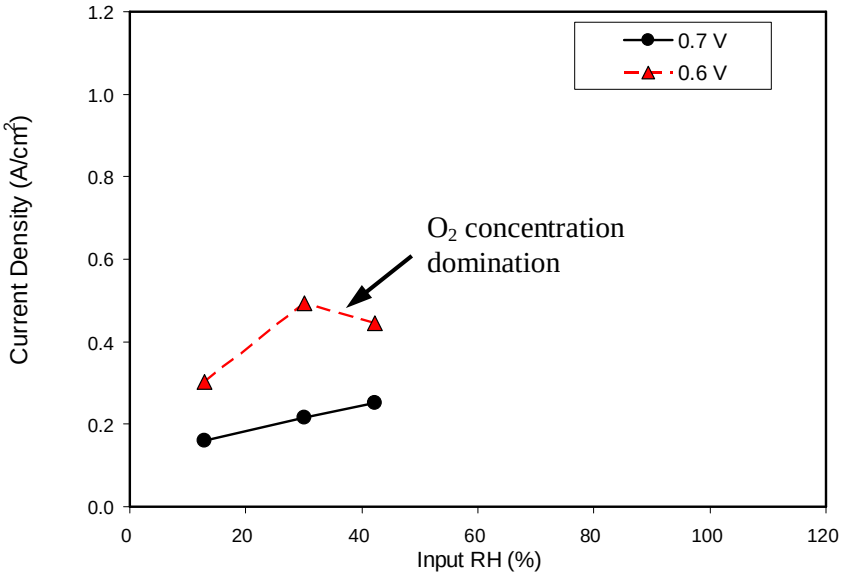

(b) Bulk current density vs. input RH

Figure **6-4**: Bulk performances comparison for different inlet humidities of 95 °C with 7.5 psig pressure.

6.3.2 Distributed performance under fully humidified baseline conditions

Current and HFR distributions were measured for three fully humidified baseline conditions. Due to the difficulty to fully humidify the reactant gases at 110 °C and 7.5 psig, the distributions were not measured for this combination of high temperature and low pressure.

The current distributions of the three conditions are shown in Figure **6-5**. For all three conditions, current density first increases slightly at the beginning and reaches a maximum, and then decreases due to decreasing oxygen concentration and flooding in the downstream region along the gas flow channel. The slight increase of cell performance at the beginning may be contributed by the variation of compression.

For the two 25 psig conditions, the 95 °C case outperformed the 110 °C case about 10 percent mainly because of high oxygen concentration (inlet O_2 14.6% vs. 10.6%, and outlet O_2 6.5% vs. 5.2%). However, the 95 °C case also is also believed to be suffered more severe flooding as indicated by the steeper decreasing slope (exit RH = 147% and 122%). The current distribution profile of the 95°C and 7.5 psig case was pretty similar to the other two high pressure cases, although the current density were much lower due to the lower oxygen concentration. Compared to current distribution for the fully humidified condition of the previous natural convection cooled fuel cell, there is no decrease of current near the inlet and no increase of current near the outlet at 0.6V, the high current density case, implying that the isothermal boundary condition restrains dry-out due to heat generation, and amplifies flooding.

Figure **6-6** shows the respective HFR distributions for the three fully humidified conditions. From the plots we can see that the HFRs at both temperatures and all four voltages are well below 0.1 Ω-cm^2 along the whole flow channel with very small variation. The similarity of HFR between 95°C and 110°C further confirms that decreased performance at higher temperature is mainly caused by decreased oxygen concentration. It also should be noticed that the HFR values at a given location for four different cell voltages were almost identical, implying the electro-osmotic drag was evenly balanced by water back diffusion from the cathode, and there was no severe anode

dry-out taking place under fully humidified conditions if the elevation of temperature of the membrane and the thermal boundary condition are well controlled the flow field temperature.

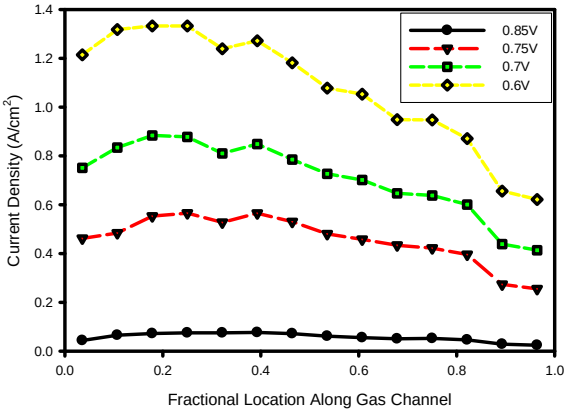

(a) T_{cell} = 95°C, pressure = 25 psig

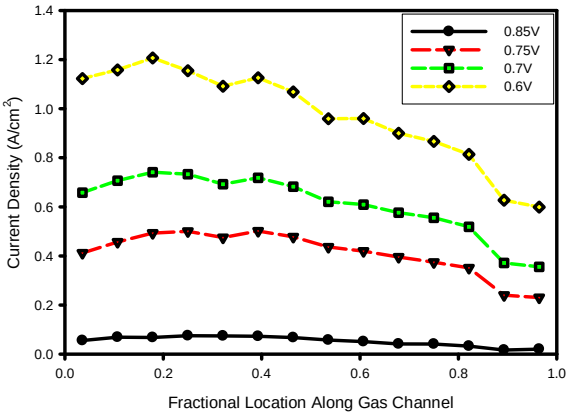

(b) T_{cell} =110°C, pressure =25 psig

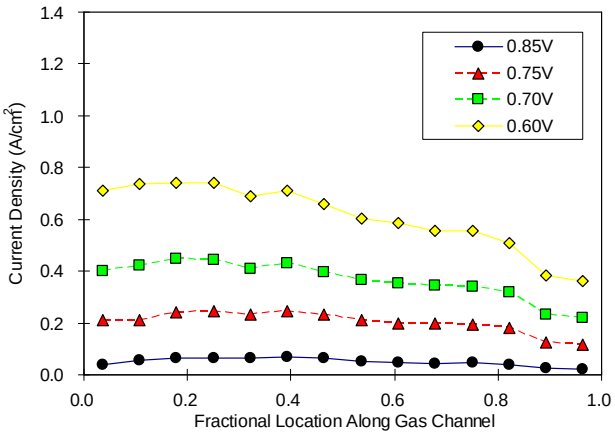

(c) T_{cell} =95°C, pressure = 7.5 psig

Figure **6-5**: Distributed steady-state current density as function of fractional distance from the inlet for the three fully humidified baseline conditions

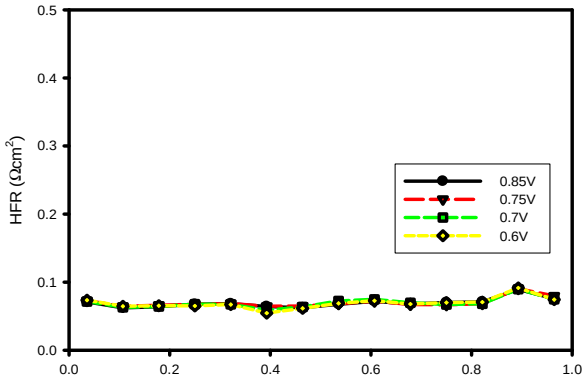

(a) T_{cell} = 95°C, pressure = 25 psig

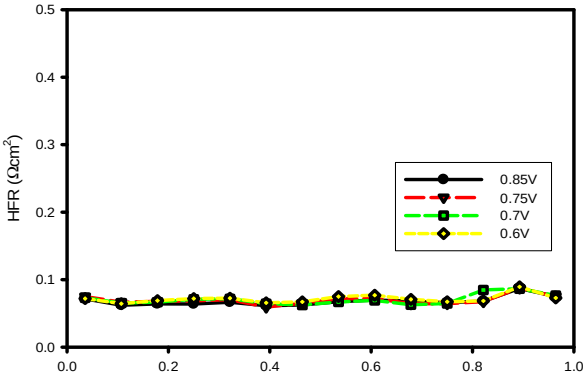

(b) T_{cell} =110°C, pressure =25 psig

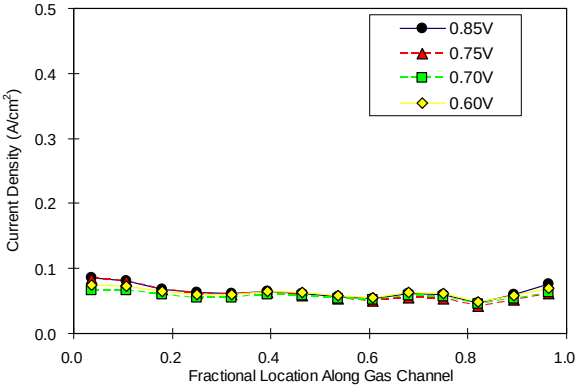

(c) T_{cell} =95°C, pressure = 7.5 psig

Figure **6-6**: Distributed steady-state HFR as function of fractional distance from the inlet for the three fully humidified baseline conditions

6.3.3 Distributed performance under low humidity conditions

Distributed performances of PEFCs including current density, HFR, and species were measured for three low humidity conditions, two elevated temperatures and two pressures using the new instrumented fuel cell.

A/C RH = 50/0 is a representative under humidified cathode condition because the cathode inlet was absolutely dry, while the anode inlet was also under humidified. Figure **6-7** shows the distributed steady-state current density as function of fractional distance from the gas inlet for this humidity condition at the two elevated cell temperatures of 95 and 110 °C and the high pressure of 25 psig. Because of possible variation of local compression, there is small scatter with measured local current densities of the 4^{th} and 12^{th} segments. Similar to the previous tests with the old cell, for this dry cathode condition, the current density shows a decreasing to a local minimum, then increasing profile. The current density turn-back point indicates water flux reversal in the electrolyte membrane, as discussed in Chapter 5, although in general they don't overlap together because current density is also affected by cathode side hydration and should be slightly earlier than the water flux reversal point. Due to the isothermal boundary condition, the initial decrease of performance is milder. The lower temperature case obviously outperformed the higher temperature case (about 50 percent at 0.6V) because the better self-humidification (outlet RH 70% vs. 48%), and slightly higher oxygen mole fraction (outlet O_2 mole fraction 9.2% vs. 8.9%). It also can be seen from Figure **6-7** that at two cell temperatures of 95°C and 110°C, the measured current densities at 0.7V are very close (~10% higher at 95°C) in the front 32% (5^{th} segment) region of the fuel cell despite the 95°C curve increases with a much steeper slope in the downstream, indicating that the electrolyte hydration in inlet region is mainly controlled by humidity in gas flow channel. However, at 0.6V, the increased water activity difference between catalyst layer and gas flow channel shows obvious effect on local current densities, the front 32% of the fuel cell outperforms 42% better at 95 °C than at 110°C although the water activities in gas flow channel are basically same with constant stoichiometry.

Figure **6-8** shows the distributed HFR for this dry cathode humidity condition and two temperatures. Possibly due to the unstable nature of the water transport phenomena under dry cathode condition [**103**], the HFR data has much bigger scatter than the fully humidified baseline conditions. The correlation between HFR and current density might be overwhelmed by the big scatter, and is not as good compared to the HFR taken for other conditions. This can be further explained by the data acquisition procedure: the local current density data shown here are averaged values over 5 minutes, so most of the instability of cell performance can be eliminated by this average, whereas unlike a impedance spectroscopy, the multi-channel potentiostat doesn't have the capability to measure HFR continuously and the shown HFR values are not averaged value over a long enough time period. And unlike the negligible effect of cell temperature on the resistance of fully humidified conditions, the higher cell temperature of 110°C leads to an obvious increase of cell resistance mainly because of the weakened humidification effect by produced water compared to 95°C.

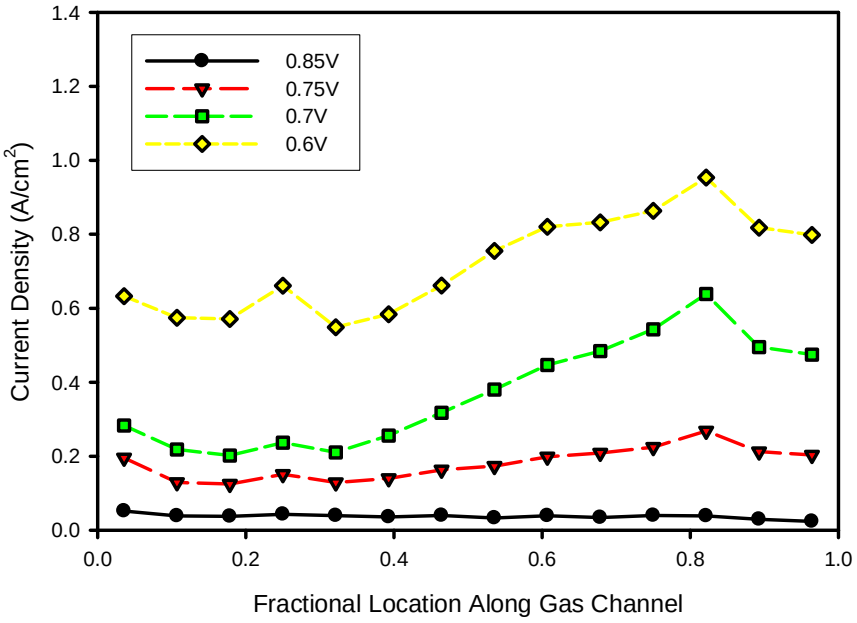

(a) T_{cell}=95°C

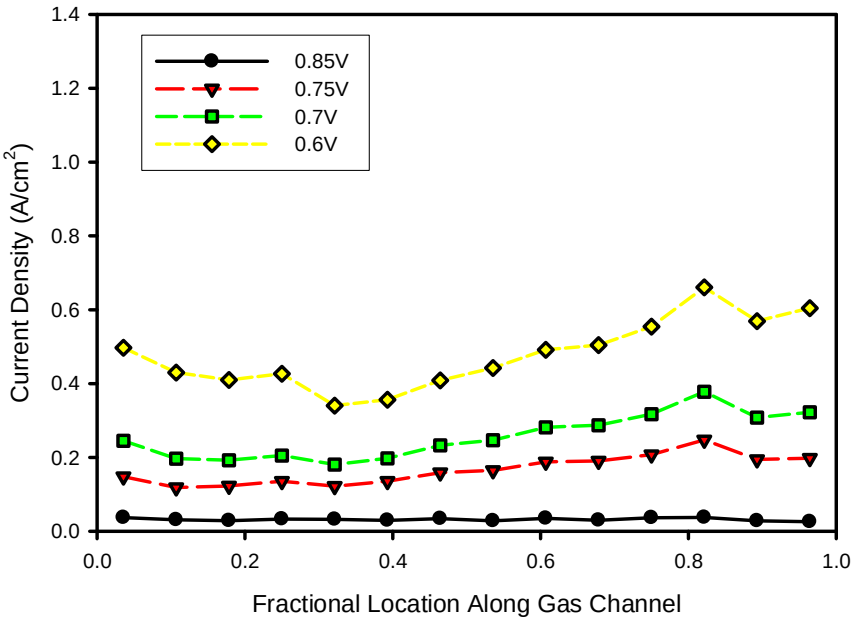

(b) T_{cell}=110°C

Figure **6-7**: Distributed steady-state current density of A/C RH = 50/0, pressure = 25 psig

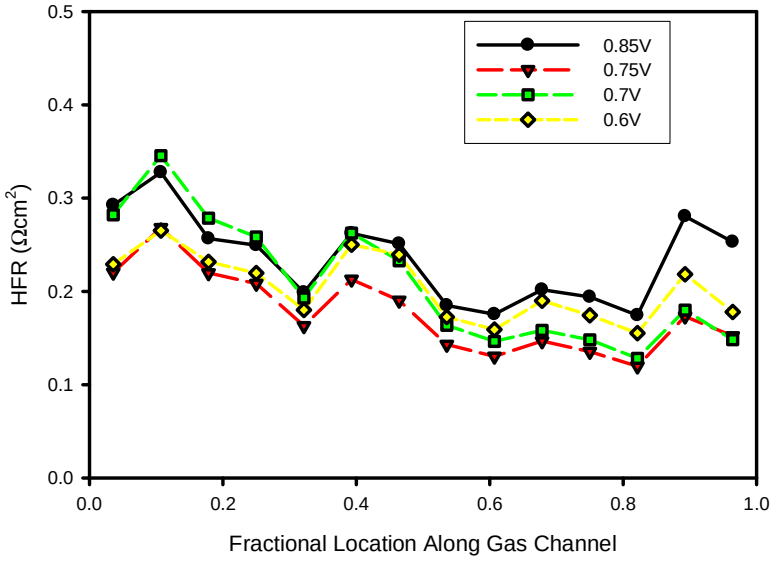

(a) T_{cell}=95°C

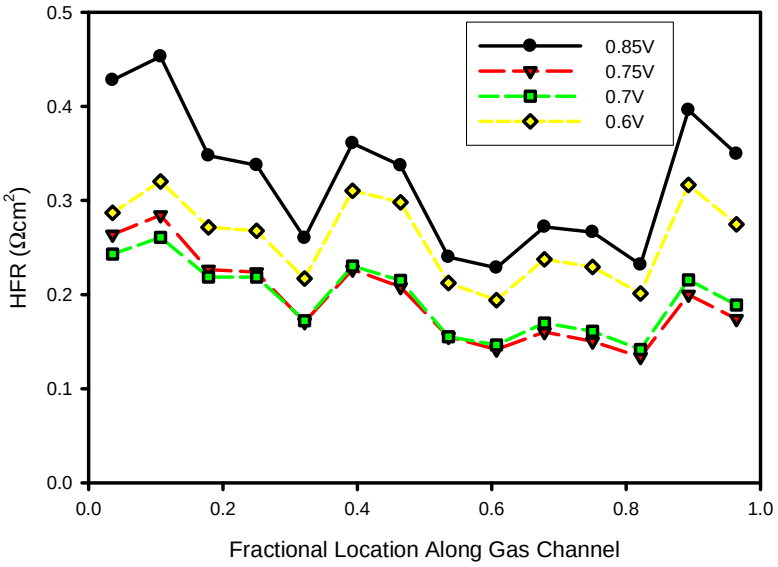

(b) T_{cell}=110°C

Figure **6-8**: Distributed steady-state high frequency resistance (HFR) of A/C RH = 0/50, pressure = 25 psig

Figure **6-9** and Figure **6-10** show the steady-state species distributions on the anode and cathode for this dry cathode case at 95°C and 110°C respectively. Similar to the results of previous study in Chapter 5, because of diffusion and electro-osmotic drag toward the cathode, the anode water first decreases to a local minimum, then increases because of the reversal of net water flux. Also, the hydrogen mole fraction decreases along the flow channel because it is the only reacting species in the anode. On the cathode side, water content kept increased along the flow channel because of water transported from the anode by diffusion and electro-osmotic drag, as well as water generation on cathode itself. The oxygen mole fraction decreases almost monotonically due to consumption and the increasing water content. Similar to previous results shown in Chapter 5, the distributed steady-state current density also followed the *anode* water content profile well. For 95°C cell temperature, the anode outlet water mole fraction slightly exceeds the water saturation limit while the cathode outlet water content is still several percents lower than the water saturation limit. For 110°C cell temperature, as indicated by the bulk relative humidity calculation shown in Table **6-2**, both the anode and cathode outlet water mole fraction are significant lower than the water saturation limit at that temperature. Similar to 95°C, the anode outlet water mole fraction of 110°C is also slightly higher than the cathode outlet water mole fraction.

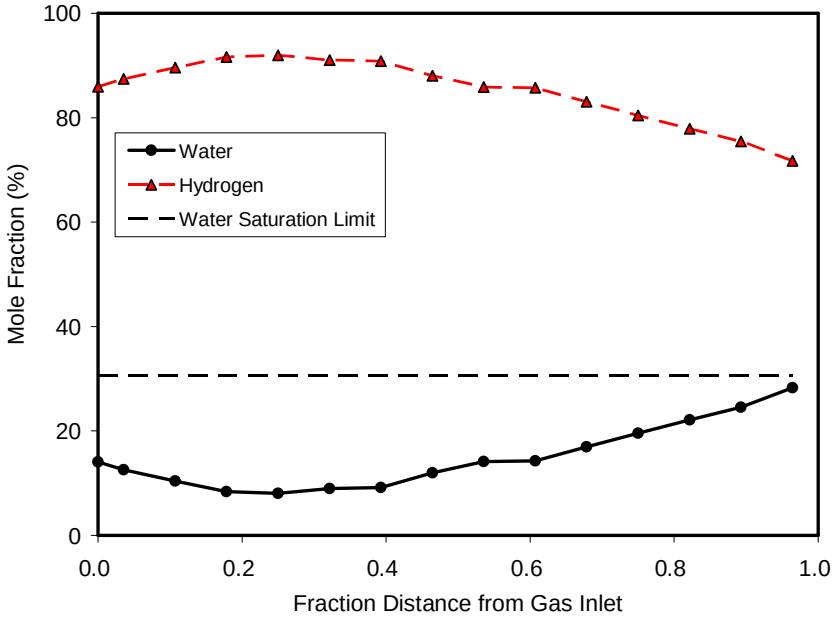

(a) Anode

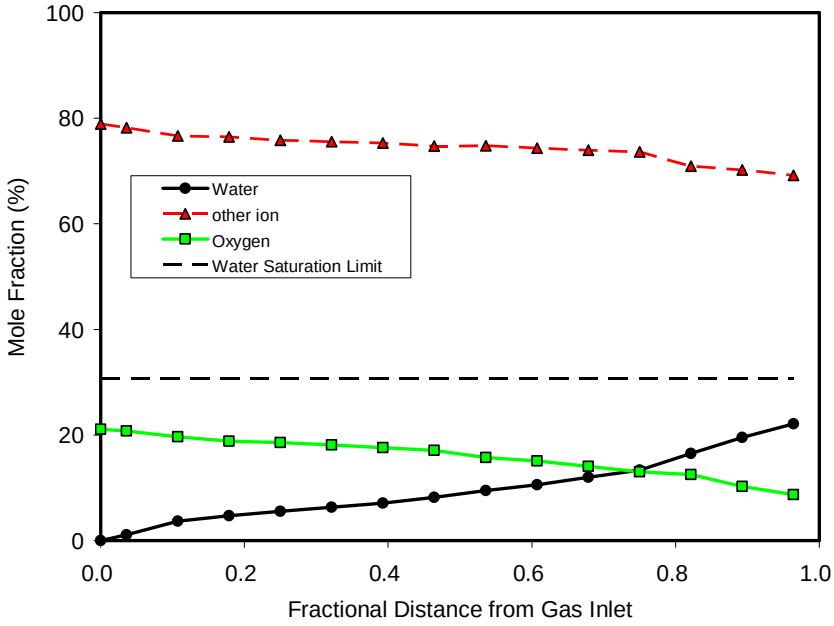

(b) Cathode

Figure **6-9**: Steady-state species distribution on the anode and cathode for A/C RH=50/0, T_{cell} = 95°C, pressure = 25 psig

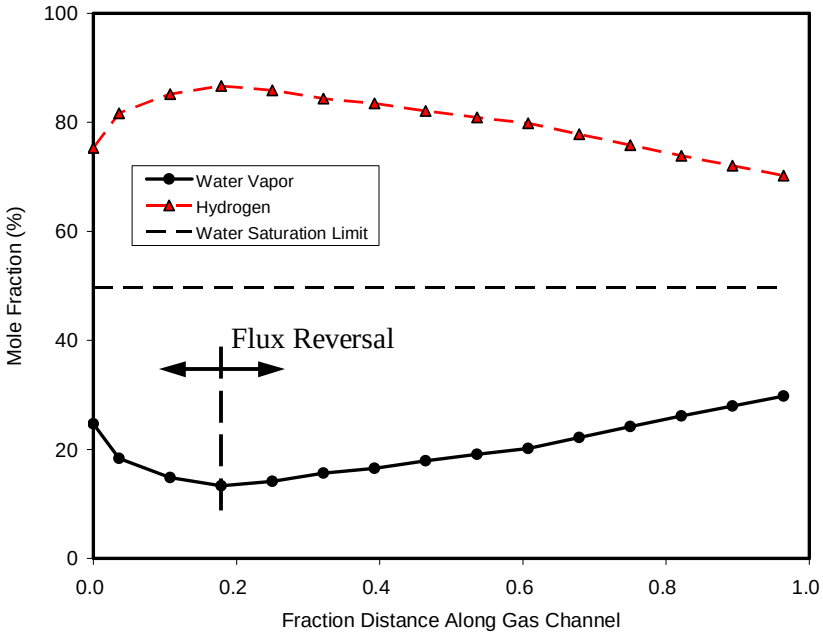

(a) Anode

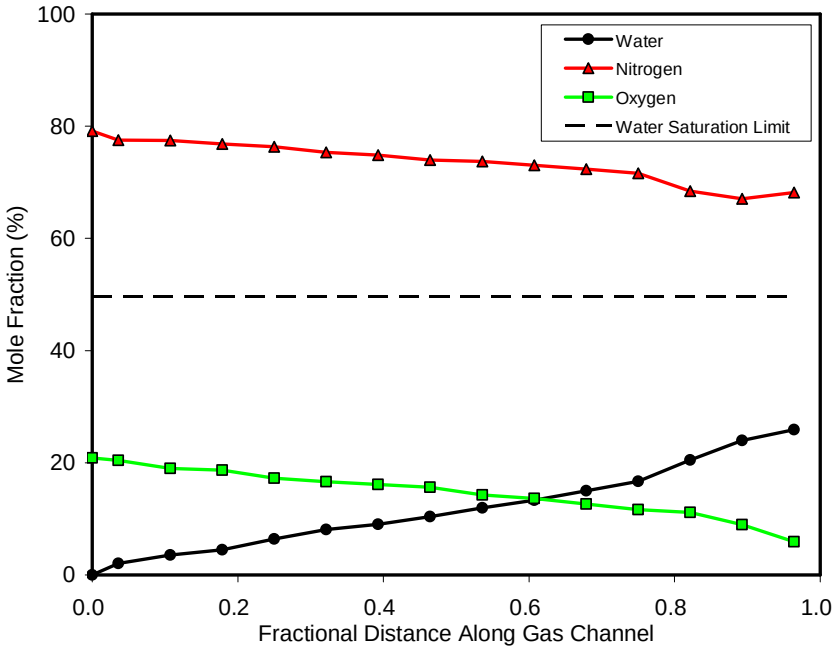

(b) Cathode

Figure **6-10**: Steady-state species distribution on the anode and cathode for A/C RH=50/0, T_{cell} = 110°C, pressure = 25 psig

Figure **6-11** shows the distributed steady-state current density for the representative dry anode condition of A/C RH = 0/50 at the two elevated cell temperatures and the higher pressure. Compared to the results of Chapter 5 with the previous generation fuel cell, for this dry anode condition, the current density shows a similar increasing to local maximum due to anode dry-out at the inlet and anode water pickup at locations further along the serpentine gas flow path, and then decreasing profile due to the dominating effect of oxygen depletion. However, because of the negative contribution of membrane temperature increase on electrolyte hydration was partially eliminated by the isothermal boundary condition in this cell design, current density increased much closer to the inlet than the previous natural convection cooled cell. Compared with respective fully humidified baseline conditions, the decrease of local current density in fuel cell downstream region is much gentler due to the alleviation of cathode flooding. Similar to the dry cathode case, because of the reduced humidification effect by generated water (outlet RH 74% vs. 96%) and lower oxygen mole fraction (inlet O_2 15.8% vs. 18.7%, outlet O_2 7.4% vs. 8.3%), the higher cell temperature of 110°C yielded obvious lower cell performance (about 30% lower at 0.6V).

Figure **6-12** shows the distributed steady-state HFR for this dry anode condition of A/C RH = 0/50. Reversing the general trend of current density, there is an overall decreasing trend in the cell resistance with the increase of fractional location from the gas inlet, corresponding to the increasing hydration of electrolyte in the membrane and catalyst layers. The inlet resistances are more than 50% higher than the outlet resistances for most conditions except at 0.85V of 95°C. For both temperatures, the HFR data for 0.6V are higher than those for 0.75V and 0.7V, implying more severe anode dry-out under higher current density.

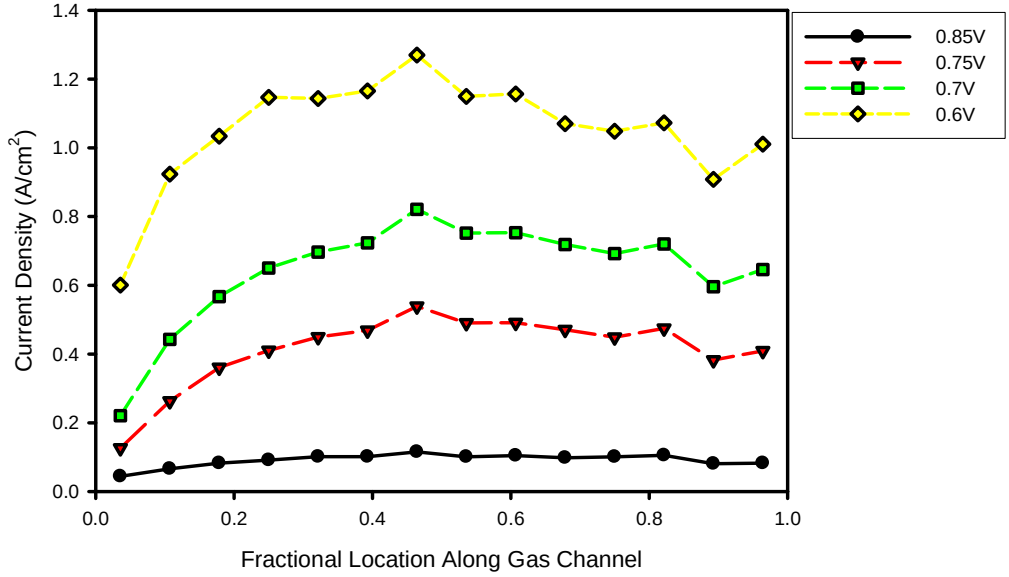

(a) T_{cell}=95°C

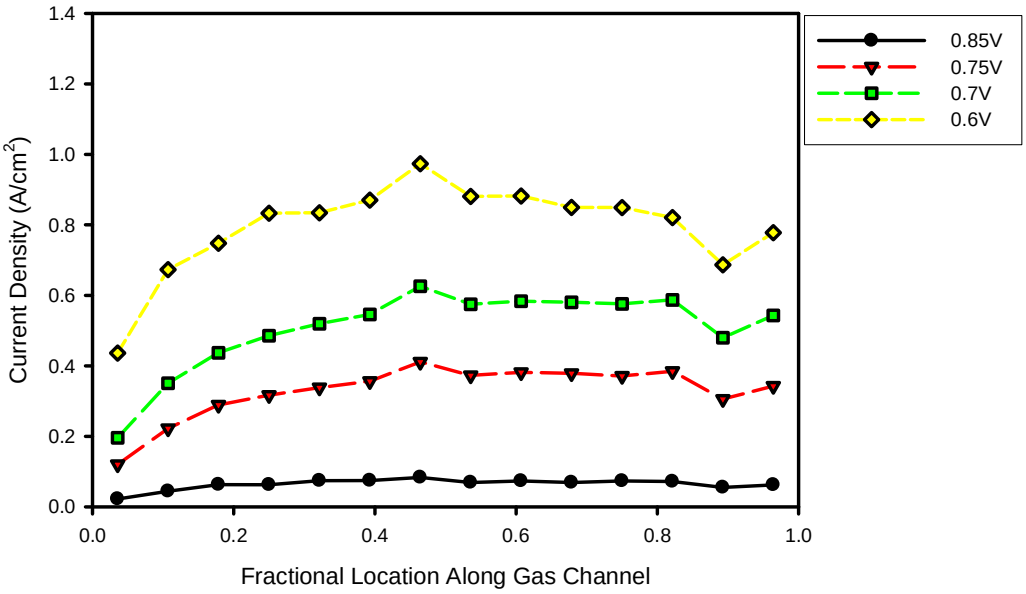

(b) T_{cell}=110°C

Figure **6-11**: Distributed steady-state current density of A/C RH = 0/50, pressure = 25 psig

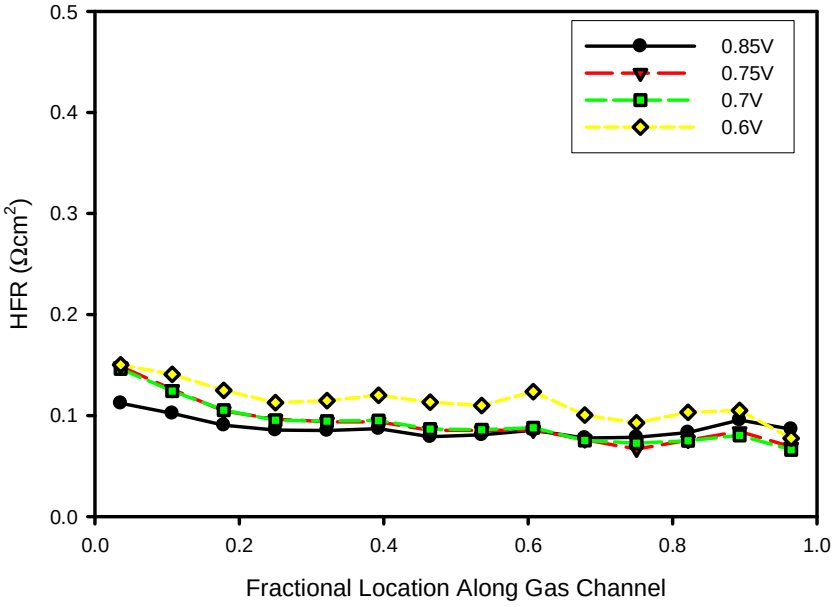

(a) T_{cell}=95°C

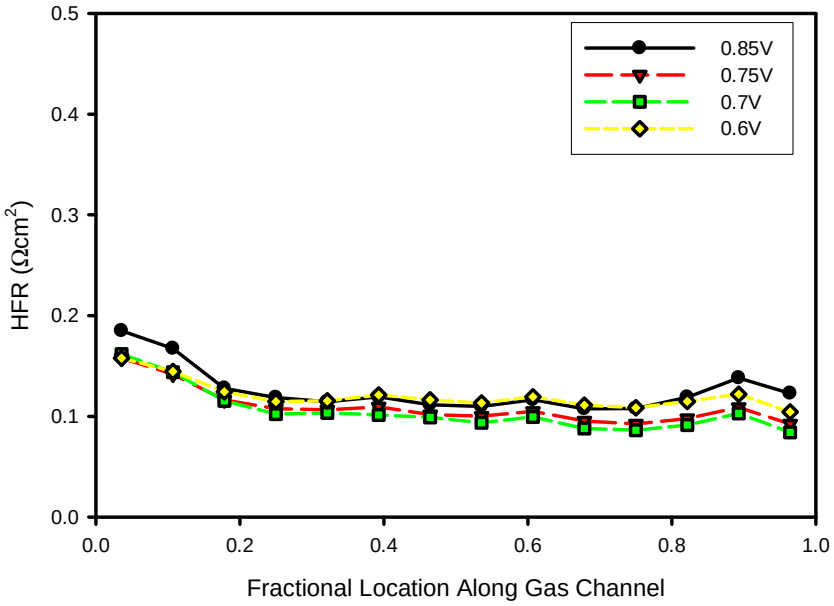

(b) T_{cell}=110°C

Figure **6-12**: Distributed steady-state high frequency resistance (HFR) of A/C RH = 0/50, pressure = 25 psig

Figure **6-13** and Figure **6-14** are the steady-state species distributions on the anode and cathode at 0.7 V for this dry anode case with 95°C and 110°C flow field temperature. Similar to the species distributions of the previous cell, on the anode side, the water content increases almost monotonically due to back-diffusion from the cathode side, and the hydrogen mole fraction decreases along the flow channel because it is the only major balance species in the anode. On the cathode side, the oxygen mole fraction decreases almost monotonically due to consumption and water uptake; and the water content first decreases to a minimum because of water loss to the dry anode, and then increases due to water generation; as the only major inert balance component of cathode, the nitrogen content varies in the reverse trend of the sum of cathode water content and oxygen mole fraction. For the 95°C case, the anode water mole fraction exceeds the saturation limit of 95°C after 80% fractional distance from the gas inlet, and the cathode outlet water content is also very close to the saturation limit (28.4% vs. 30.6%). Compared to 95°C, the 35.2% anode outlet water mole fraction and the 34.3% cathode outlet water mole fraction for the 110°C case are significantly lower than the 49.7% water saturation limit at 110°C. These measured outlet water mole fractions agree very well with the bulk relative humidity calculations shown in Table **6-2**. It also should be noticed that in the region after 60% fractional distance from the gas inlet, the anode water mole fraction is very close to or even 4~5 percent higher than the cathode water mole fraction for both elevated fuel cell temperatures. Because water back-diffusion from the cathode is the only water source of the anode side, and also considering the water activity gradient across the membrane caused by electro-osmotic drag, there could be considerable difference of water activity between cathode catalyst layer and cathode gas channel.

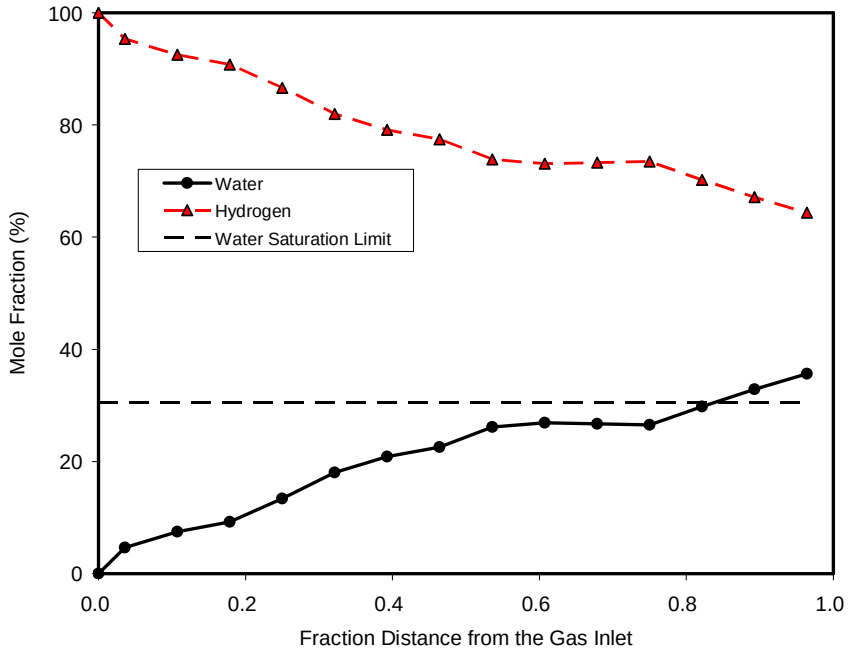

(a) Anode

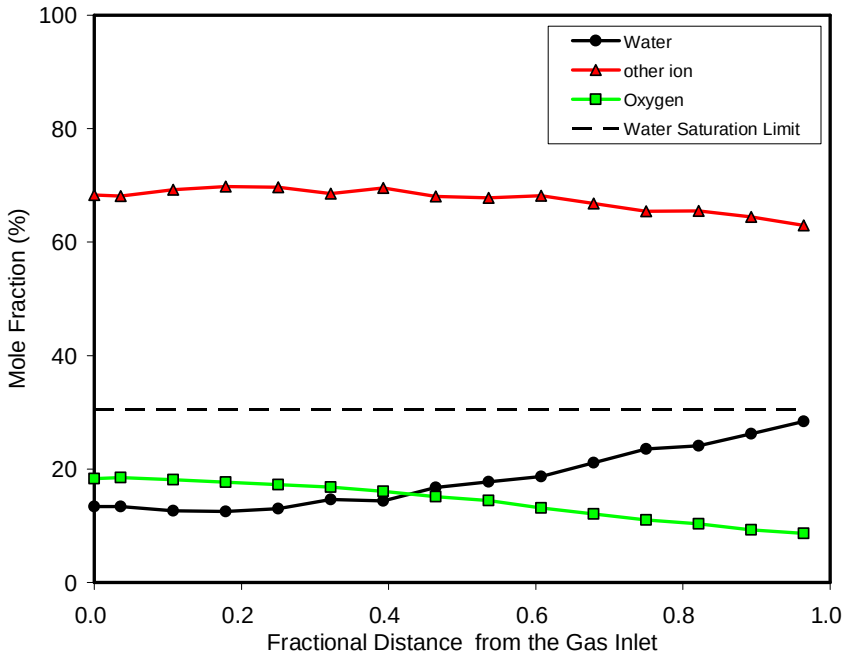

(b) Cathode

Figure **6-13**: Steady-state species distribution on the anode and cathode for A/C RH=0/50, T_{cell} = 95°C, pressure = 25 psig

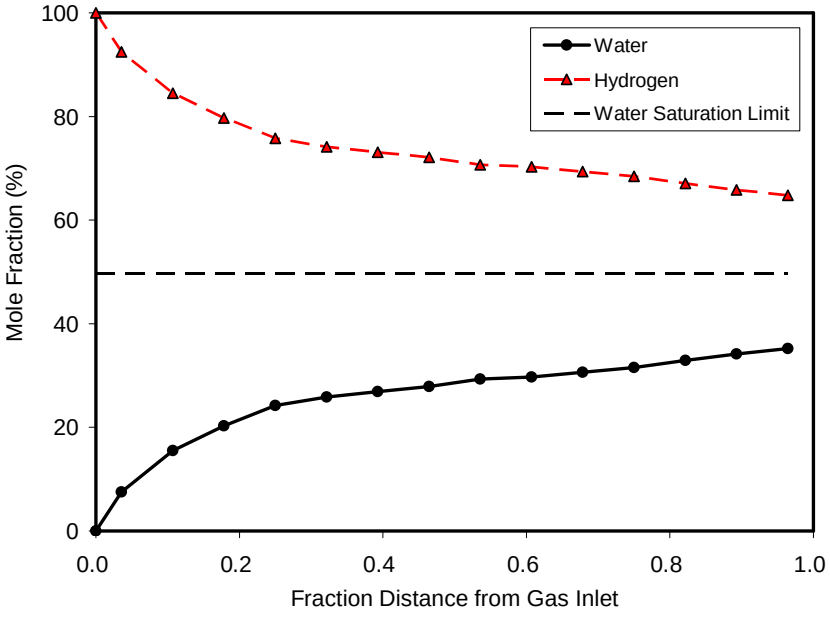

(a) Anode

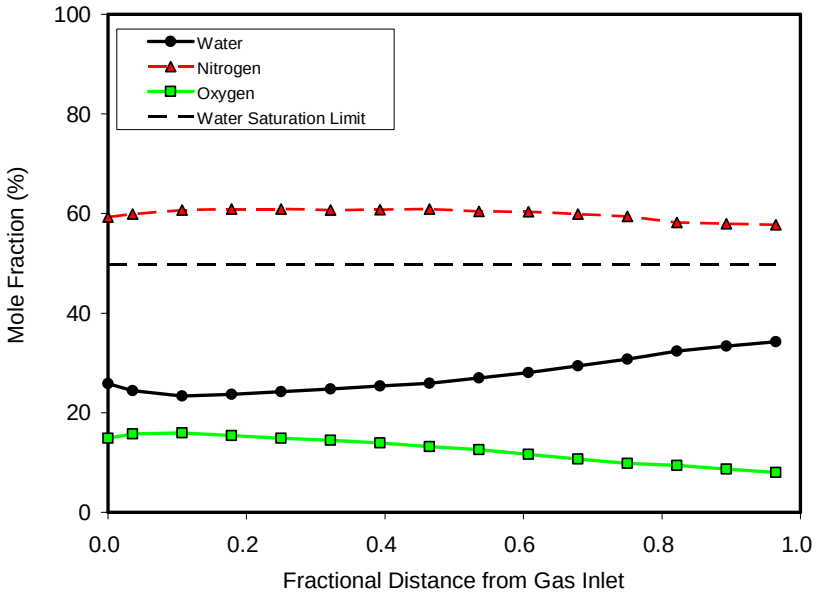

(b) Cathode

Figure **6-14**: Steady-state species distribution on the anode and cathode for A/C RH=0/50, T_{cell} = 110°C, pressure = 25 psig

Figure **6-15** shows the distributed steady-state current density for the representative partially humidified anode and cathode case of A/C RH = 30/30 at two cell temperatures and 25 psig pressure. Different from the results of the previous cell, for this partially humidified condition the current density does not show a small decreasing to a local minimum, then increasing profile. This difference may be caused by changed boundary condition or flow field configurations. Compared with respective fully humidified baseline conditions, the decrease of local current density in fuel cell downstream region appears much further from the inlet due to the alleviation or even elimination of cathode flooding. Similar to other low inlet humidity conditions, the higher cell temperature of 110°C yielded obvious lower cell performance (about 35% at 0.6V) also because of worse self-humidification (outlet relative humidity 63% vs. 86%) and lower oxygen mole fraction (inlet O_2 17.9% vs. 19.7%, outlet O_2 8.0% vs. 8.6%),

Figure **6-16** are the distributed steady-state HFR for this partially humidified anode and cathode condition of A/C RH = 30/30. Reversing the general trend of current density, there is an overall decreasing trend in the cell resistance with the increase of fractional location from the gas inlet, corresponding to the increasing hydration of electrolyte in the membrane and catalyst layers. The inlet resistances are almost 100% higher than the outlet resistances. Different from the old cell, there is no increasing-decreasing profile of HFR with the new isothermal boundary condition and flow field configurations. For both temperatures, the HFR data for 0.6V are higher than those for 0.75V and 0.7V, implying more severe anode dry-out under higher current density.

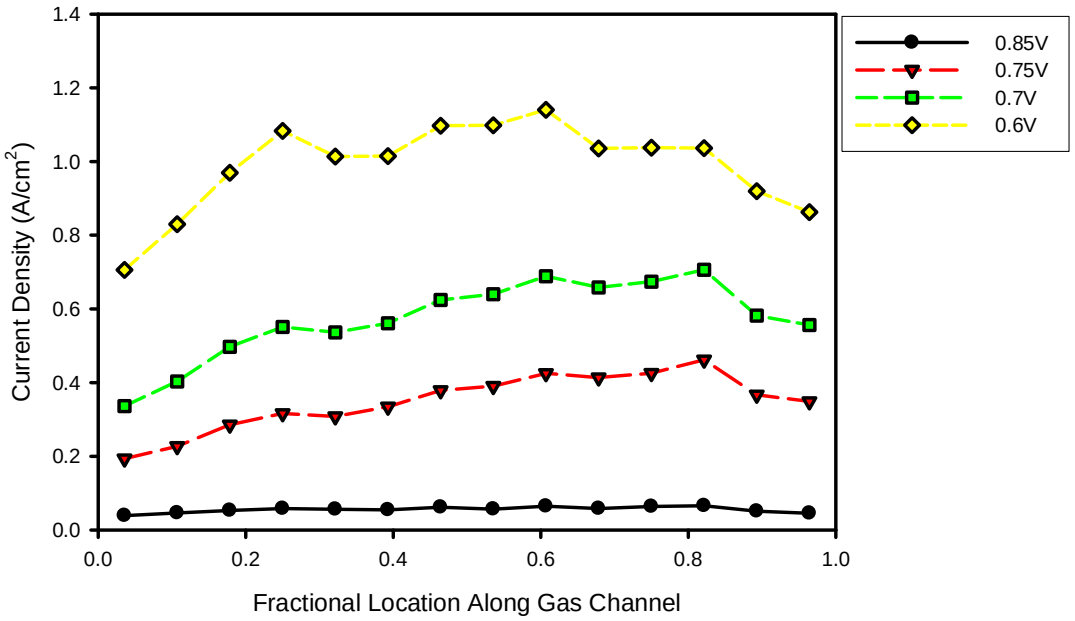

(a) T_{cell}=95°C

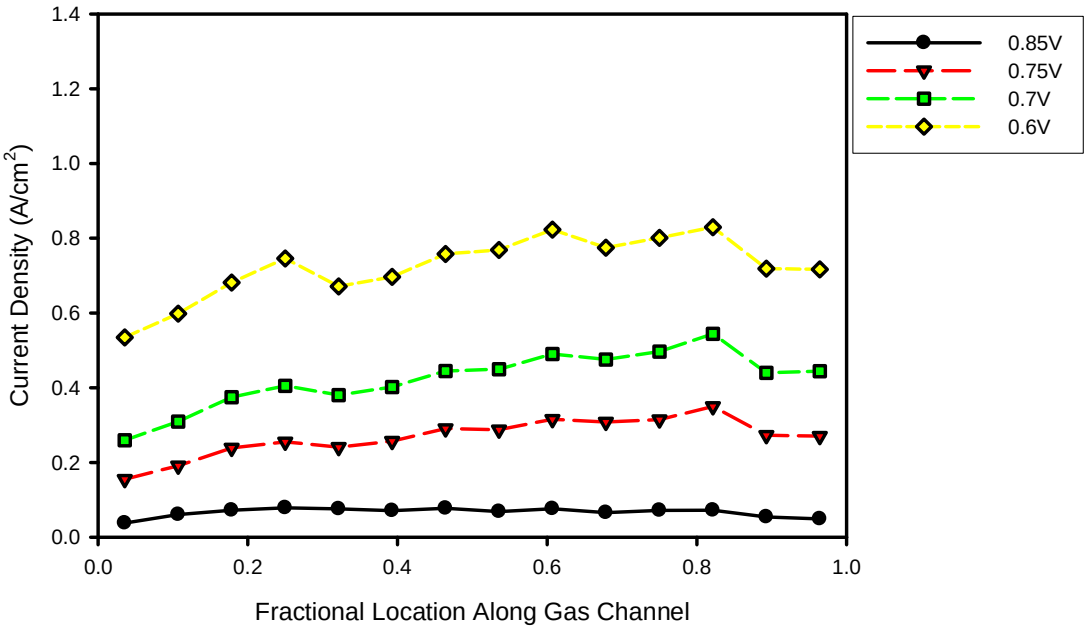

(b) T_{cell}=110°C

Figure **6-15**: Distributed steady-state current density of A/C RH = 30/30, pressure = 25 psig

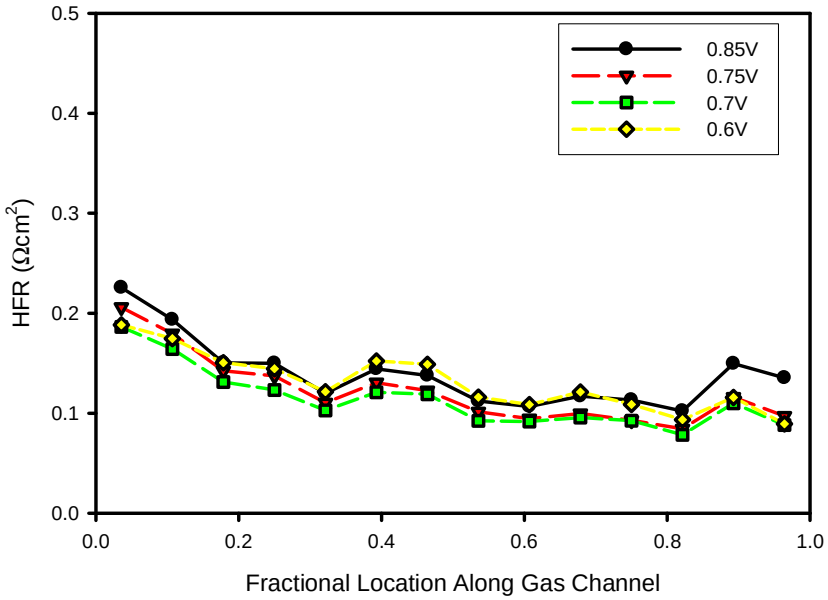

(a) T_{cell}=95°C

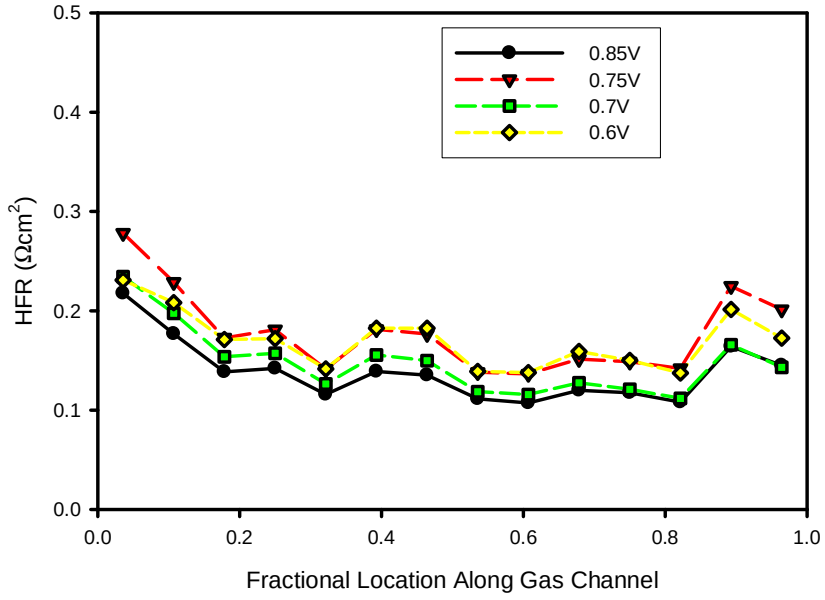

(b) T_{cell}=110°C

Figure **6-16**: Distributed steady-state high frequency resistance (HFR) of A/C RH = 30/30, pressure = 25 psig

Figure **6-17** and Figure **6-18** are the steady-state species distributions on the anode and cathode at 0.7 V for this partially humidified anode and cathode, but relatively dry cathode inlet condition, respectively. Different from other two inlet humidity conditions, no decrease of water mole fraction is observed on either side, and both water contents increases monotonically with the increase of fractional distance due to water generation. Again, the anode water mole fraction is 3~5% higher than the cathode water mole fraction in the downstream half of the fuel cell, which means mass transport resistance of the micro-porous layer and GDL can create a considerable water concentration difference between cathode catalyst layer and cathode gas channel and help membrane hydration.

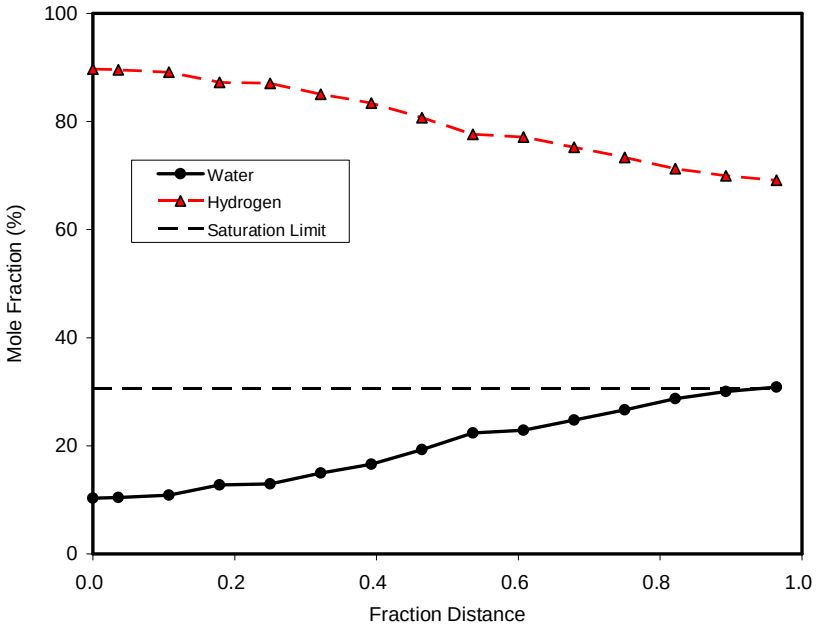

(a) Anode

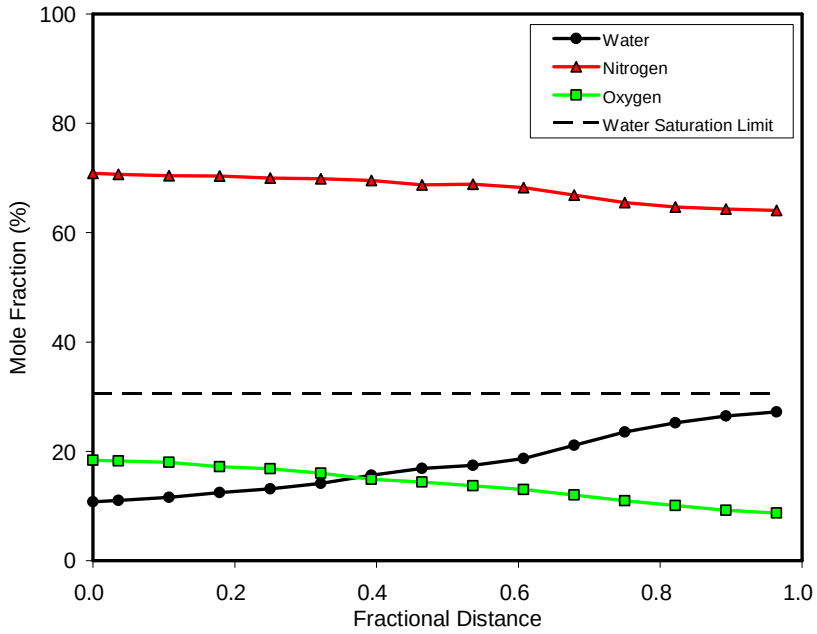

(b) Cathode

Figure **6-17**: Steady-state species distribution on the anode and cathode for A/C RH=30/30, T_{cell} = 95°C, pressure = 25 psig

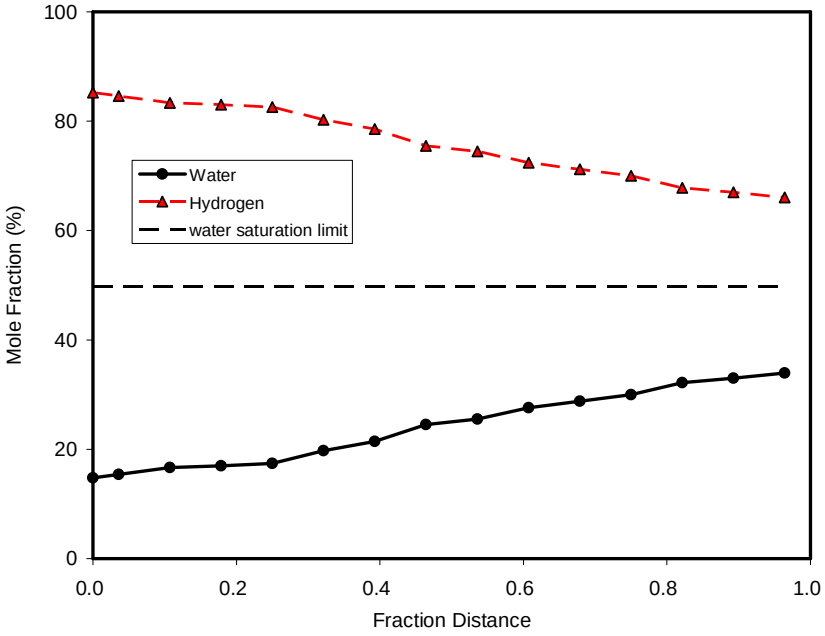

(a) Anode

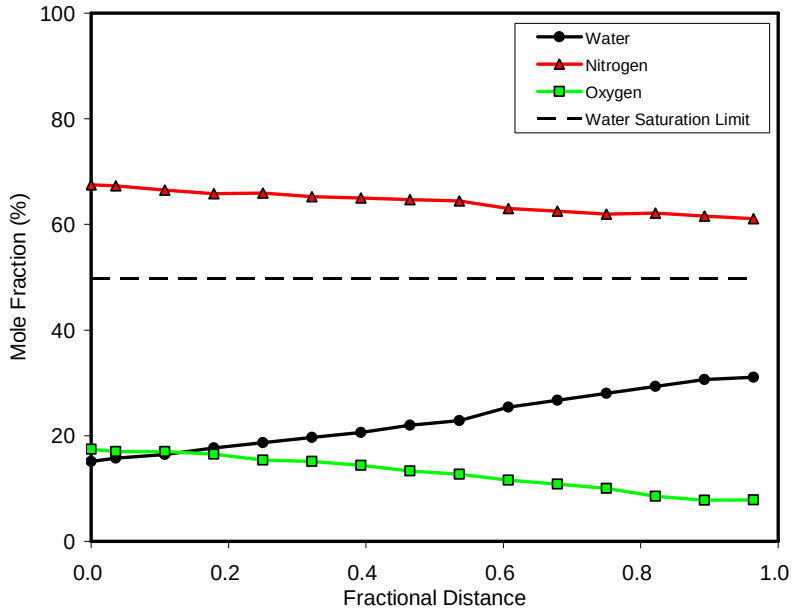

(b) Cathode

Figure **6-18**: Steady-state species distribution on the anode and cathode for A/C RH=30/30, T_{cell} = 110°C, pressure = 25 psig

Figure **6-19** shows comparisons of the current density profiles at 0.7V and 25 psig for the four humidity conditions at the two cell temperatures. Note, because the hydrogen inlet mole flow rate is only 25.2% of the air inlet mole flow rate at constant stoichiometries of 1.2 for anode and 2.0 for cathode, A/C RH=50/0 is the driest condition and A/C RH=0/50 is the moistest low humidity condition. At both temperatures, the fully humidified condition shows flooding as indicated by an overall decreasing current density profile after a local maximum is reached around 20% fractional location. At the outlet, the local current density of fully humidified condition is the lowest among four conditions. Of course, the lower oxygen mole fraction also contributes some to this performance decrease. By contrast, none of the three low humidity conditions shows obvious flooding, especially the very dry condition of A/C RH=50/0, in which current density almost keeps increasing after the local minimum, indicating the dominating effect of electrolyte hydration. It also can be noticed from the plot that the higher inlet relative humidity at the anode leads to higher inlet performance, despite the cathode relative humidity does play a role in the case of A/C RH=30/30.

Figure **6-20** shows comparisons of HFR profiles at 0.7V and 25 psig for the four humidity conditions and two cell temperatures. In general, the lower input water, the higher resistance, despite more scatter with the dry cathode case of A/C RH=50/0. The general pattern is basically same as the old cell, although there are some differences due to changes of temperature boundary condition and flow field configureations.

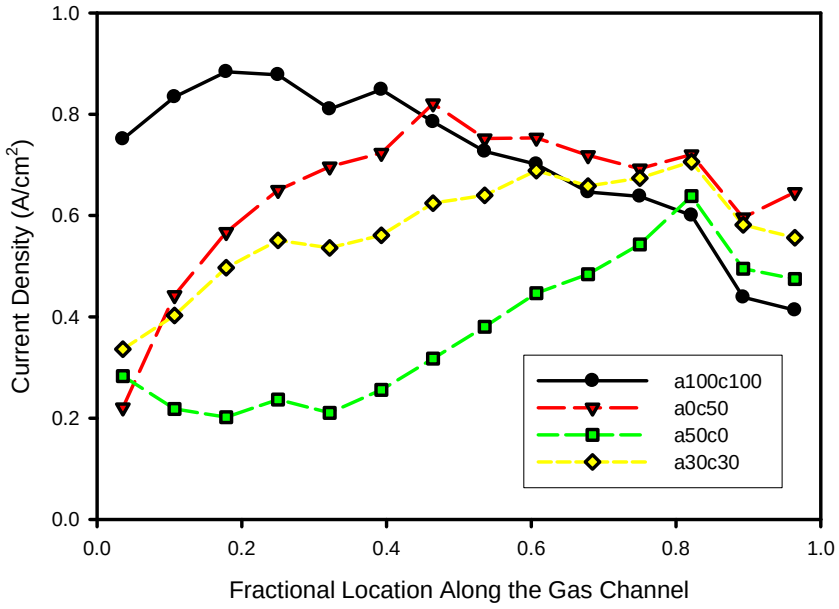

(a) T_{cell}=95°C

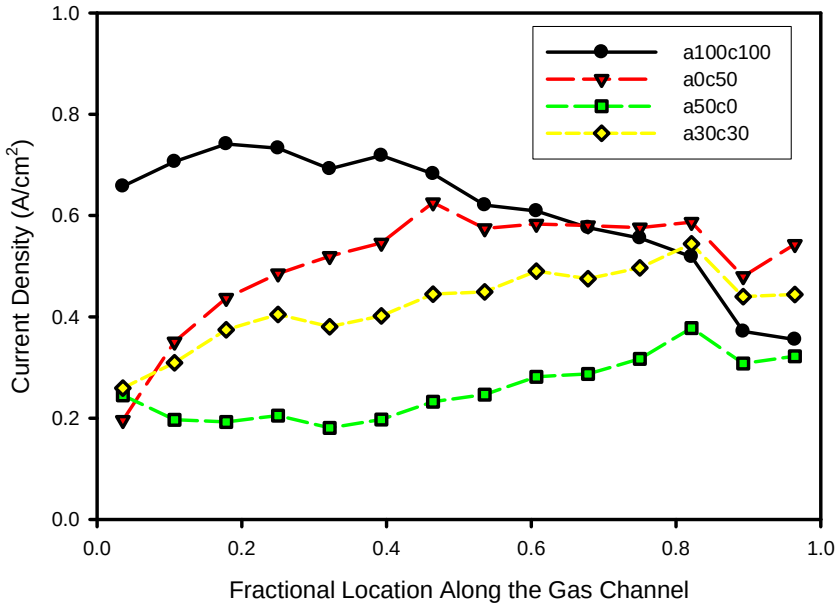

(b) T_{cell}=110°C

Figure **6-19**: Comparison of distributed steady-state current density at 0.7Vand 25 psig for different humidity conditions at two cell temperatures.

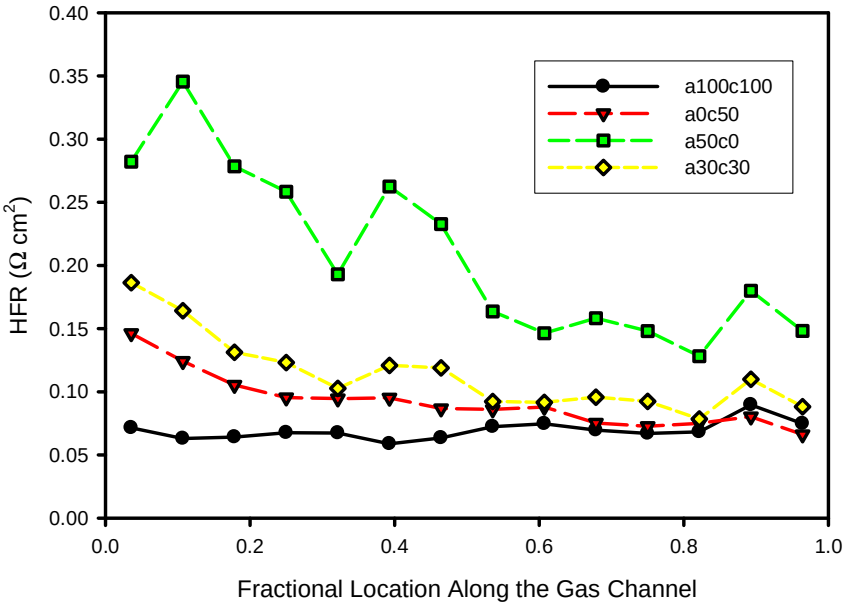

(a) T_{cell}=95°C

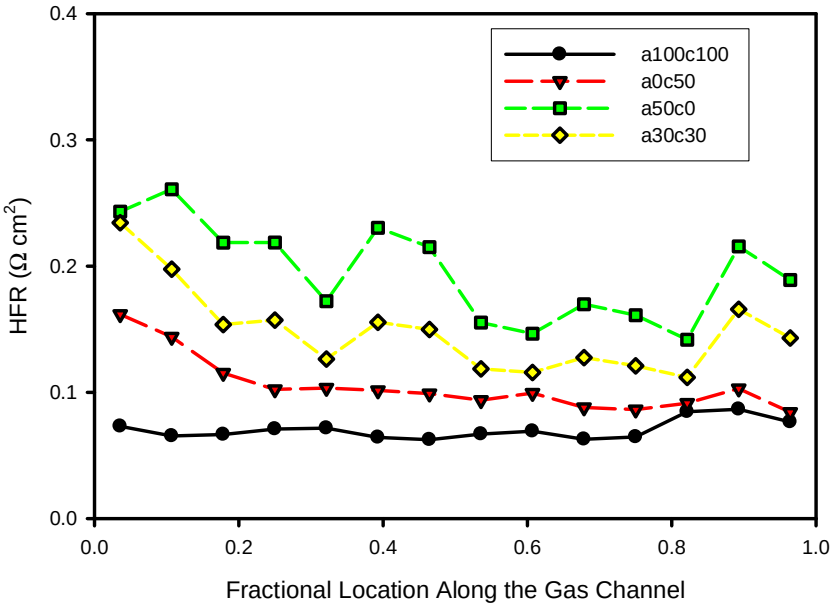

(b) T_{cell}=110°C

Figure **6-20**: Comparison of distributed steady-state high frequency resistance (HFR) at 0.7V, pressure = 25 psig

6.3.4 Effect of pressure on low humidity operation

Steady-state distributed performances of PEFCs under lower back pressure were measured according to the test conditions listed in Table **6-1** and Table **6-3**. The purpose is to investigate the impact of lower pressure on low humidity operations of PEFCs because lower pressure means less cost and less parasitic power consumption by gas compressor.

Figure **6-21** shows the distributed steady-state current for the dry cathode condition with 7.5 psig pressure. Different from the 25 psig case, the current density profile doesn't show the strong increase following the local minimum, just a relative flat and overall low profile, especially for 110°C. The low current density along the whole flow channel is due to low humidity in gas flow channel as well as insufficient water activity gradient across the gas diffusion media because of the low through-plain water flux. Figure **6-22** shows the steady-state current distribution for the dry anode condition with 7.5 psig pressure. The current density profile is qualitatively similar to the profile of 25 psig, although the overall performance is reduced due to weakened humidification by water generation and lower oxygen concentration. Figure **6-23** shows the steady-state current distribution for the partially humidified anode and cathode condition with the lower pressure. Again, the current density profile is similar to the profile of 25 psig, except much lower current density due to worse self-humidification and lower oxygen concentration.

Basically, the impact of lower pressure on low humidity operation is very similar to the effect of higher fuel cell temperature. Both of them can dramatically increase the water saturation limit of anode and cathode gaseous mixtures, and then reduce the humidifying effect of by water generation. Similar to high temperature, low cell operating pressure also reduces the oxygen concentration in cathode by reduced oxygen mole fraction and decreased overall concentration of gaseous mixture.

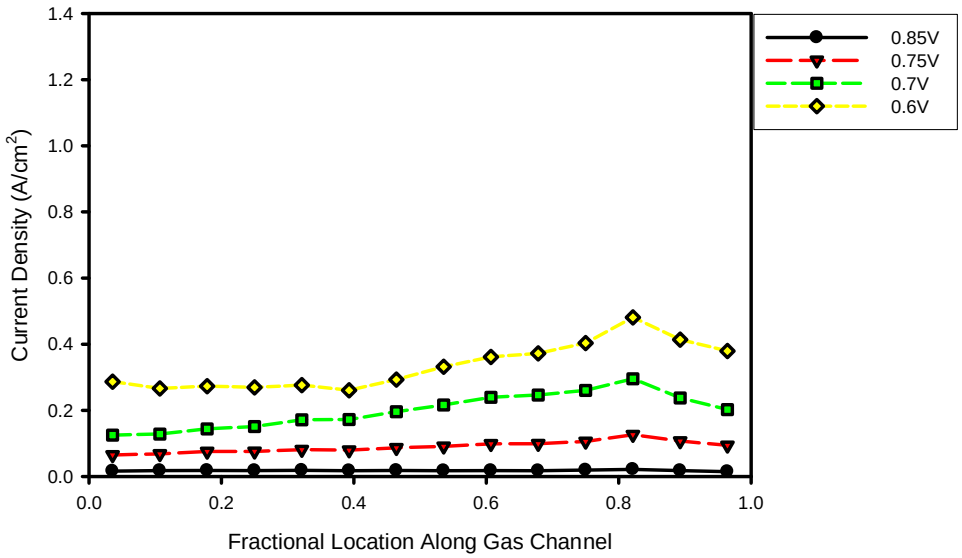

(a) T_{cell}=95°C

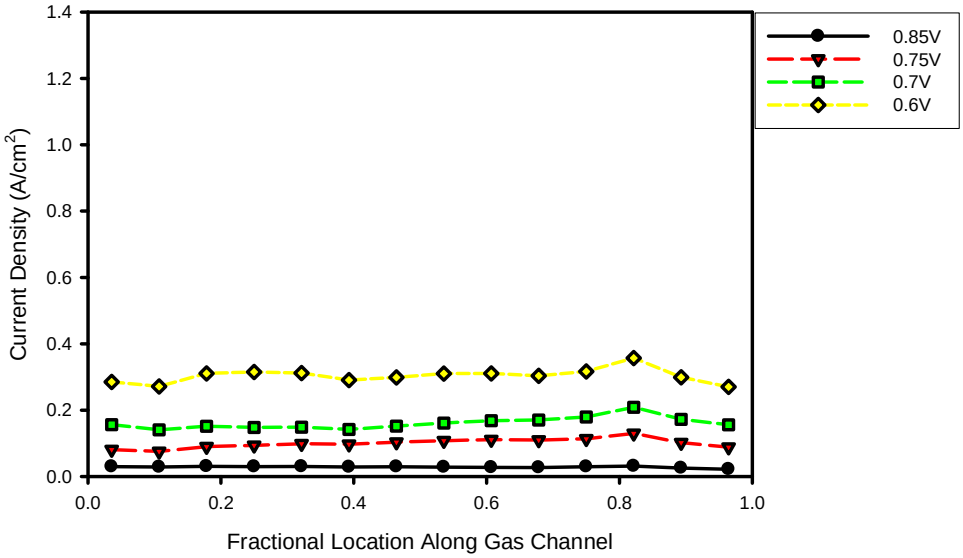

(b) T_{cell}=110°C

Figure **6-21**: Distributed steady-state current density of A/C RH = 50/0, pressure = 7.5 psig

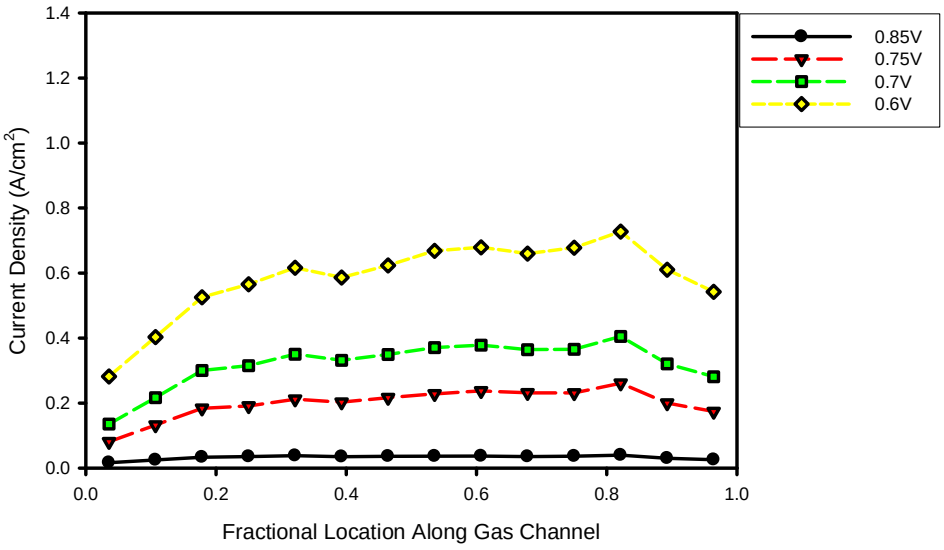

(a) T_{cell}=95°C

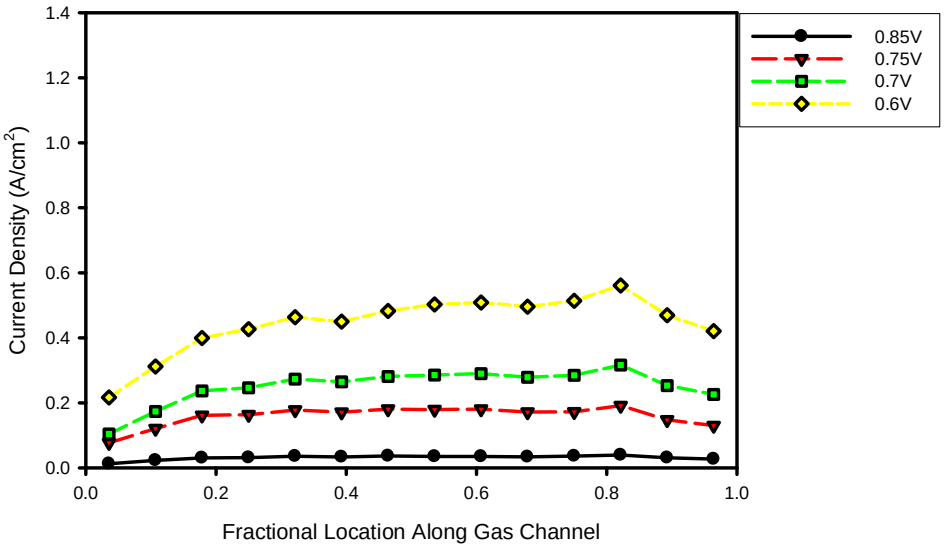

(b) T_{cell}=110°C

Figure **6-22**: Distributed steady-state current density of A/C RH = 0/50, pressure = 7.5 psig

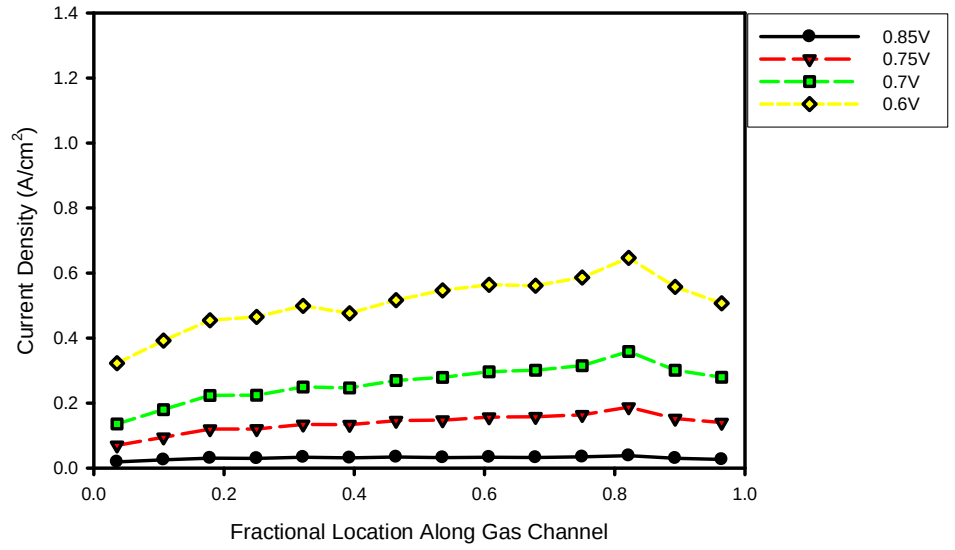

(a) T_{cell}=95°C

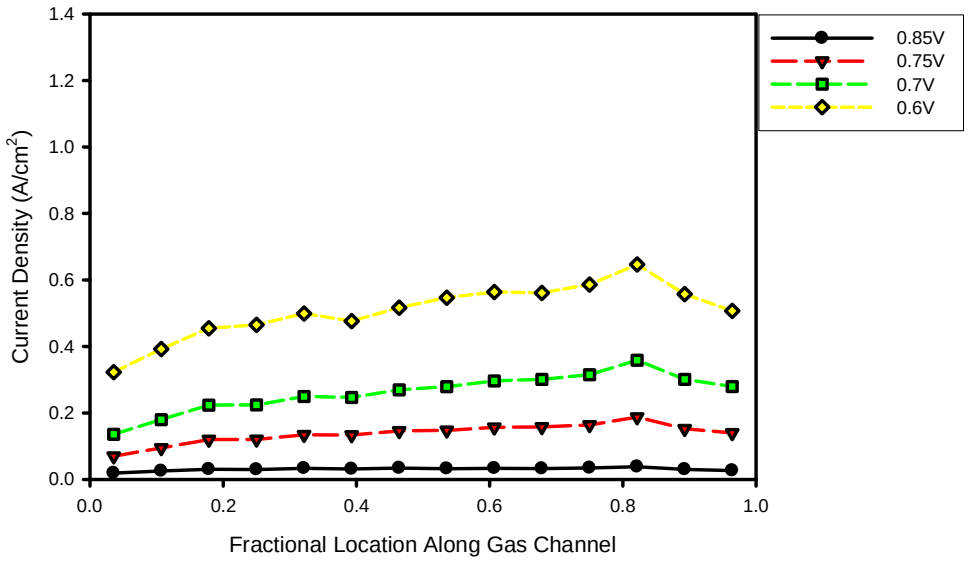

(b) T_{cell}=110°C

Figure **6-23**: Distributed steady-state current density of A/C RH = 30/30, pressure = 7.5 psig

6.3.5 Overall water mass balance check

Since the local current distribution is known along the gas flow channel, and inlet relative humidity is well-calibrated and steady, the expected total water mass at each location can be calculated and compared with measured value to check the accuracy of RTGA measurement. Steady-state flow and heat transfer, single phase (no liquid water accumulation/depletion), and ideal gas mixture are assumed.

According to the conservation of total water mass, at a given location *x* along the gas flow channel, the sum of measured anode and cathode water should equal to the sum of input water and the total produced water before this location, as described by Equation **6.1**:

$$\dot{n}_{H_2O,an,in} + \dot{n}_{H_2O,ca,in} + \dot{n}_{H_2O,gen,x} = \dot{n}_{H_2O,an,x} + \dot{n}_{H_2O,ca,x} \qquad [\mathbf{6.1}]$$

where $\dot{n}_{H_2O,an,in}$ is water molar flow rate at the anode inlet, $\dot{n}_{H_2O,ca,in}$ is water molar flow rate at the cathode inlet, $\dot{n}_{H_2O,gen,x}$ is the total molar water generation rate before location *x*, $\dot{n}_{H_2O,an,x}$ is the measured anode water molar flow rate at location *x*, and $\dot{n}_{H_2O,ca,x}$ is the measured cathode water molar flow rate at location *x*. To evaluate the accuracy of species measurement technique, a normalized water measurement error is introduced and defined as:

$$Err_{H_2O,x} = \left(\frac{\dot{n}_{H_2O,an,x} + \dot{n}_{H_2O,ca,x}}{\dot{n}_{H_2O,an,in} + \dot{n}_{H_2O,ca,in} + \dot{n}_{H_2O,gen,x}} - 1 \right) \times 100\% \qquad [\mathbf{6.2}]$$

If the value of the normalized measurement error is greater than zero, the amount of measured water by RTGA is higher than the amount of actual water. If the value of the normalized error is less than zero, the amount of measured water is lower than the amount of actual water.

The water molar flow rates contained in Equation **6.1** can be calculated from dry gas molar flow rates and measured mole fractions at gas inlets and location. The dry gas flow rates are determined by mass flow controller installed in the gas supply pipeline before the humidifier. Then the equation for water molar flow rate at anode inlet is

$$\dot{n}_{H_2O,an,in} = \dot{n}_{H_2,an,in} \times \frac{y_{H_2O,an,in}}{y_{H_2,an,in}} \qquad [\mathbf{6.3}]$$

where $\dot{n}_{H_2,an,in}$ is the hydrogen molar flow rate, $y_{H_2O,an,in}$ and $y_{H_2,an,in}$ are water vapor and hydrogen mole fractions at anode inlet determined by RTGA.

Equation **6.4** shows the method to calculate cathode inlet water molar flow rate:

$$\dot{n}_{H_2O,ca,in} = \dot{n}_{N_2,ca,in} \times \frac{y_{H_2O,ca,in}}{y_{N_2,an,in}} \qquad [\mathbf{6.4}]$$

Nitrogen is used as a reference for cathode side because it is an inert component and is not consumed in fuel cell. Here, $\dot{n}_{N_2,ca,in}$ is nitrogen molar flow rate calculated from the molar flow rate of air and 0.79 mole fraction of nitrogen. $y_{H_2O,ca,in}$ and $y_{N_2,an,in}$ are mole fractions of water vapor and nitrogen measured by RTGA at the cathode gas inlet.

Equation **6.5** is the equation for calculating the total water generation rate from gas inlet to location *x*:

$$\dot{n}_{H_2O,gen,x} = \frac{A}{2F}\int_0^{x/L} i d(z/L) \qquad [\mathbf{6.5}]$$

where i is a polynomial approximation of local current density as a function of fractional location along the gas channel, A is the total active area of the MEA.

Equation **6.6** shows the method for calculating the measured anode water molar flow rate at location *x*. Hydrogen is used as a reference. $y_{H_2O,an,x}$ and $y_{H_2,an,x}$ are the water vapor and hydrogen mole fractions measured by RTGA at location *x*.

$$\dot{n}_{H_2O,an,x} = \left(\dot{n}_{H_2,an,in} - \frac{A}{2F}\int_0^{x/L} i d(z/L)\right) \times \frac{y_{H_2O,an,x}}{y_{H_2,an,x}} \qquad [\mathbf{6.6}]$$

Equation **6.7** are the equation for calculating the measured cathode water molar flow rate at location *x*. Nitrogen is used as a reference. $y_{H_2O,ca,x}$ and $y_{N_2,an,x}$ are the water vapor and nitrogen mole fractions measured by RTGA at location *x*.

$$\dot{n}_{H_2O,ca,x} = \dot{n}_{N_2,ca,x} \times \frac{y_{H_2O,ca,x}}{y_{N_2,an,x}} \qquad [\mathbf{6.7}]$$

Figure **6-24** shows the normalized water measurement errors for the three inlet humidity conditions and two cell temperatures at 25 psig. For most conditions, the normalized water measurement errors along the gas flow channel are less than 10%. For the case of A/C RH=50/0 at 95°C, the error is a bit higher, but still less than 15%. These small errors indicate that the RTGA technique has good accuracy for PEFC species transport study.

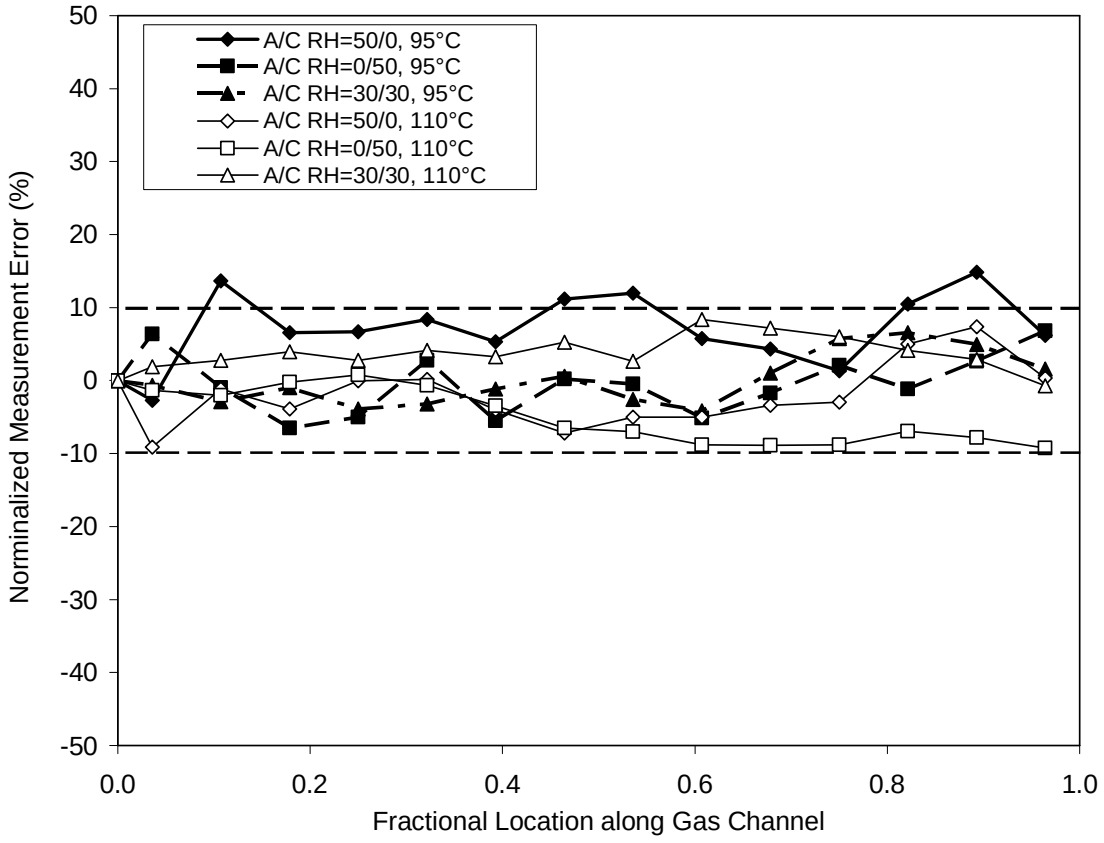

Figure **6-24**: Normalized water measurement error along the gas flow channel. Cell pressure= 25 psig,

6.3.6 Distribution of water effective drag coefficient

The water balance check verifies the accuracy of RTGA technique on species measurement as well as indirectly proves the overall dependability of the whole test setup. Based on the measured steady-state current density distribution and species distribution, the water effective drag coefficient (or net drag coefficient) can be calculated along the gas channel. Although both the anode and cathode species distribution data can be used for the calculation, anode data is used because there are only two major components in the anode, so the calculation is a bit simpler.

Due to the diffusion of water across the membrane driven by water activity gradient and electro-osmotic drag from anode to cathode driven by proton current, the molar flow rate of water vapor in anode gas flow channel changes as moist hydrogen flows through the fuel cell. Because the anode and cathode are always maintained the same pressure, the water permeation driven by pressure difference is neglected here. At a given location *x* from the gas inlet, according to the water balance of the anode, the local anode water molar flow rate can be expressed as:

$$\dot{n}_{H_2O,an,x} = \dot{n}_{H_2O,an,in} - \dot{n}_{H_2O,drag,x} \qquad [\mathbf{6.8}]$$

where $\dot{n}_{H_2O,drag,x}$ is the total net water molar flow rate from anode to the cathode before location *x*, in other words, the combination of water diffusion and electro-osmotic drag. And the term has the following relation with the total accumulative current from the gas inlet to location *x*:

$$\dot{n}_{H_2O,drag,x} = \frac{A}{F}\int_0^{x/L} \alpha i d(z/L) \qquad [\mathbf{6.9}]$$

Where α is so called effective drag coefficient.

Substituting Equation **6.6** and Equation **6.9** into Equation **6.8** gives

$$\left(\dot{n}_{H_2,an,in} - \frac{A}{2F}\int_0^{x/L} i d(z/L)\right) \times \frac{y_{H_2O,an,x}}{y_{H_2,an,x}} = \dot{n}_{H_2O,an,in} - \frac{A}{F}\int_0^{x/L} \alpha i d(z/L) \qquad [\mathbf{6.10}]$$

Because both α and i depend on x, it is difficult to get an analytical expression for α even with simplified polynomial approximations of current density and species. To further simplify the calculation, α is assumed constant over the whole length between two species sampling ports. Thus, the effective drag coefficient at the *Nth* segment is

$$\alpha_N = \frac{\lambda_{H_2O,an,x_{N-1}} - \lambda_{H_2O,an,x_N}}{\frac{A}{FL}\int_{x_{N-1}/L}^{x_N/L} id(z/L)} \qquad [\mathbf{6.11}]$$

Figure **6-25** shows the effective drag coefficient distributions for the three inlet humidity conditions at 95°C and 25 psig. For the dry cathode condition of A/C RH=50/0, in the upstream 40% region of the fuel cell, the effective drag coefficient is positive, representing net water flux towards the cathode by both diffusion and electro-osmotic drag. At the middle of the gas flow channel, the coefficient becomes negative, representing water flux reversal from the cathode to the anode. At 75% and 82% fractional locations along the gas flow channel, the values of the coefficient are very close to zero, meaning the back-diffusion and electro-osmotic drag reaches a rough balance and the water activity difference between the anode and cathode is not significant. Due to the small anode stoichiometry of 1.2, the consumption of hydrogen significantly reduces the amount of water that the anode stream can carry, so small positive values (~0.3) of the coefficient are observed in the outlet region. The overall effective drag coefficient of 0.231 means the overall water flux is from the anode to the cathode. For the dry anode condition of A/C RH=0/50, the very negative value at the 1st location (x/L=3.57%) suggests strong back-diffusion from the cathode to the anode due to the very different anode and cathode water activity. Then the absolute value of the coefficient decreases dramatically due to the rapidly decreasing water activity gradient across the membrane. At the middle of the gas channel, the coefficient values are close to zero, representing a rough balance of back-diffusion and electro-osmotic drag. Similar to the dry cathode condition, positive values of the coefficient (around 1.0) near the outlet is a result of high hydrogen consumption. Because the anode is initially dry, the overall effective drag coefficient has a small negative value of -0.116. For the partially humidified anode and cathode condition of A/C RH=30/30, the coefficient is a small

positive number at the inlet, meaning water is transported from anode to cathode by electro-osmotic drag, but the drag is almost evenly balanced by back-diffusion from the cathode. At middle of the gas channel, the coefficient values are negative with scatter, but are believed to be greater than -0.5, representing anode gets water from cathode due to water production, also meaning back-diffusion exceeds the electro-osmotic drag. Again, positive values of the coefficient near the outlet are observed as a result of hydrogen consumption. The small positive value of 0.090 of the overall effective drag coefficient means the anode losses water to the cathode by electro-osmotic drag, but most of the loss is compensated by water back-diffusion from the cathode.

Figure **6-26** is the effective drag coefficient distributions for the three inlet humidity conditions at 110°C and 25 psig. All three effective drag coefficient profiles are very similar to the respective profiles at 95°C.

Figure **6-27** compares the overall effective drag coefficients for three inlet humidity conditions and two cell temperatures. With the same inlet relative humidity, the overall coefficient has the same sign no matter what the cell temperature is. In other words, the cell temperature does not change the direction of net water transport. However, the overall coefficient for higher temperature has higher absolute value, mainly due to the higher water saturation limit and concomitantly higher diffusion gradients. Higher water diffusion coefficients in the electrolyte membrane and in the anode and cathode gas mixtures at higher temperature also contribute to this difference of overall effective drag coefficient.

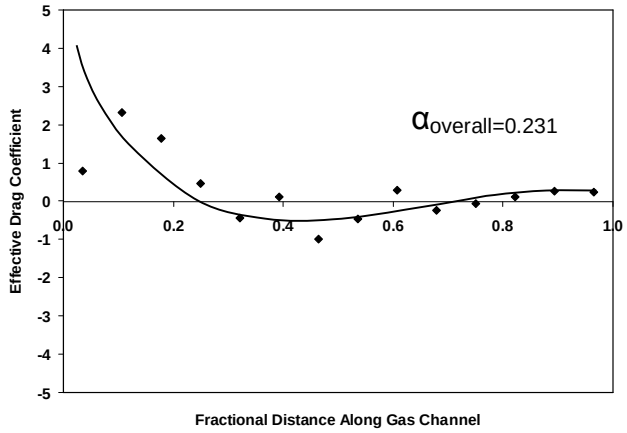

(a) A/C RH=50/0

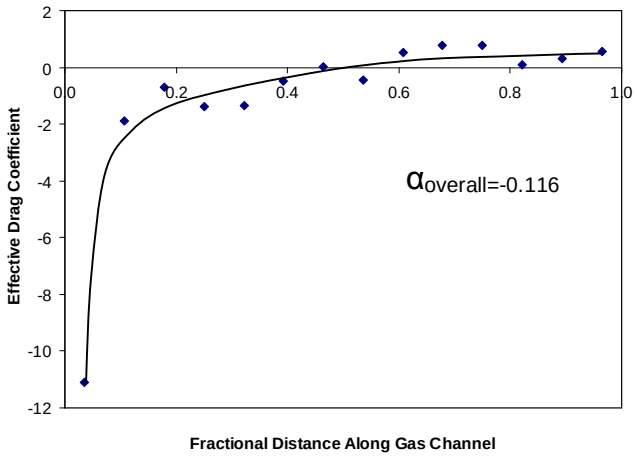

(b) A/C RH=0/50

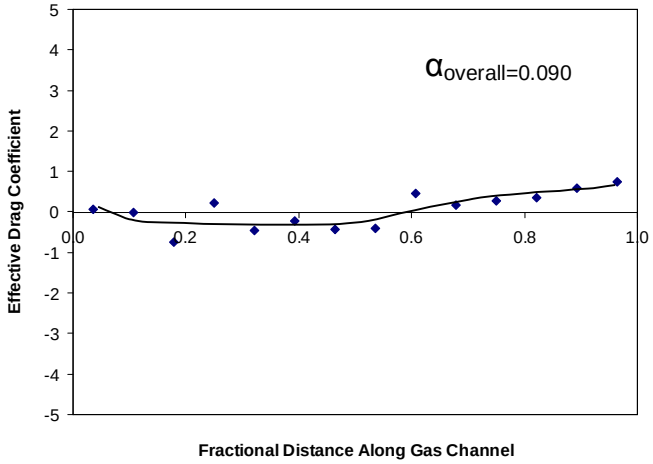

(c) A/C RH=30/30

Figure **6-25**: Effective drag coefficient distributions along the gas flow channel at 0.7V, T_{cell}=95°C, Pressure=25 psig.

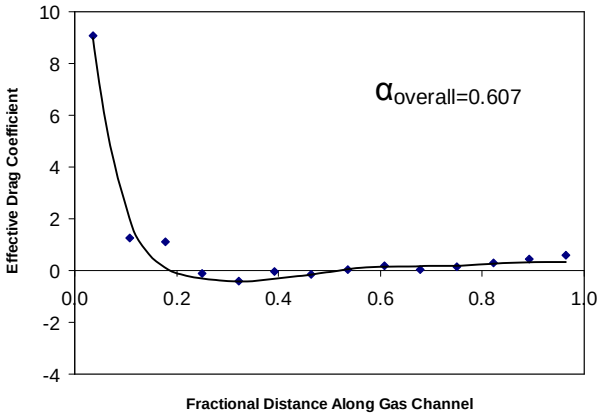

(a) A/C RH=50/0

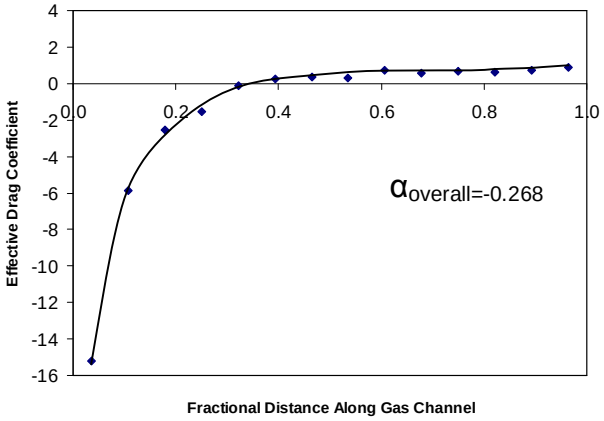

(b) A/C RH=0/50

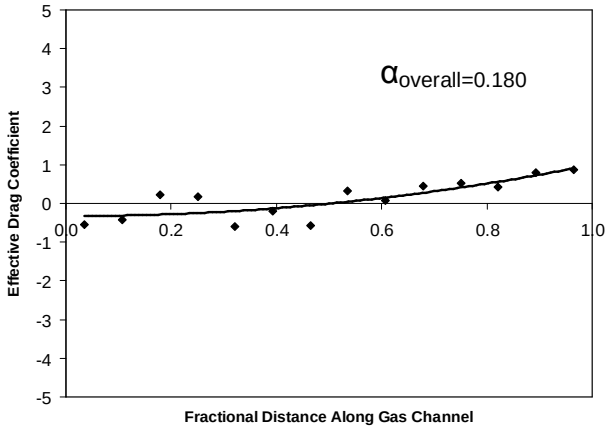

(c) A/C RH=30/30

Figure **6-26**: Effective drag coefficient distribution along the gas flow channel at 0.7V, T_{cell}=110°C, Pressure=25 psig.

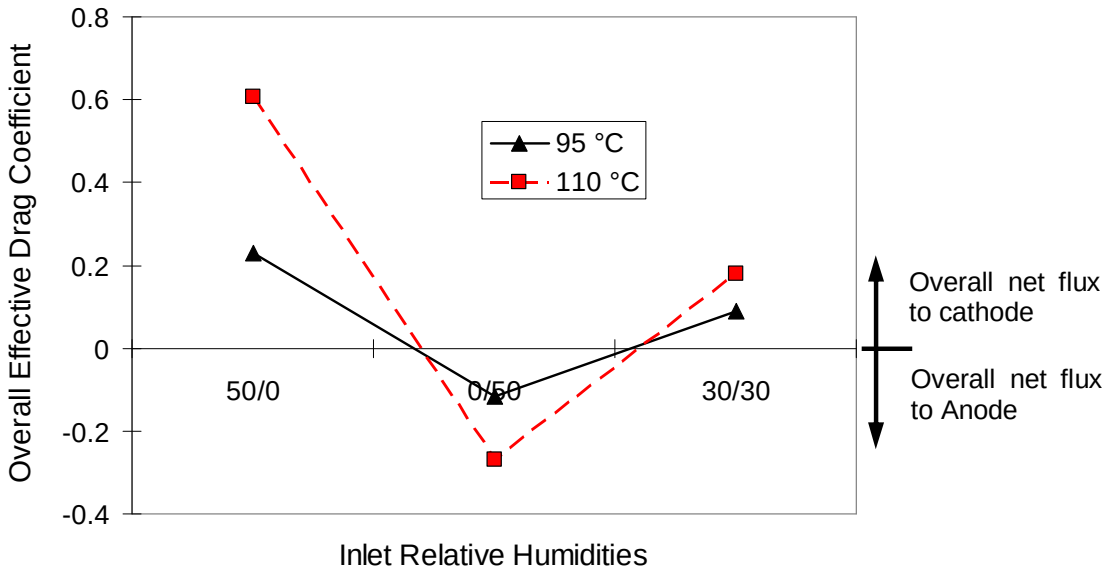

Figure **6-27**: Comparison of overall effective drag coefficient for three inlet relative humidities and two cell temperatures.

6.4 Summary

A new instrumented fuel cell with five-channel serpentine co-flow flow field configurations and isothermal boundary condition was applied to investigate the distributed performances of PEFCs including current density, species, and HFR with an emphasis on the impacts of elevated temperature. The influence of operating pressure was also investigated by current density and HFR distributions measurements. With improved flow field configurations and boundary conditions, the cell achieved comparable performance with un-segmented fuel cell and can provide more suitable validating data for the development of advanced PEFC models.

Previous results were confirmed at higher temperatures. There is a diffusion reversal for low cathode relative humidity. In general, the greater the average water content, the better the overall cell performance, although local performance still follows

the anode moisture profile. However, for the combination of high cell temperature and low pressure, the cell performance under high humidity conditions is limited by lack of oxygen and higher humidity has negative impact on cell performance.

With ultra purity hydrogen and commercial air as feeding reactants to the fuel cell, test results indicates that increased operating temperature >80°C results in lower fuel cell performance although the dominating mechanisms are different according the inlet humidity. For fully humidified condition, this decrease of performance is mainly resulted from the lower oxygen concentration in the cathode primarily due to dilution of water vapor, and lower operating pressure can greatly exaggerate the dilution effect. For low humidity conditions, the higher temperature affects the lower average relative humidity due to greatly increased water saturation limit. Due to sensitivity of water boiling point to pressure, it is difficult to achieve good performance at both high temperature and low pressure with Perfluorosulfonic acid (PFSA) based membranes which require good humidification to get high proton conductivity. A key to future high temperature MEAs is the tolerant to low water content or has to operate under elevated pressure.

Evaluated by the overall water balance, the accuracy of the whole test technique for current and species distribution measurements is verified. For all conditions, the normalized water measurement error is less than 15%, and almost always less than 10%. This high accuracy meets the requirements for deduction of the water diffusion coefficient in the membrane.

Based on the current and species distribution data, the effective drag coefficient was calculated and shown along the gas flow channel. The overall effective drag coefficients for higher temperature are amplified compared to lower temperatures, mainly due to the higher water saturation limit and concomitantly higher diffusion gradient in gas phase. Higher water diffusion coefficients in the membrane and gaseous mixtures at higher temperatures also contribute to this difference.

Chapter 7

Model of Water Transport and Determination of Diffusion Coefficient for Reinforced Polymer Electrolyte Membranes Operating in Low Humidity Environment

7.1 Introduction

Gore PRIMEA® series #57 MEA is a specially developed MEA by W. L. Gore and Associates, Inc. for low humidity operation, which is highly preferred by automotive applications. Unlike pure Nafion® membranes, the Gore SELECT® electrolyte membrane used in the MEA is a microscopically reinforced composite membrane. Due to the reinforcement matrix, the membrane can be much thinner than an un-reinforced membrane, while maintaining good mechanical strength. However, also due to the reinforcement, the water diffusivity and other transport properties in the membrane could be quite different from un-reinforced membranes. In the three-dimensional non-isothermal PEFC model reported by Ju and Wang [**75**][**76**], the water diffusivity in Gore SELECT® membrane was assumed to be approximately half of the value of an un-reinforced Nafion® membrane.

Based on the measured species distributions and respective current distributions shown in Chapter 6, a quasi-two-dimensional, steady-state mass transport model is developed to examine transport and fit the diffusion coefficient of water in Gore PRIMEA® series#57 MEA. The model is formulated in a two-dimensional slice manner along the gas flow channel from the inlet to the outlet. Due to the high aspect ratio of the MEA, local transport phenomena are considered in the through-the-plane direction only, and then coupled together through the flow channel model.

7.2 Model region and assumptions

Table **7-1** shows the dimensions and operational parameters of the fuel cell and thicknesses of the MEA components acquired from W. L. Gore. Compared to the ultra thin 18 μm thickness of the reinforced membrane, the thicknesses of the catalyst layer and MPLs are in the same order and the thickness of the GDL is 15.7 times thicker, so they may affect the mass transport significantly. The current and species distribution measurements shown in Chapter 6 suggest the existence of a considerable water activity difference between the cathode catalyst layer and the cathode gas flow channel, which contributes to the decreasing current profile in the inlet region of a dry cathode condition, and also the higher anode water content in the downstream region of the fuel cell. So it is necessary to account for the porous gas diffusion media in the mass transport model.

Table **7-1**: Fuel cell design and operational parameters

Description	Value
Gas diffusion layer thickness, δ_{GDL}	0.3 mm
Micro porous layer thickness, δ_{MPL}	0.06 mm
Catalyst layer thickness, δ_{CL}	0.01 mm
Reinforced electrolyte membrane thickness, δ_{re}	0.018 mm
Membrane width (segment width), w	1.01 cm
Gas flow channel length, L	51.5 cm
Membrane Area, A	50 cm^2
Anode/cathode pressure, P	2.7 atm
Fuel cell voltage, V_{cell}	0.7 V
Anode/cathode Stoichiometies, ξ_A/ξ_C	1.2/2.0
Fuel cell temperature, T	95 and 110 ˚C
Anode/cathode nominal inlet humidification conditions, RH	50/0, 30/30, 0/50

Figure **7-1** shows the modeling domain, which consists of two GDLs, two MPLs, two catalyst layers, and one reinforced electrolyte membrane. The flow field has a five-channel serpentine and co-flow design.

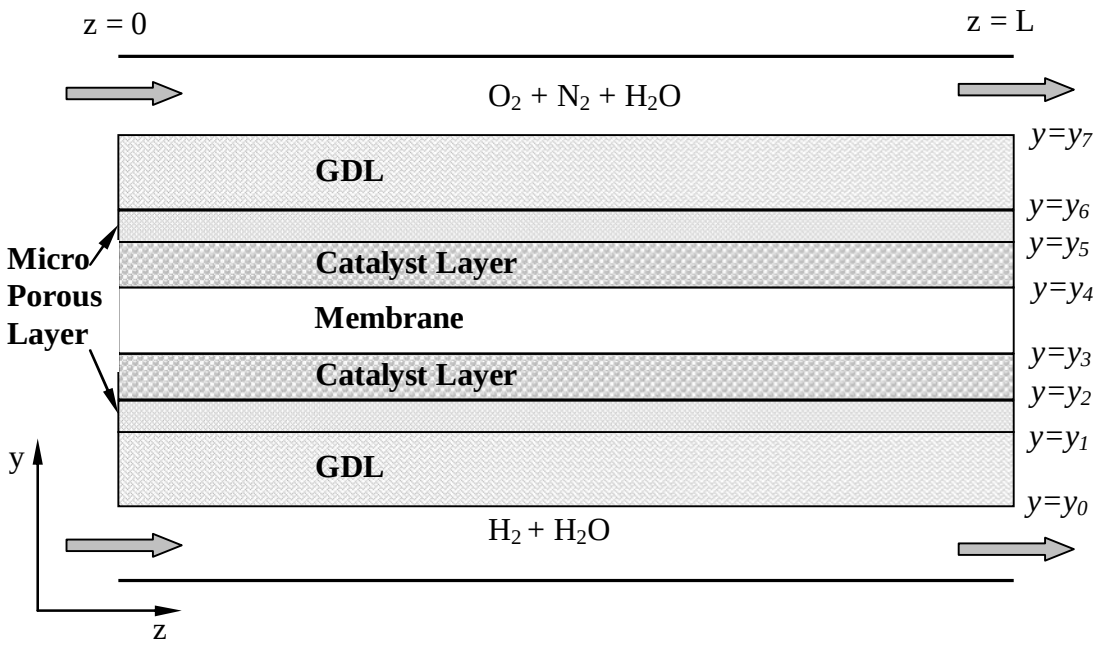

Figure **7-1**: Schematic of the modeling domain.

The main assumptions and simplifications of the model are summarized below:

1) The humidified anode and cathode gas mixtures obey the ideal gas law.
2) Minor compositions in air such as argon and CO_2 are negligible, and air is assumed to contain only oxygen and nitrogen at a mole ratio of 0.21/0.79.
3) Total pressure throughout the flow channel, gas diffusion media and catalyst layer is uniform; only concentration gradients are considered.
4) The gases in the anode and cathode flow channels are well mixed in through-the-plane direction, and the diffusion in *z* direction is negligible compared to convection.
5) Temperature throughout the fuel cell is assumed to be uniform and constant.
6) Single phase flow is assumed, there is no liquid water transport in the cell. This assumption is valid because all the test conditions for species distribution measurements are low humidity conditions, and the respective

bulk outlet relative humidities are all lower than 100%, as shown in Table **6-2**.

7) Current is evenly generated over the thickness of the catalyst layer.
8) Crossover of hydrogen and oxygen in the electrolyte membrane is negligible.

7.3 Model Equations

Inlet conditions

Based on the overall material balance of hydrogen and oxygen through the fuel cell, the inlet mole flow rates for species can be expressed by current density and stoichoimetry as

$$N_H^{in} = \xi_A \frac{w\int_0^L i dz}{2F};\ N_{W,A}^{in} = N_H^{in} \frac{x_{W,A}^{in}}{x_H^{in}} \qquad [\mathbf{7.1}]$$

$$N_O^{in} = \xi_C \frac{w\int_0^L i dz}{4F};\ N_{W,C}^{in} = N_O^{in} \frac{x_{W,C}^{in}}{x_O^{in}};\ N_N^{in} = N_O^{in} \frac{x_N^{in}}{x_O^{in}} \qquad [\mathbf{7.2}]$$

where N_H^{in}, N_O^{in}, and N_N^{in}, are the inlet mole flow rate of hydrogen, oxygen, and nitrogen; $N_{W,A}^{in}$ and $N_{W,C}^{in}$ are the inlet water mole flow rates for the anode and cathode; ξ_A and ξ_C are the anode and cathode stoichiometries; x_H^{in}, $x_{W,A}^{in}$, x_O^{in}, $x_{W,C}^{in}$, and x_N^{in} are the mole fractions for species at the inlets; $i(z)$ is the current density along the flow channel; and w is the width of the membrane.

Material balances for species in the flow channel

Under steady state, the storage rates of species in the GDL and micro-porous layer are zero. So the molar flux of oxygen and water vapor in the GDL and micro-porous layer flow channel are equal to their respective rates of consumption or generation on the

catalyst layer, and the molar flux of nitrogen is always zero. Then the differential mole balances for the three species in the cathode flow channel are

$$\frac{dN_O}{dz} = -w\frac{i}{4F} \quad [\mathbf{7.3}]$$

$$\frac{dN_{W,C}}{dz} = w\left(\frac{i}{2F} + \frac{\alpha i}{F}\right) \quad [\mathbf{7.4}]$$

$$\frac{dN_N}{dz} = 0 \quad [\mathbf{7.5}]$$

where N_O, $N_{W,C}$, and N_N are the respective mole flow rates for oxygen, water vapor and nitrogen in the cathode flow channel, and α is the effective water drag coefficient, which is unknown and needs to be determined. The mole fractions for three species in the cathode flow channel can be expressed in the local molar flow rates as

$$x_O = \frac{N_O}{N_O + N_{W,C} + N_N} \quad [\mathbf{7.6}]$$

$$x_{W,C} = \frac{N_{W,C}}{N_O + N_{W,C} + N_N} \quad [\mathbf{7.7}]$$

$$x_N = 1 - x_O - x_{W,C} \quad [\mathbf{7.8}]$$

Similar to the cathode, under steady state, the differential mole balance of hydrogen and water vapor in the anode flow channel are

$$\frac{dN_H}{dz} = -w\frac{i}{2F} \quad [\mathbf{7.9}]$$

$$\frac{dN_{W,A}}{dz} = -w\left(\frac{\alpha i}{F}\right) \quad [\mathbf{7.10}]$$

where N_H and $N_{W,A}$ are the respective molar flow rate of hydrogen and water vapor in the anode flow channel. The mole fractions of hydrogen and water vapor in the anode flow channel are

$$x_H = \frac{N_H}{N_H + N_{W,A}} \quad [\mathbf{7.11}]$$

$$x_{W,A} = 1 - x_H \quad [\mathbf{7.12}]$$

Gas diffusion in the GDL and micro-porous layer

As stated in assumption 1, the anode and cathode gas mixtures including water vapor are assumed ideal gases. According to the Stefan-Maxwell equation[1] for multi-component diffusion in ideal gases, the gradients of mole fractions of the components in GDL expressed in the mole fractions and total mole fluxes are

$$\frac{dx_i}{dy} = \frac{1}{C}\sum_{j \neq i} \frac{x_i n_j - x_j n_i}{D_{ij,GDL}^{eff}} \quad [\mathbf{7.13}]$$

where C is the total molar concentration of the gas mixtures, which can be determined by the fuel cell internal pressure and temperature based on the ideal gas law

$$C = \frac{P}{RT} \quad [\mathbf{7.14}]$$

The n terms are molar flux of components. $D_{ij,GDL}^{eff}$ is the effective binary diffusion coefficient of gas species in porous medium to account for the effects of porosity and tortuosity as follows

$$D_{ij,GDL}^{eff} = \frac{\varepsilon_{GDL}}{\tau_{GDL}} D_{ij} \quad [\mathbf{7.15}]$$

where ε_{GDL} and τ_{GDL} are the porosity and tortuosity of the GDL respectively. The binary diffusion coefficients D_{ij} for gaseous species are calculated from the binary diffusion coefficients under specified temperature and pressure according to the Chapman-Enskog equation [**106**]

$$D_{ij} = D_{ij,0}\left(\frac{T}{T_0}\right)^{3/2}\left(\frac{P_0}{P}\right) \quad [\mathbf{7.16}]$$

From Equation **7.13**, we get following equations for the gradients for oxygen and water vapor mole fractions in the cathode GDL

$$\frac{dx_O}{dy} = \frac{RT}{P}\left(\frac{x_O n_W - x_W n_O}{D^{eff}_{WO,GDL}} + \frac{x_O n_N - x_N n_O}{D^{eff}_{ON,GDL}} \right) \quad [\mathbf{7.17}]$$

$$\frac{dx_W}{dy} = \frac{RT}{P}\left(\frac{x_W n_O - x_O n_W}{D^{eff}_{WO,GDL}} + \frac{x_W n_N - x_N n_W}{D^{eff}_{WN,GDL}} \right) \quad [\mathbf{7.18}]$$

Under steady state, the cathode species molar fluxes in GDL have the following relations with local current density i and the total water molar flux across the membrane

$$n_O = -\frac{i}{4F};\ n_W = \frac{i}{2F} + \frac{\alpha i}{F};\ n_N = 0 \quad [\mathbf{7.19}]$$

Then the gradients for oxygen and water vapor mole fractions become

$$\frac{dx_O}{dy} = \frac{RT}{P}\frac{i}{4F}\left[\frac{x_O(2+4\alpha) + x_W}{D^{eff}_{WO,GDL}} + \frac{1 - x_O - x_W}{D^{eff}_{ON,GDL}} \right] \quad [\mathbf{7.20}]$$

$$\frac{dx_W}{dy} = \frac{RT}{P}\frac{i}{4F}\left[-\frac{x_O(2+4\alpha) + x_W}{D^{eff}_{WO,GDL}} - \frac{(1 - x_O - x_W)(2+4\alpha)}{D^{eff}_{WN,GDL}} \right] \quad [\mathbf{7.21}]$$

Also based on Equation **7.13**, the gradient for water vapor in anode GDL is

$$\frac{dx_W}{dy} = \frac{RT}{P}\left(\frac{x_W n_H - x_H n_W}{D^{eff}_{WH,GDL}} \right) \quad [\mathbf{7.22}]$$

And the molar flux for hydrogen and water expressed in current density are

$$n_H = \frac{i}{2F};\ n_W = \frac{\alpha i}{F} \quad [\mathbf{7.23}]$$

Substituting Equation **7.20** into Equation **7.19** yields

$$\frac{dx_W}{dy} = \frac{RT}{P}\frac{i}{2F}\left[\frac{x_W - 2\alpha(1 - x_W)}{D^{eff}_{WH,GDL}} \right] \quad [\mathbf{7.24}]$$

The governing differential equations for the mole fractions of species for the MPL region have the similar form to the equations for the GDL region, except the different values of the effective binary diffusion coefficients due to the difference of the porosity.

Mass transport in catalyst layers

Within the catalyst layer, water is transported in both gas and ionomer phases because the catalyst layer itself consists of ionomer, catalyst, carbon support, and pore structure. For the gas phase diffusion of the cathode catalyst layer, we can get the following differential equations for the mole fractions of oxygen and water vapor based on the Stefan-Maxwell equation

$$\frac{dx_O}{dy} = \frac{RT}{P}\left(\frac{x_O n_W^g - x_W n_O}{D_{WO,CL}^{eff}} + \frac{x_O n_N - x_N n_O}{D_{ON,CL}^{eff}} \right) \qquad [\mathbf{7.25a}]$$

$$\frac{dx_W}{dy} = \frac{RT}{P}\left(\frac{x_W n_O - x_O n_W^g}{D_{WO,CL}^{eff}} + \frac{x_W n_N - x_N n_W^g}{D_{WN,CL}^{eff}} \right) \qquad [\mathbf{7.25b}]$$

With the assumption of homogeneous current generation throughout the catalyst layer in *y* direction, the molar flux of oxygen at position *y* can be easily expressed as

$$n_O = -\frac{1}{4F}\frac{i}{\delta_{CL}}(y - y_4) \qquad [\mathbf{7.26}]$$

where y_4 is the location at the membrane surface, as shown in Figure **7-1**. However, the molar flux of water vapor in gas phase needs to be considered together with the water diffusion and electro-osmotic drag in the ionomer phase.

Based on the overall balance of water, the differential governing equation for water transport in the cathode catalyst layer can be described as the following equation.

T
$$\frac{d}{dy}\left(-D_{W,CL}^{m,eff}\frac{dC_W^m}{dy} \right) + \frac{dn_W^g}{dy} + \frac{n_d}{F}\frac{di^m}{dy} = \frac{1}{2F}\frac{i}{\delta_{CL}} \qquad [\mathbf{7.27}]$$

The first term at the left side of the equation represents the water diffusion in the ionomer phase; the second term describes the water transport in the gas phase; and the third term

is the water electro-osmotic drag term for the ionomer phase; and the term at the right side of the equation represents the water generation by cathode electrode reaction. In the equation, n_d is the electro-osmotic drag coefficient; i^m is the proton current density in the ionomer; and C_W^m is the water concentration in the ionomer. $D_{W,CL}^{m,eff}$ is the effective water diffusion coefficient in the ionomer phase and is determined by the following equation

$$D_{W,CL}^{m,eff} = \frac{\varepsilon_{m,CL}}{\tau_{m,CL}} D_W^m \qquad [\mathbf{7.28}]$$

where $\varepsilon_{m,CL}$ and $\tau_{m,CL}$ are the ionomer volume fraction in the catalyst layer and the tortuosity of the ionmer phase; and D_W^m is the water diffusion coefficient in ionmer. Because in the cases studied, the fuel cell is always under low humidity conditions, the value of n_d is assumed to be unity according to the results reported by Zawodzinski *et al.*[**37**] With the assumption of uniform current generation throughout the catalyst layer in *y* direction, the differential proton current density in the ionomer phase is given by the following equation based on the conservation of total proton and electron current

$$\frac{di^m}{dy} = -\frac{i}{\delta_{CL}} \qquad [\mathbf{7.29}]$$

Substituting Equation **7.26** into Equation **7.25** and then integrating the equation from the membrane/catalyst layer interface y_4 to position y yields Equation **7.30**

$$\left(-D_{W,CL}^{m,eff} \frac{dC_W^m}{dy} + n_W^g \right)_y - \left(-D_{W,CL}^{m,eff} \frac{dC_W^m}{dy} + n_W^g \right)_{y_4} = \frac{1}{2F} \frac{(1+2n_d)i}{\delta_{CL}} (y - y_4) \qquad [\mathbf{7.30}]$$

At the cathode interface, water flux by diffusion is the total water flux minus the flux by electro-osmotic drag.

$$\left(-D_{W,CL}^{m,eff} \frac{dC_W^m}{dy} + n_W^g \right)_{y_4} = \frac{(\alpha - n_d)i}{F} \qquad [\mathbf{7.31}]$$

then we obtain the expression for the gas phase water molar flux in the cathode catalyst layer Equation **7.32**

$$n_W^g = \frac{1}{2F}\frac{(1+2n_d)i}{\delta_{CL}}(y-y_4)+\frac{(\alpha-n_d)i}{F}+D_{W,CL}^{m,eff}\frac{dC_W^m}{dy} \qquad [\mathbf{7.32}]$$

Similar to the condition of the cathode catalyst layer, based on the Stefan-Maxwell equation, the differential governing equation for water mole fraction in the gas phase of the anode catalyst layer can be written out as the following equation

$$\frac{dx_W}{dy} = \frac{RT}{P}\left(\frac{x_W n_H - x_H n_W^g}{D_{WH,CL}^{eff}}\right) \qquad [\mathbf{7.33}]$$

With the assumption of uniform current generation throughout the catalyst layer in *y* direction, the molar flux of hydrogen at any point in the anode catalyst layer is Equation **7.34**

$$n_H = \frac{1}{2F}\frac{i}{\delta_{CL}}(y_3-y) \qquad [\mathbf{7.34}]$$

The molar flux of water vapor in gas phase also must be considered together with the water diffusion and electro-osmotic drag in the ionomer phase, as in the cathode.

Based on the overall conservation of water, the differential governing equation for water transport in the anode catalyst layer is given as the following equation.

$$\frac{d}{dy}\left(-D_{W,CL}^{m,eff}\frac{dC_W^m}{dy}\right)+\frac{dn_W^g}{dy}+\frac{n_d}{F}\frac{di^m}{dy}=0 \qquad [\mathbf{7.35}]$$

S

Similar to the governing equation for the cathode catalyst layer, the first term at the left side of the equation represents the water diffusion in the ionomer phase; the second term describes the water transport in the gas phase; and the third term is the water electro-osmotic drag term for the ionomer phase.

Within the anode catalyst layer, the proton current density in the ionomer phase increases as *y* increases

$$\frac{di^m}{dy} = \frac{i}{\delta_{CL}} \qquad [\mathbf{7.36}]$$

Substituting Equation **7.36** into Equation **7.35** and then integrating the equation from position y to the anode side membrane/catalyst layer interface y_3 yields Equation **7.37**

$$n_W^g = \frac{n_d}{F}\frac{i}{\delta_{CL}}(y_3 - y) + \frac{(\alpha - n_d)i}{F} + D_{W,CL}^{m,eff}\frac{dC_W^m}{dy} \qquad [\mathbf{7.37}]$$

To solve the mole fractions for the gas phase species through Equation **7.25** to Equation **7.33**, we need determine the relation between the ionomer water concentration C_W^m and the gas phase water vapor mole fraction x_W. If we neglect the volume change of the ionomer caused by water uptake, C_W^m the water concentration in the ionomer phase can be expressed by the ionomer water content λ as:

$$C_W^m = \frac{\rho_{dry}}{EW}\lambda \qquad [\mathbf{7.38}]$$

where ρ_{dry} is the density of dry ionomer, EW is the equivalent molecular weight of the ionomer material, and the water content λ is defined as the ratio of the number of water molecules to the number of sulfonic acid groups within the ionomer. Water content for Nafion® was investigated by Zawodzinski *et al.* [**18**] as function of water activity by measuring the weight changes of partially hydrated Nafion® 117 membranes equilibrated with water vapors at various activities. They reported following relationship between water content of Nafion® and water vapor activity at 30 °C

$$\lambda = 0.043 + 17.81a_W - 39.85a_W^2 + 36.0a_W^3 \qquad [\mathbf{7.39}]$$

Although the equation above is fitted based on the 30 °C data, it is commonly assumed to hold at other temperatures. According to this equation, as the water vapor activity increases from zero to unity, the water content of the ionomer phase increases from 0.043 to 14.0. Because the fuel cell was always under dry condition, the effect of liquid water was not included here. However, one should note that higher water content values around 20 were measured for perfluorosulfonic acid based ionomers such as Nafion® equilibrated with liquid water, although the activity of liquid water is also unity. The

difference of water uptake of ionomer for saturated water vapor and liquid water is the so called “Schroeders paradox”.

Because the dimensions of the micro pores and micro channels in the catalyst layer are very small, we assume the thermodynamic equilibrium of water between the ionomer and gas phases within the catalyst layer, then the water concentration in the ionomer phase can be correlated to the gas phase water activity by Equation **7.38** . With the isobaric and isothermal assumption, the water activity in the gas phase can be calculated based on the water mole fraction and the water saturation pressure at the cell operation temperature

$$a_W = \frac{x_W P}{P_{sat}} \qquad [\mathbf{7.40}]$$

Here, the water saturation pressure, P_{sat} is given by the empirical expression fitted by Springer *et al.*[4] according to tabulated values

$$\log_{10} P_{sat} = -2.1794 + 0.02953T - 9.1837\times10^{-5}T^2 + 1.4454\times10^{-7}T^3 \qquad [\mathbf{7.41}]$$

The remaining necessary transport property to calculate the water flux in the ionomer phase of the catalyst layer is D_W^m, the diffusion coefficient of water in the ionomer material as a function of ionomer water content λ. Then the effective water diffusion coefficient in the ionomer phase of the catalyst layer can be determined according to Equation **7.28**. Zawodzinski *et al.* [**19**] measured the ^{1}H self-diffusion coefficients in hydrated Nafion membrane at 30 °C by pulse field gradient Nuclear Magnetic Resonance (NMR) and indicated the identification of the measured ^{1}H self-diffusion coefficients with the water self-diffusion coefficient in Nafion®. Inglefield and coworkers [**76**] also reported similar water self-diffusion coefficient for Nafion® with NMR. Based on the measured water self-diffusion coefficients, Springer and Zawodzinski *et al.* [**20**] further developed a corrected diffusion coefficient which accounted the effect of membrane swelling and can be directly applied to the coordinate system fixed to the dry membrane. The corrected diffusion coefficient increases with increasing water content at low water content region, whereas decreases with inceasing

water content at high water content region, and attains a peak value around λ=3. As shown in the following equations, the corrected diffusion coefficient was fitted to a third order polynomial for $\lambda > 4$, and was fitted to two linear interpolations for $2 \le \lambda \le 4$ because of the sensitivity of the coefficient to water content.

$$D_W^m = 10^{-6} \exp\left[2416\left(\frac{1}{303} - \frac{1}{273+T_{cell}}\right)\right]\left(2.563 - 0.33\lambda + 0.0264\lambda^2 - 0.000671\lambda^3\right) \quad (\text{for } \lambda \ge 4) \quad [\mathbf{7.42a}]$$

$$D_W^m = 10^{-6} \exp\left[2416\left(\frac{1}{303} - \frac{1}{273+T_{cell}}\right)\right]\left(6.62 - 1.24\lambda\right) \quad (\text{for } 3 \le \lambda < 4) \quad [\mathbf{7.42b}]$$

$$D_W^m = 10^{-6} \exp\left[2416\left(\frac{1}{303} - \frac{1}{273+T_{cell}}\right)\right]\left(-3.1 + 2.0\lambda\right) \quad (\text{for } 2 \le \lambda < 3) \quad [\mathbf{7.42c}]$$

$$D_W^m = 2.69 \times 10^{-6} \quad (\text{for } \lambda < 2) \quad [\mathbf{7.42d}]$$

The unit of the effective water diffusion coefficient is [cm^2/s]. Then the effective water diffusion coefficient in the ionomer phase of the catalysts can be determined according to Equation **7.28**.

Water transport in the membrane

Under steady state, the net water molar flux does not change through the reinforced electrolyte membrane

$$-D_W^{re}\frac{\rho_{dry}}{EW}\frac{d\lambda}{dy} + \frac{n_d i}{F} = \frac{\alpha i}{F} \quad [\mathbf{7.43}]$$

where D_W^{re} is the water diffusion coefficient for the reinforced membrane. Similar to Nafion® membrane, Gore SELECT® membrane is also based on sulphonated fluoropolymer but reinforced with un-conductive reinforcement polymer. We assume the water diffusion coefficient for the reinforced membrane has the similar form to the coefficient for Nafion® and correct it with a correction factor β

$$D_W^{re} = \beta D_W^m \quad [\mathbf{7.44}]$$

And the correction factor needs to be fitted through the modeling for all 6 low humidity conditions.

Solution

In the described model, with measured local current density distribution *i(z)* and a guess value of β as model inputs, all other unknowns such as species mole fractions and membrane water content are functions of the effective drag coefficient α. At any position *z* along the gas flow channel, with an initial guess value of α, the differential model equations of species mole fractions for GDL, MPL, and catalyst layer regimes become initial value problems. Then the water activities at the catalyst layer/membrane interfaces of the anode and cathode sides is calculated with a Euler method based on the boundary conditions in the anode and cathode flow channel respectively. Then a newer value of α is solved based on the two interface water activities with the membrane water transport governing equation (Equation **7.43**) by finite difference method. The average of this new value and the original guess value is used as the new value of α and iteration occurs until enough accuracy is achieved. Repeating this process for all the elemental 1-D cells along the gas flow channel generates a set of calculated species mole fractions for the flow channel.

Then different values of the correction coefficient β and the tortuosity of porous layers were applied in the model until the model simulations well matched the experimental species distribution data for all three inlet humidities and two cell temperatures.

7.4 Results and Discussion

As shown in Chapter 6, at various inlet relative humidities and fuel cell temperatures at 25 psig pressure, current and species distributions were measured simultaneously at 0.7 V with constant anode and cathode stoichiometries of 1.2 and 2.0 respectively. The pressure drop through the fuel cell varies with different total current, humidification level, and cell temperature. However, the pressure drop over the fuel cell

with 50% humidified air at 95°C and 1061 sccm (standard referenced at 0°C), which corresponds to the highest pressure drop for the whole set of tests at 0.7V, is only around 0.45 kPa, about 0.17% of the 2.7 atm total pressure of the fuel cell. Therefore, the constant pressure assumption is appropriate. Because current density distributions were measured with 14 gold plated current collector segments and are shown respecting to the discrete center locations of the segments, in order to apply the current distributions into the model, the discrete experimental current density values were expressed analytically with fourth-order polynomial approximations. Figure **7-2** shows the approximation curves of the three inlet humidities at two cell temperatures. Overall, the fourth-order polynomial approximation closely approximates the experimental data, despite some scatter in the experimental. Transport properties of fuel cell materials and binary diffusion coefficients of gases used in the model are shown in Table **7-2**.

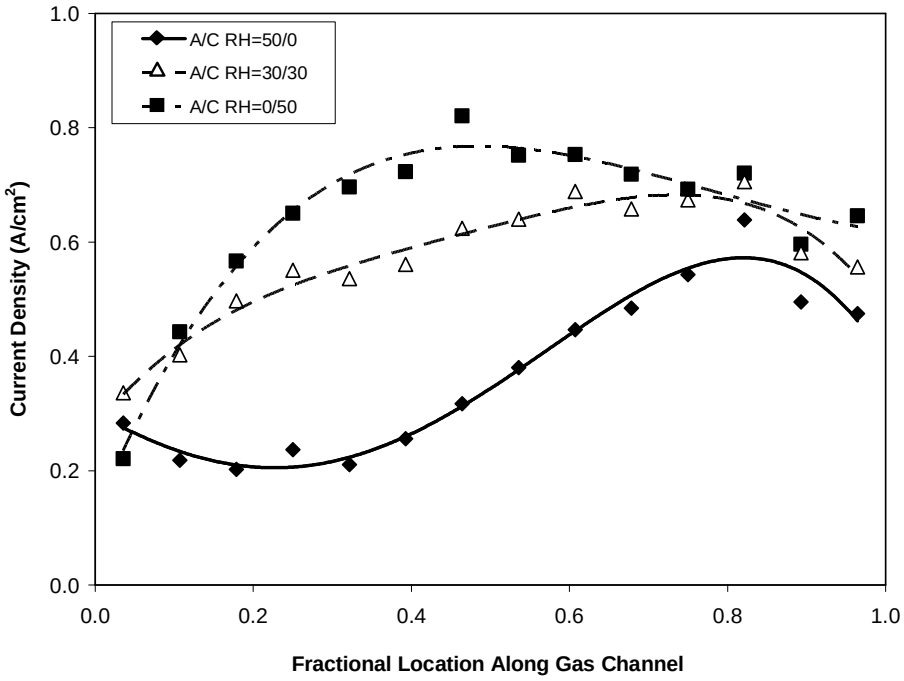

(a) T_{cell}=95 °C

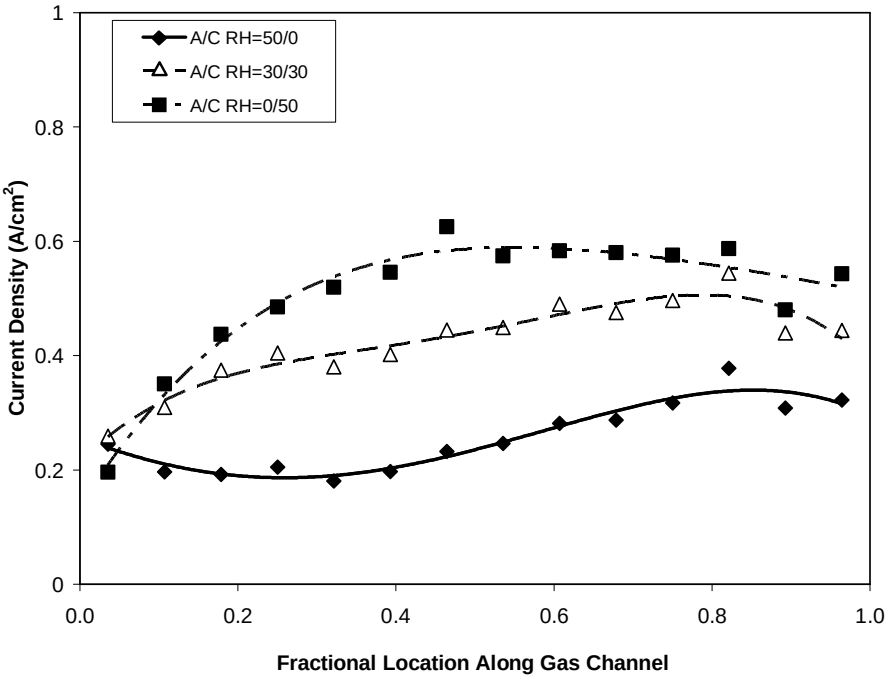

(b) T_{cell}=110°C

Figure **7-2**: Fourth order polynomial approximations of steady-state current distributions along the gas flow channel. cell pressure=25 psig.

Table **7-2**: Transport properties and parameters used in the simulations

Description	Value
Porosity of gas diffusion layers, ε_{GDL}	0.7
Porosity of micro porous layers, ε_{MPL}	0.5
Porosity of catalyst layer, $\varepsilon_{g,CL}$	0.6
Volume fraction of ionomer in catalyst layers, $\varepsilon_{m,CL}$	0.26
Tortuosity of porous layers, τ	15.0
Dry electrolyte density, ρ_{dry}	2.0 g/cm^3
Equivalent molecular weight of electrolyte, EW	1100 g/mol
H_2-H_2O binary diffusion coefficient at 307.1K and 1.0 atm[**106**], $D_{WH,0}$	0.915 cm^2/s
H_2O-O_2 binary diffusion coefficient at 308.1K and 1.0 atm[**106**], $D_{WO,0}$	0.282 cm^2/s
H_2O-N_2 binary diffusion coefficient at 298.2K and 1.0 atm[**106**], $D_{WN,0}$	0.293 cm^2/s
O_2-N_2 binary diffusion coefficient at 293.2K and 1.0 atm[**106**], $D_{ON,0}$	0.22 cm^2/s
Electro-osmotic drag coefficient for λ<14.0, n_d	1.0
Water diffusion coefficient in Nafion®, D_w^m	Equation 7.42
Correction factor for water diffusion coefficient in Gore SELECT® reinforced membrane	0.95

As shown in Figure **7-3** through Figure **7-5**, with a correction factor value of 0.95 and a tortuosity value of 15.0 for both the anode side and the cathode side, the simulation well matches the experimental for all three inlet relative humidities at two cell temperatures. The close to unity correction factor value could be a result of different material properties of the conductive phase in the reinforced membrane, or less volume expansion with water swelling due to the overall stronger mechanical structure from the reinforcement. Because the water diffusion coefficient shown in Equation **7.42** is actually a corrected diffusion coefficient which accounts for the effect of membrane thickness change for directly applying to a dry membrane coordinate system [**20**], less volume change with water means a higher equivalent water diffusion coefficient. The relatively big tortuosity of porous media resulted from the coverage as well as the compression of landing on GDL. To diffuse from the MEA active area underneath the 0.9 mm wide landings, gaseous species have to travel a much longer distance than the

region just underneath the gas flow channel, and consequently resulting a greater equivalent tortuosity in this 2-D model. The pressure exerted on GDL can reduce the pore size and the porosities of gas diffusion media, and then also leads to a greater equivalent tortuosity.

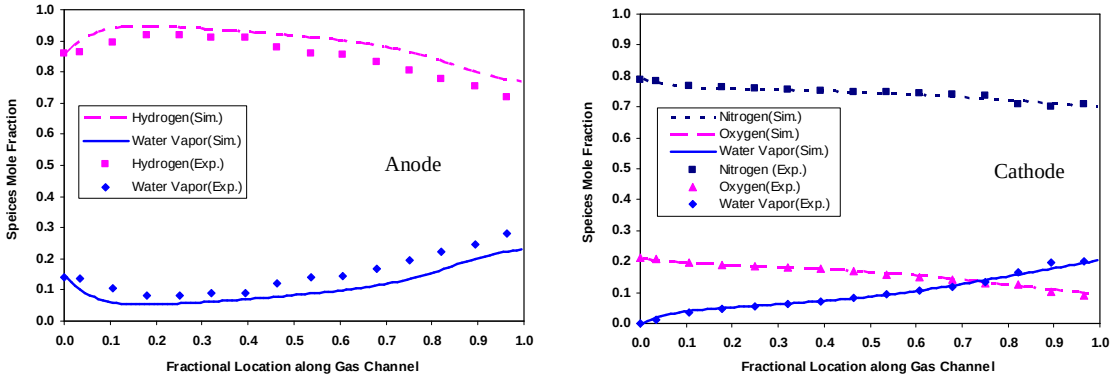

(a) T_{cell}=95 °C

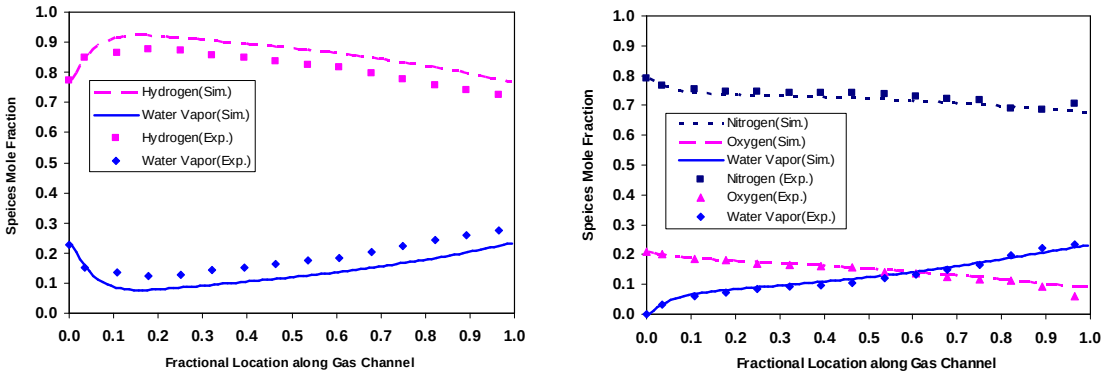

(b) T_{cell}=110°C

Figure **7-3**: Simulated and experimental species distribution as a function of fractional location along gas channel at A/C RH=50/0. The symbols are experimental data, and the curves are simulation results.

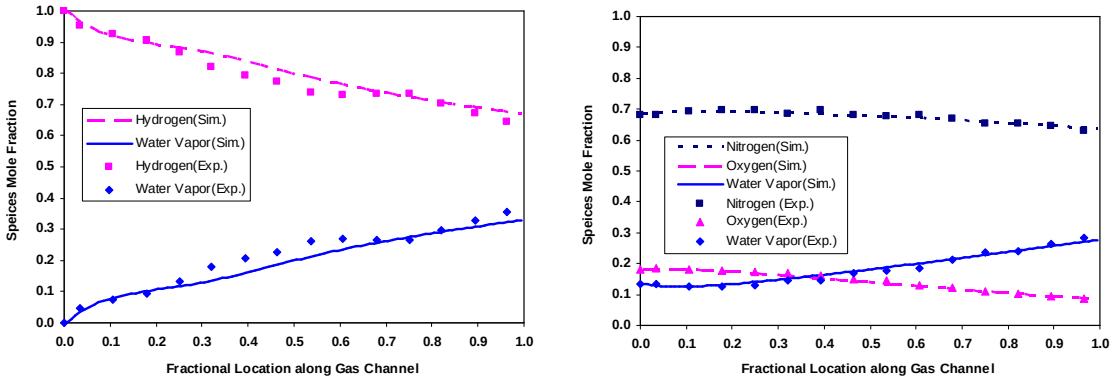

(a) T_{cell}=95°C

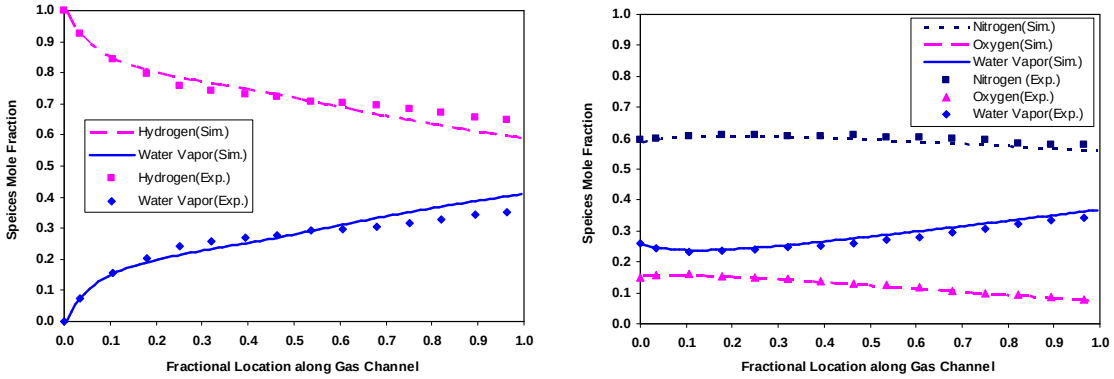

(b) T_{cell}=110°C

Figure **7-4**: Simulated and experimental species distribution as a function of fractional location along gas channel at A/C RH=0/50. The symbols are experimental data, and the curves are simulation results.

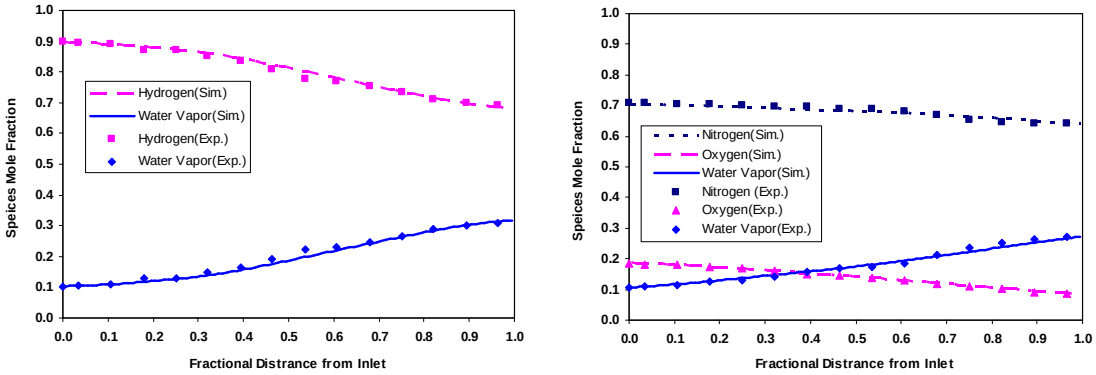

(a) T_{cell}=95 °C

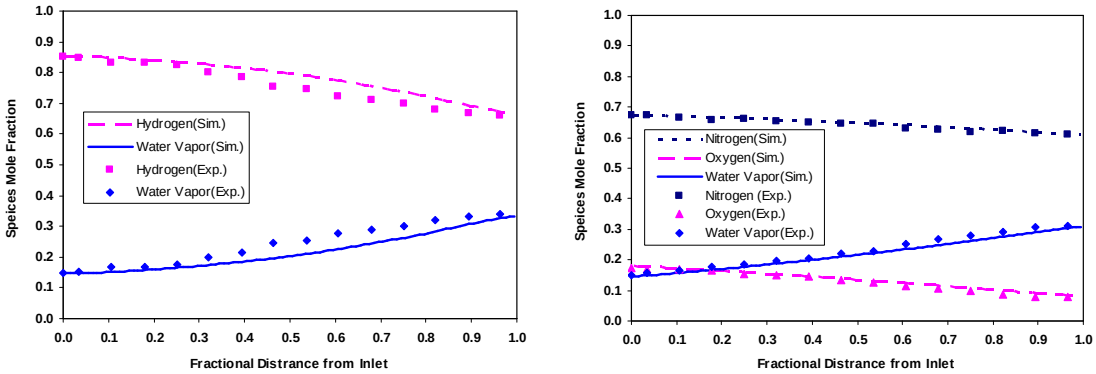

(b) T_{cell}=110°C

Figure **7-5**: Simulated and experimental species distribution as a function of fractional location along gas channel at A/C RH=30/30. The symbols are experimental data, and the curves are simulation results.

Figure **7-6** shows the anode and the cathode species profiles in the porous region at the inlet of gas channel for the dry cathode condition of A/C RH=50/0. Variation of water content in the membrane is not shown. Due to the big difference of water activity between the anode and cathode gas flow channels, water is transported in porous media by both diffusion and convection, which is introduced by consumption of reactants and also diffusion itself, as described by Equation **7.25**, the Stefan-Maxwell equation. In the porous region at the anode inlet, because of the consumption of hydrogen at catalyst layer and net water loss to the cathode at this location along the gas flow channel, both convection and water diffusion are towards the membrane. Primarily because of the high binary diffusion coefficient of H_2O/H_2, the water vapor mole fraction decreases not too

much (0.140 to 0.118), compared to the cathode, from the anode gas channel to the anode side membrane surface. At the same time, because the amount of hydrogen carried by convection exceeds the consumption rate at the catalyst layer, a positive hydrogen concentration gradient is built up and the net diffusion flux of hydrogen is from the membrane to the anode gas channel. The relative small difference of water mole fraction between the anode gas flow channel and the anode membrane surface is also because of the absence of the buildups of other inert components such as N_2 and CO_2, which present if reformate gas is used.

In the cathode porous region, water is transported by both diffusion and convection from the membrane to the cathode gas channel. However, due to the much lower binary diffusion coefficients of H_2O/O_2 and H_2O/N_2, the water concentration slope is steeper than the anode side. This big water concentration difference helps to keep the electrolyte in the membrane and the catalyst layers hydrated on the cathode side. The higher mole fractions of nitrogen and oxygen in the cathode gas flow channel indicate the diffusion fluxes are from the gas flow channel to the cathode catalyst layer.

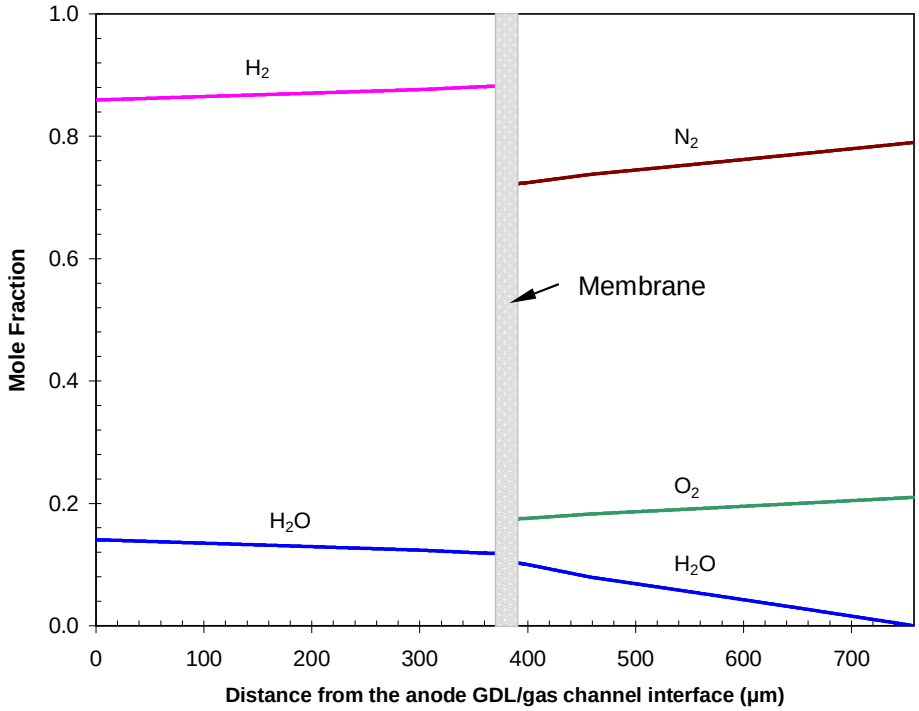

Figure **7-6**: Simulated through-the-plane species mole fractions in the anode and the cathode porous region as a function of distance from the anode GDL/gas channel interface at the gas inlet. T_{cell}=95 °C, A/C RH=50/0, Pressure=25 psig

Figure **7-7** shows the anode and the cathode species profiles in porous region at the inlet of gas channel for the dry anode condition of A/C RH=0/50. Water is transported from cathode to anode by diffusion and convection. Compared to the dry cathode case of A/C RH=50/0, although the water mole fraction in the cathode gas channel is very similar to the fraction in the anode gas channel of A/C RH=50/0 (0.134 vs. 0.140), the water mole fraction at the cathode side membrane surface is about 44% lower (0.066 vs. 0.118) due to the low diffusivity of water vapor in oxygen and nitrogen. The electro-osmotic drag from the anode to the cathode reduce the net water flux from the cathode side to the anode side, and further limits the water pickup of the anode. The high binary diffusion coefficient of H_2O/H_2 makes the hydration condition of the electrolyte membrane even worse by promoting water loss to the anode gas flow channel, which greatly reduces the shielding effect of the porous layers. This accelerated dryout explains the low inlet current density of a dry anode condition.

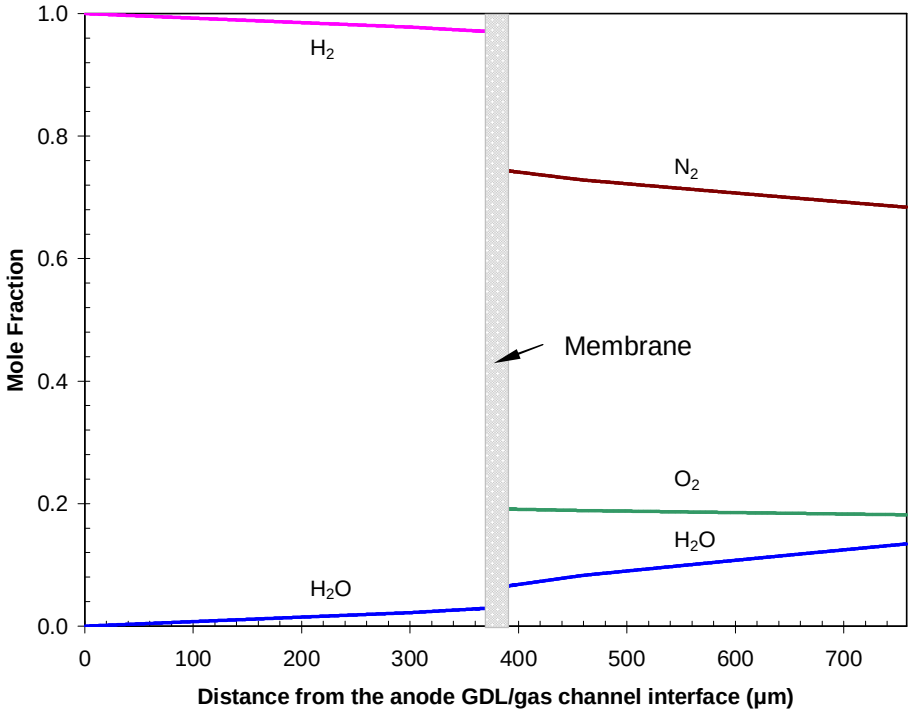

Figure **7-7**: Simulated through-the-plane species mole fractions in the anode and the cathode porous region as a function of distance from the anode GDL/gas channel interface at the gas inlet. T_{cell}=95 °C, A/C RH=0/50, Pressure=25 psig

Figure **7-8** shows the inlet through-the-plane species profiles for the partially humidified anode and cathode condition of A/C RH=30/30 at 95°C. Because of the nearly equal water mole factions in the anode and the cathode gas flow channel (anode/cathode 0.103/0.107), there is no strong net water transport across the membrane. Due to water production on the cathode catalyst layer and also the diffusion resistance in porous layers, the water mole fraction at the cathode membrane surface is 0.022 higher than the water mole fraction in the cathode gas flow channel. And the electro-osmotic drag is almost evenly balanced by the water back-diffusion from the cathode, as indicated by the very flat anode water mole fraction profile, despite the water mole fraction at the anode side membrane surface is 0.001 higher. (0.104 vs. 0.103). The enlargement plot shows the water concentration variation in the cathode catalyst layer. Because the current is assumed to be generated uniformly over the catalyst layer, there is a maximum of water mole fraction in the catalyst layer.

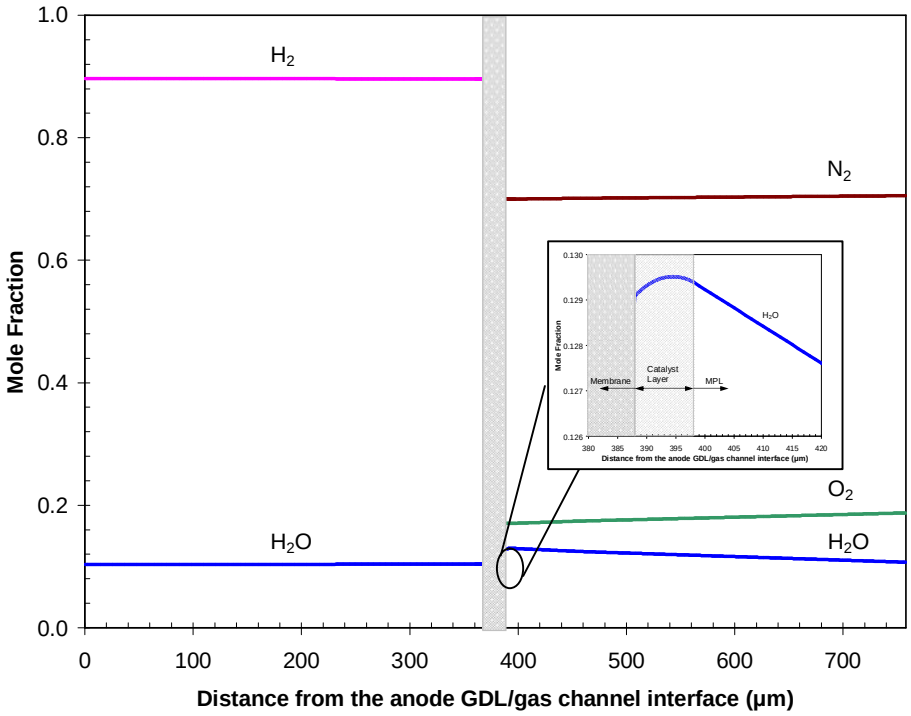

Figure **7-8**: Simulated through-the-plane species mole fractions in the anode and the cathode porous region as a function of distance from the anode GDL/gas channel interface at the gas inlet. T_{cell}=95 °C, A/C RH=30/30, Pressure=25 psig

Figure **7-9** compares the water activity profiles in the porous layers at three fractional locations along the gas channel for the dry cathode condition of A/C RH=50/0 at 95°C. At the inlet, although the cathode gas channel is dry and water is lost from the anode to the cathode gas channel, because of the mass transport resistance of the cathode porous layers, the membrane is still somewhat hydrated, and the overall water activity in the membrane is around 0.4. At z/L = 0.155, although the water activity in the cathode gas flow channel increases to 0.16 due to transport from the anode and generation, the hydration level of the membrane actually decreases with an overall water activity around 0.2. The higher water activity at the cathode membrane surface indicates water back diffuses from the cathode to the anode. Near the outlet of the fuel cell, high water flux from the cathode catalyst layer to the cathode gas flow channel creates a considerable water activity decrease, which even exceeds the water activity difference through the

membrane, and the water activity in the anode gas flow channel is higher than the activity in the cathode gas flow channel (0.75 vs. 0.66).

Figure **7-10** shows the profiles for membrane water content as a function of fractional thickness from the anode side membrane surface at the same three fractional locations along the gas flow channel. Due to the very small 18 μm thickness of the membrane, the differences of water content though the membrane are relatively small, which means the water diffusion coefficient through the membrane doesn't change much either. Because of the constant drag flux across the membrane due to the assumption of unity electro-osmotic drag coefficient for low humidity conditions, the simulated membrane water content changes almost linearly across the membrane. From inlet to the fractional location of z/L=0.155, the membrane hydration level decreases due to water loss to the cathode gas flow channel. From z/L=0.155 to the outlet, the membrane hydration level increases due to the hydration by water generation.

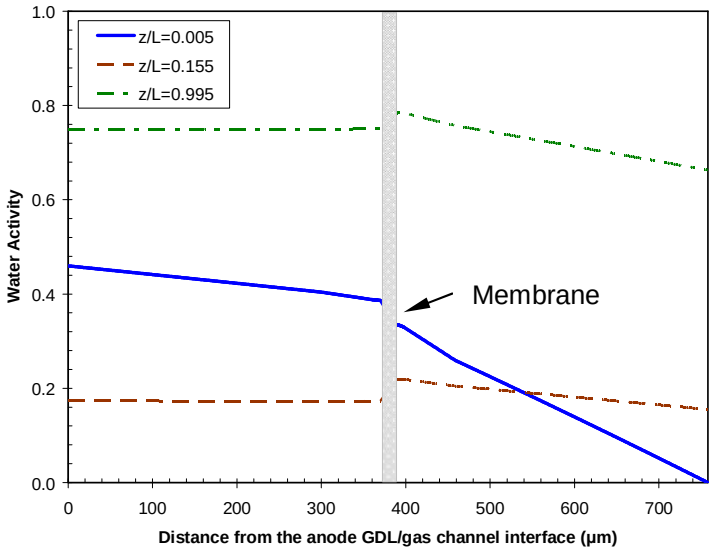

Figure **7-9**: Simulated water activity profiles in the anode and the cathode porous region as a function of distance from the anode GDL/gas channel interface at three fractional locations along the gas channel. T_{cell}=95 °C, A/C RH=50/0, Pressure=25 psig.

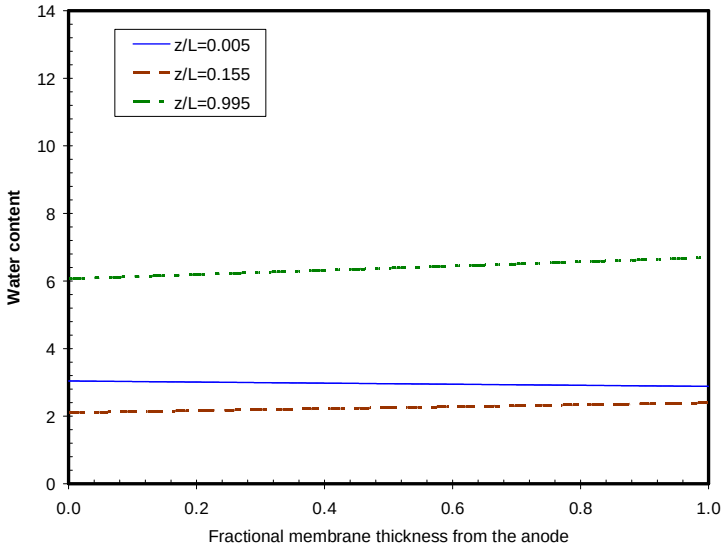

Figure **7-10**: Simulated water content profiles in the membrane as a function of fractional thickness from the anode catalyst layer/membrane interface at three fractional locations along the gas channel. T_{cell}=95 °C, A/C RH=50/0, Pressure=25 psig.

Figure **7-11** compares the simulated membrane water content at the center line of the membrane as a function of fractional location from the gas inlet for three inlet humidity conditions and two cell temperatures. At both cell temperatures, the dry cathode case of A/C RH=50/0 has the highest membrane water content at the inlet of the fuel cell, the partially humidified anode and cathode case of A/C RH=30/30 has the second highest inlet membrane water content, and the dry anode case has the lowest value of membrane water content at the same location. It should be noted that the experimental current densities of the first segment are actually average values over the whole length of the first segment (7.1% of the total length of the gas flow channel), so the case of A/C RH=30/30 the highest current densities are at the segment. This qualitatively agrees well with the measured inlet current density for these humidification conditions. Due to water loss to the dry cathode gas flow channel, the hydration of the membrane of A/C RH=50/0 decreases until a minima. Then the hydration level of the membrane starts to increase due to the increasing overall humidification level of the cell leaded from water produced on the cathode catalyst layer. For the dry anode case of A/C RH=0/50 at 95°C, the membrane water content keeps increasing over the whole length of the gas flow channel despite the mechanisms are a bit different. The membrane water content first increases relatively fast because the anode and the membrane pick up water from the cathode gas flow channel by back diffusion. Then the membrane water content curve flatters out because the electro-osmotic drag and the back-diffusion reach a rough balance and the hydration of the membrane is mainly controlled by the overall humidification level from water production. Near the outlet, the value of the membrane water content exceeds 14.0, suggesting the presence of liquid water and possible flooding. Compared to 95°C, the water content profile of the dry anode case at 110°C shows the similar trend. However, due to the greatly increased water saturation limit, the membrane water content is lower than 7.0 over the whole length of the gas flow channel. For the partially humidified anode and cathode case of A/C RH=30/30, there is no rapid change of membrane water content near the inlet due to the absence of strong water transport across the membrane. The hydration level of the membrane increases relatively slowly, dominated by the increase of the overall humidification of the fuel cell. At 95°C, the membrane water

content near the outlet also exceeds 14.0, implying the presence of liquid water and possible flooding. At 110°C, due to the greatly increased water saturation limit and thus weakened humidifying effect by water generation, the membrane water content is always lower than 4.0 over the whole length of the gas flow channel. The monotonously increasing membrane hydration also means that the previous decreasing-increasing current profile of the previous fuel cell is caused by the non-isothermal boundary condition.

It also can be noticed from the plots that, after the membrane water content reaches 4.0 the slope of the water content curve becomes much steeper. This phenomena is mainly because of the steep relation between membrane water content and water activity in the regime of a_w>0.6, as shown in Figure **7-12**.[**5**] Of course, the higher local current density also contributes to this phenomenon by creating greater water activity difference between the cathode catalyst layer and the cathode gas flow channel.

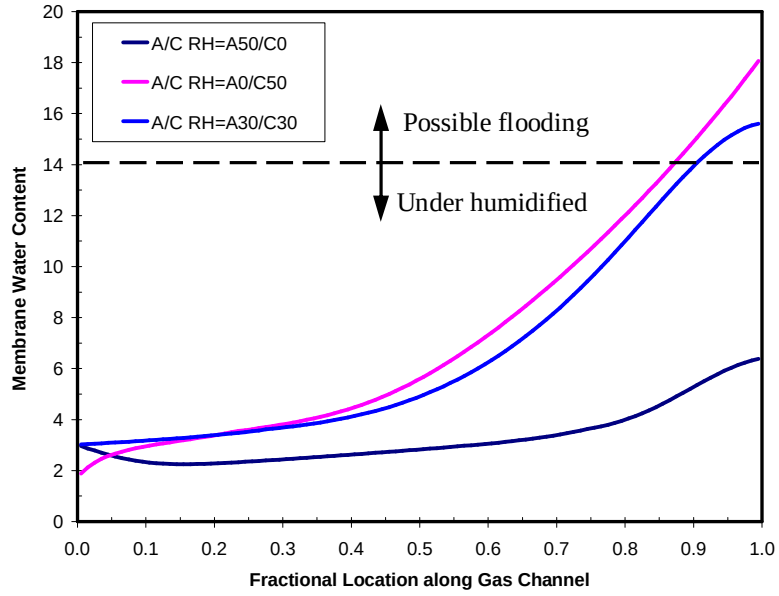

(a) T_{cell}=95°C

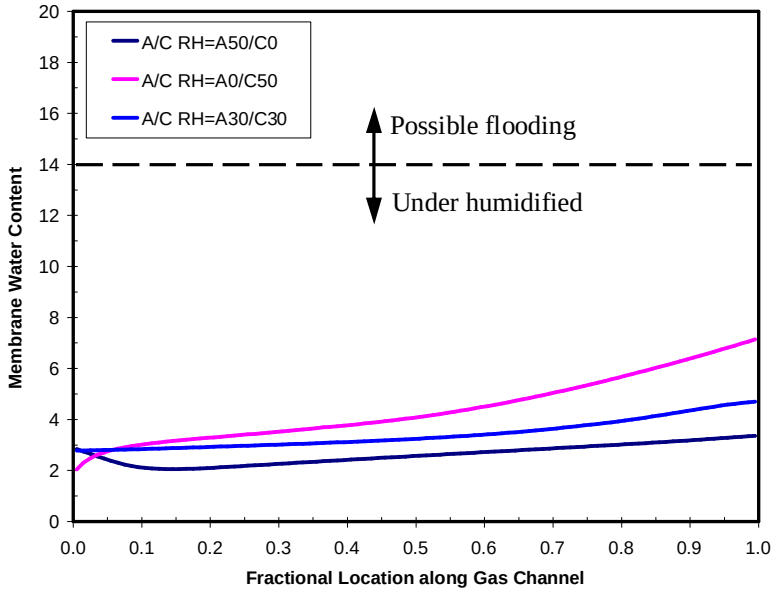

(b) T_{cell}=95°C

Figure **7-11**: Simulated membrane water content profiles at the center of the membrane as a function of fractional location along the gas channel for the three inlet relative humidity conditions. Pressure=25 psig.

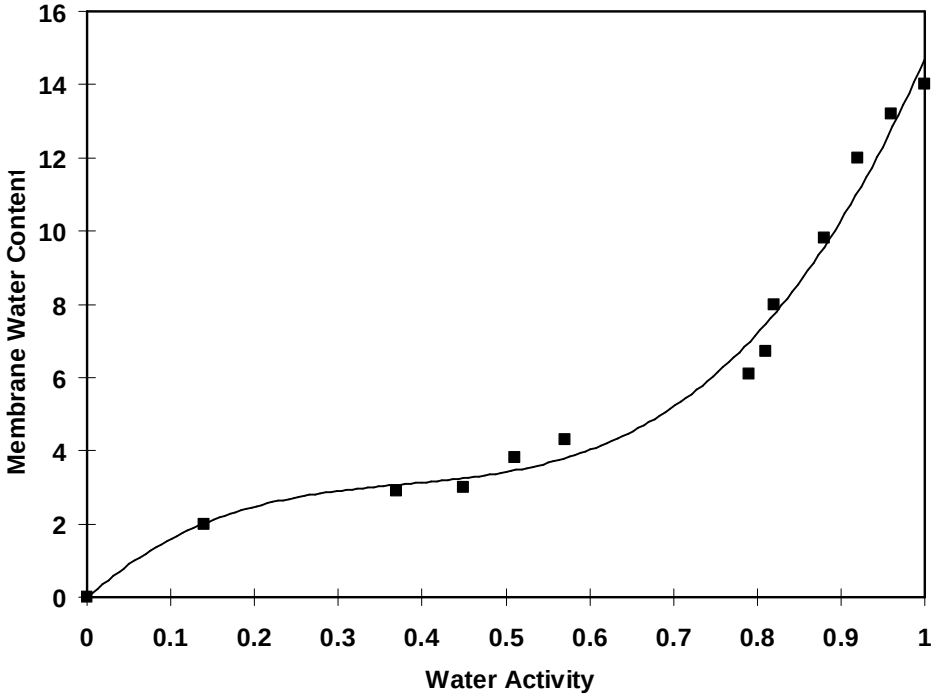

Figure **7-12**: Water Uptake of Nafion® 117 Membrane [**5**]

7.5 Summary

In this chapter, a quasi-two-dimensional, steady-state, along-the-gas-flow-channel mass transport model is developed and validated with experimentally determined current distributions and inlet species mole fractions as the input. Then the model was applied to deduce the water diffusion coefficient in Gore SELECT® reinforced polymer electrolyte membrane based on the experimental data for three low inlet relative humidity conditions at two elevated cell temperatures.

The model finds that, with a correction factor value of 0.95 and an equivalent tortuosity value of 15.0 for both the anode and the cathode, the simulation has good agreements with the experimental results for all three inlet relative humidities and two fuel cell temperatures.

High binary diffusion coefficient of H_2/H_2O is found to be one of the main contributions to the decreasing and then increasing current profile of a dry cathode inlet condition. This also explains the dominating effect of the anode water activity on the shape of current density profile.

Porous layers, including catalyst layer, micro-porous layer, and macro-porous layer have significant influence on low humidity operation of PEFCs, which help to maintain a higher water activity at the membrane surface. Bigger thicknesses, lower porosities, and higher tortuosities of the porous layers, and big land width can increase the equivalent tortuosity (or the mass transport resistance), and then boost the local performance in some region of the fuel cell under low humidity operation.

Many experimental and simulative studies have been conducted by different groups to investigate the mass transport limitation of gas diffusion media on the performance of PEFCs. [**107-111**] However, these studies mainly focused on the influence of porous layers on oxygen transport and liquid water management, and little attention is paid on the effect of mass transport barrier on electrolyte hydration under low humidity condition. Recently, Ju and Wang addressed this effect of porous layer in their non-isothermal PEFC model [**76**]. Our findings provide direct support for their modeling results, and for the first time explain the domination of anode water content on the local performance of PEFCs under low humidity operation.

For co-flow configuration, an over-humidified anode and an under-humidified cathode, overall low anode mass transport resistance, high cathode mass transport resistance near the inlet, and medium cathode mass transport resistance in downstream region, may have the potential to eliminate both dryout and flooding.

Chapter 8

Conclusions and Future Work

An experimental study combining simultaneous measurements for current density, species, and high frequency resistance (HFR) distributions was conducted to study the characteristic distributed performance of polymer electrolyte fuel cells under low inlet humidity conditions. A quasi-two-dimensional model was developed based on the experimental data to understand the contributions of cell materials on water transport, and interpret the experimental results. The conclusions drawn are based on the analysis of the experimental and simulation results obtained in this program.

8.1 Conclusions

Two new techniques for *in-situ* species measurements, MicroGC technique and RTGA technique, were developed with the capability to directly measure gaseous samples with high water content up to saturation level without the requirement of pre-dehumidification. This enables directly mapping of species variation in the anode and the cathode gas flow channel of an operating fuel cell. The low cost MicroGC technique has good capability in measuring steady-state species variations along the gas flow channel, and could be a powerful tool for study of water management and CO poisoning. The relative long 2 minutes sample processing time limits its application to steady-state study of PEFCs, however, the RTGA has a much faster response time of about 1 second per measurement, making possible the near real-time monitoring of species mole fractions, and provides the ability to determine the time scale of many intercoupled phenomena. However, the identification mechanism of RTGA based on species molecular weights limits the application to species with different molecular weights. So that N_2 and CO cannot be discrete.

Two generations of highly instrumented fuel cells capable of simultaneous measurements of current density, species, and HFR distributions were designed, fabricated and debugged for this study. Both cells share the same approach scheme of segmented current collector and cathode gas diffusion layer to facility current distribution measurement, and multiple gas sampling ports in the gas flow channel to enable species distribution measurements. While the single flow path serpentine layout of the first generation design was suited to examine the effects of dry-out, flooding, and mass transport losses, the design also has some limitations. The second generation design fixed a couple of issues negatively impacting the cell performance in the old design with more realistic flow field configurations and achieved comparable performance to un-segmented fuel cells. The flow field configurations and thermal boundary conditions are also updated. The coolant channels in the backing plates of the second generation cell enable active control on fuel cell operating temperature as well as an isothermal boundary condition.

Detailed experimental studies including species, current, and resistance distribution measurements was performed to investigate the characteristic PEFC steady-state and transient behaviors under low humidity operating conditions. The effects inlet humidity, reactant stoichiometry, temperature, and pressure, were investigated extensively.

The dynamic response of fuel cell performance to step change in voltage is quite different between dry anode and cathode conditions. For the dry cathode condition, the anode adjusts asymptotically from high to low current, while for a dry cathode condition, the adjustment is very rapid. For both cases tested, the current density adjustment time corresponds to the time scale of mass adjustment in the anode side, not the cathode side, indicating a non-linear water content profile in electrolyte.

The experimental results show that under reduced humidity conditions, the local anode water content has dominating effect on local current density. Dry-out of the anode side of the membrane can increase the membrane resistance dramatically and result in a substantial degradation of the fuel cell performance. The current distribution curves look qualitatively similar to H_2O mole fraction in the anode profiles, and the inverse of the

HFR profiles. A generalized local current distribution profile was deduced based on experimental data, which shows the expected qualitative shape of the current density for all inlet humidity conditions, with amplitude and wavelength dependent on current density and initial water imbalance between anode and cathode.

The dominating effect of local anode humidification and the generalized local current distribution were confirmed by the experimental results of the second generation segmented fuel cell at two elevated temperatures and two pressures, despite very different flow field configurations and thermal boundary conditions. However, the different current profile of the partially humidified anode and cathode condition of A/C RH=30/30 with isothermal boundary condition did reveal of the thermal boundary, confirming the importance of thermal management on water management.

The experimental results also show that, with low inlet humidities, the cell performance is more limited by insufficient electrolyte hydration instead of oxygen depletion. Although anode humidity controls the local performance profiles, in general, the higher input relative humidity still results in the higher bulk cell performance. The humidifying effect of water production on the cathode catalyst layer was found to be another critical factor for fuel cell performance. Although their mechanisms are quite different, higher cathode stoichiometry, elevated cell temperature, and lower exit pressure can all increase the amount of water required for humidification and reduce the humidifying effect of water production, and reduce the cell performance. However, due to the dilution of water vapor on oxygen concentration as well as more severe flooding, the benefit of higher inlet relative humidity decreases significantly over 40% relative humidity, and can negatively affect the performance under a combination of high temperature and low pressure due to the extremely low oxygen concentration.

With ultra purity hydrogen and commercial air as feeding reactants to the fuel cell, test results indicates that increased operating temperature >80°C results in lower fuel cell performance although the dominating mechanisms are different according the inlet humidity. For fully humidified condition, this decrease of performance is mainly resulted from the lower oxygen concentration in the cathode primarily due to dilution of water vapor, and lower operating pressure can greatly exaggerate the dilution effect. For low

humidity conditions, the higher temperature affects the lower average relative humidity due to greatly increased water saturation limit. Due to sensitivity of water boiling point to pressure, it is difficult to achieve good performance at both high temperature and low pressure with Perfluorosulfonic acid (PFSA) based membranes which require good humidification to get high proton conductivity. A key to future high temperature MEAs is the tolerant to low water content or has to operate under elevated pressure.

An overall water balance was used to validate the accuracy of the approach for current and species distribution measurements. For all inlet relative humidity conditions, the normalized water measurement error was less than 15%. This high accuracy meets the requirements of determining the water diffusion coefficient in polymer electrolyte membranes and other transport properties of PEFC materials.

Based on the current and species distribution data, the effective drag coefficient was calculated and shown along the gas flow channel for different operating conditions. The overall effective drag coefficients for higher temperature are amplified compared to lower temperatures, mainly due to the higher water saturation limit and concomitantly higher water diffusion gradient in gas phase. The higher water diffusion coefficients in the electrolyte membrane and in gaseous mixtures at higher temperatures also contribute to this difference.

A mass transport model was developed and applied to further interpret results. The model is also a tool to help understand the ideal MEA configuration for low relative humidity, high temperature conditions. The mass transport model found that the water diffusion coefficient in Gore SELECT® reinforced membrane roughly equals to the coefficient in Nafion® membrane. The mass transport resistance of porous gas diffusion media can create considerable water activity difference between the gas flow channel and the catalyst layer, which boosts the humidifying effect of generated water. The relatively high binary diffusion coefficient of H_2O/H_2 in the anode and the much lower water diffusivity in the air cathode were found to be responsible for the dominating effect of local anode water on local cell performance, as shown in the experimental study. Overall, for low relative humidity operation, a highly restrictive anode and cathode

diffusion barrier is preferred to maintain MEA moisture. These findings can provide directions to the design of MEA for low humidity operation.

8.2 Recommendations for Future Work

As a continuation of the present research work, the following recommendations are proposed in this section based on present experimental and simulation results:

1. The overall approach for present experimental study has demonstrated good accuracy. With the updated design of the second generation instrumented fuel cell, the normalized water measurement error is less than 15% for all three inlet relative humidity conditions and two cell temperatures, which meets the requirement for determining water transport properties in polymer electrolyte membranes. The water diffusion coefficient in Nafion® 117 has been experimentally determined by Zawodzinski *et al.* using pulse field gradient Nuclear Magnetic Resonance (NMR) techniques [**19**], and was further confirmed by Motupally *et al.*[**25**]. However, water diffusion coefficient in reinforced membrane, such as Gore SELECT® membrane, is still not available in literature. The non-conductive reinforcement could reduce the water diffusion coefficient by reducing the transport area for water. At the same time, the reinforcement also could increase the water diffusion coefficient by limiting the volume expansion of the membrane. In this dissertation, the water diffusion coefficient in Gore SELECT® membrane was determined based on experimental results by assuming a unity electro-osmotic drag coefficient. This assumption is somewhat questionable because very different values have been reported in literature by different groups. To decouple the water diffusion coefficient, the water electro-osmotic drag coefficient, and the mass transport resistance of porous gas diffusion layers, we could measure the species distribution along the gas flow channel with hydrogen as feeding streams for both side of the fuel cell at variant inlet relative humidities and zero current flowing through the membrane. Hydrogen for both sides can eliminate the influence of water generation, and the high diffusivity of hydrogen also can greatly reduce the effect of porous gas diffusion medium on water transport. Zero current can eliminate the influence of electro-osmotic drag.

2. With well determined water diffusion coefficient, the fuel cell can be operated in hydrogen pump mode with protonic current from anode to the cathode. With combined measurements of current and species distribution, the drag coefficient can be determined.

3. As indicated by both experimental and simulation results, the dominating effect of anode water on membrane hydration is mainly because of the high diffusivity of water in pure hydrogen. However, the finite water desorption rate in the cathode catalyst layer may also significantly contribute to this dominating effect. The presence of inert components in the anode gaseous mixture, such as N_2 and CO_2, can significantly reduce the overall diffusivity of water, and then two mechanisms can be delineated.

4. The simulation results shows that the mass transport resistance of the cathode porous layers is helpful for the local performance of the inlet region of a dry cathode inlet condition, for example A/C RH=50/0. It is recommended to do a set of comparative testing to identify the benefit. This could be achieved by use different gas diffusion medium for the cathode inlet region.

5. Due to the low heat conductivity of Lexan®, the flow field holder creates considerable temperature difference between the stainless steel current collectors and the coolant. The coolant temperature has to be lowered to maintain an isothermal boundary with an increase of cell current density. This limits the application of the instrumented fuel cell in transient study. It is highly desired to replace the Lexan® flow field holder with a metal one while the insulation between current collectors still can be maintained.

6. It is recommended to further expand the mass transport model to include the absorption and desorption of water at membrane/porous region interfaces, as well as the current generation.

Bibliography

1. U. Pasaogullari, "Two-Phase Modeling and Flooding Prediction of Polymer Electrolyte Fuel Cells", Ph.D. Dissertation, Penn State University, PA, (2005)

2. S. J. Paddison, R. Paul, and T. A. Zawodzinski, "A Statistical Mechanical Model of Proton and Water Transport in a Proton Exchange Membrane", *J. Electrochem. Soc.*, **147**, 617 (2000)

3. U.S. DOE, "Fuel Cell Handbook (Sixth Edition)", published by U.S. Department of Energy, National Energy Technology Laboratory, 2-9, 2002.

4. K. K. Pushpa, D. Nandan, and R. M. Iyer, " Thermodynamics of Water Sorption by Perfluorosulphonate (Nafion-117) and Polystyrene-Divinylbenzene Sulphonate (Dowex 50W) Ion-exchange Resins at 298 ± 1 K", *J. Chem. Soc., Faraday Trans 1*, **84**, 2047 (1988)

5. T.A. Zawodzinski, C. Derouin, S. Rzdzinski, R. J. Sherman, V. T. Smith, T. E. Springer, and S. Gottesfeld, "Water Uptake by and Transport Through Nafion^q 117 Membranes", *J. Electrochem. Soc.* **140**, 1041 (1993)

6. Zawodzinski, T.A., Springer, T.E., Davey, J., Jestel, R., Lopez, C., Valerio, J. and Gottesfeld, S., "A Comparative Study of Water Uptake by and Transport Through Ionomeric Fuel Cell Membranes," *J. Electrochem. Soc.*, **140**, 1981 (1993)

7. J. T. hinatsu, M. Mizuhata, and H. Takenaka, *J. Electrochem. Soc*., "Water Uptake of Perfluorosulfonic Acid Membranes from Liquid Water and Water Vapor"**, 141**, 1493 (1994)

8. X. Ren, T. E. Springer, and S. Gottesfeld, "Water and Methanol Uptakes in Nafion Membranes and Membrane Effects on Direct Methanol Cell Performance," *J. Electrochem. Soc.*, **147**, 92 (2000)

9. P. Feterko, and I-M. Hsing, "Thermodynamics of Water Vapor Uptakes in Perfluorosulfonic Acid Membranes," *J. Electrochem. Soc*., **146**, 2049 (1999)

10. K. D. Kreuer, "On the Development of Proton Conducting Meterials for Technological Applications", *Solid State Ionics*, **97**, 1(1997)

11. R. W. Kopitzke, C. A. Linkous, H. R. Anderson, and G. L. nelson, "Conductivity and Water Uptake of Aromatic-Based Proton Exchange Membrane Electrolytes", *J. Electrochem. Soc*., **147**, 1677 (2000)

12. R. S. Yeo, and H. L. Yeager, *Modern Aspects of Electrochemistry*, **16**, 437 (1985)

13. G. Gebel, "Structural evolution of water swollen perfluorosulfonated ionomers from dry membrane to solution", *Polymer*, **41**, 5829 (2000)

14. R. –L. Rollet, G. Gebel, J. –P. Simoni, P. Turq, "A SANS Determination of the Influence of External Conditions on the Nanostructure of Nafion Membrane", *J. Polym. Sci.: Part b: Polym. Phys.* **39**, 548 (2001)

15. Technical Notes, Perma Pure, Inc. 2002

16. A. Z. Weber, and J. Newman. "Transport in Polymer-Electrolyte Membranes I. Physical Model", *J. Electrochem. Soc.*, **150**, 1008 (2003)

17. A. Z. Weber, and J. Newman. "Transport in Polymer-Electrolyte Membranes II. Mathematical Model", *J. Electrochem. Soc.*, **150**, 1008 (2003)

18. A. Z. Weber, and J. Newman. "Transport in Polymer-Electrolyte Membranes III. Model Validation in a Simple Fuel-cell Model", *J. Electrochem. Soc.*, **150**, 1008 (2003)

19. T. A. Zawodzinski, M. Neeman, L. O. Sillerud, and S. Gottesfeld. "Determination of Water Diffusion Coefficient in Perfluorosulfonate Ionomeric Membranes", J. *Phys. Chem.*, **95**, 6040 (1991)

20. T. E. Springer, T. A. Zawodzinski, and S. Gottesfeld. "Polymer Electrolyte Fuel Cell Model", *J. Electrochem. Soc.*, **138**, 2334 (1991)

21. X. Ye, and M. D. LeVan. "Water Transport Properties of Nafion Membranes Part I. Single-tube Membrane Module for Air Drying", *J. Membrane Sci.*, **221**, 147 (2003)

22. X. Gong, A. Bandis, A. Tao, G. Meresi, Y. Wang, P. T. Inglefield, A. A. Jones, and W. –Y. Wen. "Self-diffusion of Water, Ethanol and Decafluoropentane in Perfluorosulfonate Ionomer by Pulse Field Gradient NMR", *Polymer*, **42**, 6485 (2001)

23. H. R. Zelsmann, M. Pineri, M. Thomas, and M. Escoubes. "Water self-diffusion coefficient determination in an ion exchange membrane by optical measurement", *J. Appl. Polym. Sci.*, **41**, 1673 (1990)

24. T. F. Fuller, Ph. D. Thesis, University of California, Berkeley, CA (1992)

25. S. Motupally, A. J. Becker, and J. W. Weidner, "Diffusion of Water in Nafion 115 Membranes", *J. Electrochem. Soc.*, **147**, 3171 (2000)

26. M. Eikerling, Y. I. Kharkats, A. A. Kornyshev, Y. M. Volfkovich, "Phenomenological Theory of Electro-osmotic Effect and Water Management in Polymer Electrolyte Proton-Conducting Membranes", *J. Electrochem. Soc.*, **145**, 2684 (1998)

27. F. Meier, G. Eigenberger, "Transport Parameters for the Modeling of Water Transport in Ionomer Membranes for PEM-fuel cells", *Electrochimica Acta*, in press.

28. D. Rivin, C. E. Kendrick, P. W. Gibson, and N. S. Schneider, "Solubility and Transport Behavior of Water and Alcohols in Nafion®", *Polymer*, 42, 623 (2001)

29. P. Krtil, A. Trojanek, and Z. Samec, "Kinetics of Water Sorption in Nafion thin films – Quartz Crystal Microbalance Study", *J. Phys. Chem. B*, 105, 7979 (2001)

30. T. Okada, "Theory for Water Management in membranes for polymer electrolyte fuel cells – Part 1. The effect of impurity ions at the anode side on the membrane performances", *J. of Electroanal. Chem.*, 465, 1 (1999)

31. F. Chen, Y. G. Su, C. Y. Soong, W. M. Yan, and H. S. Chu, "Transient Behavior of Water Transport in the Membrane of a PEM Fuel Cell", *J. of Electroanal. Chem.*, 566, 85 (2004)

32. S. Ge, X. Li, B. Yi, and I-M. Hsing, "Absorption, Desorption, and Transport of Water in Polymer Elecctrolyte Membrane for Fuel Cells", *J. Electrochem. Soc.* **152**, A1149 (2005)

33. M. W. Verbrugge, and R. F. Hill, "Ion and Solvent Transport in Ion-Exchange Membranes I. A Macrohomogeneous Mathematical Model", *J. Electrochem. Soc.* **137**, 886 (1990)

34. M. W. Verbrugge, and R. F. Hill, "Ion and Solvent Transport in Ion-Exchange Membranes II. A Radiotracer Study of the Sulfuric-Acid, Nafion ll7 System", *J. Electrochem. Soc.* **137**, 893 (1990)

35. M. W. Verbrugge, and R. F. Hill, "Transport Phenomena In Perfluorosulfonic Acid Membranes During The Passage Of Current", *J. Electrochem. Soc.* **137**, 1131 (1990)

36. T. F. Fuller, J. Newman, *J. Electrochem. Soc.* **139**, 1332 (1992)

37. T. A. Zawodzinski, J. Davey, J. Valerio, and S. Gottesfeld, "The Water Content Dependance of Electro-osmotic Drag in Proton-conducting Polymer Electrolytes", *Electrochimica Acta*, **40**, 297 (1995)

38. X. Ren, W. Henderson, and S. Gottesfeld, "Electro-osmotic Drag of Water in Ionomeric Membranes: New Measurements Employing a Direct Methanol Fuel Cell", *J. Electrochem. Soc.* **144**, L267 (1997)

39. X. Ren, and S. Gottesfeld, "Electro-osmotic Drag of Water in Poly (perfluorosulfonic acid) Membranes", *J. Electrochem. Soc.* **148**, A87 (2001)

40. M. Ise, K. D. Kreuer, J. Maier, "Electro-osmotic Drag in Polymer Electrolyte Membranes: an Electrophoretic NMR Study", *Solid State Ionics*, **128**, 213 (1999)

41. S. Motupally, A. J. Becker, and J. W. Weidner, "Water Transport in PEM Electrolyzers Used to Recycle Anhydrous HCl: I Characterization of Diffusion and electro-Osmotic Drag", *J. Electrochem. Soc.*, **149**, D63 (2002)

42. S. Ge, B. Yi, P. Ming, "Experimental Determination of Electro-Osmotic Drag Coefficient in Nafion Membrane for Fuel Cells", *J. Electrochem. Soc.* **153**, A1443 (2006)

43. X.-G. Yang, Nick Burke, C.-Y. Wang, K. Tajiri, and K. Shinohara, "Simultaneous Measurements of Species and Current Distributions in a PEFC under Low-Humidity Operation", *J. Electrochem. Soc.* **152**, A759 (2005)

44. S. A. Freunberger, M. Santis, I. A. Schneider, A. Wokaun, and F. N. Büchi, "In-Plane Effects in Large-Scale PEMFCs Model Formulation and Validation", *J. Electrochem. Soc.*, **153**, A396 (2006)

45. S. A. Freunberger, A. Wokaun, and F. N. Büchi, "In-Plane Effects in Large-Scale PEFCs II. The Influence of Cooling Strategy on Cell Performance", *J. Electrochem. Soc.*, **153**, A909 (2006)

46. S. Koter, "The Equivalent Pore Radius of Charged Membranes from Electroosmotic Flow", *J. Membr. Sci.*, **166**, 127 (2000)

47. M. K. Petersen, S. S. Iyengar, T. J. F. Day, and G. A. Voth, "The Hydrated Proton at the Water Liquid/Vapor Interface", *J. Phys. Chem. B*, **108**, 11877 (2004)

48. H. Lapid, N. Agmon, M. K. Petersen and G. a. Voth, "A Bond-order Analysis of the Mechanism for the Hydrated Proton Mobility in Liquid Water", *J. Chem. Phys.*, **122**, 041506 (2004)

49. M. K. Petersen, F. Wang, N. P. Blake, H. Metiu, and G. A. Voth, "Excess Proton Solvation and Delocalization in a Hydrophilic Pocket of the Proton Conducting Polymer Membrane Nafion™", *J. Phys. Chem. B*, **109**, 3727 (2005)

50. K. D. Kreuer, "On the Development of Proton Conducting Polymer Membranes for Hydrogen and Methanol Fuel Cells" *J. Membr. Sci.*, **185**, 29 (2001)

51. M. Eikerling, A. A. Kornyshew, and U. Stimming, "Electrophysical Properties of Polymer Electrolyte Membranes: A Random Network Model", *J. Phys. Chem. B*, **101**, 10807(1997)

52. D. M. Bernardi, and M. W. Verbrugge, "A Mathematical Model of the Solid-Polymer-Electrolyte Fuel Cell", *J. Electrochem. Soc.* **139**, 2477 (1992)

53. T. F. Fuller, and J. Newman, "Water and Thermal Management in Solid-Polymer-Electrolyte Fuel Cells", *J. Electrochem. Soc.* **140**, 1218 (1993)

54. T. E. Springer, M. S. Wilson, and S. Gottesfeld, "Modeling and Experimental Diagnostics in Polymer Electrolyte Fuel Cells", *J. Electrochem. Soc.* **140**, 3513 (1993)

55. T. V. Nguyen and R. E. White, "A Water and Heat Management Model for Proton-Exchange-Membrane Fuel Cells", *J. Electrochem. Soc.*, 140, 2178 (1993).

56. T. Okata, G. Xie, and M. Meeg, "Simulation for Water Management in Membranes for Polymer Electrolyte Fuel Cells", *Electrochimica Acta*, **43**, 2141 (1998)

57. V. Gurau, H. Liu, and S. Kakaç, "Two-Dimensional Model for Proton Exchange Membrane Fuel Cells", *AIChE J.*, **4**, 137 (1998)

58. S. Um, C. -Y. Wang, and K.S. Chen, "Computational Fluid Dynamics Modeling of Proton Exchange Membrane Fuel Cells," *J. Electrochem. Soc.*, **147**, 4485 (2000)

59. S. Shimpalee, and S. Dutta, "Numerical Prediction of Temperature Distribution in PEM Fuel Cells", *Numerical Heat Transfer, Part A*, **38**, 111 (2000)

60. G. J. M. Janssen, "A Phenomenological Model of Water Transport in a Proton Exchange Membrane Fuel Cell", *J. Electrochem. Soc.*, **148**, A1313 (2001)

61. L. Pisani, G. Murgia, M. Valentín, and B. D'Aguanno, "A Working Model of Polymer Electrolyte Fuel Cells Comparisons between Theory and Experiments", *J. Electrochem. Soc.*, **149**, A898 (2003)

62. W-k. Lee, S. Shimpalee, and J. W. Van Zee, "Verifying Predictions of Water and Current Distributions in a Serpentine Flow Field Polymer Electrolyte Membrane Fuel Cell", *J. Electrochem. Soc.*, **150**, A341 (2003)

63. A. A. Kulikovsky, "Quasi-3D Modeling of Water Transport in Polymer Electrolyte Fuel Cells", *J. Electrochem. Soc.*, **150**, A1432 (2003)

64. S. Mazumder, and J. V. Cole, "Rigorous 3-D Mathematical Modeling of PEM Fuel Cells I. Model Predictions without Liquid Water Transport", *J. Electrochem. Soc.*, **150**, A1510 (2003)

65. S. Mazumder, and J. V. Cole, "Rigorous 3-D Mathematical Modeling of PEM Fuel Cells II. Model Predictions with Liquid Water Transport", *J. Electrochem. Soc.*, **150**, A1510 (2003)

66. P. Berg, K. Promislow, J. S. Pierre, J. Stumper, and B. wetton, "Water Management in PEM Fuel Cells", *J. Electrochem. Soc.*, **151**, A341 (2004)

67. F. N. Büchi, and G. G. Scherer, "Investigation of the Transversal Water Profile in Nafion Membranes in Polymer Electrolyte Fuel Cells", *J. Electrochem. Soc.*, **148**, A183 (2001)

68. D. Natarajan, and T. V. Nguyen, "A Two-Dimensional, Two-Phase, Multicomponent, Transient Model for the Cathode of a Proton Exchange Membrane Fuel Cell Using Conventional Gas Distributors", *J. Electrochem. Soc.*, **148**, A1324 (2001)

69. T. Berning, and N. Dajilali, "A 3D, Multiphase, Multicomponent Model of the Cathode and Anode of a PEM Fuel Cell", *J. Electrochem. Soc.*, **150**, A1589 (2003)

70. U. Pasaogullari, and C. Y. Wang, "Liquid Water Transport in Gas Diffusion Layer of Polymer Electrolyte fuel Cells", *J. Electrochem. Soc.*, **151**, A399 (2004)

71. A. Z. Weber, R. M. Darling, and J. Newman, "Modeling Two-phase Behavior in PEFCs", *J. Electrochem. Soc.*, **151**, A1715 (2003)

72 S. M. Senn, and D. Poulikakos, "Multiphase Transport Phenomena in the Diffusion Zone of a PEM Fuel Cell", *J. of Heat Trans*, **127**, 1245 (2005)

73. G. Lin, and T. V. Nguyen, "A Two-Dimensional Two-Phase Model of a PEM Fuel Cell", *J. Electrochem. Soc.*, **153**, A372 (2006)

74. H. Ju, and C.-Y. Wang, "Experimental Validation of a PEM Fuel Cell Model by Current Distribution Data", *J. Electrochem. Soc.*, **151**, A1954 (2004)

75. H. Ju, C.-Y. Wang, S. Cleghorn, and U. Beuscher, "Nonisothermal Modeling of Polymer Electrolyte Fuel Cells I. Experimental Validation", *J. Electrochem. Soc.*, 152, A1645 (2005)

76. H. Ju, C.-Y. Wang, S. Cleghorn, and U. Beuscher, "Nonisothermal Modeling of Polymer Electrolyte Fuel Cells II. Parametric Study of Low-Humidity Operation", *J. Electrochem. Soc.*, 153, A249 (2005)

77. J. J. Hwang, "Thermal-Electrochemical Modeling of a Proton Exchange Membrane Fuel Cell", *J. Electrochem. Soc.*, **153**, A216 (2006)

78 Y. Wang, C.-Y. Wang, "Modeling Polymer Electrolyte Fuel Cells with Large Density and Velocity Changes", *J. Electrochem. Soc.*, 152, A445 (2005)

79. Y. Wang, and C.-Y. Wang, "Transient Analysis of Polymer Electrolyte Fuel Cells", *Electrochimica Acta*, **50**, 1307 (2005)

80. S. J. C. Cleghorn, C. R. Derouin, M. S. Wilson, and S. Gottesfeld, "A Printed Circuit Board Appoach to Measureing Current Distribution in a Fuel Cell", *J. Appl. Electrochem.*, **28**, 663 (1997)

81. J. Stumper, S. A. Campbell, D. P. Wilkinson, M. C. Johnson, and M Davis, "In-situ Methods for the Determination of Current Distributions in PEM Fuel Cells", *Electrochimica Acta*, **43**, 3773 (1998)

82. C. Wieser, a. Helmbold, and E. Gülzow, "A New Technique for Two-Dimensional Current Distribution Measurements in Electrochemical Cells", *J. Appl. Electrochem.*, **30**, 803 (2000)

83. M. M. Mench, and C. Y. Wang, "An In Situ Method for Determination of Current Distribution in PEM Fuel Cells Applied to a Direct Methanol Fuel Cell", *J. Electrochem. Soc.*, **150**, A79 (2003)

84. G. Bender, M. S. Wilson, T. A. Zawodzinski, "Further Refinements in the Segmented Cell Approach to Diagnosing Performance in Polymer Electrolyte Fuel Cells", *J. of Power Sources*, **123**, 163 (2003)

85. B. Andreaus, A. J. McEvoy, and G. G. Scherer, "Analysis of Performance Losses in Polymer Electrolyte Fuel Cells at High Current Density by Impedance Spectroscopy", *Electrochimica Acta*, **47**, 2223 (2002)

86. T. Abe, H. Shima, K. Watanabe, and Y. Ito, "Study of PEFCs by AC Impedance, Current Interrupt, and Dew Point Measurements", *J. Electrochem. Soc.*, **151**, A101 (2004)

87. B. Andreaus, G. G. Scherer, "Proton-conducting Polymer Membranes in Fuel Cells---Humidification Aspects", *Solid State Ionics*, **168**, 311 (2003)

88. I. A. Schneider, H. Kuhn, A. Wokaun, and G. G. Scherer, "Study of Water Balance in a Polymer Electrolyte Fuel Cell by Locally Resolved Impedance Spectroscopy", *J. Electrochem. Soc.*, **152**, A2383 (2005)

89. W-k. Lee, S. Shimpalee, and J. W. Van Zee, "Verifying Predictions of Water and Current Distributions in a Serpentine Flow Field Polymer Electrolyte Membrane Fuel Cell", *J. Electrochem. Soc.*, **150**, A341 (2003)

90. R. J. Bellows, M. Y. Arif, A. K. Thompson, and D. Jacobson, "Neutron Imaging Technique for In Situ Measurement of Water Transport Gradients within Nafion in Polymer Electrolyte Fuel Cells", *J. Electrochem. Soc.*, **146**, 1099 (1999)

91. M. A. Hickner, N. P. Siegel, K. S. Chen, D. N. McBrayer, D. S. Hussey, D. L. Jacobson, and M. Arif, "Real-Time Imaging of Liquid Water in an Operating Proton Exchange Membrane Fuel Cell", *J. Electrochem. Soc.*, **153**, A902 (2005)

92. G. J. M. Janssen, and M. L. J. Overvelde, "Water Transport in the Proton-exchange-membrane Fuel Cell: Measurements of the Effective Drag Coefficient", *J. of Power Source*, **101**, 117 (2001)

93. T. V. Nguyen, and M. W. Knobbe, "A Liquid Water Management Strategy for PEM Fuel Cell Stacks", *J. of Power Sources*, **114**, 70 (2003)

94. K. Tüber, D. Pócza, and C. Hebling, "Visualization of Water Buildup in the Cathode of a Transparent PEM Fuel Cell", *J. of Power Source*, **124**, 403 (2003)

95. Oliver H. Finckh, "Experimental Study on Dilution Effects and Current Distribution of a Polymer Electrolyte Membrance Fuel Cell", *Master Thesis*, Penn. State University, PA (2002)

96. M. M. Mench, Q. Dong, C.-Y. Wang, "In situ Water Distribution Measurements in a Polymer Electrolyte Fuel Cell", *J. Power Sources*, **124**, 90 (2003)

97. Q. Dong, J. Kull, and M. M. Mench, "Real-time Water Distribution in a Polymer Electrolyte Fuel Cell", *J. Power Sources*, **139**, 106 (2005)

98. D. Burford, "In-situ temperature measurement", *Masters Thesis*, Penn. State University, PA (2004)

99. B. R. Gerdes, "Design of a Distributed Polymer Electrolyte Fuel Cell and Application to Freeze-Thaw Cycling Behavior", *Masters Thesis*, Penn State Univeristy, PA (2005)

100. J. Koryta, J. Dvořák, and L. Kavan, "Principles of Electrochemistry" (Second Edition), John Wiley & Sons, New York, 1993

101. J. R. Scully, D. C. Silverman, and M. W. Kending, *Electrochemical Imperdance: Analysis and Interpretation*, ASTM, 1993

102. C.-Y. Wang, "Two-phase Flow and Transport in PEM Fuel Cells", in: Handbook of Fuel Cells, Wiley, New York, 2002

103. J. R. Atkins, S. C. Savett, S.E. Creager, "Large-scale Current Fluctuations in PEM Fuel Cells Operating with Reduced Feed Stream Humidification", *J. Power Sources*, **128**, 201 (2004)

104. Q. Li, R. He, J.-A. Gao, J. O. Jensen, and N. J. Bjerrum, "The CO Poisoning Effect in PEMFCs Operational at Temperatures up to 200°C", *J. Electrochem. Soc.*, **150**, A1559 (2003)

105. R. Jiang, H. R. Kunz, and J. M. Fenton, "Electrochemical Oxidation of H_2 and H_2/CO Mixtures in Higher Temperature (T_{cell} > 100°C) Proton Exchange Membrane Fuel Cells: Electrochemical Impedance Spectroscopy", *J. Electrochem. Soc.*, **152**, A1329 (2005)

106. E. L. Cussler, *Diffusion: Mass Transfer in Fluid Systems*, Cambridge University Press, New York, 1984

107 L. R. Jordan, A. K. Shukla, T. Behrsing, N. R. Avery, B. C. Muddle, and M. Forsyth, "Effect of diffusion-layer morphology on the performance of polymer electrolyte fuel cells operating at atmospheric pressure", *J. Appl. Electrochem.*, **30**, 641 (2000)

108 F. Jaouen, G. Lindbergh, and G. Sundholm, "Investigation of Mass-Transport Limitations in the Solid Polymer Fuel Cell Cathode I. Mathematical Model", *J. Electrochem. Soc.*, **149**, A437 (2002)

109 J. Soler, E. Hontañón, L. Daza, "Electrode permeability and flow-field configuration: influence on the performance of a PEMFC", *J. Power Sources*, **118**, 172 (2003)

110 M. V. Williams, H. R. Kunz, and J. M. Fenton, "Influence of Convection Through Gas-Diffusion Layers on Limiting Current in PEM FCs Using a Serpentine Flow Field", *J. Electrochem. Soc.*, **151**, A1617 (2004)

111 A. Z. Weber, and J. Newman, "Effects of Microporous Layers in Polymer Electrolyte Fuel Cells", *J. Electrochem. Soc.*, **152**, A677 (2005)

112. Q. Dong, M. M. Mench, S. Cleghorn, and U. Beuscher, "Distributed Performance of Polymer Electrolyte Fuel Cells under Low-Humidity Conditions", *J. Electrochem. Soc.*, **152**, A2114 (2005)

Appendix

Compaq Digital FORTRAN Code for the Quasi-2D Mass Transport Model

```
program main
!
! Quasi 2-D transport model for water diffusion coefficient in Gore Select series #57
! reinforced membrane
!
   use SetData
   use Solve

   implicit none

   integer k

!************************************
          humidity='A0/C50'
          T=110.0
          Beta=0.8
!************************************

   call SetConstant    ! Set cell dimension and material properties
   call SetInput       ! Set cell operation conditions and measured current distribution and
                       ! inlet humidities

   ! The channel model
   do k=0,99,1
      ! call the 1-D model for effective drag coefficient
      call OneDimension(NN(k),NO(k),NW_c(k),NH(k),NW_a(k),i(k),alpha(k),xN(k,0:460),xO(k,0:460)&
                        , xW_c(k,0:460),xH(k,0:460),xW_a(k,0:460),lamda(k,0:720))

      ! determine the inlet condition of the next element cell
       NN(k+1)=NN(k)  ! nitrogen molar flowrate
       NO(k+1)=NO(k)-(1.0/4.0/F)*w*dz*i(k)   ! oxygen molar flowrate
       NW_c(k+1)=NW_c(k)+alpha(k)*(1.0/F)*w*dz*i(k)+0.5*(1.0/F)*w*dz*i(k)

       NH(k+1)=NH(k)-(1.0/2.0/F)*w*dz*i(k)
       NW_a(k+1)=NW_a(k)-alpha(k)*(1.0/F)*w*dz*i(k)

   enddo

   ! Output cathode water mole fraction
   OPEN(11,FILE='cathode water.out')
   do k=0,460,1
         write(11, 20) xW_c(0:99,k)
   enddo
20 format (100(1x, f8.5))
    close (11)
```

```
30  format (a8,100(1x, f12.8))
! Output effective drag coefficient and mole fractions in gas channel
   Open (12, file='alpha.out')
   write(12,30) 'alpha',alpha(0:99)
   write(12,30) 'NN', NN(0:99)
   write(12,30) 'NO', NO(0:99)
   write(12,30) 'NW_c', NW_c(0:99)
   write(12,30) 'NH',NH(0:99)
   write(12,30) 'NW_a',NW_a(0:99)
   close (12)

   ! Output anode water mole fraction
   Open (13, file='anode water.out')
   do k=0,460,1
      write(13, 20) xW_a(0:99,k)
   enddo
   close(13)

   ! Output Cathode Oxygen mole fraction
   open (14, file='Oxygen.out')
   do k=0,460,1
       write(14, 20) xO(0:99,k)
   enddo
   close(14)

   ! Output Cathode Nitrogen mole fraction
   open (15, file='Nitrogen.out')
   do k=0,460,1
      write(15, 20) xN(0:99,k)
   enddo
   close(15)

   ! Output Hydrogen mole fraction
   open (16, file='Hydrogen.out')
   do k=0,460,1
       write(16, 20) xH(0:99,k)
   enddo
   close(16)

   ! output membrane wate
    open (17,file='lamda.out')
        do k=0,720,1
            write(17,20) lamda(0:99,k)
        enddo
    close(17)

end program main


module SetData
!  setup fuel cell dimensions, operation conditions and material properties
     implicit none
```

```
    double precision :: delta_GDL, delta_MPL, delta_CL, delta_re   ! Thicknesses
    double precision :: w, L, Area    ! Fuel cell dimensions
    double precision :: P, T, Stoi_a, Stoi_c, Psat     ! Fuel cell operation condition
    double precision :: e_GDL, e_MPL, e_gCL, e_mCL   ! Porosity of fuel cell materials,
    double precision :: Tor     ! tortuosity
    double precision :: rho_dry, EW    ! Density and equavalent molecular weight
    double precision :: DWH_0, DWN_0, DWO_0       ! Diffusion coefficients in open spaces
    double precision :: DON_0, DW_m     ! Diffusion coefficients in open spaces
    double precision :: DWH_eff, DWN_eff, DWO_eff ! Effective diffusion coefficients in porous media

    double precision ::, DON_eff, DWm_eff   ! Effective diffusion coefficients in porous media
    double precision :: nd   ! Electro-osmotic drag coefficient

   double precision :: NN(0:100), NO(0:100), NW_c(0:100), NH(0:100), NW_a(0:100)   ! Molar flowrates
   double precision :: i(0:99), alpha(0:99), beta ! Measured local current density, effective drag coefficient,
                                                  ! and correction factor for reinforced membrane

   double precision :: xN(0:100, 0:460), xO(0:100, 0:460), xW_c(0:100, 0:460) ! Mole fractions of cathode
                                                                              ! species
   double precision :: xH(0:100, 0:460), xW_a(0:100, 0:460)    ! Mole fractions of anode species
   double precision :: lamda(0:99, 0:720), aw_c(0:100, 0:460), aw_a(0:100, 0:460), aw_re(0:100, 0:720)
                                                                 ! Water activities in the fuel cell

   double precision :: dz, dy_GDL, dy_MPL, dy_CL, dy_re   ! Element sizes

   double precision, parameter :: F=96485, R=8.314      ! Farady constant F and universal gas constant R

    character  humidity*7     ! inlet humidity

Contains

    subroutine SetConstant
      ! Set dimension and material property constants
      implicit none

      delta_GDL=0.03     ! Thickness of Gas Diffusion Layer, cm
      delta_MPL=0.006    ! Thickness of Micro Porous Layer, cm
      delta_CL=0.001     ! Thickness of Catalyst Layer, cm
      delta_re=0.0018    ! Thickness of Reinforced Membrane, cm


      w=1.01           ! Width of the membrane, cm
      L=49.5           ! Length of the gas flow channel
      Area=50.0         ! Area of the membrane, cm^2

      dz=L/100.0                ! Element length
      dy_GDL=delta_GDL/300.0      ! Element thickness in GDL
      dy_MPL=delta_MPL/60.0       ! Element thickness in MP
      dy_CL=delta_CL/100.0        ! Element thickness in catalyst layer
      dy_re=delta_re/720.0        ! Element thickness in membrane

      e_GDL=0.5         ! Porosity of GDL
      e_MPL=0.5         ! Porosity of MPL
      e_gCL=0.6         ! Porosity of catalyst layer
```

```
    e_mCL=0.26       ! Volume fraction of ionmer in catalyst layer
    Tor=5.0

    rho_dry=2.0      ! Density of dry ionmer, g/cm^3
   EW=1100          ! Equivalent molecular weight of ionmer, g/mol

   DWH_0=0.915      ! Binary diffusion coefficient of H2O-H2 at 307.1K and 1.0 atm, cm^2/s
   DWO_0=0.282      ! Binary diffusion coefficient of H2O-O2 at 308.1K and 1.0 atm, cm^2/s
   DWN_0=0.256      ! Binary diffusion coefficient of H2O-N2 at 307.5K and 1.0 atm, cm^2/s
   DON_0=0.22       ! Binary diffusion coefficient of O2-N2 at 293.2K and 1.0 atm, cm^2/s

    nd=1.0          ! Electro-osmotic drag coefficient for lamda<14.0

   Stoi_a=1.2       ! Anode Stoichiometry
   Stoi_c=2.0       ! Cathode Stoichiometry
   P=2.7           ! Fuel cell internal Pressure, atm


end subroutine SetConstant




subroutine SetInput
   ! Fuel cell operation conditions, A/C RH=0/50, need to be updated for different conditions
    implicit none
    double precision FracDis      ! Fractional distrance from the inlet
    integer j

    Psat=CalPsat(T)          ! Water saturation pressure

    Call MoleFlowRate

    ! Load the measured current density
    do j=0,99,1
        FracDis=(real(j)+0.5)/100.0  ! Fractional distance the gas channel inlets
        i(j)=Cali(FracDis, T, humidity)
    enddo

    alpha(0:99)=0.0          ! Give the initial guess value of water effective drag coefficient

 end subroutine SetInput


 subroutine MoleFlowRate
   implicit none

   if (T==95.0) then

       if (humidity=='A0/C50') then
           NN(0)= 6.238d-4          ! Nitrogen molar flowrate at cathode inlet
           NO(0)= 1.658d-4          ! Oxygen molar flowrate at cathode inlet
           NW_c(0)= 1.225d-4        ! Water vapor molar flowrate at cathode inlet
```

```
            NH(0)= 1.990d-4          ! Hydrogen molar flowrate at anode inlet
            NW_a(0)= 0.0d-4            ! Water vapor molar flowrate at anode inlet

        elseif (humidity=='A30/C30') then
            NN(0)= 5.575d-4          ! Nitrogen molar flowrate at cathode inlet
            NO(0)= 1.482d-4          ! Oxygen molar flowrate at cathode inlet
            NW_c(0)= 0.8901d-4        ! Water vapor molar flowrate at cathode inlet

            NH(0)= 1.778d-4          ! Hydrogen molar flowrate at anode inlet
            NW_a(0)= 0.1788d-4           ! Water vapor molar flowrate at anode inlet

        else
            NN(0)= 3.704d-4          ! Nitrogen molar flowrate at cathode inlet
            NO(0)= 0.9846d-4          ! Oxygen molar flowrate at cathode inlet
            NW_c(0)= 0.0d-4         ! Water vapor molar flowrate at cathode inlet

            NH(0)= 1.182d-4          ! Hydrogen molar flowrate at anode inlet
            NW_a(0)= 0.239d-4            ! Water vapor molar flowrate at anode inlet

        endif

    elseif(T==110.0) then

        if (humidity=='A0/C50') then
            NN(0)= 4.932d-4          ! Nitrogen molar flowrate at cathode inlet
            NO(0)= 1.311d-4          ! Oxygen molar flowrate at cathode inlet
            NW_c(0)= 2.151d-4         ! Water vapor molar flowrate at cathode inlet

            NH(0)= 1.573d-4          ! Hydrogen molar flowrate at anode inlet
            NW_a(0)= 0.0d-4            ! Water vapor molar flowrate at anode inlet

        elseif (humidity=='A30/C30') then
            NN(0)= 4.113d-4          ! Nitrogen molar flowrate at cathode inlet
            NO(0)= 1.093d-4          ! Oxygen molar flowrate at cathode inlet
            NW_c(0)= 0.889d-4         ! Water vapor molar flowrate at cathode inlet

            NH(0)= 1.312d-4          ! Hydrogen molar flowrate at anode inlet
            NW_a(0)= 0.228d-4            ! Water vapor molar flowrate at anode inlet

        else
            NN(0)= 2.495d-4          ! Nitrogen molar flowrate at cathode inlet
            NO(0)= 0.663d-4          ! Oxygen molar flowrate at cathode inlet
            NW_c(0)= 0.0d-4         ! Water vapor molar flowrate at cathode inlet

            NH(0)= 0.796d-4          ! Hydrogen molar flowrate at anode inlet
            NW_a(0)= 0.261d-4            ! Water vapor molar flowrate at anode inlet

        endif

    endif

    return

end subroutine MoleFlowRate
```

```
double precision function Cali(d, T, humidity)
! Calculate local current density based on the trend line of          measured current density

    implicit none
    double precision d, T
    character humidity*7

    if (T==95.0) then
        if (humidity=='A0/C50') then
            Cali=2.1511*d**3-4.7839*d**2 + 3.1293*d+ 0.1343
        elseif (humidity=='A30/C30') then
            Cali=-0.6064*d**3+0.05*d**2 + 0.7586*d+ 0.3276
        else
            Cali=-3.2316*d**3+4.9812*d**2- 1.6596*d+ 0.3478
        endif
    elseif(T==110.0) then
        if (humidity=='A0/C50') then
            Cali=1.1883*d**3- 2.813*d**2 + 2.0005*d+ 0.1459
        elseif (humidity=='A30/C30') then
            Cali=-0.3467*d**3+ 0.0821*d**2 + 0.4371*d+ 0.263
        else
            Cali=-1.2735*d**3+ 2.1091*d**2- 0.7966*d+ 0.2701
        endif
    endif
    return
end function Cali


double precision function CalDWH_eff(porosity, T, P, DWH_0)
     ! Calculate the effective binary diffusion coefficient of Water Vapor-Hydrogen
      implicit none
     double precision :: porosity, T, P, DWH_0

    CalDWH_eff=porosity/Tor*(DWH_0*((T+273.15)/307.1)**1.5*(1.0/P))

end function CalDWH_eff


double precision function CalDWO_eff(porosity, T, P, DWO_0)
    ! Calculate the effective binary diffusion coefficient of Water Vapor-Oxygen
    implicit none
   double precision :: porosity, T, P, DWO_0

   CalDWO_eff=porosity/Tor*(DWO_0*((T+273.15)/308.1)**1.5*(1.0/P))

end function CalDWO_eff


double precision function CalDWN_eff(porosity, T, P, DWN_0)
    ! Calculate the effective binary diffusion coefficient of Water Vapor-Oxygen
    implicit none
   double precision :: porosity, T, P, DWN_0
```

```
      CalDWN_eff=porosity/Tor*(DWN_0*((T+273.15)/307.5)**1.5*(1.0/P))

  end function CalDWN_eff
   double precision function CalDON_eff(porosity, T, P, DON_0)
       ! Calculate the effective binary diffusion coefficient of Water Vapor-Oxygen
       implicit none
       double precision :: porosity, T, P, DON_0

       CalDON_eff=porosity/Tor*(DON_0*((T+273.15)/307.5)**1.5*(1.0/P))

   end function CalDON_eff


   double precision function CalDW_m(T, lamda)
       ! Calculate the diffusion coefficient of Water in ionmer
       implicit none
      double precision :: T, lamda

      if (lamda>=4.0) then
          CalDW_m=1.0E-6*exp(2416.0*(1/303.0-1.0/(273.15+T)))*(2.563-0.33*lamda+0.0264*&
                      lamda**2- 0.000671*lamda**3)
      elseif (lamda>=3.0 .and. lamda<4.0) then
          CalDW_m=1.0E-6*exp(2416.0*(1/303.0-1.0/(273.15+T)))*(6.62-1.24*lamda)
      elseif (lamda>=2.0 .and. lamda<3.0) then
          CalDW_m=1.0E-6*exp(2416.0*(1/303.0-1.0/(273.15+T)))*(-3.1+2.0*lamda)
      else
          CalDW_m=2.69E-6
      endif

   end function CalDW_m


   double precision function CalLamda(aw)
       ! Calculate the water content in membrane
      double precision :: aw
      Callamda=0.043+17.81*aw-39.85*aw**2+36.0*aw**3
   end function CalLamda


   double precision function CalPsat(T)
       implicit none
      double precision ::T
       CalPsat=10.0**(-2.1794+0.02953*T-9.1837E-5*T**2+1.4454E-7*T**3)
   end function CalPsat

End module SetData
```

```
Module Solve
! Solve local water effective drag coefficients by shooting iteration.
! Explicit Euler method for GDL, MPL and Catalyst Layer, iteration for the membrane.
  use SetData
  implicit none


contains

subroutine
    OneDimension(NN1,NO1,NW_c1,NH1,NW_a1,i1,alpha1,xN1,xO1,xW_c1,xH1,xW_a1,lamda1)
       !  The 1-D model

       implicit none

       double precision :: NN1,NO1,NW_c1,NH1, NW_a1, i1, alpha1, alpha2, flag1, flag2
                                  ! channel molar flowrates and local current density, effective drag coefficient
       double precision :: xN1(0:460), xO1(0:460), xW_c1(0:460), xH1(0:460),
       double precision :: xW_a1(0:460), lamda1(0:720),  lamda2(0:720)
       double precision :: nO,nN, nW_c, nH, nW_a, nWg_c, nWg_a
                                  ! gas phase water molar flux in catalyst layer
       double precision :: dCwm_c_dy,  dCwm_a_dy
                                  ! derivation of ionmer phase water concentration in catalyst layers
       double precision :: aw, lamda_CL ! water activity and water content
       double precision :: Dw_re(0:720)
       integer :: j, iteration

       !  Calculate species mole fractions in gas flow channels
       xO1(0)=NO1/(NN1+NO1+NW_c1)  ! oxygen mole fraction in cathode gas flow channel
       xW_c1(0)=NW_c1/(NN1+NO1+NW_c1)   ! cathode water vapor mole fraction in gas flow channel
       xN1(0)=1.0-(xO1(0)+xW_c1(0))    ! nitrogen mole fraction in cathode gas flow channel


       xW_a1(0)=Nw_a1/(NH1+Nw_a1)  ! anode water vapor mole fraction in gas flow channel
       xH1(0)=1.0-xW_a1(0)

      !  Calculate effective water drag coefficient by shooting iteration
       alpha2=0.1
       flag1=1.0d-3
       flag2=1.0d-5

       do while (abs(alpha2-alpha1)>flag1)

            ! First, calculate the boundary conditions at the two electrolyte membrane/catalyst layer interfaces
            ! by Euler method with initial alpha value

            ! Cathode side species molar flux in GDL and MPL
           nO=i1/(4.0*F)   ! oxygen molar flux through plain
```

```
 nW_c=-i1*(1.0/(2.0*F)+alpha1/F)  !  cathode water molar flux through plain
 nN=0.0  !  nitrogen molar flux through plain

 ! Anode side species molar flux in GDL and MPL
 nH=i1/(2.0*F)  ! Hydrogen molar flux through plain
 nW_a=alpha1*i1/F   ! Water vapor molar flux through plain

 ! Calculate species mole fractions in GDL
 DWO_eff = CalDWO_eff(e_GDL, T, P, DWO_0)
                        ! effective binary diffusion coefficient of water vaper-oxygen
 DON_eff = CalDON_eff(e_GDL, T, P, DON_0)
                        ! effective binary diffusion coefficient of oxygen-nitrogen
 DWN_eff = CalDWN_eff(e_GDL, T, P, DWN_0)
                        ! effective binary diffusion coefficient of water vapor-nitrogen

 DWH_eff = CalDWH_eff(e_GDL, T, P, DWH_0)
                       ! effective binary diffusion coefficient of water vapor-hydrogen

 do j=1,300, 1
     xO1(j)= xO1(j-1) + dy_GDL*dxO_dy(DWO_eff, DON_eff, xO1(j-1), xW_c1(j-1),&
              xN1(j-1), nO, nW_c, nN)          ! oxygen mole fraction
    xW_c1(j)=xW_c1(j-1) + dy_GDL*dxW_c_dy(DWO_eff, DWN_eff, xO1(j-1),&
              xW_c1(j-1), xN1(j-1), nO, nW_c, nN)        ! cathode water vapor mole fraction
    xN1(j)=1.0-xO1(j)-xW_c1(j)         ! nitrogen mole fraction

    xW_a1(j)=xW_a1(j-1) + dy_GDL*dxW_a_dy(DWH_eff, xH1(j-1), xW_a1(j-1),nH, nW_a)
                                    ! anode water vapor mole fraction
    xH1(j)=1.0 - xW_a1(j)  ! hydrogen mole fraction
enddo

!  Calculate species mole fractions in MPL,
!  Renew effective diffusion coefficients first with the porosity of MPL
DWO_eff = CalDWO_eff(e_MPL, T, P, DWO_0)
                                    ! effective binary diffusion coefficient of water vaper-oxygen
DON_eff = CalDON_eff(e_MPL, T, P, DON_0)
                                    ! effective binary diffusion coefficient of oxygen-nitrogen
DWN_eff = CalDWN_eff(e_MPL, T, P, DWN_0)
                                    ! effective binary diffusion coefficient of water vapor-nitrogen

DWH_eff = CalDWH_eff(e_MPL, T, P, DWH_0)
                                    ! effective binary diffusion coefficient of water vapor-hydrogen

do j=301,360, 1
    xO1(j)= xO1(j-1) + dy_MPL*dxO_dy(DWO_eff, DON_eff, xO1(j-1), xW_c1(j-1),&
              xN1(j-1), nO, nW_c, nN)          ! oxygen mole fraction
    xW_c1(j)=xW_c1(j-1) + dy_MPL*dxW_c_dy(DWO_eff, DWN_eff, xO1(j-1),&
                xW_c1(j-1),xN1(j-1), nO, nW_c, nN)         ! cathode water vapor mole fraction
    xN1(j)=1.0-xO1(j)-xW_c1(j)            ! nitrogen mole fraction

    xW_a1(j)=xW_a1(j-1) + dy_MPL*dxW_a_dy(DWH_eff, xH1(j-1), xW_a1(j-1),nH, nW_a)
                                        ! anode water vapor mole fraction
    xH1(j)=1.0 - xW_a1(j)  ! hydrogen mole fraction
enddo
```

```
   !  Calculate species mole fractions in catalyst layer
   !  Renew effective diffusion coefficient first with the porosity of catalyst layer
   DWO_eff = CalDWO_eff(e_gCL, T, P, DWO_0)
                                  ! effective binary diffusion coefficient of water vaper-oxygen
   DON_eff = CalDON_eff(e_gCL, T, P, DON_0)
                                  ! effective binary diffusion coefficient of oxygen-nitrogen
   DWN_eff = CalDWN_eff(e_gCL, T, P, DWN_0)
                                  ! effective binary diffusion coefficient of water vapor-nitrogen
   DWH_eff = CalDWH_eff(e_gCL, T, P, DWH_0)
                                  ! effective binary diffusion coefficient of water vapor-hydrogen

  do j=361,460,1

     ! Cathode cathode side species molar flux in catalyst layer

     nO=i1/(4.0*F)*real(460-j+1)/100.0          ! oxygen molar flux through plain
     nN=0.0         !  nitrogen molar flux through plain

     nWg_c=-(alpha1-nd)*i1/F-((2.0*nd+1.0)/(2.0*F))*(real(460-j+1)/100.0)*i1

     xO1(j)= xO1(j-1) + dy_CL*dxO_dy(DWO_eff, DON_eff, xO1(j-1), xW_c1(j-1),&
              xN1(j-1), nO, nWg_c, nN)       ! oxygen mole fraction
     xW_c1(j)=xW_c1(j-1) + dy_CL*dxW_c_dy(DWO_eff, DWN_eff, xO1(j-1), &
                 xW_c1(j-1),xN1(j-1), nO, nWg_c, nN)   ! cathode water vapor mole fraction
     xN1(j)=1.0-xO1(j)-xW_c1(j)  ! nitrogen mole fraction

     nH=i1/(2.0*F)*real(460-j+1)/100.0  ! Hydrogen molar flux through plain
     nWg_a=(alpha1-nd)*(i1/F)+(nd*i1/F)*(real(460-j+1)/100.0)

     xW_a1(j)=xW_a1(j-1) + dy_CL*dxW_a_dy(DWH_eff, xH1(j-1), xW_a1(j-1),nH, nWg_a)
                                    ! anode water vapor mole fraction
     xH1(j)=1.0 - xW_a1(j)  ! hydrogen mole fraction

  enddo


! With interface conditions got from last step, solve membrane water content by iteration

! Calculate  water content at the anode membrane-catalyst interface
 aw=xW_a1(460)*P/Psat
 lamda1(0)=Callamda(aw)

 ! Calculate water content at the cathode membrane-catalyst interface
 aw=xW_c1(460)*P/Psat
 lamda1(720)=Callamda(aw)

! initialize the value of lamda1
do j=1,719,1
    lamda1(j)=lamda1(j-1)+(lamda1(720)-lamda1(0))/720.0
enddo

! initialize the old value

do while (abs(lamda1(719)-lamda2(719))>flag2)
```

```
        do j=0,720,1
           Dw_re(j)=beta*calDw_m(T, lamda1(j))
           lamda2(j)=lamda1(j)
        enddo

        do iteration=1,10,1
           do j=719,1,-1
                lamda1(j)=Dw_re(j)/(Dw_re(j)+Dw_re(j-1))*lamda1(j+1)+&
                          Dw_re(j1)/(Dw_re(j)+Dw_re(j-1))*lamda1(j-1)
           enddo
          ! new lamda1
        enddo

        ! calculate a new alpha according to the calculated water content
        Dw_re(719)=beta*calDw_m(T, lamda1(719))
        alpha2=nd-Dw_re(719)*(rho_dry/EW)*(F/i1)*(lamda1(720)-lamda1(719))/dy_re

        ! improve the value of alpha
        alpha1=0.9*alpha1+0.1*alpha2

    enddo

    return
end subroutine



! calculate the derivation of oxygen mole fraction in cathode GDL and MPL
 double precision function dxO_dy(DWO_eff, DON_eff, xxO, xxW, xxN, nO, nW_c, nN)
      implicit none
      double precision :: DWO_eff, DON_eff, xxO, xxW, xxN, nO, nW_c, nN
      dxO_dy=  (1.0e6*R*T/(P*1.01e5))*((xxO*nW_c-xxW*nO)/DWO_eff+(xxO*nN-xxN*nO)/DON_eff)
end function dxO_dy


! calculate the derivation of water mole fraction in cathode GDL and MPL
 double precision function dxW_c_dy(DWO_eff, DWN_eff, xxO, xxW, xxN, nO, nW_c, nN)
      implicit none
      double precision :: DWO_eff, DWN_eff, xxO, xxW, xxN, nO, nW_c, nN
      dxW_c_dy= (1.0e6*R*T/(P*1.01e5))*((xxW*nO-xxO*nW_c)/DWO_eff+(xxW*&
                nN-xxN*nW_c)/DWN_eff)
 end function dxW_c_dy

! calculate the derivation of water mole fraction in anode GDL and MPL
 double precision function dxW_a_dy(DWH_eff, xxH, xxW,nH, nW)
      implicit none
     double precision :: DWH_eff, xxH, xxW, nH, nW
     dxW_a_dy= (1.0e6*R*T/(P*1.01e5))*((xxW*nH-xxH*nW)/DWH_eff)
 end function dxW_a_dy

end module Solve
```

VITA

Qunlong Dong was born in 1976 in a small village in Henan Province, China. He earned his Bachelor of Science degree in automotive engineering and his minor in environmental engineering in July 1998, and his Master of Engineering degree in power machinery and engineering in July 2001, all from Tsinghua University, Beijing, China. Then he started to pursue Ph.D. study in the Pennsylvania State University, and earned his doctoral degree in mechanical engineering in 2006.